Synthesis of aqueous inks for the deposition of Al doped ZnO thin films and patterns

Kenny Vernieuwe

Promoter : Prof. Dr. Klaartje De Buysser

Thesis submitted in fulfilment of the requirements for the degree of Doctor (Ph.D.) in Science : Chemistry

Department of Inorganic and Physical Chemistry
Faculty of Science

"Stop walking through life as if you were blind,

You should reach for your goals

cause I'm reaching for mine."

Shawn Moltke, 1987

Dankwoord

Na iets meer dan 4 jaar, is het eindelijk zover. Met het schrijven van dit dankwoord leg ik de laatste hand aan deze thesis. Als doctoraatsstudent heb ik een aangename tijd gehad in gebouw S3 van Campus de Sterre. Ik ben gegroeid als wetenschapper maar ook als mens. Daarom zou ik graag enkele woorden richten aan mensen die mij geholpen hebben om het avontuur, wat een doctoraat is, af te ronden.

Eerst en vooral wil ik de alle leden van de examencommissie bedanken. Met hun kritische blik hebben ze geholpen om dit werk verder op punt te stellen. Prof. Vrielinck, ik wil je bedanken voor het enthousiasme waarmee je me altijd te woord stond. Ook al leverde de uitgevoerde analyses niet het gewenste resultaat op. Dr. Cuypers, ik wil jou bedanken voor de oneindig veel resistiviteitsmetingen en de hulp wanneer ik even zonder substraten zat, of iets nodig had dat niet in ons labo beschikbaar was. Dr. Lommens, telkens wanneer ik jouw bureau binnenstapte, was je bereid om mij te helpen. Of het nu kleine of grote problemen/vragen waren, het maakte je allemaal niet uit. Je was altijd bereid om een handje toe te steken. Waarvoor dank! Daarnaast wil ik ook graag Prof. Van Driessche bedanken voor haar financiële steun tijdens het eerste jaar van mijn onderzoek en het managen van de onderzoeksgroep SCRiPTS en de vakgroep Anorganische en Fysische Chemie. Als een goede moeder zorg je voor de leden van de vakgroep en onderzoeksgroep. Zonder jou zou de vakgroep en onderzoeksgroep niet zijn wat ze nu zijn.

Prof. De Buysser, als promotor heb jij mij al die jaren bijgestaan. Ik veronderstel dat je regelmatig eens raar opkeek van mijn fratsen. Zo heb jij o.a. bij Piazza del Popolo (Montecatini Terme) geleerd dat mijn oriëntatiegevoel niet zo goed is. Maar dit hield je niet tegen om mij altijd wetenschappelijk bij te staan, zoals die ontelbare keren dat ik jouw bureau binnenstapte met vragen of bedenkingen. Dankzij jouw inspanningen ben ik wetenschappelijk gegroeid en kon ik het onderzoek onder de beste omstandigheden uitvoeren.

Glenn, onze wegen kruisten de eerste keer ergens in september 2006. Al snel bleek dat wij het goed met elkaar konden vinden. Bijna 10 jaar na datum, mag ik wel zeggen dat er voor velen een onafscheidelijke band is tussen ons. Samen hebben we veel meegemaakt en er zal nog veel volgen! Maar toch wil ik je nog

eens speciaal bedanken voor alle hulp. We lachen soms wel eens met het feit dat we samen 2 doctoraten hebben afgewerkt, maar onze gesprekken omtrent het onderzoek leverden vaak nieuwe ideeën op. En naast het onderzoek was je er ook altijd voor mij!

De mannen van de koffiepauze of 'Iemand een Fabrizio kwijt' zorgden voor een aangename sfeer rond 10u30, tussen 12 en 13u en na 15u. Danny, Pierre, Pat, Bart, Tom, Matthias, Joni, Glenn, Sander, Hannes, JJ. Billet, dr. Feys en Niels, met de nodige schuine praat werden verschillende pauzemomenten opgesmukt tot een levendige boel. Deze goede band is niet enkel te voelen tijdens de werkuren maar ook erna. Samen eens gaan eten, op café of naar een toneelvoorstelling zorgt altijd voor de nodige ambiance. Dit zijn zaken die ervoor zorgen dat iedereen met plezier komt werken. Keep up the good work!

Pieter en Jonas F., jullie verdienen een eervolle vermelding voor jullie behulpzaamheid. Pieter, ook al was je niet meer veel te vinden op S3, ik kon je altijd mailen of bellen om raad te vragen. Jonas F., jij hebt me alles geleerd wat ik moest weten omtrent het inkjet printen. Bedankt voor jullie input!

Pierre, Claudine en later ook An, ik zou jullie graag bedanken voor alle administratieve rompslomp dat jullie voor mij hebben verricht. Pierre, jij verdient een extra woordje van dank. Niet enkel de administratie regelde jij, maar ook alle andere randactiviteiten. Ik zal je missen!

Graag zou ik ook alle huidige en voormalige SCRiPTS leden willen bedanken. Onze onderzoeksgroep heeft een bepaald karakter, welke door zijn leden bepaald wordt. Hierdoor is het ook prettig samenwerken met iedereen. Zo was Katrien altijd bereid om artikels op te zoeken~~,~~ waar ik geen toegang tot had. Jonathan stond altijd te popelen om NMR metingen uit te voeren. Joni bestelde alles wat nodig was voor het onderzoek. En samen hebben we (Glenn, Joni en ik) een ongelofelijke reis naar Maleisië gehad. Zo had/heeft ieder lid een positieve bijdrage tot het succes van SCRiPTS.

Zonder Olivier, Els, Tom, Koen, Glenn zou deze thesis weinig analyses kunnen voorleggen. Ik wil jullie dan ook bedanken voor het uitvoeren van alle XRD, XPS, SEM of TEM metingen die jullie uitvoerden.

Doorheen de jaren als doctoraatsstudent mocht ik ook enkele thesisprojecten begeleiden. Nicolas, Rutger en Charles, met jullie werkkracht en enthousiasme hebben jullie een steentje bijgedragen tot dit alles. Dankjewel voor de aangename samenwerking!

Daarnaast wil ik ook graag alle collega's van S3 (ZAP, WP, ATP, PCN, COMOC, L3, Quantum en Xstruct) bedanken. Jullie zorgden voor een aangename werkomgeving. Iedereen was bereid om een handje te helpen indien nodig. Collegialiteit op en top dus! Iedereen bedankt, zonder jullie allemaal zou deze ervaring voor mij compleet anders geweest zijn. Ik weet op dit moment niet hoe ik mijn 4 jaren aan de S3 anders zou moeten voorstellen. Merci voor de leuke momenten!

Last but not least, zou ik ook graag mijn familie bedanken. Wie had 27 jaar geleden durven denken dat er ooit een moment als deze zich zou voordoen? Mama, Dirk & Brian, jullie waren er altijd om mij te ondersteunen of aan te moedigen wanneer dit nodig was. Niets was te veel gevraagd en jullie zorgden dat ik niks te kort kwam. Samen hebben we leuke en minder leuke momenten meegemaakt, maar we zijn er voor elkaar. Hierdoor zou ik jullie dan ook willen bedanken voor de steun en ondersteuning! Marleentje, ook jij verdient een dikke merci! Ook al was je er niet bij vanaf het begin. Jij hebt de moeilijkste periode van dit avontuur ook mee gemaakt. Zonder jou zou dit alles niet mogelijk geweest zijn. Jij bent er gewoon altijd voor mij!

Bedankt aan iedereen!!!!

Kenny

27 augustus 2015

Table of contents

Symbols and abbreviations

ALD	Atomic Layer Deposition
AZO	Al doped ZnO
cfr.	confer
CIJ	Continuous Ink Jet Printing
CSD	Chemical Solution Deposition
DOD	Drop-On-Demand
DOSY	Diffusion Ordered SpectroscopY
e.g.	exampli gratia
EDS	Energy Dispersive X-ray Spectroscopy
et al.	et alii
etc.	et cetera
FTIR	Fourier Transform Infrared spectroscopy
FWHM	Full Width Half Maxima
HOMO	highest occupied molecular orbital
ITO	Indium Tin Oxide
LUMO	lowest unoccupied molecular orbital
NMR	Nuclear Magnetic Resonance
OLEDs	Organic Light-Emitting Diodes
PEDOT:PSS	poly(3,4,-ehtylenedioxythione):polystyrebesulphonate
PLD	Pulsed Laser Deposition
PVD	Physical Vapour Deposition
ref.	refer to
SEM	Scanning Electron Microscopy

SPD	Suspended Particle Devices
TCFs	Transparent Conductive Films
TCOs	Transparent Conductive Oxides
TGA	ThermoGravimetric Analysis
XRD	X-Ray Diffraction
$	US dollar
μ	Mobility of charge carriers
Å	Angström
A	Surface
a	Acceleration
α (cm^{-1})	Absorption coefficient
α	Polaron coupling constant
at%	Atom percentage
β	Stability constant of metal complexes
Bo	Bond number
C	Capacitance
δ	Deformation mode (IR)
d	Droplet diameter
d	Thickness
d_o	Diameter droplet in flight
d_{con}	Contact diameter droplet
ΔG_e	Elastic strain energy
ΔG_{homo}	Change in free energy by homogeneous crystallisation
ΔG_{hetero}	Change in free energy by heterogeneous crystallisation

ΔG_v	Volume free energy
e	Elementary charge of electron
ε	Electrical field
E_g	Band gap energy
E_H	First ionisation energy
ε_o	Vacuum permittivity
ε_∞	High frequency dielectric constant
ε_s	Low frequency dielectric constant
ε_r	Dielectric constant
ϕ	Varying function of temperature
ϕ_b	Grain boundary potential
F	Force
Fcc	Screening function
γ	Interfacial energy
γ	Surface tension
g	Acceleration of gravity
γ^-	Basic component of the surface tension
γ^+	Acidic component of the surface tension
γ^d	Dispersive part of the surface tension
γ^p	Polar part of the surface tension
γ_{tot}	Total surface tension
η	Viscosity
$\hbar$	Reduced Planck constant
I	Current

J	Current density
κ	Extinction coefficient
k	Boltzmann constant
K_a	Acid dissociation constant
k_f	Force constant of bound in a lattice
λ	Wavelength
L	Length
l	Grain size
λ_{mfp}	Mean free path of the charge carriers
λ_p	Plasma wavelength
m^*	Effective mass
m_e	Vacuum electron mass
N	Refractive index
n	Carrier density
n_{Al}	Number of Al molecules
ν	Vibration mode (IR)
ν_a	Asymmetric vibration stretch
N_i	Concentration ionised impurities
ν_s	Symmetric vibrational stretch
n_{Zn}	Number of Zn molecules
Oh	Ohnesorge number
P	Average piezoelectric electro-mechanical coupling coefficient
π	Pi
Q	Total charge

θ	Contact angle
ρ (C m^{-3})	Charge density
ρ (Ω m)	Resistivity
ρ (Kg m^{-3})	Density
r	radius
r_{ac}	Hall coefficient for phonon scattering
Re	Reynolds number
r_{opt}	Hall coefficient for optical mode
r_{pie}	Hall coefficient for piezoelectric scattering
ρ_r	Rocking mode (IR)
R_s	Sheet resistance
σ (S m^{-1})	Electrical conductivity
σ	Bonding molecular orbitals
σ*	Anti-bonding molecular orbitals
τ_c	Average time between 2 consecutive scattering events
T	Temperature
t	Time
v	Velocity
v%	Volume percent
V_f	Fermi velocity
Ω	Unit of resistance
We	Weber number
ω_p	Plasma frequency
x	Doping concentration

Z	Charge ionised centre

Chapter 1 – Thesis outline

This chapter covers the introduction of this dissertation. A broader context of the research topic is created and the aim of this work is discussed more in detail. Indium tin oxide is by far the most important transparent conductive thin film. However, the high cost and rarity of indium promotes the research towards alternative materials. This thesis suggests an alternative for transparent conductive films, synthesised by a scalable and environmentally friendly process.

1.1 Motivation

Transparent Conductive Films (TCFs) have become part of our everyday lives. These films are mostly found in (organic) light-emitting diodes (OLEDs), thin film photovoltaics, smart windows and display technology. Due to its use in numerous devices, the TCF market was valued at $1,94 billion in 2013. It is expected that this market reaches close to $6 billion in 2020 [1]. As can be noticed from table 1.1, in 2012 Indium Tin Oxide (ITO) had by far the largest market share, followed by other metal oxides, organic materials and metals & composites [2].

Table 1.1 Commercial available TCFs and their market share at 2012.

Type of TCFS	Market share (%)
ITO	93
Other metal oxides	6
Transparent organic compounds	0.9
Metals & composites	0.1

Although **ITO** is the **primary used transparent conductor,** research towards alternative candidates is promoted. An expanding TCF market and unstable supply of indium requests an indium free transparent conductor. Indium's natural scarcity and the increasing demand for ITO resulted in a booming of the market value for indium. Before 1960 the price of **indium** metal was steady at $72/kg [3] but rose to **$590/kg** [4] in 2014. As noticed in table 1, the TCFs market is dominated by transparent conductive oxides (TCOs) (99%). Their excellent transmittance in the visible range of the electromagnetic spectrum and good conductivity combined with their mechanical and chemical stability make these metal oxides perfectly suited as TCFs. Indium oxide [5, 6], SnO_2 [7, 8], ZnO [9] and TiO_2 [10, 11] based transparent conductive oxides are subjects of many research topics. **Doped ZnO** is an **excellent candidate** to replace ITO as leading TCF because of its good abundance, low cost, non-toxicity and good opto-electrical properties [12, 13].

Beside the search for suitable TCF candidates to replace ITO, new technologies and low cost synthesis routes are attractive from a commercial point of view. Nowadays, vacuum deposition methods dominate industrial and research production processes. Even though these result in supreme properties, the high production cost and complexity of the production process opens the market for alternative low cost synthesis routes [14]. Solution deposition is an attractive way to prepare thin films because of its simplicity and low cost. The rich chemistry of solution deposition processing and pyrolysis even allow the synthesis of complex materials and homogeneously doped oxides [14, 15]. **Up till now**, dip coating and spin coating are frequently used deposition methods for Al doped ZnO thin films by chemical solution processing. However, these films require **multiple deposition steps.** Each coating is followed by a drying step and/or **intensive thermal treatment** [16-18]. Those multi-layer processes are less scalable due to the excessive amount of coatings one has to perform before the final product is obtained. By selecting a **scalable** and **versatile** deposition approach we want to tackle this issue. **Ink jet printing** is selected as a **fast and accurate deposition** technique for TCFs thin films. The ability to deposit thin films and patterns allows us to dream of skipping the intensive etching procedure needed to obtain patterns. By optimising the parameters of the ink such as chelating agents and precursor concentration we **aim to deposit a TCF by a single deposition step.**

1.2 Outline

The aim of this thesis is the synthesis of **Al doped ZnO thin films by an aqueous chemical solution approach**. The focus is on the development of an environmental friendly, scalable and versatile production process without deteriorating the high electrical and optical performance commonly achieved via vacuum approaches or by using a multi-layer chemical solution approach. A better understanding of the fundamental aspects of TCFs will be helpful to optimise and develop these materials.

Chapter 2 introduces the term transparent conductive oxides and its properties. The selection of new and possible candidates for transparent conductive oxide materials is briefly discussed. Finally, some worldwide applications of TCOs are given as example.

Chapter 3 covers the fabrication process of Al doped ZnO thin films. Firstly, chemical solution deposition and its required production steps to develop high quality thin films are introduced. Secondly, the first principles of ink jet printing are covered, followed by state of the art of fabrication of Al doped ZnO thin films via chemical solution deposition.

Chapter 4 and 5 deal with the synthesis of an Al doped ZnO ink. A stable and clear precursor solution has to be fabricated. To reach this goal, a general strategy is followed. Precursor salts (zinc acetate, aluminium chloride or aluminium nitrate) are dissolved in water. The addition of well selected chelating agents, acids and bases help to maintain the stability of the precursor at neutral pH levels. Several precursor solutions with water as primary solvent are synthesised. These precursor solutions are examined in detail to understand the precursor chemistry. These stable precursor solutions are examined towards their printability. The jetting of a single droplet without satellite droplets is intended. Once a jettable ink is obtained, the wetting of the ink with the substrate is adapted till a homogeneous film can be printed.

Chapter 6 and 7 cover the optimisation of the thermal process and the dopant concentration. First, the wet deposited thin films are converted to an Al doped ZnO thin film by an oxidative thermal treatment. The focus is on the processing atmosphere and the drying step prior to the thermal treatment. Second, these thin films were thermally activated by an additional thermal treatment in forming gas. Once the thermal process is optimised, the dopant variation is varied to find the optimal opto-electrical properties of the synthesised thin films.

Chapter 8 discusses the deposition of Al doped ZnO patterns and focusses on printing Al doped ZnO tracks on glass substrates. Mainly the line stability and thickness of the pattern are discussed.

1.3 Reference list

1. Research, A.M., *Global Transparent Conductive Films Market (Technology, Application and Geography) - Size, Share, Global Trends, Company Profiles, Demand, Insights, Analysis, Research, Report, Opportunities, Segmentation and Forecast, 2013 - 2020*. 2014. p. 140.
2. Thiele, C. and R. Das, *Transparent Conductive Films (TCF) 2012-2022: Forecasts, Technologies, Players*. 2013. p. 159.
3. Hoel, C.A., et al., *Transparent conducting oxides in the ZnO-In2O3-SnO2 System.* Chemistry of Materials, 2010. **22**(12): p. 3569-3579.
4. Limited, A.M. *metal-pages: indium metal prices, news and information*. 2014 [cited 2014 20/09/2014]; Available from: http://www.metal-pages.com/metals/indium/metal-prices-news-information/.
5. Liu, H., et al., *Transparent conducting oxides for electrode applications in light emitting and absorbing devices.* Superlattices and Microstructures, 2010. **48**(5): p. 458-484.
6. Kim, S.S., et al., *Transparent conductive ITO thin films through the sol-gel process using metal salts.* Thin Solid Films, 1999. **347**(1-2): p. 155-160.
7. Lee, J.Y., *Effects of oxygen concentration on the properties of sputtered SnO2 : Sb films deposited at low temperature.* Thin Solid Films, 2008. **516**(7): p. 1386-1390.
8. Vaufrey, D., et al., *Reactive ion etching of sol-gel-processed SnO2 transparent conducting oxide as a new material for organic light emitting diodes.* Synthetic Metals, 2002. **127**(1-3): p. 207-211.
9. Minami, T., et al., *Preparations of ZnO-Al transparent conducting films by DC magnetron sputtering.* Thin Solid Films, 1990. **193**(1-2): p. 721-729.
10. Fallah, M., et al., *Effect of annealing treatment on electrical and optical properties of Nb doped TiO2 thin films as a TCO prepared by sol-gel spin coating method.* Applied Surface Science, 2014. **316**: p. 456-462.
11. Furubayashi, Y., et al., *A transparent metal: Nb-doped anatase TiO2.* Applied Physics Letters, 2005. **86**(25): p. 3.
12. El Mir, L., et al., *Multifunctional ZnO:V thin films deposited by rf-magnetron sputtering from aerogel nanopowder target material.* Thin Solid Films, 2011. **519**(17): p. 5787-5791.
13. Minami, T., *Transparent conducting oxide semiconductors for transparent electrodes.* Semiconductor Science and Technology, 2005. **20**(4): p. S35-S44.
14. Pasquarelli, R.M., D.S. Ginley, and R. O'Hayre, *Solution processing of transparent conductors: from flask to film.* Chemical Society Reviews, 2011. **40**(11): p. 5406-5441.
15. Exarhos, G.J. and X.-D. Zhou, *Discovery-based design of transparent conducting oxide films.* Thin Solid Films, 2007. **515**(18): p. 7025-7052.
16. Ohyama, M., H. Kozuka, and T. Yoko, *Sol-gel preparation of ZnO films with extremely preferred orientation along (002) plane from zinc acetate solution.* Thin Solid Films, 1997. **306**(1): p. 78-85.
17. Natsume, Y. and H. Sakata, *Zinc oxide films prepared by sol-gel spin-coating.* Thin Solid Films, 2000. **372**(1-2): p. 30-36.
18. Damm, H., et al., *Factors Influencing the Conductivity of Aqueous Sol(ution)-Gel-Processed Al-Doped ZnO Films.* Chemistry of Materials, 2014. **26**(20): p. 5839-5851.

Chapter 2 - General introduction to Al doped ZnO as transparent conductive oxide

This chapter is an introduction to transparent conductive oxides. The optical and electrical properties are discussed. An emphasis is given to the requirements for the selection of transparent conductive oxides. Some world wide applications of TCOs are given as an example.

2.1 Introduction

Transparent conducting materials own unique properties. This type of materials achieves large values for electrical conductivity, while a high transmittance in the visible range of the electromagnetic spectrum is maintained [1]. The first coexistence of optical transparency and electrical conductivity was reported by K. Badeker in 1907 [2]. A sputtered cadmium thin film was heat treated in air resulting in partial oxidation of the metal. The non-stoichiometric cadmium oxide possessed oxygen vacancies. This led to pentavalent cadmium ions, resulting in occupied defect energy levels wherefrom the electrons could easily promote to the conduction band [3]. Since 1940, the technological improvement arised as the potential application for industry and research became more and more obvious [4, 5]. Almost simultaneously, Rupprecht [6] & Thelen [7] discovered the good opto-electrical properties of In_2O_3. After years of intensive research SnO_2 doped In_2O_3 (ITO) with brilliant opto-electrical properties was obtained [8]. Around 1970, the upcoming flat-panel displays made ITO the most frequently used transparent conductive material for transparent electrodes [9].

Three main groups of materials that can act as transparent conducting films are distinguished: (1) Extremely thin metal coatings (average of 10 nm) such as Ag, Cu or Au are possible candidates. A transmittance in the visible range of the electromagnetic spectrum of 50% can be obtained. Higher optical transmittance (up to 80%) is obtained when the metal coating is embedded between two anti-reflective coatings. These extremely small dimensions however limit the electrical conductivity [8, 10]. When the dimensions of the thin film meet the dimensions of the free path of the charge carriers, smaller grains and surface roughness induce grain boundary scattering and surface scattering which are limiting the conductivity of these thin films [11-13]. (2) Organic based transparent conductive materials such as conducting polymers and carbon nanotubes gain more and more interest. Carbon nanotubes can form a new class of transparent conductive materials that are complementary with ITO for several niche-applications [14]. Still, the promising properties of an individual carbon nanotube do not result in carbon nanotube films superior electrical and optical properties [15]. Conductive polymers such as polyanilines, polythiophenes and poly(3,4,-ethylenedioxythione):polystyrenesulphonate (better known as PEDOT:PSS) are promising for the use in flexible devices due to their good mechanical strengths under bending [16]. However, diverse

drawbacks such as inhomogeneous electrical conductivity, degradation due to oxygen and water lead to short lifetimes of the devices [17, 18]. (3) Wide-band-gap semiconductors, e.g. doped In_2O_3, SnO_2 and ZnO are currently commercially used as transparent conductive films, and are known as transparent conductive oxides (TCOs) [5]. Due to their wide band gap they are highly transparent in the visible range of the electromagnetic spectrum, with values up to 90% [19]. The electrical conductivity is strongly promoted by doping which is increasing the number of charge carriers [5].

Doped ZnO is in this dissertation thesis suggested as a good and cheap alternative for ITO. Therefore we will further on focus on the properties of wide-band-gap semiconductors.

2.2 Solid conductors

One can distinguish 3 classes of materials based on their electrical conductivity: metals, semiconductors and insulators. To understand the principles about electrical conductivity in these materials one should take a closer look to the electronic structure of these materials. The building blocks of these materials are atoms. Those atoms contain electrons orbiting the nucleus in a specific atomic orbital (s, p, d, f, …) with a discrete energy level. If atoms react with one another to form a molecule, electrons are shared and the atomic orbitals combine to form hybrid orbitals (e.g. sp^3) resulting in bonding (σ, π) and anti-bonding (σ^*, π^*) molecular orbitals (Figure 2.1) [20].

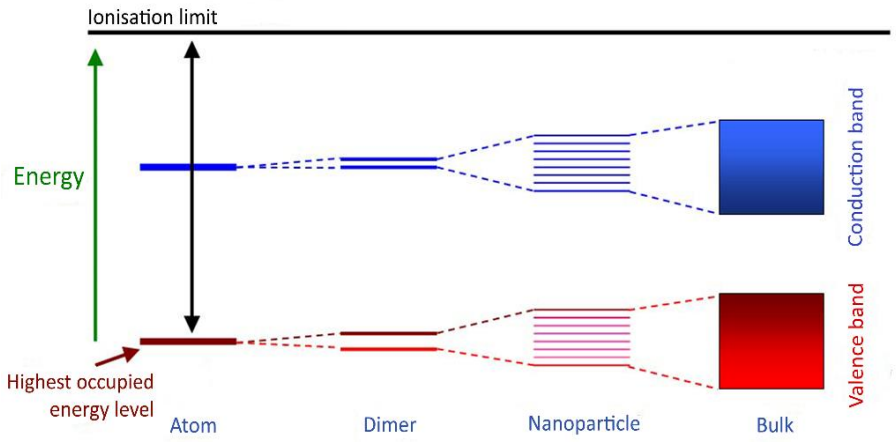

Figure 2.1: From atomic orbitals to bulk semiconductor with their typical band structure. Adapted from [21].

As materials exist out of multiple atoms, N valence electron atomic orbitals are recombined and result in N molecular orbitals. The more atoms, the more atomic orbitals that are combined, resulting in more molecular orbitals. The energy difference between contiguous energy levels is very small and eventually leads to the formation of the valence band and conduction band. The highest occupied molecular orbital (HOMO) is situated at the top of the valence band while the lowest unoccupied molecular orbital (LUMO) is situated at the bottom of the conduction band. The energy gap between the highest energy level of the fully occupied valence band and the lowest energy level of the unoccupied empty conduction band can be described as the band gap energy [22]. Depending on the band gap energy a differentiation can be made between an insulator and semiconductor. The boundary between a semiconductor and insulator is not well-defined but in general a material with a band gap larger than 3 eV is defined as an insulator. However, several ceramics such as ZnO [23] and TiO_2 [24] have a band gap around 3 eV but are considered as semiconductors. These materials are referred to as wide-band-gap semiconductors. Metals don't have any band gap due to a semi-filled valence band or overlap of the conduction band with the valence band. The unoccupied energy levels just above the highest occupied energy levels are accessible. The delocalised 'electron sea' can freely move, resulting in high conductivity. Insulators have a band gap sufficiently large to prevent a significant population of electrons in the conduction band by thermal excitation. If an electrical field is intense enough to provide electrons the required energy to promote from the valence band to the conduction band, the insulator undergoes dielectric breakdown.

Semiconductors have an intermediate electrical conductivity between insulators and metals. If the band gap is sufficiently small electrons in the valence band can be promoted to the conduction band by thermal excitation. In contrary to metals, where the lattice vibrations interfere with the transfer of momentum by the electron field, the electrical conductivity of a semiconductor increases with increasing temperature. The current in semiconductors flows through the movement of free electrons and/or 'holes', collectively known as charge carriers. Intrinsic semiconductors (e.g. pure Si with a carrier density of 1.45×10^{10} electrons cm^{-3} at 298K [25]) have a fully occupied valence band at absolute zero temperature. If the temperature is increased, thermal excitation promotes a number of electrons from the valence band to the conduction band, resulting in an equal amount of holes in the valence band and electrons in the

conduction band. If a voltage is applied, both will contribute to a small electrical current. The electrical conductivity of the intrinsic semiconductors can be improved by the addition of impurities, also known as doping. Depending on the valence state of the dopant n-type or p-type semiconductors are obtained.

For example, the electrical conductivity of silicon can be improved by a factor 10^6 when doped with a trivalent or pentavalent impurity [26]. Trivalent (e.g. B, Al and Ga) or pentavalent (e.g. P, As and Sb) dopants result respectively in a p-type and n-type silicon conductor (Figure 2.2). In case of a trivalent dopant an electron–accepting level will be introduced nearby the top of the valence band. Hereby positively charged holes will be introduced in the valence band and will contribute to an improved electrical conductivity. This class of semiconductors is called p-type semiconductors because the majority charge carriers are positively charged. If a pentavalent dopant is introduced into the Si matrix electron-donor levels nearby the bottom of the conduction band will appear. An excess of electrons in the conduction band improves the electrical conductivity. Because the majority charge carriers are negatively charged, this class of semiconductors will be called n-type semiconductors [26, 27].

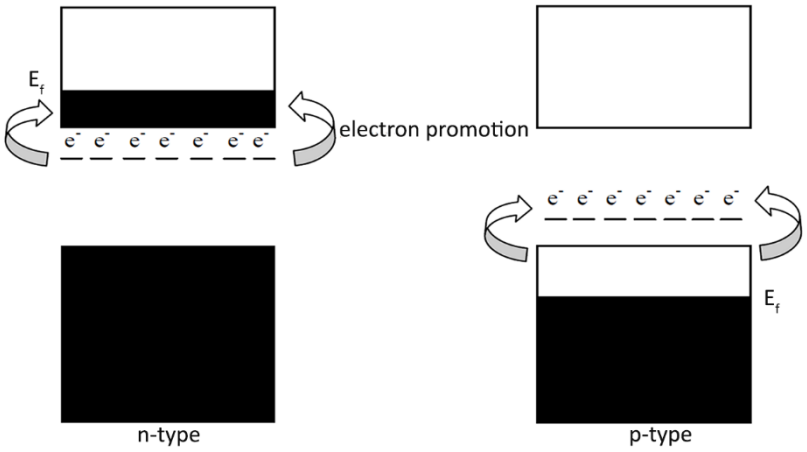

Figure 2.2 Doping of a semiconductor. The donor levels near the conduction band donate electrons to the conduction band (n-type semiconductor) while acceptor levels accept electrons from the valence band (p-type semiconductor). Adapted from [3].

2.2.1 Optical properties of TCOs

Transparent conductive oxides should have a good optical transmittance in the near UV-VIS-NIR region. A typical schematic of this optical window is represented in figure 2.3. The optical properties of TCOs (transmission, reflection and absorption) are set by its refraction index N, extinction coefficient κ, band gap E_g, and morphology (film thickness, uniformity and roughness).

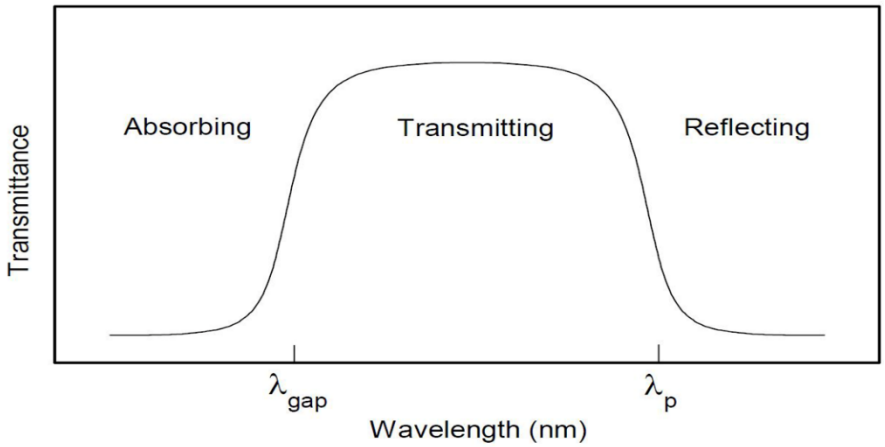

Figure 2.3 A typical optical window of a TCO thin film with λ_{gap}, the wavelength at which the band gap starts absorbing and λ_p, the wavelength at which the plasmon phenomenon take place [28].

The transmission window is confined by two regions where no light is transmitted. At the first region, where $\lambda < \lambda_{gap}$, the absorption due to band transitions dominate. If the photon energy is high enough to overcome the band gap energy, the energy is absorbed and an electron is promoted from the valence band to the conduction band. Finally, no light will be transmitted. A typical TCO material has a band gap energy larger than 3.1 eV, corresponding with a wavelength smaller than 400 nm [29].

At the second region, where $\lambda > \lambda_p$, no light is transmitted because of the plasma edge. Light with a wavelength higher than the plasma edge is electronically reflected. This can best be described by the classical Drude free electron theory [30]. A TCO can be considered as a matrix where fixed positive charges from dopants are homogeneously dispersed and surrounded by mobile electrons. The total matrix is neutral because there is no excess of charges. The carriers are considered to have an effective mass m*, and are weakly bound in a lattice by a

restoring force with a force constant k_f. In this model the conducting electrons (carriers) can be considered as a plasma. The electron cloud oscillates relative to the dopant cores with a natural frequency ω_p, also known as the plasma frequency [31]:

$$\omega_p = \sqrt{\frac{n\,e^2}{\varepsilon_o m^*}} \qquad \text{Eq.2.1}$$

Where n represents the carrier density, ε_o the vacuum permittivity and e the charge of the carriers. The plasma frequency corresponds to a plasma wavelength λ_p. The dielectric constant of the material (ε_r), which is expressed as a complex numbers, is influenced by the interaction of the free charge carriers with an electromagnetic field:

$$\varepsilon_r = (N + i\kappa)^2 = 1 - \frac{\omega_p^2}{\omega^2} \qquad \text{Eq.2.2}$$

Where N represents the refractive index and κ the extinction coefficient.

Near the plasma frequency the properties of the material changes drastically. Once the frequency of the electromagnetic field is smaller than the plasma frequency ($\omega < \omega_p$), the dielectric constant is negative, the complex refraction index is purely imaginary, meaning that the material is near to unity reflection. When $\omega > \omega_p$ the refractive index is real, positive and smaller than 1. As a result, a wave can be partially transmitted and reflected [32].

It can be noticed (eq. 2.1) that the plasma frequency and therefore the starting frequency of the plasma edge, is dependent on the charge carrier density. By controlling the number of charge carriers, one can tune the plasma edge. Typically for TCOs, the plasma edge has a wavelength in the order of 1-4μm [33]. Finally, the optical window of a TCO thin film is determined by its band gap and the number of charge carriers.

2.2.2 Electrical conductivity of TCOs

As mentioned above, besides a high transmittance in the visible range of the electromagnetic spectrum, a TCO thin film should have a high electrical

conductivity. Therefore, one should have a closer look to electrical conductivity in a transparent conductive oxide [34, 35].

The motion of a charged carrier inside a semiconductor due to an applied electrical field ε, is illustrated in figure 2.4

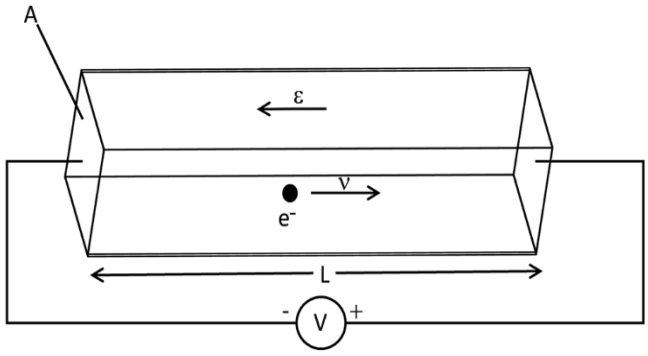

Figure 2.4 The motion of an electron in a semiconductor with a length L, and a surface A due to an applied electrical field ε .

The electrical field ε, forces the carrier to move with an average velocity v. If all carriers in the semiconductor move with the same average velocity, the current can be described as the total charge Q, divided by the time needed to travel from one side of the semiconductor to the other, t:

$$I = \frac{Q}{t} = \frac{Q}{L/v} \qquad \text{Eq.2.3}$$

The current density J, can be expressed as a function of the charge density ρ:

$$\vec{J} = \frac{\vec{I}}{A} = \frac{Q}{AL}\vec{v} = \rho\,\vec{v} \qquad \text{Eq.2.4}$$

In case of a n-type semiconductor the charge density can be rewritten as a function of the carrier density n, and the elementary electron charge e, resulting in the following equation for the current density:

$$\vec{J} = -\,e\,n\,\vec{v} \qquad \text{Eq.2.5}$$

In the absence of an electrical field the charge carriers move randomly in a Brownian motion. They will get deflected in different directions by scattering and no net movement is noticed. When an electric field is applied the electrons

will be accelerated and still move randomly but with a net movement in the opposite direction of the electrical field.

If Newton's law is considered for a moving carrier with an average velocity $\langle\vec{v}\rangle$, the acceleration will be proportional to the applied force:

$$\vec{F} = m^* \vec{a} = m^* \frac{d\langle\vec{v}\rangle}{dt} \qquad \text{Eq.2.6}$$

Where the effective mass of the charge carriers m^*, is used instead of the mass of a free carrier in order to incorporate the effect of periodic potential of the atoms in the material.

The net force on the carriers consists of the difference between the electrostatic force and the scattering force due to the loss of momentum at the time of scattering. The scattering force is equal to the momentum divided by the average time between 2 consecutive scattering events τ_c:

$$\vec{F} = -e\vec{\varepsilon} - \frac{m^* \langle\vec{v}\rangle}{\tau_c} \qquad \text{Eq.2.7}$$

If both equations are combined an expression for the average particle velocity is obtained:

$$-e\vec{\varepsilon} = m^* \frac{d\langle\vec{v}\rangle}{dt} + \frac{m^*\langle\vec{v}\rangle}{\tau_c} \qquad \text{Eq.2.8}$$

If a steady state situation is considered, the carrier has already accelerated and moves with a constant average velocity. In that case, the velocity is proportional to the applied electrical field. The mobility of the carriers μ, is defined as the velocity to electrical field ratio:

$$\mu = \frac{|\vec{v}|}{|\vec{\varepsilon}|} = \frac{-e\,\tau_c}{m^*} \qquad \text{Eq.2.9}$$

Hereby, the current density can be rewritten as:

$$\vec{J} = -e\,n\,\mu\,\vec{\varepsilon} \qquad \text{Eq.2.10}$$

Electrical conductivity σ, is defined as the current density to electrical field ratio and equals the inverse of the electrical resistivity (ρ):

$$\sigma = \frac{J}{\varepsilon} = -\,e\,n\,\mu = \frac{1}{\rho} \qquad \text{Eq.2.11}$$

The electrical conductivity is the product of the number of charge carriers in a material, the mobility of these carriers and the elementary electron charge while the inverse of the conductivity is defined as the resistivity.

The sheet resistance is a commonly used expression to describe the resistance of an uniform thin film since it's easier to determine the sheet resistance than the resistivity of these materials. Hence, the thickness needs to be determined before the sheet resistance can be calculated (eq. 2.12). The sheet resistance R_s, of thin film with a thickness d, and a resistivity ρ, is given by their ratio:

$$R_s = \frac{\rho}{d} \qquad \text{Eq.2.12}$$

The unit of the sheet resistance is Ohm, but commonly used nomenclature is Ohms per square.

Scattering mechanisms

As can be extracted from eq. 2.11, the conductivity of a TCO thin film is depending on the charge carrier concentration and their mobility. Achieving a low resistivity TCO film requires a high carrier mobility and a high carrier concentration. The carrier concentration in a TCO is limited by the solubility of the dopant in the matrix, whereas the carrier mobility is affected by scattering phenomena and is limited to a finite carrier mobility:

$$\mu = \frac{e\,\tau_c}{m^*} = \frac{e\lambda_{mfp}}{V_F m^*} \qquad \text{Eq.2.13}$$

Where the time between 2 consecutive scattering events depends on the Fermi velocity V_F, and the mean free path of the charge carriers λ_{mfp}. These parameters are influenced by different scattering mechanisms: lattice scattering, ionised impurity scattering, neutral impurity scattering, electron-electron scattering and grain boundary scattering. Finally, the carrier mobility is affected by the contribution of all these scattering phenomena and can therefore be written as [36]:

$$\frac{1}{\mu_{tot}} = \sum_i \frac{1}{\mu_i} \qquad \text{Eq.2.14}$$

Where μ_i is related to the scattering mechanism i.

The mobility of the charge carriers in degenerated semiconductors is mainly depending on the ionised impurity scattering [5, 37], while Minami [38] stated that ionised impurity scattering plays a dominant role in carrier scattering once the carrier concentration exceeds 10^{21} cm^{-3}. At lower carrier concentrations other scattering mechanisms should been considered as well. Therefore, other scattering mechanisms such as lattice scattering and grain boundary scattering also have a contribution to the reduction in mobility of the charge carriers [36, 39, 40]. According to Chen *et al*. [36] other scattering mechanisms, such as neutral impurity scattering which play an import role in the mobility of the charge carriers at low temperatures and electron-electron scattering, can be ruled out.

Ionised impurity scattering

Ionised impurity scattering is basically a deviation of the charge carrier trajectory by a Coulomb interaction of an ionised impurity and a charge carrier. This scattering mechanism is the most important mechanism at low temperature. However, large dopant concentrations may extend this till room temperature [41]. TCO thin films are containing a lot of point defects due to stoichiometric deviation (excess of metal atoms and/or oxygen vacancies) and the incorporation of the dopants. These point defects are mostly ionised. The high concentration of these ionised impurities (> 10^{20} cm^{-3} in a typical TCO thin film) and the long distance effect of the electrical field due to these impurities have the greatest influence on the carrier mobility [36, 39].

In 1955, Brooks [42] and Dingle [43] independently developed a theory that explained the influence of the ionised impurity scattering on the resistivity by making use of the Born approximation including Thomas Fermi screening. This theory assumes that the ionised impurities form an uniform background of immobile charge where they act as Coulomb scattering centres. The mobile charges provide screening. Finally, Pisarkiewicz *et al*. [44] applied corrections to this model by taking into account the non-parabolic band shape. The mobility of the carriers due to ionised impurity scattering μ_{ii}, is:

$$\mu_{ii} = \frac{3\pi}{2}\frac{(4\pi\varepsilon_0\varepsilon_s)^2\hbar^3}{Z^2e^3}\frac{1}{F_{cc}}\frac{n}{N_i}\frac{1}{m^{*2}} \qquad \text{Eq.2.15}$$

Where ε_s is the low frequency dielectric constant, $\hbar$ is the reduced Planck constant, Z is the charge of the ionised centre, F_{cc} the screening function, n the electron concentration and N_i the concentration of ionised impurities.

Grain boundary scattering

The grain boundary scattering mechanism has an important contribution to the mobility of the charge carriers in a polycrystalline TCO with small grains. These grain boundaries contain a high density of lattice defect-induced trapping states that trap free carriers from the bulk of the grains and scatter free carriers due to the presence of defects and trapped charges. The lattice defect-induced states result in a space charge region at the grain boundaries. These space charge regions initiate band bending, resulting in potential barriers to charge transport [36, 39]. According to Petritz [45] the mobility of the charge carriers is affected by grain boundary scattering following this relation:

$$\mu_{gb} = \mu_0 \exp\left(-\frac{\phi_b}{kT}\right) \qquad \text{Eq.2.16}$$

Where:

$$\mu_0 = \sqrt{\frac{l^2e^2}{2\pi kTm^*}} \qquad \text{Eq.2.17}$$

The grain boundary potential, the grain size and Boltzmann constant are respectively represented as ϕ_b, *l* and *k*.

For high resistivity oxide films the grain boundary potential can vary between 0.6 and 1.2 eV [46], while ITO, doped SnO_2 and doped ZnO can have a grain boundary potential of respectively 0.01 eV, 0.03 eV and 0.09 eV [47-49]. Due to this low grain boundary potentials grain boundary scattering will have a small contribution, unless the mean free path of the carriers has similar dimension as the grain size. The mean free path of the carriers can be calculated using the following equation:

$$\lambda_{mfp} = \mu \left(\frac{h}{2e}\right) \sqrt[3]{\frac{3n}{\pi}} \qquad \text{Eq.2.18}$$

In low-resistive ITO and Al doped ZnO films the mean free path of the carriers is smaller than 15 nm and as the average grain size is 50-100nm, this results in a non-significant contribution to the carrier mobility [36, 39]. Nevertheless, Ellmer et al. [40, 50] discovered that grain boundary scattering is more effective in polycrystalline ZnO-based TCOs than in ITO due to the higher density of traps located at the grain boundaries of Al doped ZnO, respectively 3 x 10^{13} cm^{-2} for AZO versus 1.5 x 10^{12} cm^{-2} for ITO.

Lattice scattering

Acoustic scattering, polar-optical scattering and piezoelectric scattering events are merged into the category of lattice scattering. The polar-optical and piezoelectric scattering events are specific towards certain semiconductors, such as ZnO [51].

The optical vibration mode in polar semiconductor crystals can induce polarisation, where the charge carriers are scattered through the interaction of Coulomb forces of the lattice polarisation waves. This affects the mobility according to the following correlation:

$$\mu_{opt} = r_{opt}\phi \frac{e}{2\alpha\omega_0 m^*}\left[\exp\left(\frac{\hbar\omega_0}{kT}\right) - 1\right] \qquad \text{Eq.2.19}$$

Where the polaron coupling constant α, is given by:

$$\alpha = \left(\frac{1}{\varepsilon_\infty} - \frac{1}{\varepsilon_s}\right)\sqrt{\frac{m^* E_H}{m_e \hbar\omega_0}} \qquad \text{Eq.2.20}$$

E_H represents the first ionisation energy of the hydrogen atom, ε_∞ is the high frequency dielectric constant, while ε_s is the low frequency dielectric constant. The vacuum electron mass is represented by m_e, while $\hbar\omega_0$ is the energy of the longitudinal optical phonon (lattice vibration polarisation). Usually, r_{opt} multiplied by ϕ equals 1, where ϕ is a slowly varying function of temperature and r_{opt} is the Hall coefficient factor for optical mode.

Acoustic scattering is a lattice deformation scattering process where lattice deformation is induced by a local energy shift of the band edges originating from acoustic phonons. If an acoustic wave propagates in a crystal lattice the atoms will oscillate around their equilibrium positions. The semiconductor can be treated as a continuous medium because the wavelength is much longer than the interatomic distance. Due to this small lattice displacements there will be a small variation of the valence band edge. This variation is linear for a small change in lattice spacing. So, the change in energy of a charge carrier at a transition from one atom to its neighbour is therefore proportional to the lattice displacement [52]. The mobility for this scatter event is given by:

$$\mu_{ac} = r_{ac} \frac{\sqrt{8\pi} c_l e \hbar^4}{3 E_d^2 \sqrt{(kT)^3 m^{*5}}} \qquad \text{Eq.2.21}$$

The average longitudinal elastic constant is c_l, E_d is the deformation potential and $r_{ac} = 3\pi/8$ is the Hall coefficient for phonon scattering. The deformation potential isn't well known for ZnO. In literature the values vary from 1.4 to 31.4 eV [51].

Piezoelectric scattering only occurs in piezoelectric materials. A semiconductor with different atoms such as ZnO will have an ionic character of the bonds and if no centre of symmetry is present in the unit cell, carriers may be scattered by longitudinal acoustic waves due to piezoelectric scattering. Polarisation occurs due to the oscillation of ions. The electrical field created by the deformation of the atoms may scatter the carriers. Also, intrinsic stress due to lattice mismatch and/or growth defects can induce piezoelectric scatter events [40]. Finally, the mobility of the carriers is affected according to the following equation:

$$\mu_{pie} = r_{pie} \frac{16\sqrt{2\pi} \hbar^2 \varepsilon_r \varepsilon_0}{3 e P^2 \sqrt{(kT) m^{*3}}} \qquad \text{Eq.2.22}$$

Where the Hall coefficient for piezoelectric scattering $r_{pie} = 45\pi/128$, P is the averaged piezoelectric electro-mechanical coupling coefficient and ε_r and ε_0 are the relative dielectric constant and the vacuum permittivity.

2.3 Metal oxide selection for TCO materials

The unique combination of high electrical conductivity and high optical transparency in the visible region of the spectrum limits the number of possible

candidates that can act as transparent conductive oxide. To obtain stable, highly conductive and transparent wide-band-gap semiconductors, doping is necessary. The selection of a proper dopant will be crucial towards the creation of a sufficient amount of charge carriers. One should select a dopant wisely and consider the difficulties that may appear by doping the host matrix with a certain dopant:

- The dopant solubility in the host matrix should be high enough to create an appropriate amount of charge carriers. If the solubility limit is exceeded competing phases, impurity segregation or precipitation can be induced. These secondary phases will affect the mobility and the number of charge carriers and will reduce the electrical conductivity. Therefore, a dopant should have a good chemical similarity and a similar size as the host atom that it has to replace. Even if a dopant has a high solubility, the fraction of dopant atoms on the desired atom sites still can be low [53, 54].

- To promote free electrons into the conduction band at room temperature the donor level of the dopant should be situated near the bottom of the conduction band. If the energy difference is too large (deep donor levels) no electrons will be promoted and no charge carriers will be created [53].

- If the dopant is soluble and ionisable, it can still spontaneously create a compensating defect, i.e. an opposite-charged native defect formed when the dopant produces a free carrier. This defect compensates and annihilates the effect by the intentional dopant [53].

Also, the selection of the host matrix for TCOs is of great importance. Next to the abundance and price of selected candidates, the following properties are of great importance:

- A possible candidate should have a band gap larger than 3.2 eV to prevent absorption of the visible light. This large band gap makes also doping of the metal oxide matrix very difficult [55].

- The selected TCO host matrix should have a large electron affinity and low conduction band minimum to simplify the doping process and to maintain the charge carriers [31].

- The conduction band should contain a large amount of energy states in order to reduce the scattering caused by degeneration due to the lack of available energetic pathways [31].

- The host matrix should be structurally stable even with high doping concentrations because an increasing number of dopant atoms can lead to phase separation. The structural deformation of the host matrix can also cause killer effects [31].

Most TCOs consist of heavy metal cations with an outer shell electronic configuration of $(n-1)d^{10}ns^0$ where n equals 4 or 5 combined with oxygen atoms. The filled d-levels prevent d-d transition in the visible region of the spectrum [56]. The ns orbitals from the cation primarily constitute the bottom part of the conduction band while the 2p orbitals from oxygen form the top of the valence band. Due to the large overlap of the ns-ns orbitals the mobility of the carriers is less sensitive to any angular variation or bond stretching in the M-O-M bonds, i.e. the mobility of the charge carriers in TCOs is less influenced by structural disorder [57].

2.3.1 ZnO as host matrix for TCOs

As mentioned in chapter 1, ITO is commercially the most used TCO. However, the high cost and the abundance of indium stimulate the research towards alternative TCOs. When we consider the selection criteria mentioned above, ZnO is an excellent candidate as TCO. It has a band gap of 3.37 eV and an electron affinity of 4.35 eV [31]. Also, the Zn cations consist of the classical $(n-1)d^{10}ns^0$ electronic configuration where n equals 4. Due to the high overlap of the 4 s orbitals, n-type ZnO single crystals have a high mobility (205 cm^2/Vs [58]), which is comparable to In_2O_3 single crystals (160 cm^2/Vs [59]). Next to its promising material properties, ZnO is also non-toxic, has a good stability in hydrogen plasma and the mineral sources are cheap and abundant [60-62]. However, undoped ZnO has 2 major drawbacks. ZnO has an electrical resistivity of at least one order of magnitude higher than ITO and it is also chemically less stable [63, 64]. Luckily, ZnO is easily doped and numerous dopants demonstrate

that they improve the electrical properties and chemical stability [65]. All these characteristics make ZnO the most important candidate to substitute ITO as state of the art TCO.

ZnO is a II-VI semiconductor compound used in a broad variation of industrial branches such as cosmetics, paint, plastics or food industry [66]. Recently, improved processing and better theoretical understanding expanded the scientific interest for ZnO to new applications in optoelectronics, spintronics and nanotechnology [67]. ZnO has an ionicity that resides at the borderline between covalent and ionic semiconductors. The crystallisation of ZnO can result in ZnO with a wurtzite, zinc blende or rocksalt crystal structure. Wurtzite is the thermodynamically stable phase at ambient conditions, while the zinc blende can be stabilised by growth on cubic substrates. Rocksalt structures can only be obtained at high pressure [68]. ZnO with a wurtzite crystal structure has a hexagonal unit cell with lattice parameters a = 3.2495 Å and c = 5.2069 Å [69], and belongs to the spacegroup $P6_3mc$ as represented in figure 2.5. The ideal wurtzite structure exist out of 2 interpenetrating hexagonal close-packed (hcp) sublattices each consisting of one kind of atoms displaced with respect to each other along the *c*-axis. Each sublattice contains 4 atoms of one type which are surrounded by 4 atoms of the other type. These atoms are coordinated at the edges of a tetrahedron. An ideal wurtzite structure shows a c/a-ratio of 1.63 [68], while this ratio for pure ZnO is 1.60 [70]. This small structural distortion induces spontaneous polarisation.

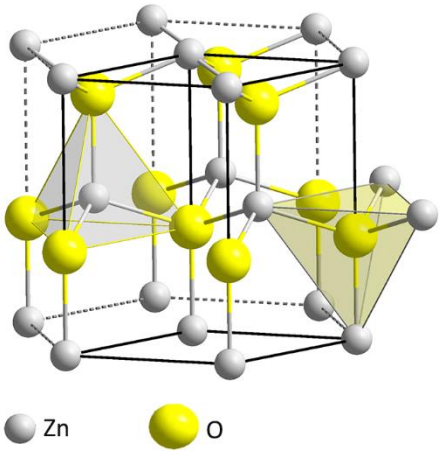

Figure 2.5 Wurtzite crystal structure of ZnO with Zn as the grey atoms and O as the yellow atoms.

Normally, pure undoped ZnO would be expected to be an insulator due to its relatively high band gap energy, but it shows intrinsic n-type behaviour. It is believed that the presence of native defects such as oxygen vacancies and interstitial zinc play an important role in the n-type character of ZnO [71, 72]. Nevertheless, the exact species that act as electron donor have still to be identified. Ab-initio calculations and electron paramagnetic resonance experiments suggest that oxygen vacancies have high formation energies and have rather deep donor levels which makes it impossible to donate electrons to the conduction band by thermal excitation [73-76]. While Janotti *et al*. [74] state by first-principles investigations that Zn interstitials are shallow donors that have a high formation energy under equilibrium conditions. They are fast diffusers and hence unlikely to act as a stable point defect. Other theories suggest the unintentional incorporation of impurities such as hydrogen [77, 78]. But this can be ruled out as the n-type behaviour of ZnO is still present when the hydrogen is annealed out [76]. Normally, all these possible electron donors are ruled out but Lany and Zunger [76, 79] suggest that the oxygen vacancies contribute to the n-type conductivity of ZnO. They are by far the most abundant point defect in equilibrium grown ZnO. The ground state of the oxygen vacancy generates a deep donor level whereas the excited vacancy has a metastable conductive state. By photo-excitation the empty deep donor level moves up in the conduction band while the electrons are situated in a shallow donor level nearby the conduction band.

Highly conductive ZnO by doping

The properties of metal doped ZnO show variation with the used dopant. For example, group I element (Li, Na and K) doped ZnO thin films have a high resistivity due to the dopant that accepts a carrier [80]. On the other hand, group IIIA element (B, Al, Ga and In) doped ZnO has a low resistivity and a high carrier density [81]. Some 3d-transition-metals such as Co induce ferromagnetic properties [82]. To improve ZnO towards TCO applications n-type doped ZnO with a low resistivity and high carrier density is needed. Therefore, ZnO can be doped by group IIIA elements or group IV elements (Si, Ge, Ti, Zr and Hf) or group VII elements such as F [38]. Among these, Al, Ga and In doped ZnO are the most frequently used dopants. Resistivities of the order of 10^{-4} Ωcm can be realised with those dopants, making this kind of doped ZnO competitive with ITO.

We favour aluminium as dopant for the ZnO host matrix because of the following reasons: (1) When aluminium is introduced in the host matrix under reducing conditions, defect levels close to minimum of the ZnO conduction band are created [31]. (2) The experimental solubility limit of 3-4 at% [83] allows the introduction of a large quantity of charge carriers (>10^{20} cm^{-3}) [84, 85]. (3) Of all the other group IIIA elements Al is cheap and abundant. Thus Al doped ZnO thin films can be a low-cost alternative for the expensive ITO [86].

In order to improve the electrical properties the dopant needs to be incorporated in the crystal structure of the host matrix (figure 2.6). Regarding Al doped ZnO, the Al^{3+} ions should occupy a Zn^{2+} site to render a free electron and enhance the conductivity [87]. Next to substitutional doping, the Al^{3+} ions also can occupy other sites in the wurtzite structure. Half of the tetrahedral and all octahedral sites are empty and these can act as possible dopant sites [87, 88]. Theoretical studies showed that the tetrahedral sites are energetically more favoured [89]. If the solubility limit is exceeded, the Al^{3+} ions may occupy the interstitial octahedral coordinated sites [83]. Al^{3+} ions positioned on the empty octahedral or tetrahedral sites aren't able to provide the host material with free carriers. Hence, these sites are considered as inactive dopant sites. The occupation of the octahedral sites would require that the Al^{3+} ions acts as acceptors and that would even decrease the conductivity [87, 88, 90]. Thus, the Al^{3+} ions should occupy the substitutional tetrahedral sites to have a positive influence on the conductivity of the host matrix.

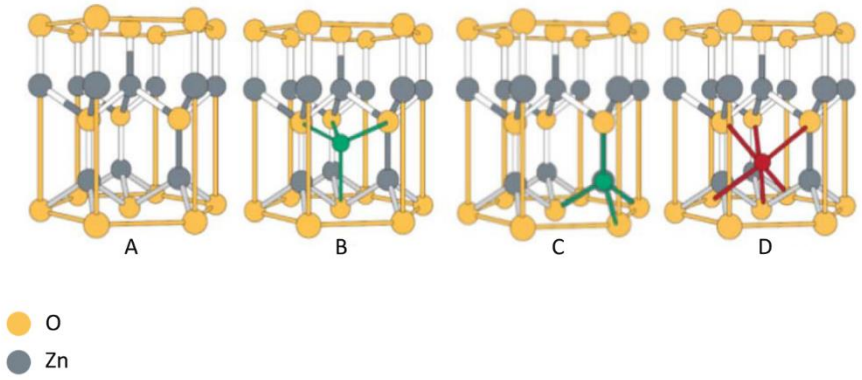

Figure 2.6 Possible dopant position of Al inside the wurtzite ZnO crystal structure. a) An undoped ZnO crystal lattice, b) Al can occupy an empty tetrahedral site, c) Al can substitute a Zn atom and d) Al can occupy an empty octahedral site. Adapted from [88].

2.4 Applications

Transparent conductive oxides are essential components in a large variety of photosensitive electronic devices. They act as transparent electrical contacts or electrodes in thin film solar cells[8], touch screens [91], LEDs [92], displays [93] and smart windows [94]. Accompanied with the large variety in applications there is a wide range of requirements for these transparent conductive oxides towards the electrical and optical properties. Foremost, the sheet resistance should fit the electrical functionality of the device. For example, touch screens necessitate a sheet resistance from 400 – 700 Ω/sq., while large area displays and thin film solar cells require sheet resistances in the range of 10 - 100 Ω/sq. [95]. The optical transmittance of the transparent conductive thin film in the spectral range of interest should also be tuned. This spectral range is depending on the device application, e.g., the sensitivity of the human eye, the emission spectra of the active component in lighting technologies or the quantum efficiency of the absorbing component in solar cells [96].

2.4.1 Photovoltaic devices

To meet the world's increasing demand for energy and environmental issues concerning fossil fuels, the collection of solar energy is one of the alternative energy sources. Solar cells exploit the photovoltaic effect to convert the energy of the incident light into electricity. The photovoltaics market is still growing

(figure 2.7). At the end of 2013, the global capacity of the installed photovoltaic solar systems reached 140 GW. The market share of these installations is about 90% for the silicon solar cells, while thin film solar cells have a market share of 10%.

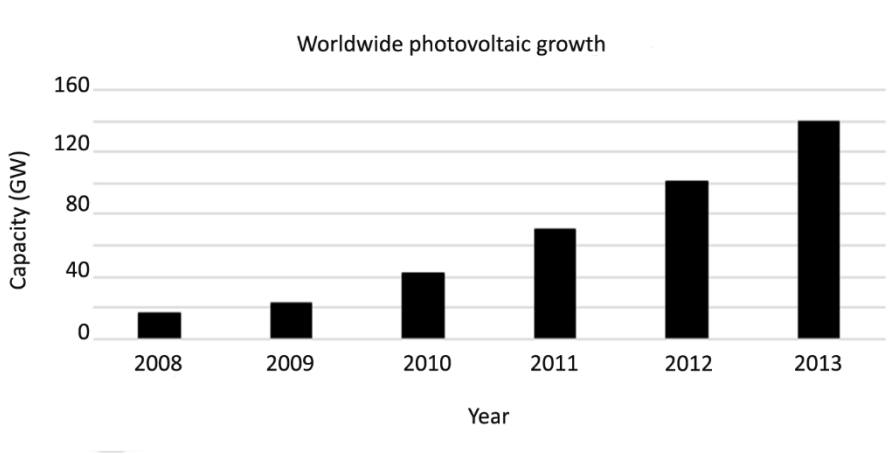

Figure 2.7 Global overview of the power generation of the installed photovoltaic systems. Adapted from [97].

In solar cells TCOs are used as transparent electrode. Therefore, the trade-off between the sheet resistance and the optical window should be made. As mentioned above, the optical window of a TCO nearby the IR is influenced by the carrier concentration. For photovoltaic applications the carrier concentration should be as small as possible while the carrier mobility should be as high as possible. TCOs in photovoltaic applications are in fact used as transparent electrodes to collect the generated photocurrent and let the light pass through the complete area of the absorbing layer. Also, the TCO contacts can be used to trap the light in the absorbing matrix. The path length of incoming rays can be increased by light scattering at the interface of the TCO layer and the absorbing layer. In general, the use of TCOs in photovoltaics increases the efficiency [8].

For example, silicon solar cells make use of a raster of silver lines as front contacts to collect the photocurrent. But these contacts mask the light-absorbing layer and thus reduce the efficiency. If a TCO pattern is used as front contact, the light will be able to reach the absorbing layer and the generated photocurrent can be collected along the entire device area [98]. Another

example is the incorporation of TCO thin films where the absorbing material (Si) is sandwiched between 2 TCO layers (figure 2.8). At the interface of the Si and TCO layer the light will be scattered because of the difference in refractive indices. By embedding the Si in between 2 TCO layers, the light is 'trapped' and the path length of the incoming light is increased [8, 99].

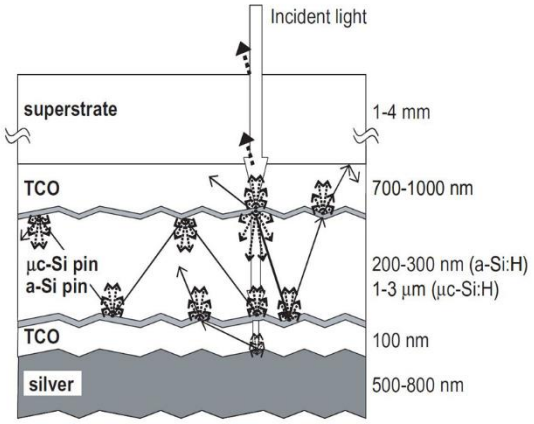

Figure 2.8 Cross-sectional view of a Si thin film solar cell where TCOs are incorporated as electrode and light trapping layer [99].

2.4.2 Functional glasses

Sustainable energy is a hot topic nowadays, but energy-saving applications are as important in sustainable development. Up to 25% of the heat is lost through windows [100]. Double and triple glazing in windows prevents conductive and convective heat losses. An additional layer of TCO material can significantly reduce the radiative heat loss of rooms in cold climates due to their ability to reflect IR radiation [101]. The glass used in colder climates, also known as "low-e" glass allows the near IR part of the solar spectrum to heat up to room, while the longer IR waves coming from radiation of a blackbody are reflected back into the room [29]. Therefore, the plasma frequency of the TCO layer should be tuned around 2.5 µm, allowing the visible light and the near IR region from the solar spectrum to pass through the window into the room. This preserves the maximum solar gain and maximum radiative insulation for buildings in cold climates [102]. Finally, "low-e" glass can reduce the energy loss via windows up to 75% [100].

Another type of functional glasses are smart windows, which darken or become opaque upon application of a voltage, tuning the amount of daylight passing through windows [103]. These smart windows allow to switch to complete privacy or any state in between without the need for blinds or curtains and they protect against UV radiation. Possible applications are situated in corporate office buildings, residential buildings, healthcare facilities, transportation, etc.. A typical example of a smart window are electrochromic glass and suspended particle devices (SPD) [104].

Electrochromic windows consist out of multi-layer coatings on glass. The multi-layer is built up as a purely ionic conductor (electrolyte) placed between an electrochromic and counter electrode. This stack is sandwiched between a TCO acting as a transparent electrode. A voltage applied to the TCO thin films results in a electrochemical reaction where the ions are inserted or extracted from the electrochromic layer. As a result, the optical properties of the window are changed [94]. One enormous advantage is that the applied voltage is only required to switch the state of the device.

A suspended particle device contains rod-like particles in an organic liquid or gel laminated between 2 transparent electrodes. When no voltage is applied, the particles are randomly aligned and thus, blocking and absorbing the light. Applying a voltage will align the suspended particles and let the light pass. Depending on the applied voltage, the orientation of the particles varies and thereby the tinted state of the glass [105]. Typical transmission ranges are 0.1-10%, 10-50% and 20-60%. To obtain complete transparancy a continuous voltage is required [106].

2.4.3 Touch screens

A touch screen is a touch sensitive display. It can detect the presence and location of a touch on the display area [91]. Nowadays, touch screens are widely used in industrial and public facing computer systems, car navigation systems, handheld devices such smartphones, tablets etc. [91, 107]. Several sensing technologies are used in commercial products such as resistive [108], capacitive [109], optical using infrared [110] and acoustic using surface acoustic wave [111] detection methods. Among them, the resistive touch screen system is one of its most widely used sensing methods because of its simple structure [107]. However, since the launch of the iPhone© in 2007, capacitive touch screens are

getting well established in the touch screen technology [112]. Both detection methods did undergo a transformation from a single touch point recognition towards a multiple simultaneous touch point recognition system by introducing patterned electrodes. A XY-raster of transparent electrodes is formed by merging 2 substrates with tracks of these electrodes parallel to each other [113].

A capacitive device relies on the change in capacitance when the screen is touched by a finger or conductive stylus. The device consists of small capacitors created by patterned electrodes and a non-conductive layer in between (figure 2.9). The electrodes are usually organised in rows and columns. When a finger or stylus touches the screen at an intersection of the electrodes a capacitance (ΔC) is added in parallel with the inherent mutual capacitance ($\bar{C}$) at that node. Because every node has its specific XY coordinates, the exact position of the change in capacitance can be detected [91, 112].

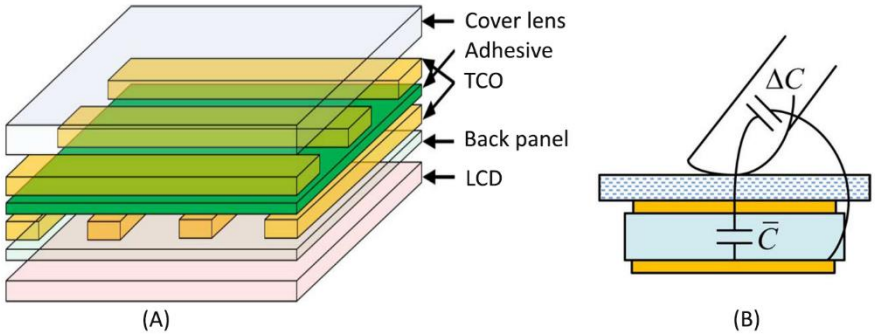

Figure 2.9 (A) a schematic design of a capacitive touch screen setup with stacked layers and a X/Y raster transparent electrodes (TCO). (B) Capacitance change when a finger touches the screen. Adapted from [112].

A resistive device consists of 2 sheets with an electronically resistive material (such as a transparent conductor) which are separated by air or microdots. If the display is touched, these sheets are pressed together, resulting in electrical contact. The microprocessor generates a positive voltage which is uniformly decreasing to 0 V applied on the X electrodes. The Y electrodes are used to determine the position at the X electrodes by measuring the voltage as a distance. After the X coordinate is located, this process repeats itself with the Y

electrodes to located the Y coordinate. This all happens in a few milliseconds [114].

The sensor requirements are based on the detection of a human finger touch. For a precise detection of the human finger touch the ideal spacing between each row or column of electrodes should be half of tip-to-tip distance of a typical index finger or thumb when pinched together. This is roughly 5 mm[112]. Depending on the design of the touchscreen the pattern of the transparent electrodes is also changing. One can use straight electrode lines [112, 115], interconnected diamond shape electrodes [116], zig-zag structure [117], etc.. Due to this large variation of designs, the electrode dimensions and space in between are changing along with the design [118]. The spacing between the electrodes can vary from 5 mm till a couple of 100 µm. The width itself can vary from 30 µm up to 2 mm [115, 116, 118]. Concluding, depending on the chosen design, the dimensions, shape and spacing of the electrodes change along.

2.5 Reference list

1. Edwards, P.P., et al., *Basic materials physics of transparent conducting oxides.* Dalton Transactions, 2004(19): p. 2995-3002.
2. Badeker, K., Annals of Physics, 1907. **22**: p. 749-766.
3. Waugh, M.R., *The synthesis, characterisation and application of transparent conducting thin films*. 2011, University College London. p. 266.
4. Preston, J.S., *Constitution and mechanism of the selenium rectifier photocell.* Proceedings of the Royal Society of London. Series A. Mathematical and Physical Sciences, 1950. **202**(1071): p. 449-466.
5. Ellmer, K., *Past achievements and future challenges in the development of optically transparent electrodes.* Nature Photonics, 2012. **6**(12): p. 808-816.
6. Rupprecht, G., *Untersuchungen der elektrischen und lichtelektrischen Leitfähigkeit dünner Indiumoxydschichten.* Zeitschrift für Physik, 1954. **139**(5): p. 504-517.
7. Thelen, A. and H. Konig, *Elektrische leitfahigkeit und struktur aufgestaubter indiumoxyschichten.* Naturwissenschaften, 1956. **43**(13): p. 297-298.
8. Liu, H., et al., *Transparent conducting oxides for electrode applications in light emitting and absorbing devices.* Superlattices and Microstructures, 2010. **48**(5): p. 458-484.
9. White, D.L. and M. Feldman, *Liquid-crystal light valves.* Electronics Letters, 1970. **6**(26): p. 837-839.
10. Granqvist, C.G. and A. Hultaker, *Transparent and conducting ITO films: new developments and applications.* Thin Solid Films, 2002. **411**(1): p. 1-5.
11. Mayadas, A.F. and M. Shatzkes, *Electrical-resistivity model for polycrystalline films: the case of arbitrary reflection at external surfaces.* Physical Review B, 1970. **1**(4): p. 1382-1389.
12. Hoffmann, H. and G. Fischer, *Electrical conductivity in thin and very thin platinum films.* Thin Solid Films, 1976. **36**(1): p. 25-28.
13. Yoshikatsu, N., *Resistivity and temperature coefficient of thin metal films with rough surface.* Japanese Journal of Applied Physics, 1970. **9**(11): p. 1326.
14. Zhang, D., et al., *Transparent, conductive, and flexible carbon nanotube films and their application in organic light-emitting diodes.* Nano Letters, 2006. **6**(9): p. 1880-1886.
15. Ho, X. and J. Wei, *Films of carbon nanomaterials for transparent conductors.* Materials, 2013. **6**(6): p. 2155-2181.
16. Takamatsu, S., et al., *Transparent conductive-polymer strain sensors for touch input sheets of flexible displays.* Journal of Micromechanics and Microengineering, 2010. **20**(7).
17. Jorgensen, M., K. Norrman, and F.C. Krebs, *Stability/degradation of polymer solar cells.* Solar Energy Materials and Solar Cells, 2008. **92**(7): p. 686-714.
18. Yun, J.-M., et al., *Solution-processable reduced graphene oxide as a novel alternative to PEDOT:PSS hole transport layers for highly efficient and stable polymer solar cells.* Advanced Materials, 2011. **23**(42): p. 4923-4928.
19. Chopra, K.L., S. Major, and D.K. Pandya, *Transparent conductors- a status review.* Thin Solid Films, 1983. **102**(1): p. 1-46.
20. Atkins, P., *The elements of physical chemistry*. 2001, Oxford: Oxford University Press.
21. Liao, Y., *Energy level diagrams for single atoms, dimers, clusters & bulk materials*, in *Practical electron microscopy and database*, GlobalSino, Editor. 2007.
22. West, A.R., *Basic solid state chemistry / Anthony R. West*, ed. A.R.S.s.c. West and a. its. 1988, Chichester [West Sussex] ; New York: Wiley.
23. Tang, W. and D.C. Cameron, *Aluminium-doped zinc-oxide transparent conductors deposited by the sol-gel process.* Thin Solid Films, 1994. **238**(1): p. 83-87.

24. Arin, M., et al., *Durability and efficiency of ink-jet printed TiO2 coatings: Influence of processing temperature.* Thin Solid Films, 2014. **556**: p. 160-167.
25. Sze, S.M. and N.K. Kwok, *Physics of semiconductor devices*. 2007, Hoboken, N.J.: Wiley-Interscience.
26. Sze, S.M., *Semiconductor Devices, Physics and Technology*. 1985: AT & T Bell Laboratories.
27. Zeghbroeck, V., *Principles of Semiconductor Devices and Heterojunctions*. 2007: Prentice Hall PTR.
28. Dekkers, J.M., *Transparent conducting oxides on polymeric substrates by pulsed laser deposition*. 2007, Universiteit Twente: Twente. p. 146.
29. Granqvist, C.G., *Transparent conductors as solar energy materials: A panoramic review.* Solar Energy Materials and Solar Cells, 2007. **91**(17): p. 1529-1598.
30. Drude, P., *Zur Elektronentheorie der Metalle.* Annalen der Physik, 1900. **306**(3): p. 566-613.
31. Exarhos, G.J. and X.-D. Zhou, *Discovery-based design of transparent conducting oxide films.* Thin Solid Films, 2007. **515**(18): p. 7025-7052.
32. Hens, Z., P. Vandervoort, and I. Van Driessche, *Solid state chemistry*, ed. G. university. 2012, Ghent. 199.
33. Gordon, R.G., *Criteria for choosing transparent conductors.* Mrs Bulletin, 2000. **25**(8): p. 52-57.
34. Singh, R., *Electronic devices and integrated circuits*. 2009: Pearson Education Canada.
35. Panda, S., *Microelectronics and optoelectronics technology*. 2009: Laxmi Publications Pvt Limited.
36. Chen, M., et al., *Intrinsic limit of electrical properties of transparent conductive oxide films.* Journal of Physics D-Applied Physics, 2000. **33**(20): p. 2538-2548.
37. Minami, T., et al., *Conduction mechanism of highly conductive and transparent zinc oxide thin films prepared by magnetron sputtering.* Journal of Crystal Growth, 1992. **117**(1–4): p. 370-374.
38. Minami, T., *New n-type transparent conducting oxides.* Mrs Bulletin, 2000. **25**(8): p. 38-44.
39. Zhang, D.H. and H.L. Ma, *Scattering mechanisms of charge carriers in transparent conducting oxide films.* Applied Physics a-Materials Science & Processing, 1996. **62**(5): p. 487-492.
40. Ellmer, K. and R. Mientus, *Carrier transport in polycrystalline transparent conductive oxides: A comparative study of zinc oxide and indium oxide.* Thin Solid Films, 2008. **516**(14): p. 4620-4627.
41. Chattopadhyay, D. and H.J. Queisser, *Electron-scattering by ionized impurities in semiconductors.* Reviews of Modern Physics, 1981. **53**(4): p. 745-768.
42. Brooks, H., *Theory and electrical properties of germanium and silicon*, in *Advances in electronics and electron physics*, Marton L., Editor. 1955: 1955. p. 87.
43. Dingle, R.B., *Scattering of electrons and holes by charged donors and acceptors in semiconductors.* Philosophical Magazine, 1955. **46**(379): p. 831-840.
44. Pisarkiewicz, T., K. Zakrzewska, and E. Leja, *Scattering of charge-carriers in transparent and conducting thin oxide-films with a non-parabolic conduction -band.* Thin Solid Films, 1989. **174**: p. 217-223.
45. Petritz, R.L., *Theory of photoconductivity in semiconductor films.* Physical Review, 1956. **104**(6): p. 1508-1516.
46. Tansley, T.L., D.F. Neely, and C.P. Foley, *Conduction mechanism in sputtered polycrystaline zinc-oxide thin-films.* Thin Solid Films, 1984. **117**(1): p. 19-32.

47. Bandyopadhyay, S., et al., *Study of structural and electrical properties of grain-boundary modified ZnO films prepared by sol-gel technique.* Materials Chemistry and Physics, 2002. **74**(1): p. 83-91.
48. Shanthi, E., et al., *Eelectrical and optical-properties of undoped and antimony-doped tin oxide-films.* Journal of Applied Physics, 1980. **51**(12): p. 6243-6251.
49. Kulkami, A.K. and S.A. Knickerbocker, *Estimation and verification of the electrical properties of indium tin oxide based on the energy band diagram.* Journal of Vacuum Science & Technology a-Vacuum Surfaces and Films, 1996. **14**(3): p. 1709-1713.
50. Ellmer, K. and R. Mientus, *Carrier transport in polycrystalline ITO and ZnO:Al II: The influence of grain barriers and boundaries.* Thin Solid Films, 2008. **516**(17): p. 5829-5835.
51. Ginley, D., H. Hosono, and D.C. Paine, *Handbook of Transparent Conductors*. 2010: Springer.
52. Seeger, K., *Semiconductor physics: an introduction*. 2004: U.S. Government Printing Office.
53. Zhang, S.B., S.H. Wei, and A. Zunger, *Overcoming doping bottlenecks in semiconductors and wide-gap materials.* Physica B-Condensed Matter, 1999. **273-4**: p. 976-980.
54. Zhang, S.B., *The microscopic origin of the doping limits in semiconductors and wide-gap materials and recent developments in overcoming these limits: a review.* Journal of Physics-Condensed Matter, 2002. **14**(34): p. R881-R903.
55. Hosono, H., *Recent progress in transparent oxide semiconductors: Materials and device application.* Thin Solid Films, 2007. **515**(15): p. 6000-6014.
56. Hoel, C.A., et al., *Transparent conducting oxides in the ZnO-In2O3-SnO2 System.* Chemistry of Materials, 2010. **22**(12): p. 3569-3579.
57. Wang, K., *Transparent oxide semiconductors: Fabrication, properties, and applications*. 2008, University of Waterloo: Waterloo, Canada. p. 120.
58. Look, D.C., et al., *Electrical properties of bulk ZnO.* Solid State Communications, 1998. **105**(6): p. 399-401.
59. Preissler, N., et al., *Electrical transport, electrothermal transport, and effective electron mass in single-crystalline In2O3 films.* Physical Review B, 2013. **88**(8).
60. Major, S., et al., *Effect of hydrogen plasma treatment on transparten conducting oxides.* Applied Physics Letters, 1986. **49**(7): p. 394-396.
61. Jin, Z.C., I. Hamberg, and C.G. Granqvist, *Optical-properties of sputter-deposited ZnO-Al thin films.* Journal of Applied Physics, 1988. **64**(10): p. 5117-5131.
62. Chen, M., et al., *Structural, electrical, and optical properties of transparent conductive oxide ZnO : Al films prepared by dc magnetron reactive sputtering.* Journal of Vacuum Science & Technology a-Vacuum Surfaces and Films, 2001. **19**(3): p. 963-970.
63. Minami, T., S. Suzuki, and T. Miyata, *Transparent conducting impurity-co-doped ZnO : Al thin films prepared by magnetron sputtering.* Thin Solid Films, 2001. **398**: p. 53-58.
64. Hartnagel, H., *Semiconducting transparent thin films*. 1995: Taylor & Francis.
65. Owen, J.I., *Growth, etching, and stability of sputtered ZnO:Al for thin-film silicon solar cells*. 2011: Forschungszentrum Jülich.
66. Association, I.Z. *Zinc oxide applications* 2011 [cited 2014 04/09/2014]; Available from: http://www.zinc.org/info/zinc_oxide_applications.
67. Ozgur, U., D. Hofstetter, and H. Morkoc, *ZnO devices and applications: A review of current status and future prospects.* Proceedings of the Ieee, 2010. **98**(7): p. 1255-1268.
68. Ozgur, U., et al., *A comprehensive review of ZnO materials and devices.* Journal of Applied Physics, 2005. **98**(4).
69. Lide, D.R., *CRC Handbook of chemistry & physics 73rd edition*. 1992: Taylor & Francis.

70. Reeber, R.R., *Lattice parameters of ZnO from 4.2 degrees to 296 degrees K.* Journal of Applied Physics, 1970. **41**(13): p. 5063-&.
71. Morkoç, H. and Ü. Özgür, *General properties of ZnO*, in *Zinc Oxide*. 2009, Wiley-VCH Verlag GmbH & Co. KGaA. p. 1-76.
72. Weigand, C.C., *Zinc oxide nanostructures and thin films grown by pulseed laser deposition* in *Department of Electronics and Telecommunications*. 2012, Norwegian University of Science and Technology: Trondheim. p. 129.
73. Kohan, A.F., et al., *First-principles study of native point defects in ZnO.* Physical Review B, 2000. **61**(22): p. 15019-15027.
74. Janotti, A. and C.G. Van de Walle, *Native point defects in ZnO.* Physical Review B, 2007. **76**(16).
75. Vanheusden, K., et al., *Correlation between photoluminescence and oxygen vacancies in ZnO phosphors.* Applied Physics Letters, 1996. **68**(3): p. 403-405.
76. Lany, S. and A. Zunger, *Dopability, intrinsic conductivity, and nonstoichiometry of transparent conducting oxides.* Physical Review Letters, 2007. **98**(4): p. 045501.
77. Van de Walle, C.G., *Hydrogen as a cause of doping in zinc oxide.* Physical Review Letters, 2000. **85**(5): p. 1012-1015.
78. McCluskey, M.D. and S.J. Jokela, *Sources of n-type conductivity in ZnO.* Physica B-Condensed Matter, 2007. **401**: p. 355-357.
79. Lany, S. and A. Zunger, *Anion vacancies as a source of persistent photoconductivity in II-VI and chalcopyrite semiconductors.* Physical Review B, 2005. **72**(3): p. 035215.
80. Nam, S.-H., S.-J. Cho, and J.-H. Boo, *Physical properties of metal-doped zinc oxide films for surface acoustic wave application.* Nanoscale Research Letters, 2012. **7**.
81. Minami, T., et al., *Group-III impurity doped zinc-oxide thin-films prepared by RF magnetron sputtering.* Japanese Journal of Applied Physics Part 2-Letters, 1985. **24**(10): p. L781-L784.
82. Ueda, K., H. Tabata, and T. Kawai, *Magnetic and electric properties of transition-metal-doped ZnO films.* Applied Physics Letters, 2001. **79**(7): p. 988-990.
83. Bazzani, M., et al., *Optoelectronic properties of Al:ZnO: Critical dosage for an optimal transparent conductive oxide.* Applied Physics Letters, 2011. **98**(12): p. 3.
84. Shen, H.-l., et al., *Preparation and properties of AZO thin films on different substrates.* Progress in Natural Science: Materials International, 2010. **20**(0): p. 44-48.
85. Minami, T., T. Yamamoto, and T. Miyata, *Highly transparent and conductive rare earth-doped ZnO thin films prepared by magnetron sputtering.* Thin Solid Films, 2000. **366**(1-2): p. 63-68.
86. Maldonado, F. and A. Stashans, *Al-doped ZnO: Electronic, electrical and structural properties.* Journal of Physics and Chemistry of Solids, 2010. **71**(5): p. 784-787.
87. Kemmitt, T., B. Ingham, and R. Linklater, *Optimization of sol-gel-formed ZnO:Al processing parameters by observation of Dopant Ion location using solid-state Al-27 NMR spectrometry.* Journal of Physical Chemistry C, 2011. **115**(30): p. 15031-15039.
88. Kelchtermans, A., et al., *Relation between synthesis conditions, dopant position and charge carriers in aluminium-doped ZnO nanoparticles.* Rsc Advances, 2013. **3**(35): p. 15254-15262.
89. Saniz, R., et al., *A simplified approach to the band gap correction of defect formation energies: Al, Ga, and In-doped ZnO.* Journal of Physics and Chemistry of Solids, 2013. **74**(1): p. 45-50.
90. Serier, H., M. Gaudon, and M. Menetrier, *Al-doped ZnO powdered materials: Al solubility limit and IR absorption properties.* Solid State Sciences, 2009. **11**(7): p. 1192-1197.
91. Kim, H.-K., S. Lee, and K.-S. Yun, *Capacitive tactile sensor array for touch screen application.* Sensors and Actuators a-Physical, 2011. **165**(1): p. 2-7.

92. Tak, Y.H., et al., *Criteria for ITO (indium-tin-oxide) an organic light thin film as the bottom electrode of emitting diode.* Thin Solid Films, 2002. **411**(1): p. 12-16.
93. Yuan, Y.-z. and H. Wang, *Co-doped ZnO Transparent Conductive Films for LCD and UV Detectors*, in *Advanced Materials in Microwaves and Optics*, D. Wang, Editor. 2012. p. 226-230.
94. Lee, E.S. and D.L. DiBartolomeo, *Application issues for large-area electrochromic windows in commercial buildings.* Solar Energy Materials and Solar Cells, 2002. **71**(4): p. 465-491.
95. Fahland, M., et al., *Optical properties of metal based transparent electrodes on polymer films.* Thin Solid Films, 2008. **516**(17): p. 5777-5780.
96. Guillén, C. and J. Herrero, *TCO/metal/TCO structures for energy and flexible electronics.* Thin Solid Films, 2011. **520**(1): p. 1-17.
97. Technologies, F.P. *PV solar growth*. 2011 [cited 2014 15/09/2014]; Available from: http://solarcellcentral.com/markets_page.html#solar_growth.
98. Pasquarelli, R.M., D.S. Ginley, and R. O'Hayre, *Solution processing of transparent conductors: from flask to film.* Chemical Society Reviews, 2011. **40**(11): p. 5406-5441.
99. Muller, J., et al., *TCO and light trapping in silicon thin film solar cells.* Solar Energy, 2004. **77**(6): p. 917-930.
100. Nippon Sheet Glass Co., L. *Pilkington: Low-emissivity glass*. 2013 [cited 2014 15/09/2014]; Available from: http://www.pilkington.com/en-gb/uk/householders/types-of-glass/energy-efficient-glass/low-emissivity-glass.
101. Lewis, B.G. and D.C. Paine, *Applications and processing of transparent conducting oxides.* Mrs Bulletin, 2000. **25**(8): p. 22-27.
102. Eicker, U., *Solar technologies for buildings*. 2003: Wiley.
103. Wang, S.-M., et al., *High performance visible and near-infrared region electrochromic smart windows based on the different structures of polyoxometalates.* Electrochimica Acta, 2013. **113**: p. 240-247.
104. Lampert, C.M., *Large-area smart glass and integrated photovoltaics.* Solar Energy Materials and Solar Cells, 2003. **76**(4): p. 489-499.
105. Vergaz, R., et al., *Modelling and electro-optical testing of suspended particle devices.* Solar Energy Materials and Solar Cells, 2008. **92**(11): p. 1483-1487.
106. Lampert, C.M., *Smart switchable glazing for solar energy and daylight control.* Solar Energy Materials and Solar Cells, 1998. **52**(3–4): p. 207-221.
107. Kikuchi, N., et al., *Electrical and mechanical properties of SnO2 : Nb films for touch screens.* Vacuum, 2002. **66**(3-4): p. 365-371.
108. Cok, R., R. Bourdelais, and C. Kaminsky, *Flexible resistive touch screen*. 2004, Google Patents.
109. Kalendra, P.W. and W.J. Piazza, *Automatic calibration of a capacitive touch screen used with a fixed element flat screen display panel*. 1994, Google Patents.
110. Doering, R.W., *Infrared touch panel*. 1989, Google Patents.
111. Adler, R. and P.J. Desmares, *An economical touc panel using SAW absorption.* Ieee Transactions on Ultrasonics Ferroelectrics and Frequency Control, 1987. **34**(2): p. 195-201.
112. Luo, C., et al., *Compressive Sensing for Sparse Touch Detection on Capacitive Touch Screens.* Ieee Journal on Emerging and Selected Topics in Circuits and Systems, 2012. **2**(3): p. 639-648.
113. Kim, H., et al., *Transparent and flexible tactile sensor for multi touch screen application with force sensing* in *Transducers*. 2009, IEEE: Denver, USA. p. 1146-1149.
114. Bhalla, M.R. and A.V. Bhalla, *Comparative study of various touchscreen technologies.* Internation Journcal of Computer Applications, 2010. **6**(8): p. 12-18.

115. Sleeman, P., et al., *Capacitive Touch Screen with Noise Suppression*. 2010, Google Patents.
116. Hwang, T.-H., et al., *A Highly area-efficient controller for capacitive touch screen panel systems.* Ieee Transactions on Consumer Electronics, 2010. **56**(2): p. 1115-1122.
117. Philipp, H., *Touchscreen electrode configuration*. 2013, Google Patents.
118. Kent, J. and A. Ravid, *Projective capacitive touchscreen*. 2001, Google Patents.

Chapter 3 - Al doped ZnO thin film fabrication process

This chapter covers the fabrication process of Al doped ZnO thin films. Firstly, an introduction is given towards chemical solution deposition and its required production steps to develop high quality thin films. Secondly, the first principles of ink jet printing are covered, followed by state of the art of the fabrication of Al doped ZnO thin films via chemical solution deposition.

3.1 Developments in thin film technology

Thin film technology evolved during the last decades towards a branch with a broad variety of sophisticated deposition methods allowing a high control over the production process. New deposition techniques have become necessary and old deposition techniques have become cleaner, greener and more complex. Nowadays, thin films from several atomic layers thick till several micrometres can be produced in a uniform and reproducible manner [1]. Each deposition method coupled with well-defined parameters generate films of different properties [2]. One should notice that many of the traditional TCO thin films had their processing roots in chemical solution processing such as spray pyrolysis. But since the 1970's, vacuum-based physical vapour deposition (PVD) techniques such as sputtering and pulsed laser deposition (PLD) have become the first-hand deposition techniques for research and industry. The ability to produce dense films with excellent properties and the good control of the process makes PVD techniques ideal for exploring new materials [3, 4]. Nevertheless, at this moment there is a trend to get back to the roots of TCO processing, being chemical solution deposition (CSD). This atmospheric technique is an attractive alternative for the conventionally used high-vacuum techniques because of its easy fabrication process, good scalability and potential to lower the manufacturing costs of device [4-7]. The equipment and operation costs for CSD methods may be considered lower than for vacuum deposition methods. Nevertheless, the costs associated with the preparation of precursor solutions (chemical precursors, solvents, additives) and post-processing criteria may be a critical additional cost [8, 9]. Still, research and insights into the chemistry of these systems is important to defeat these drawbacks and to further improve the quality of the deposited films.

An overview of Al doped ZnO (AZO) thin films and their properties is projected in table 3.1 and illustrates the differences in quality of AZO thin films produced through several deposition methods. Overall, the PVD techniques produce AZO thin films of higher quality concerning the electrical properties. However, CSD techniques are closing in. It's up to research to create new insights in CSD processing of TCOs, which necessary to make CSD processing a competitive competitor of PVD processing of TCOs.

Table 3.1 Literature overview of AZO thin films fabricated through various deposition techniques such as pulsed laser deposition (PLD), sputtering, atomic layer deposition (ALD) and chemical solution deposition (CSD). Note: The data are well selected and exhibit an average result.

Dopant concentration (at%)	Deposition method	Deposition temperature (°C)	Resistivity (Ω cm)	Carrier concentration (cm^{-3})	Carrier mobility ($cm^2 V^{-1} s^{-1}$)	Average transmittance (%)	Spectral range (µm)	Ref.
1.0	PLD	750	$3.0 * 10^{-3}$	$4.0 * 10^{19}$	49	80	0.4-0.8	[10]
2.0	PLD	300	$3.1 * 10^{-4}$	$1.4 * 10^{21}$	20	80	0.4-0.8	[11]
2.0	sputtering	250	$2.7 * 10^{-4}$	$9.0 * 10^{20}$	25	/	/	[12]
2.0	sputtering	250	$2.5 * 10^{-4}$	$9.5 * 10^{20}$	18	/	/	[13]
3.6	sputtering	200	$8 * 10^{-4}$	$5 * 10^{20}$	16	80	0.4-0.8	[14]
2.1	ALD	250	$5.9 * 10^{-4}$	$6.8 * 10^{20}$	17	86	0.4-0.8	[15]
2.2	ALD	240	$1.4 * 10^{-4}$	/	/	/	/	[16]
1.5	CSD	530	$6.2 * 10^{-4}$	/	/	80	0.4-0.8	[17]
1	CSD	600	$1.1 * 10^{-2}$	/	/	90	0.4-0.8	[18]
0.6	CSD	600	$5 * 10^{-3}$	$3 * 10^{19}$	42	88	0.55	[19]
1	CSD	550	$1.4 * 10^{-2}$	$2 * 10^{19}$	17	80	0.55	[20]

3.2 Chemical solution deposition

The past decades chemical solution deposition has developed into an important technique for the deposition of functional oxides thin films because of a number of advantages, cfr. 3.1. The preparation of inorganic solid state materials through chemical solution processing dates back to mid-1800, where Ebelmen [21, 22] discovered that silicon alkoxides react with humidity to hydrated silica gels. The evolution of wet chemistry made it possible to deposit single oxides as complex oxide thin films on various substrates. These functional oxide thin films can have a wide range of applications, such as superconductors in coated conductors [23], photo-catalytic coatings in self-cleaning windows [24], ion conductors in solid oxide fuel cells [25], electron conductors in displays [26], etc.

A typical CSD process consist of several fabrication steps, as illustrated in figure 3.1: Firstly, the formulation of the precursor solution starts with the selection of the metal precursors. The metal precursors will be dissolved in a solvent of choice by simple dissolution or refluxing. Solvent selection is a balance between solids-loading (solubility) and the deposition requirements. Aqueous solutions are favoured because of their cost-effectiveness and low impact on the environment. However, organic solvents or mixtures are frequently used to improve the solubility of metal alkoxides and to tune the properties for deposition. A good wetting of the substrate is an essential parameter to fabricate high quality coatings. However, there is also a trade-off between viscosity and volatility. High molecular weight solvents increase the viscosity but lack the volatility to be removed by mild heating. On the other hand, highly volatile solvents can be easily removed but the evaporation can happen too quickly, resulting in porous or rough film morphologies.

Once a solution is formulated, one can coat a substrate with a wet film of this solution. Several deposition methods can be employed such as dip coating, spin coating, drop casting, spray coating, ink jet printing, etc.. The applied deposition method influences the chosen solvent. For example, 2-methoxyethanol is due to its relatively high viscosity (1.71 cP) and high boiling point (125°C) an appropriate choice for spin and dip coating, while methanol (viscosity of 0.59 cP and boiling point of 65°C) is more suited for spray coating. In case of ink jet printing, the solvent will influence the jetting of the ink and wetting/clogging of nozzles. If the selected solvent results in a solution with inappropriate properties

the addition of additives may adjust the rheology, viscosity, stability of the solution and wetting of the substrate [4]. Because this dissertation handles about ink jet printing of AZO thin film, ink jet printing as deposition technique for ceramic coatings will be discussed in detail further on.

After deposition the (wet) as-deposited film is heated with a controlled and well selected thermal process, resulting in gel formation, the removal of organic components (pyrolysis), crystallisation and densification. Figure 3.1 illustrates the individual processing steps such as gel formation and pyrolysis. In reality, it is hard to distinguish such individual processing steps. The thermal process is selected towards the decomposition of the wet film as the nucleation and growth behaviour of Al-doped ZnO.

To quantify or control each part of the fabrication process the selection of an appropriate characterisation tool is necessary. Only a continuous interplay between each part of the fabrication process will improve the final quality of the deposited thin film.

Finally, the incorporation of the oxide thin film in a device will confirm a successful deposition of the oxide thin film.

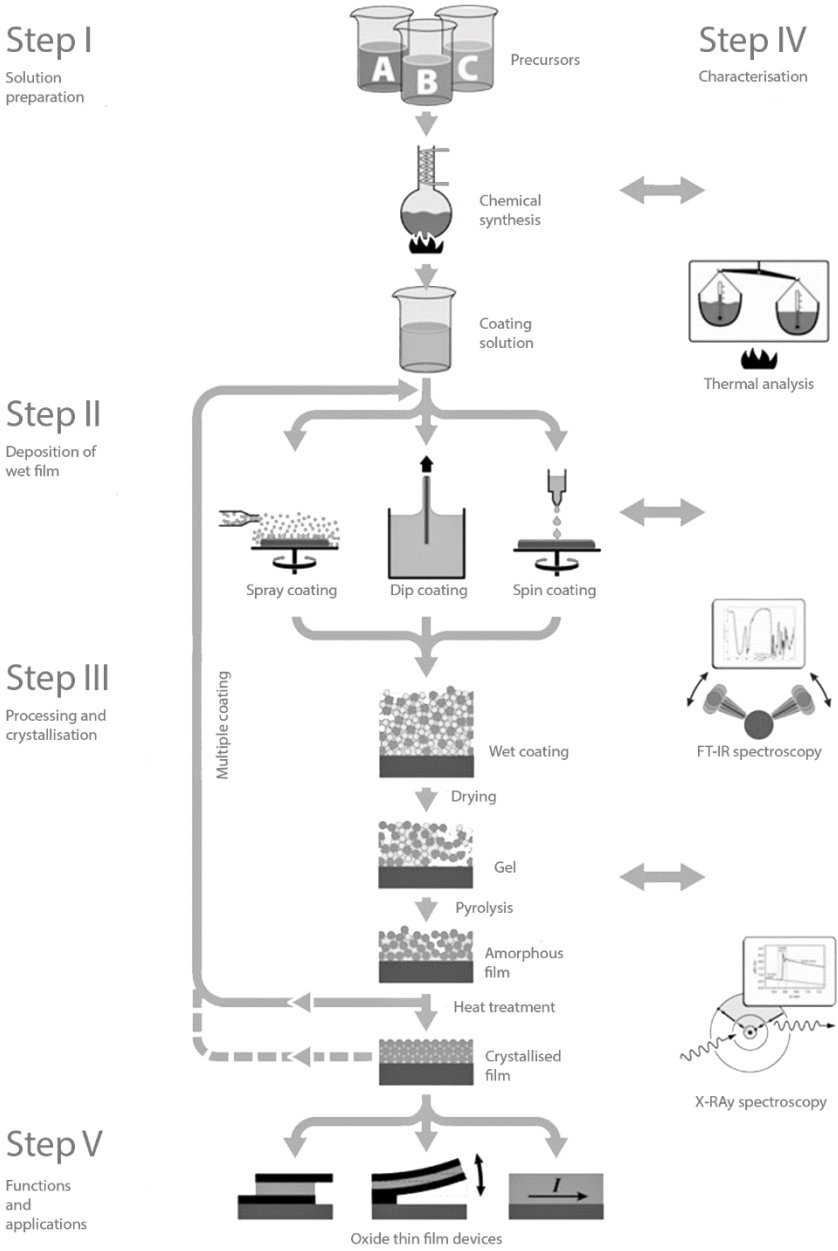

Figure 3.1 Flow chart of a typical CSD process. Five separate parts in the fabrication process can be distinguished: Step I: Solution preparation, Step II: deposition of wet film, Step III: Processing and crystallization, Step IV: Characterisation and Step V: Functions and applications. Adapted from [27].

3.3 Ink jet printing as deposition method for TCOs

To compete against vacuum deposition techniques in the world of TCOs, a versatile and scalable deposition method is important. Therefore, in this dissertation ink jet printing is favoured. It has many advantages: (1) Ink jet printing is known as a direct writing technique that makes additional lithography or etching unnecessary. This allows the printing of patterns without the deposition of a continuous layer first. So, it is cost-saving and precursor materials are efficiently used [28]. (2) Ink jet printing is a non-contact deposition technique where the ink is stored in a cartridge avoiding any form of contamination [29]. (3) During printing the substrates aren't spinning or moving vertically in contrast to spin coating or dip coating. (4) Ink jet printing is a scalable technique. Large areas can be coated at high throughput by increasing the number of nozzles in a printhead. However, ink jet printing goes along with some challenges which will be addressed in this work: ink chemistry and formulation not only determine the quality of the as-deposited layers but also the ink stability and jettability. For example, clogging of the printhead and dewetting of the substrate are undesired but frequently happening with random formulated precursor solutions.

3.3.1 Ink jet printing setup

The first principles of ink jet printing as a technique by itself can be traced to Lord William Kelvin. Electrostatic forces were used to direct droplets [30]. Without the need to generate detailed instructions to control the movement of the droplets, the concept stayed unused until 1951. Siemens used the technique to plot output data, such as from a medical strip chart recorder. In the period of 1960-1980 major advances took place. The technology based on the deflection of ink droplets was used to create a printer that was able to print computer graphics output [30, 31]. Sweet [32] demonstrated that uniform and equispaced droplets at high frequencies can be jetted by applying a pressure wave to an orifice. The ink is continuously forced out of the nozzle by applying a disturbance at fixed rates, resulting in a uniform stream of droplets. Certain droplets are charged and deflected by an electrical field. They are collected in the ink reservoir and recirculated to the orifice. The uncharged and undeflected droplets create a pattern on a substrate. This particular concept is further catalogued as continuous ink jet printing (CIJ) (figure 3.2). Nowadays, the

primary commercial application of ink jet printing is printing of graphics and other conventional digital printing operations [30, 33-35]. Due to its benefits, ink jet printing gained more and more attention as manufacturing technology in other fields than the latter, e.g. ceramics [24, 33, 35, 36], functional organics [37-39], biomaterials [40, 41] etc.

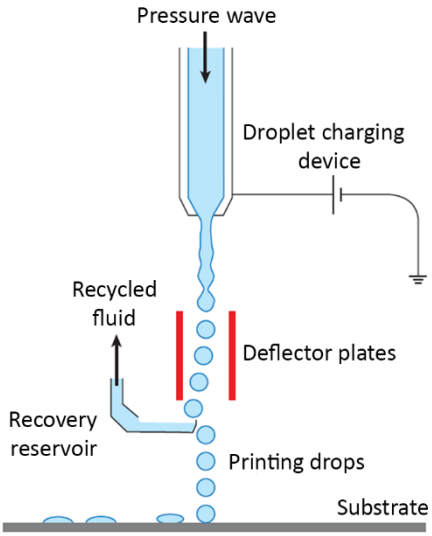

Figure 3.2 Schematic of a continuous ink jet printhead [42].

Continuous ink jet printing is a fast printing technique (up to 120 000 droplets per second) and frequently used in printing of labels and barcodes on a diverse range of products [43]. The formation of satellite droplets is very common in the case of the continuous ink jet printing systems. Depending on the applied pressure wave, they either will collide with the main droplet or either be deflected to unwanted positions on the substrate, what is lowering the overall print resolution [44]. Therefore, the majority of materials science research is performed with a drop-on-demand (DOD) printing system (figure 3.6). DOD printheads are less complex due to the absence of deflection plates and the recovery reservoir. If the ink is well formulated and the parameters are well chosen, they can eject droplets on command without satellite droplets. This will improve the printing resolution and there is less chance for contamination of the ink (no recirculation of the ink). A change in the cavity volume of the printhead will lead to a momentum that ejects a droplet. The propagation of the wave in the ink and the geometry of the cavity have a considerable effect on the jetting of droplets [44].

DOD printheads have several mechanisms to eject droplets out of the cavity (figure 3.3). A first system contains a micro heater inside the nozzle chamber that generates a vapour bubble. Pressure waves induced by the growth and collapse of the bubble cause drop formation. This type of printheads is defined as a thermal DOD printing system. Another type of printhead is the piezoelectric model. The incorporation of a piezoelectric ceramic element in the nozzle chamber will deform by applying an electrical pulse.

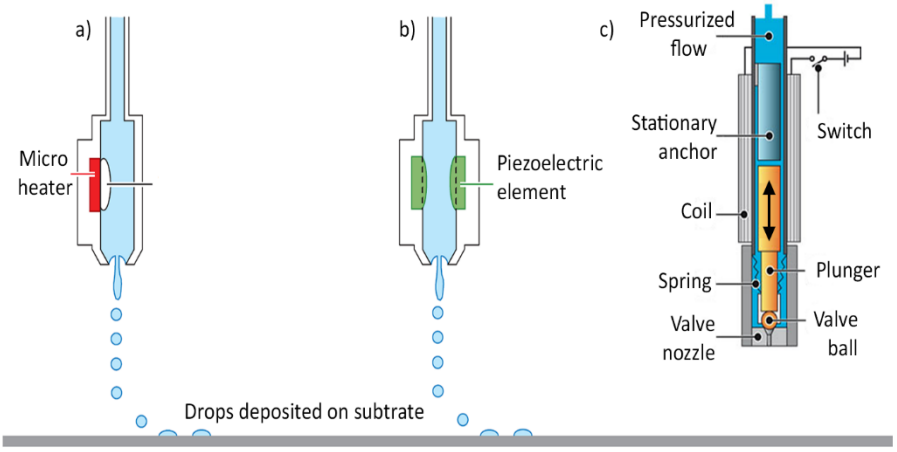

Figure 3.3 Schematic of different types of DOD printheads. a) a thermal DOD printhead, b) a piezoecletric DOD printhead and c) a electromagnetic DOD printhead [42].

An electromagnetic printhead is also a type of a DOD printhead. An electrical pulse passing through the coil will induce a magnetic field which pulls up the plunger and uncovers the nozzle valve. The positive pressure applied on the ink reservoir forces out a droplet. At the end of the electrical pulse, the plunger moves back down and further jetting is avoided.

Thermal and electromagnetic printheads have limitations. The used inks for thermal printheads should be thermally stable. The electromagnetic printhead is built up from metal parts that come in contact with the ink. To prevent corrosion of the inner parts, the use of aggressive chemicals should be avoided. Piezoelectric printing devices are commonly used in research due to their ability to jet a broad range of solvents. In this research the printing experiments are performed with a piezoelectric printing device of MicroFab Technologies, Inc. consisting of a quartz capillary covered with a piezoelectric filament. Those printheads are suited for inks with the following properties:

- Ink viscosity up till 20 x 10^{-3} Pa s
- Ink surface tension in the range of 20 - 70 mN/m
- Ink pH in the range of 2 – 11
- Broad range of solvents (water, alcohol, ketones, aromatics and aliphatics)

3.4 State of the art CSD processing of AZO

In general, two main types of precursors are applied for thin oxide film deposition: nanoparticle suspensions [45, 46] and dissolved metal salts in solvents [47, 48]. The nanoparticle routes are using pre-synthesised nanoparticles of the desired materials, resulting in reduced thermal treatments as the preferred material is already formed [4]. Niederberger [49, 50] and Pinna [51] describe the formation of diverse crystalline oxide nanoparticles which can be used to deposit thin film oxides. The high solid loading required for thin film deposition involves the use of stabilisers (capping agents). The formed network after deposition results in small contact points between two particles which is a bottle-neck for charge transport in TCOs [27]. Additionally, if a dense film is required an intense thermal process is required to sinter the particles and to remove the organic capping agents [4, 52, 53]. When metal salts are dissolved in a solvent of choice, the species in solution resemble the starting material if no oligomerisation or complexation has taken place. A thermal process is necessary to burn off the organics and counter-ions and to generate the desired oxide phase from the wet deposited thin film. For a more comprehensive overview about chemical solution processing, one is advised to glance through: *Introduction to Sol-Gel processing* by Pierre [54], *Sol-Gel Science: The Physics and Chemistry of Sol-Gel Processing* by Brinker and Scherrer [55] and *Chemical Solution Deposition of Functional Oxide Thin Films* by Schneller *et al*. [27].

Figure 3.4 represents the number of publications covering CSD processing of ZnO based thin films from the past 15 years. The increasing amount of publications allows us to collect a lot of information about the synthesis of CSD ZnO thin films. This input is of great help towards the development of excellent AZO thin films by CSD processing. For ZnO thin film processing organic solvents such as methanol [56, 57], ethanol [58-60], 2-propanol [61, 62] and 2-

methoxyethanol [63, 64] are frequently used and additives such as mono-ethanolamine [60, 64], di-ethanolamine [61, 62] and lactic acid [58, 65] are used as chelating species. The selected Zn precursor is mainly zinc acetate. Other precursors such as zinc alkoxides, zinc nitrates, zinc chlorides and zinc perchlorates have to be avoided. Zinc alkoxides are expensive, very sensitive to moisture and highly reactive, while the use of zinc nitrates, zinc chlorides or zinc perchlorates result in a low reproducibility or precipitation. Zinc acetate is favoured because of its low cost that makes it suitable for large-scale applications. The competing chelating effect of the acetate groups with the other stabilisers results in stable precursor solutions [60]. The knowledge build up from processing ZnO thin films by CSD is transferred towards processing of AZO thin films. The commonly used aluminium precursor is aluminium nitrate [19, 27, 66, 67].

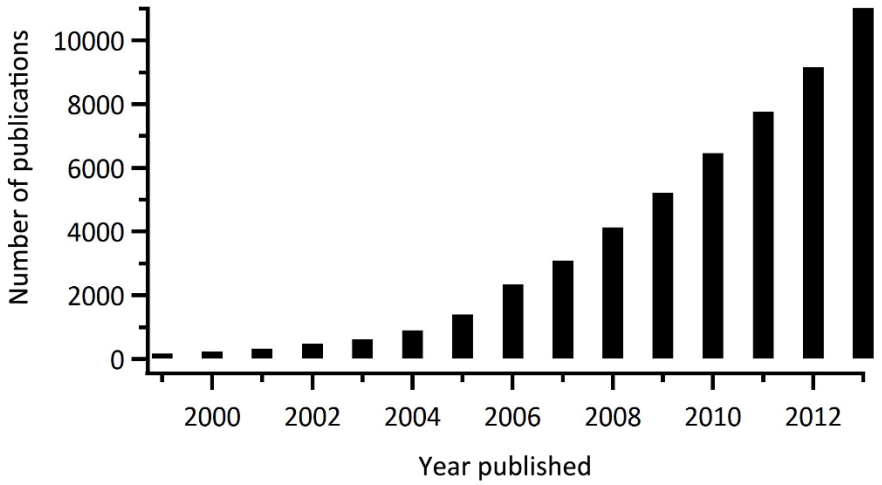

Figure 3.4 number of publication concerning CSD of ZnO based thin films according to Web of Knowledge™.

3.4.1 Preferential growth of ZnO thin films

Zinc oxide and doped zinc oxide thin films have the unique property that a preferred crystal orientation can be obtained when they are deposited on an amorphous substrate. In general, oxide thin films derived through chemical solution deposition exhibit a random orientation of crystalline grains due to the nucleation and growth in the bulk of the film. However, texture can be

transferred from the substrate to the oxide thin film. Therefore, the substrate must have a structure and lattice match with the oxide material to induce epitaxial growth. Because the AZO thin films are deposited on amorphous glass substrates texture can't be transferred from the substrate to the coating, however oriented AZO films are obtained due to the nucleation and crystal growth at the substrate interface. The influence of the substrate should be considered regardless of epitaxial or non-epitaxial growth. Two possible mechanisms are suggested: an initial orientation due to nucleation and a final growth orientation. Both originate from nucleation at the film/substrate interface. The final growth orientation is a result of survival of nuclei with a certain orientation because of different growth rates. The initial orientation is favored on smooth surfaces where a minimum free energy configuration can be developed [68].

Compared to vapour deposition methods chemical solution deposition is characterised by post-deposition crystallisation which implies the formation of a metastable amorphous film before the crystallisation takes part [60]. The amorphous thin film has a higher free energy than a crystalline solid or the equilibrium super-cooled liquid (figure 3.5). The high free energy of the amorphous thin film can be assigned to chemical, physical and structural factors such as an excess of organic compounds, hydroxyl groups, a porous structure and a lower density compared to the equilibrium liquid. Crystallisation of the amorphous thin film goes along with a change in volume free energy, ΔG_v [27]

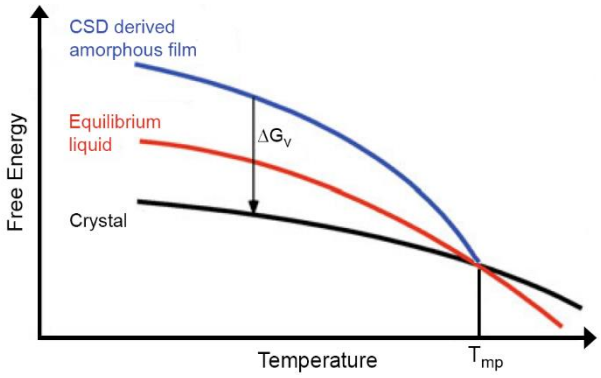

Figure 3.5 Schematic representation of the free energy in respect to the temperature for a CSD derived amorphous thin film, an equilibrium liquid and crystalline solid [42].

When the homogenous nucleation of a spherical nucleus takes place the free energy change is represented by [68]:

$$\Delta G_{homo} = \frac{4}{3}\pi r^3(\Delta G_v + \Delta G_e) + 4\pi r^2\gamma \qquad \text{Eq.3.1}$$

Where r, ΔG_v, ΔG_e and γ are the radius of the formed nuclei, the volume free energy, the elastic strain energy and the interfacial energy between the formed crystal and the amorphous matrix. A subcritical nucleus must overcome a free energy barrier to become supercritical, which can be derived from $\delta(\Delta G)/\delta r = 0$.

$$r^* = \frac{-2\gamma}{(\Delta G_v + \Delta G_e)} \qquad \text{Eq.3.2}$$

$$\Delta G^*_{homo} = \frac{16\pi\gamma^3}{3(\Delta G_v + \Delta G_e)^2} \qquad \text{Eq.3.3}$$

Where r^* is the critical radius of the nuclei and ΔG^* the energy barrier that must be overcome to obtain stable nuclei.

The nucleation on the substrate's surface will result in nuclei that aren't spherical. The nuclei will be a spherical cap that have a contact angle θ, with the substrate. The reduction in the nucleus's surfaces reduce the barrier height to nucleation. The free energy barrier for heterogeneous nucleation is given by [68]:

$$\Delta G^*_{hetero} = \Delta G^*_{homo}\, f(\theta) \qquad \text{Eq.3.4}$$

Where:

$$f(\theta) = \frac{1}{4}(2 + \cos\theta)(1 - \cos\theta)^2 \qquad \text{Eq.3.5}$$

The contact angle is set by the interfacial energy of the substrate and the amorphous matrix, γ_{sa}, the interfacial energy of the substrate and the crystalline nucleus, γ_{sc} and the interfacial energy of the crystalline nucleus and the amorphous matrix, γ_{ca}:

$$\gamma_{sa} = \gamma_{ca}\cos\theta + \gamma_{sc} \qquad \text{Eq.3.6}$$

These equations can now be used to interpret the mechanism of nucleation and growth behaviour of CSD thin films.

Because the growth of *c*-axis oriented AZO film is independent of the deposition method [11, 69-71], one can suggest that nucleation and growth of *c*-axis AZO thin films are a consequence of a system that is trying to reduce its free energy. Due to the high interfacial energy of the amorphous AZO layer and the substrate, crystalline nuclei will be formed at the interface of the substrate. Some high-energy amorphous AZO/substrate interfaces will be replaced by lower-energy crystalline AZO/substrate interfaces which contributes to an overall smaller interfacial energy and thus a reduction in the free energy barrier. The nuclei with their (0001) plane parallel to the substrate will be most favoured due to the largest reduction of the total interfacial energy. The fast growth velocity of this plane results in an overall growth direction perpendicular to the substrate. However, this all can be influenced by experimental parameters such as growth temperatures, heating rates and precursor composition [60].

Multi-layer approach towards preferential growth of the crystal structure

Chemical solution deposited grown AZO thin films are most commonly deposited by a multi-layer approach. Multiple coatings are applied on top of each other [19, 70, 72-74]. The number of layers deposited to obtain the final coating can run up to 25 [73]. Each layer undergoes a thermal 'pre-treatment' to bake out the organics before the next coating step. Finally, the complete stack of coatings undergoes a thermal treatment to improve the density and crystallinity. One can already imagine the limited scalability of this process but this multi-layer approach can lead to an interesting morphology. As discussed in chapter 2, the electrical properties of a AZO thin film are strongly depending on the charge carriers concentration and their mobility. The coating morphology has an important contribution to increase the electrical properties. Schuler *et al*. [75] distinguished 3 types of structural parameters (figure 3.6), e.g. the granular structure, the layered structure and the columnar structure. These structural parameters of the thin films have an enormous effect on the resistivity, whereas the columnar structure shows the highest carrier density and mobility and where the granular structure exhibit the lowest values. A possible explanation can be found within the porosity of the coatings and the scattering phenomena at grain boundaries. When neighboring grains have parallel *c*-axis the number of

traps and/or defects at the grain boundaries decreases, resulting in lower barrier heights at the grain boundaries. The carrier density and mobility will increase, resulting in better electrical properties [76].

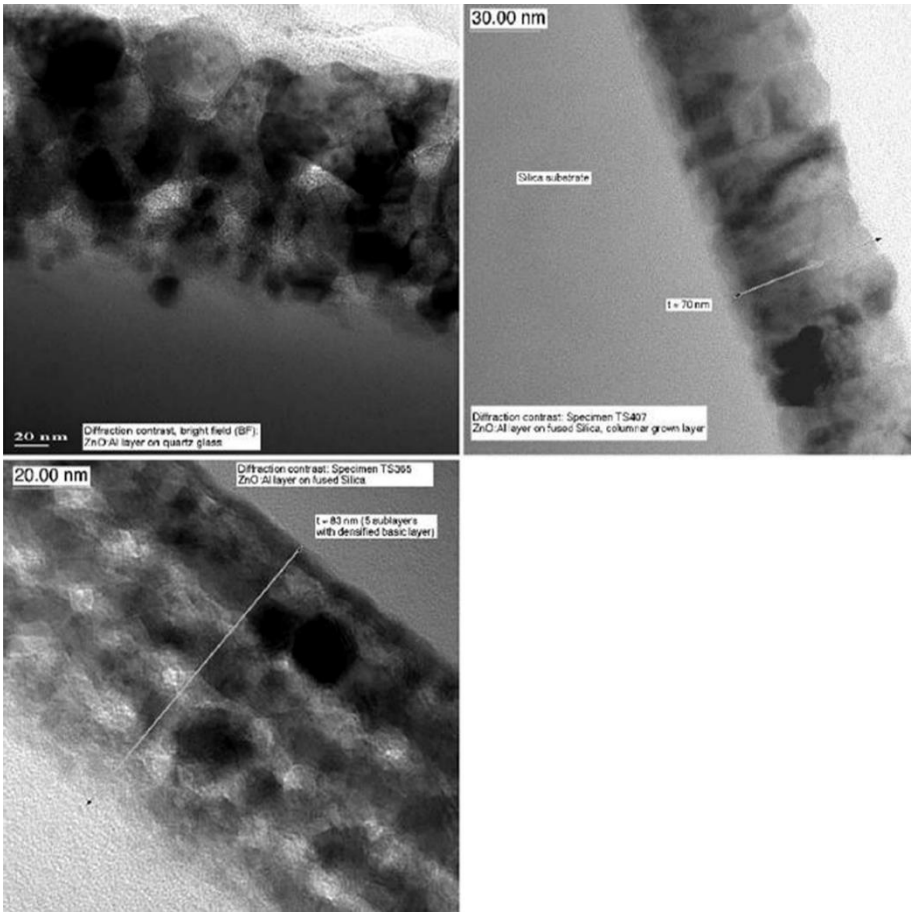

Figure 3.6 Structural parameters: Top left: Diffraction contrast, bright field image of a granular structured AZO thin film deposited by one single layer on quartz glass. Top right: Diffraction contrast image of a columnar structured AZO thin film deposited by 20 repetitive coatings on fused silica. Bottom left: Diffraction contrast image of a layered structured AZO thin film deposited by 5 repetitive coatings on fused silica [75].

Schuler *et al.* [75] defined that the ratio between the intrinsic crystal size and the single layer thickness is an indication for the type of growth (granular, layered of columnar structure). When the ratio is larger than 1 columnar growth is obtained, while a ratio smaller than 0.42 stimulates granular growth. Values in between result in a layered structure. The observations by Schuler *et al.* [75] help to understand the success of the multi-layer approach. Many authors [19,

70, 72, 75, 77] reported that the deposition of multiple thin layers improved the electrical properties of AZO thin films. Multiple coatings reduce pores but also induce a columnar growth if each single deposited layer is thin enough which is beneficial for the final properties of the transparent conductive thin films.

3.5 Reference list

1. Seshan, K., *Handbook of Thin-Film Deposition Processes and Techniques - Principles, Methods, Equipment and Applications (2nd Edition)*. William Andrew Publishing/Noyes.
2. Chopra, K.L., S. Major, and D.K. Pandya, *Transparent conductors- a status review.* Thin Solid Films, 1983. **102**(1): p. 1-46.
3. Ellmer, K., *Magnetron sputtering of transparent conductive zinc oxide: relation between the sputtering parameters and the electronic properties.* Journal of Physics D-Applied Physics, 2000. **33**(4): p. R17-R32.
4. Pasquarelli, R.M., D.S. Ginley, and R. O'Hayre, *Solution processing of transparent conductors: from flask to film.* Chemical Society Reviews, 2011. **40**(11): p. 5406-5441.
5. Mitzi, D.B., *Solution-processed inorganic semiconductors.* Journal of Materials Chemistry, 2004. **14**(15): p. 2355-2365.
6. Khan, Z., et al., *Optical and structural properties of ZnO thin films fabricated by sol-gel method.* Materials Sciences and Applications, 2011. **2**(5): p. 340-345.
7. Exarhos, G.J. and X.-D. Zhou, *Discovery-based design of transparent conducting oxide films.* Thin Solid Films, 2007. **515**(18): p. 7025-7052.
8. Zweibel, K., *Issues in thin film PV manufacturing cost reduction.* Solar Energy Materials and Solar Cells, 1999. **59**(1–2): p. 1-18.
9. Mitzi, D.B., *Solution processing of inorganic materials*. 2009, Hoboken, NJ: Wiley. 501.
10. Mass, J., P. Bhattacharya, and R.S. Katiyar, *Effect of high substrate temperature on Al-doped ZnO thin films grown by pulsed laser deposition.* Materials Science and Engineering: B, 2003. **103**(1): p. 9-15.
11. Papadopoulou, E.L., et al., *Undoped and Al-doped ZnO films with tuned properties grown by pulsed laser deposition.* Thin Solid Films, 2008. **516**(22): p. 8141-8145.
12. Minami, T., et al., *Preparations of ZnO-Al transparent conducting films by DC magnetron sputtering.* Thin Solid Films, 1990. **193**(1-2): p. 721-729.
13. Tominaga, K., et al., *Transparent conductive ZnO film preparation by alternating sputtering of ZnO:Al and Zn or Al targets.* Thin Solid Films, 1998. **334**(1–2): p. 35-39.
14. Kusayanagi, M., et al., *Al-doped ZnO films deposited on a slightly reduced buffer layer by reactive dc unbalanced magnetron sputtering.* Thin Solid Films, 2014. **555**(0): p. 93-99.
15. Choi, Y.-J., et al., *Characteristics of the electromagnetic interference shielding effectiveness of Al-doped ZnO thin films deposited by atomic layer deposition.* Applied Surface Science, 2013. **269**(0): p. 92-97.
16. An, K.-S., et al., *Atomic layer deposition of undoped and Al-doped ZnO thin films using the Zn alkoxide precursor methylzinc isopropoxide.* Journal of Nanoscience and Nanotechnology, 2008. **8**(9): p. 4856-4859.
17. Xu, Z.Q., et al., *Characteristics of Al-doped c-axis orientation ZnO thin films prepared by the sol–gel method.* Materials Research Bulletin, 2006. **41**(2): p. 354-358.
18. Lee, J.-H. and B.-O. Park, *Transparent conducting ZnO:Al, In and Sn thin films deposited by the sol–gel method.* Thin Solid Films, 2003. **426**(1–2): p. 94-99.
19. Schuler, T. and M.A. Aegerter, *Optical, electrical and structural properties of sol gel ZnO : Al coatings.* Thin Solid Films, 1999. **351**(1-2): p. 125-131.
20. Sobajima, Y., et al., *Study of the light-trapping effects of textured ZnO : Al/glass structure TCO for improving photocurrent of a-Si : H solar cells.* Journal of Materials Science-Materials in Electronics, 2007. **18**: p. S159-S162.
21. Ebelmen, J., *Üntersuchungen über dir verbindung ber borsaüre and kieselsaüre mit aether.* Annale de Chimie et de Physique, 1846. **16**: p. 129.
22. Ebelmen, J., *Sur les e´thers siliciques.* C R Hebd Seances Acad Sci, 1844. **19**: p. 398–400.

23. Vermeir, P., et al., *Influence of the heating ramp on the superconducting properties of YBa2Cu3O7 − δ films using chemical solution deposition in a direct sintering method.* Thin Solid Films, 2013. **548**(0): p. 498-501.
24. Arin, M., et al., *Durability and efficiency of ink-jet printed TiO2 coatings: Influence of processing temperature.* Thin Solid Films, 2014. **556**: p. 160-167.
25. Gaudon, M., et al., *Thick YSZ films prepared via a modified sol–gel route: Thickness control (8–80 µm).* Journal of the European Ceramic Society, 2006. **26**(15): p. 3153-3160.
26. Hosono, H., *Recent progress in transparent oxide semiconductors: Materials and device application.* Thin Solid Films, 2007. **515**(15): p. 6000-6014.
27. Schneller, T., et al., *Chemical solution deposition of functional oxide thin films*. 2014: Springer Vienna.
28. Duineveld, P.C., *The stability of ink-jet printed lines of liquid with zero receding contact angle on a homogeneous substrate.* Journal of Fluid Mechanics, 2003. **477**: p. 175-200.
29. Tekin, E., P.J. Smith, and U.S. Schubert, *Inkjet printing as a deposition and patterning tool for polymers and inorganic particles.* Soft Matter, 2008. **4**(4): p. 703-713.
30. Derby, B., *Inkjet printing of functional and structural materials: fluid property requirements, feature stability, and resolution*, in *Annual Review of Materials Research, Vol 40*, D.R. Clarke, M. Ruhle, and F. Zok, Editors. 2010. p. 395-414.
31. Feys, J., *Digitally printed superconductiong coatings and patterns* in *Department of Inorganic and Physical Chemistry*. 2014, Ghent University Ghent. p. 174.
32. Sweet, R.G., *High frequency recording with electrostatically deflected ink jets.* Review of Scientific Instruments, 1965. **36**(2): p. 131-136.
33. Derby, B., *Inkjet printing ceramics: From drops to solid.* Journal of the European Ceramic Society, 2011. **31**(14): p. 2543-2550.
34. Jang, D., D. Kim, and J. Moon, *Influence of fluid physical properties on ink-jet printability.* Langmuir, 2009. **25**(5): p. 2629-2635.
35. Dou, R., et al., *Ink-jet printing of zirconia: Coffee staining and line stability.* Journal of the American Ceramic Society, 2011. **94**(11): p. 3787-3792.
36. Feys, J., et al., *Ink-jet printing of YBa2Cu3O7 superconducting coatings and patterns from aqueous solutions.* Journal of Materials Chemistry, 2012. **22**(9): p. 3717-3726.
37. Krebs, F.C., *Fabrication and processing of polymer solar cells: A review of printing and coating techniques.* Solar Energy Materials and Solar Cells, 2009. **93**(4): p. 394-412.
38. Hebner, T.R., et al., *Ink-jet printing of doped polymers for organic light emitting devices.* Applied Physics Letters, 1998. **72**(5): p. 519-521.
39. Yin, Z.P., et al., *Inkjet printing for flexible electronics: Materials, processes and equipments.* Chinese Science Bulletin, 2010. **55**(30): p. 3383-3407.
40. Roth, E.A., et al., *Inkjet printing for high-throughput cell patterning.* Biomaterials, 2004. **25**(17): p. 3707-3715.
41. Nakamura, M., et al., *Biomatrices and biomaterials for future developments of bioprinting and biofabrication.* Biofabrication, 2010. **2**(1): p. 6.
42. Pollefeyt, G., *Chemical Solution Deposition of alternative buffer materials for coated conductors*, in *Department of Inorganic and Physical Chemistry*. 2014, Ghent Univeristy: Ghent. p. 153.
43. Matthews. *Matthews intelligent identification: Small character continuous inkjet (CIJ)*. 2014 [cited 2014 14/11/2014]; Available from: http://www.matthews.com.au/solutions/our-technology/small-character-continuous-inkjet/CIJ.
44. Martin, G.D., et al., *Inkjet printing - the physics of manipulating liquid jets and drops.* Engineering and Physics - Synergy for Success, 2008. **105**.

45. Lee, S., et al., *Solution-processed ZnO nanoparticle-based semiconductor oxide thin-film transistors.* Superlattices and Microstructures, 2008. **44**(6): p. 761-769.
46. Lee, D., M.F. Rubner, and R.E. Cohen, *All-nanoparticle thin-film coatings.* Nano Letters, 2006. **6**(10): p. 2305-2312.
47. Pollefeyt, G., et al., *Ink-jet printing of SrTiO3 buffer layers from aqueous solutions.* Superconductor Science & Technology, 2014. **27**(9): p. 8.
48. Cloet, V., et al., *A Water-Based Sol-Gel Precursor for Deposition of Thin La2Zr2O7 Layers on Ni-W Substrates.* Ieee Transactions on Applied Superconductivity, 2009. **19**(3): p. 3467-3470.
49. Niederberger, M., et al., *Non-aqueous routes to crystalline metal oxide nanoparticles: Formation mechanisms and applications.* Progress in Solid State Chemistry, 2005. **33**(2-4): p. 59-70.
50. Niederberger, M., et al., *Nonaqueous synthesis, assembly and formation mechanisms of metal oxide nanocrystals.* International Journal of Nanotechnology, 2007. **4**(3): p. 263-281.
51. Pinna, N. and M. Niederberger, *Surfactant-free nonaqueous synthesis of metal oxide nanostructures.* Angewandte Chemie-International Edition, 2008. **47**(29): p. 5292-5304.
52. Luo, L., et al., *Microwave-assisted nonaqueous sol-gel synthesis: From Al:ZnO nanoparticles to transparent conducting films.* Acs Sustainable Chemistry & Engineering, 2013. **1**(1): p. 152-160.
53. Lu, Z.H., et al., *Synthesis of aluminium-doped ZnO nanocrystals with controllable morphology and enhanced electrical conductivity.* Journal of Materials Chemistry, 2011. **21**(12): p. 4161-4167.
54. Pierre, A.C., *Introduction to sol-gel processing*. 1998: Springer US.
55. Brinker, C.J. and G.W. Scherer, *Sol-gel science: The physics and chemistry of sol-gel processing*. 1990: Academic Press.
56. Natsume, Y. and H. Sakata, *Zinc oxide films prepared by sol-gel spin-coating.* Thin Solid Films, 2000. **372**(1-2): p. 30-36.
57. Santos, A.M.P. and E.J.P. Santos, *Pre-heating temperature dependence of the c-axis orientation of ZnO thin films.* Thin Solid Films, 2008. **516**(18): p. 6210-6214.
58. Bao, D., H. Gu, and A. Kuang, *Sol-gel-derived c-axis oriented ZnO thin films.* Thin Solid Films, 1998. **312**(1–2): p. 37-39.
59. Kavanagh, Y. and D.C. Cameron, *Zinc sulfide thin films produced by sulfidation of sol-gel deposited zinc oxide.* Thin Solid Films, 2001. **398**: p. 24-28.
60. Znaidi, L., et al., *Oriented ZnO thin films synthesis by sol-gel process for laser application.* Thin Solid Films, 2003. **428**(1-2): p. 257-262.
61. Wang, M.R., et al., *Effect of preheating and annealing temperatures on quality characteristics of ZnO thin film prepared by sol-gel method.* Materials Chemistry and Physics, 2006. **97**(2-3): p. 219-225.
62. Dutta, M., S. Mridha, and D. Basak, *Effect of sol concentration on the properties of ZnO thin films prepared by sol-gel technique.* Applied Surface Science, 2008. **254**(9): p. 2743-2747.
63. Li, H.X., et al., *Sol-gel preparation of transparent zinc oxide films with highly preferential crystal orientation.* Vacuum, 2004. **77**(1): p. 57-62.
64. Lee, J.H., K.H. Ko, and B.O. Park, *Electrical and optical properties of ZnO transparent conducting films by the sol-gel method.* Journal of Crystal Growth, 2003. **247**(1-2): p. 119-125.
65. Bole, M.P. and D.S. Patil, *Effect of annealing temperature on the optical constants of zinc oxide films.* Journal of Physics and Chemistry of Solids, 2009. **70**(2): p. 466-471.

66. Alam, M.J. and D.C. Cameron, *Preparation and properties of transparent conductive aluminum-doped zinc oxide thin films by sol-gel process.* Journal of Vacuum Science & Technology a-Vacuum Surfaces and Films, 2001. **19**(4): p. 1642-1646.
67. Xu, Z.Q., et al., *Characteristics of Al-doped c-axis orientation ZnO thin films prepared by the sol-gel method.* Materials Research Bulletin, 2006. **41**(2): p. 354-358.
68. Fujihara, S., C. Sasaki, and T. Kimura, *Crystallization behavior and origin of c-axis orientation in sol-gel-derived ZnO : Li thin films on glass substrates.* Applied Surface Science, 2001. **180**(3-4): p. 341-350.
69. Wang, Y.P., et al., *Transparent conductive Al-doped ZnO thin films grown at room temperature.* Journal of Vacuum Science & Technology A, 2011. **29**(3): p. 6.
70. Ohyama, M., H. Kozuka, and T. Yoko, *Sol-gel preparation of ZnO films with extremely preferred orientation along (002) plane from zinc acetate solution.* Thin Solid Films, 1997. **306**(1): p. 78-85.
71. Kim, H.J., et al., *Growth of highly oriented zinc oxide thin films by plasma enhanced chemical vapor deposition*, in *Advanced Nondestructuve Evaluation I, Pts 1 and 2, Proceedings*, S.S. Lee, et al., Editors. 2006, Trans Tech Publications Ltd: Zurich-Uetikon. p. 1687-1690.
72. Ohyama, M., H. Kozuka, and T. Yoko, *Sol-gel preparation of transparent and conductive aluminum-doped zinc oxide films with highly preferential crystal orientation.* Journal of the American Ceramic Society, 1998. **81**(6): p. 1622-1632.
73. Damm, H., et al., *Factors influencing the conductivity of aqueous sol(ution)-gel-processed Al-doped ZnO films.* Chemistry of Materials, 2014. **26**(20): p. 5839-5851.
74. Kuo, S.Y., et al., *Effects of doping concentration and annealing temperature on properties of highly-oriented al-doped ZnO films.* Journal of Crystal Growth, 2006. **287**(1): p. 78-84.
75. Schuler, T., et al., *Influence of structure zone model parameters on the electrical properties of ZnO : Al sol-gel coatings.* Thin Solid Films, 2006. **502**(1-2): p. 67-71.
76. Maejima, K., et al., *Correlation between Electrical Properties and Crystal c-Axis Orientation of Zinc Oxide Transparent Conducting Films.* Japanese Journal of Applied Physics, 2012. **51**(10).
77. Damm, H., et al., *Factors Influencing the Conductivity of Aqueous Sol(ution)-Gel-Processed Al-Doped ZnO Films.* Chemistry of Materials, 2014. **26**(20): p. 5839-5851.

Chapter 4 - Precursor solution formulation

The fabrication of a stable and clear precursor solution is a vital step in preparing good quality chemical solution deposited thin films. To reach this goal, a general strategy is followed. Several precursor solutions with water as primary solvent are synthesised. These precursor solutions are examined in detail to understand the precursor chemistry.

4.1 Strategy for precursor solution preparation

The research group 'SCRiPTS' has a tradition of using aqueous precursor solutions for the preparation of thin film oxides [1-10]. The knowledge built up with the preparation of aqueous precursor solutions can also be applied in the research of AZO thin films. The introduction of water as solvent results in a more environmental friendly precursor solution and will reduce the costs. However, water-based precursors induce a number of difficulties, e.g. metal salts can exceed their solubility limit or precipitation of insoluble metal hydroxides can occur. To tackle these difficulties metal chelate chemistry is used. The formation of water soluble metal chelate complexes decreases the concentration of free metal ions avoiding precipitation while the homogeneity in solution is preserved [11]. Therefore, highly water-soluble precursor salts (metal nitrates and acetates) are stabilised with chelating components (derivatives of carboxylic acids, amino compounds, amino acids, etc.). When a stable precursor solution is prepared, the stability should be maintained upon removal of the solvent. Otherwise after drying, inhomogeneous thin films are obtained which result in inhomogeneous morphologies or compositions of the final oxide thin film.

4.2 Precursor solution formulation

The formulation of an AZO precursor solution started with the preparation of separate Zn and Al precursor solutions. Mixing of the stable Zn and Al precursor solutions results in the final AZO precursor. The dopant concentration in this dissertation is defined as following:

$$x = \frac{n_{Al}}{n_{Zn} + n_{Al}} * 100\ \% \qquad \text{Eq.4.1}$$

Where x, n_{Al} and n_{Zn} represent the atomic dopant percentage, the number of Al molecules and the number of Zn molecules in the final precursor solution.

4.2.1 Solution A

Solution A is a Zn precursor solution prepared as follows: 0.01 mol of $Zn(CH_3COO)_2.2H_2O$ (Sigma Aldrich, 99%) was dissolved in 8 mL water. The pH was elevated till 10.7 by the addition of 3.5 mL of ethanolamine ($NH_2CH_2CH_2OH$, Sigma Aldrich, 99%). Afterwards, the pH was adapted with formic acid (HCOOH, Acros Organics, 98%). At the end, the precursor solution was diluted till 20 mL.

Finally, a 0.5 mol L^{-1} zinc acetate precursor solution is obtained. As further mentioned in this dissertation, other additives can be added before the pH is adapted with formic acid.

The stability of the precursor solution in respect to the pH was checked at room temperature (25°C) (figure 4.1). After a couple of hours precipitation at pH 5 was observed. The precursor solution with pH levels varying from 9 to 7 were stable for more than a month, while the precursor solution at pH 6 showed a small amount of precipitation.

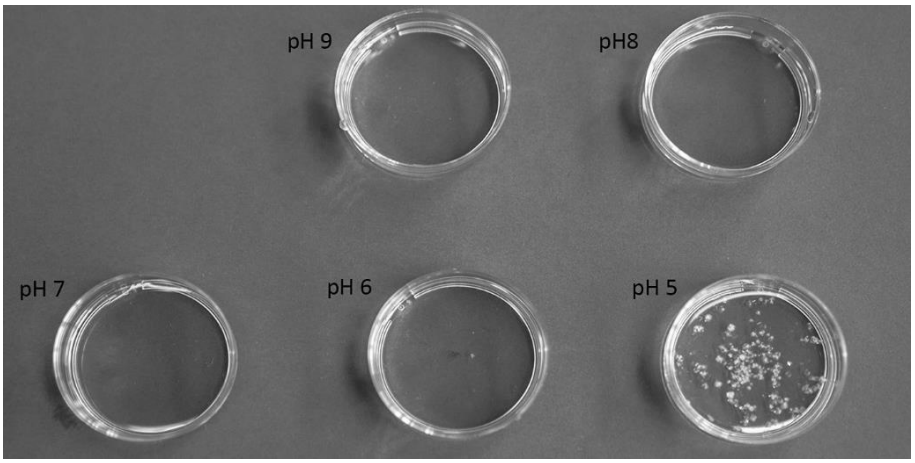

Figure 4.1 Stability of precursor solution A in respect to the pH at room temperature.

The precipitates were filtered, washed multiple times with water and ethanol before they were dried at 60°C and analysed by Raman spectroscopy. The Raman spectrum matches the one of zinc formate described in 'Handbook of Infrared and Raman Spectra of Inorganic Compounds and Organic Salts' [12]. The Raman shifts at 235 and 386 cm^{-1} are unindexed, but the other Raman shifts are assigned to the symmetric deformation of the carboxyl group (756 cm^{-1}), the out of plane bend of the CH group (1075 cm^{-1}), the symmetric vibration of the carboxyl group (1356 and 1373 cm^{-1}) and the in plane bend of the CH group (1399 cm^{-1}) [13]. The precipitation of zinc formate is caused by exceeding its solubility product. The large amount of formic acid added to lower the pH leads to the formation of these zinc formate precipitates.

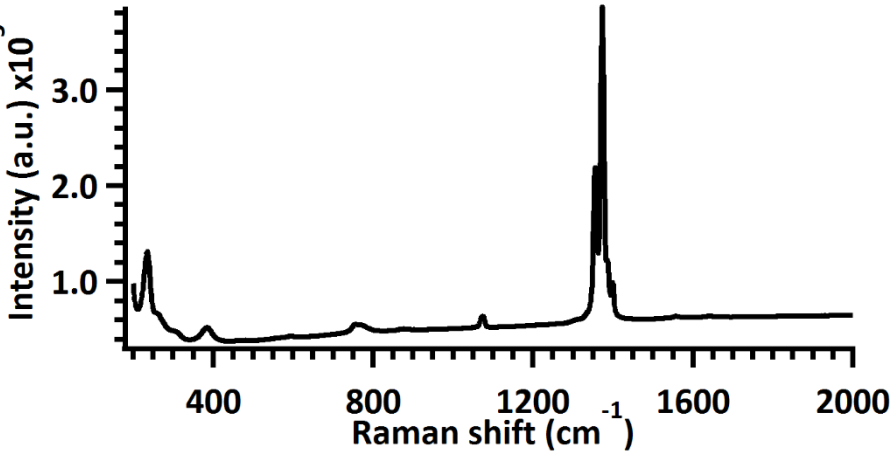

Figure 4.2 Ramam spectrum of washed and dried precipitates obtained from precursor solution A at pH 5.

The importance of precursor stability at elevated temperatures is addressed in the introduction of this chapter. Therefore, the precursor stability with various pH levels was checked at 75°C during 24h (figure 4.3). Remarkably, none of the precursors showed any form of precipitation not even at pH 5. The latter can be explained by the increased solubility at elevated temperatures.

A pH neutral precursor solution is preferred towards environmental issues and to avoid corrosion of the printing equipment. Due to its stability at room temperature and elevated temperature, the precursor solution at pH level 7 was selected. To maintain this neutral pH, the aluminium precursors were modified to be compatible with the Zn precursor by selecting a proper chelating agent and adjusting the pH of the Al precursor solution in line with the Zn precursor solution.

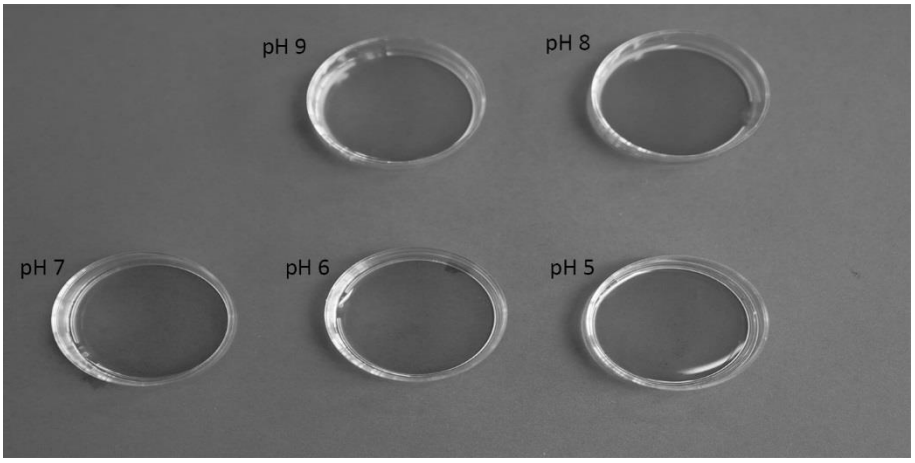

Figure 4.3 Stability of precursor solution A in respect to the pH at 75°C during 24h.

Chemical analysis of solution A

As mentioned in the introduction of this chapter, the formation of metal chelates is important towards the stability of the precursor solution. A prediction of the formed metal chelates as a function of the pH was made through speciation plots (figure 4.4). In this work, HySS-2009 software [14] was used to create these plots based on published complexation constants [15-19] and the precursor solution composition (table 4.1).

Table 4.1 Stability constants of possible complexes for precursor solution A.

Formula	Abbreviation	Log β
$Zn(CH_3COO)^+$	ZnOAc	0.91
$Zn(CH_3COO)_2$	$Zn(OAc)_2$	1.36
$Zn(HCOO)^+$	ZnFA	0.70
$Zn(HCOO)_2$	$Zn(FA)_2$	1.08
$Zn(NH_2CH_2CH_2OH)^{2+}$	ZnEA	2.70
$Zn(NH_2CH_2CH_2OH)_2^{2+}$	$Zn(EA)_2$	5.18

Table 4.2 Protonation constants of possible chelating components of precursor solution A.

Formula	Log K_a
CH_3COO^-	4.57
$HCOO^-$	3.53
$NH_2CH_2CH_2OH$	9.62

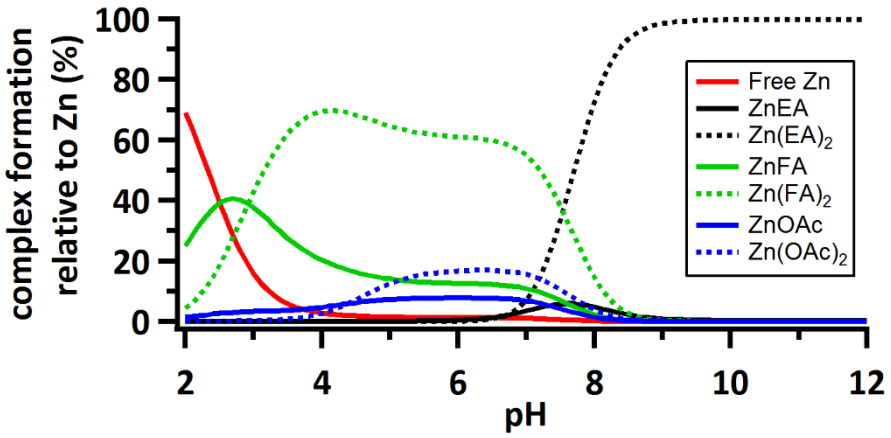

Figure 4.4 Speciation distribution of possible formed zinc complexes in solution A as a function of the pH level.

The speciation distribution shows that around pH of interest (pH 7) multiple species could be present in solution A. It can be noted that almost no free zinc ions are present and the stability of the precursor solution is mainly due to the presence of carboxylates such as acetic acid and formic acid where zinc formate (± 55%) is the most dominant species. At a pH level higher than 8, the EA-complexes are dominant (± 100%).

To correlate the software generated plot with reality, the functional groups that are involved in the formation of metal chelates were examined by Fourier Transform InfraRed (FTIR) spectroscopy. Metal-ion free blanks and the precursor solutions were studied (figure 4.5). To improve the quality of both spectra, samples were dried at 75°C during 2h in order to reduce the possible interfering water absorption around 1636 cm^{-1}.

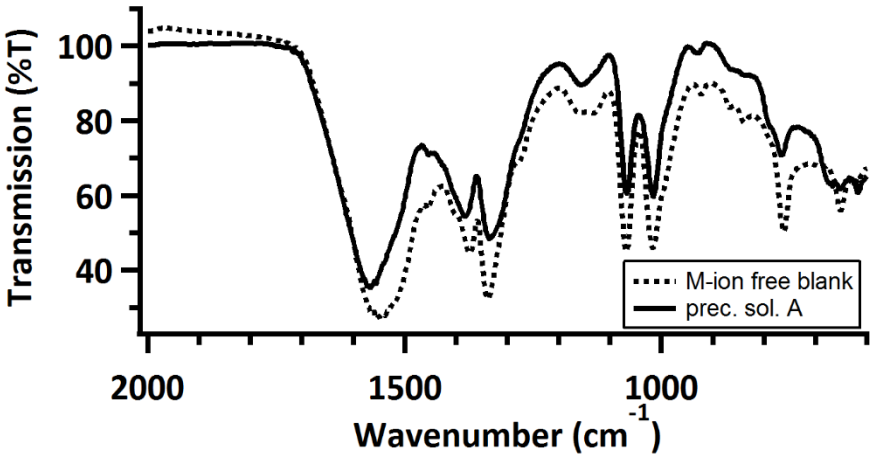

Figure 4.5 FTIR measurement of precursor solution A(solid line) and metal-ion free blank (dashed line).

A minimal difference between the metal-ion free blank and the solution A could be seen. This is mainly due to the overlap of many absorption peaks of different components. Also, the high concentration of the possible chelating components (acetic acid, ethanolamine and formic acid) makes it hard to distinguish between free and chelating components. This all together makes the interpretation of these FTIR spectra difficult. For the metal-ion free blank and solution A the peaks of the FTIR spectra are assigned in table 4.3 [11, 20-22]. The peak located at 1574 cm^{-1} represents the ν_a (COO) of formic acid and acetic acid. The ν_s (COO) of acetic acid is located in the blank as a shoulder at 1406 cm^{-1}, but is not visible anymore in the spectrum of solution A. The ν_s (COO) of formic acid is located at 1336 cm^{-1} and can be seen in both spectra. The ρ_r (CH_3) of acetic acid overlaps with the ν (C-N) and ν (C-O) of ethanolamine, respectively at 1068 and 1016 cm^{-1}. Due to the high concentration of the ethanolamine these vibration modes can be assigned mainly to ethanolamine. Compared to the spectrum of the blank, no visible shift of the characteristic peaks of ethanolamine is noticed. This allows us to conclude that ethanolamine is not contributing as a chelating agent which could also be concluded from the theoretical simulation via the HySS-2009 software. The shift of the ν_a (COO) of formic acid and acetic acid compared to the blank are an indication that one or both components are forming a complex with the zinc ions. However, the symmetric stretches of the carbonyl function do not allow to generate a definite conclusion. In case of formic acid,

the difference of δ (COO) and ν_s (COO) between the blank and the precursor is not large enough to include chelating behaviour.

Table 4.3 Overview of the FTIR spectra: peak assignment according to the specific vibration of the IR active groups.

Vibration mode	Metal-ion free blank (cm^{-1})	Solution A (cm^{-1})
ν_a (COO) formic acid and acetic acid	1550	1574
δ (CH_2) ethanolamine	1454w	1454w
ν_s (COO) acetic acid	1406sh	
δ (CH) formic acid	1372	1384
ν_s (COO) formic acid and δ (CH_3) acetic acid	1340	1336
ρ_r (CH_2) ethanolamine	1280sh	1280sh
δ (C-O) ethanolamine	1148	1154
ρ_r (CH_3) acetic acid and ν (C-O) ethanolamine	1070	1068
ρ_r (CH_3) acetic acid and ν (C-N) ethanolamine	1018	1016
ν (C-C) acetic acid	922	930
ν (C-C) ethanolamine	866	866
ρ_r (NH_2) ethanolamine	840	834
δ (COO) formic acid	762	766
δ (COO) acetic acid	652	650
π (CH) acetic acid	616	618

The FTIR analyses suggest that formic acid and/or the acetate groups are forming complexes with Zn, while the ethanolamine isn't contributing at all. This matches with the software based plot (figure 4.4), where zinc formate and zinc acetate species mainly presented. Although a small amount of zinc-

ethanolamine complex is present in the theoretical simulation, no firm conclusion can be made from the IR-results. Therefore, the diffusion coefficients of the metal-ion free blank and solution A were compared based on two dimensional Nuclear Magnetic Resonance (NMR) spectroscopy, so called Diffusion Ordered SpectroscopY (DOSY). The extracted information of the DOSY experiment is illustrated in figure 4.6. No difference can be seen between the diffusion coefficient of ethanolamine and water measured in the blank nor precursor solution. However, formic acid and acetic acid show a decrease in diffusion coefficient compared to the blank, which indicates that these acids are present in the Zn complexes. The diffusion coefficient is a weighted average between the diffusion coefficient of the free molecules and the one forming complexes. This makes it impossible to differentiate the species as represented in speciation plot generates by HySS-2009 (figure 4.4). However, together with information gathered by FTIR, we can now conclude that ethanolamine is not contributing to the formation of stable Zn complexes. No remarkable shifts in the FTIR spectrum are noticed and the diffusion coefficient in the blank and precursor solution are equal. However, formic acid and acetic acid are stabilising partners. A visible shift of the asymmetric stretch of the carbonyl function is noticed in the FTIR spectra. Also, a change in diffusion coefficient between the blank and the precursor solution confirms that complexes of zinc with formic acid and/or acetic acid are present in the solution.

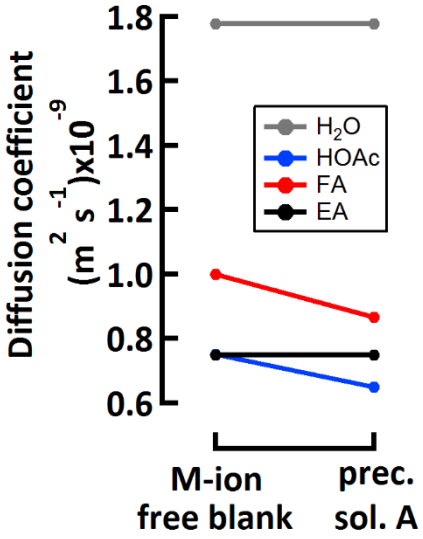

Figure 4.6 DOSY experiment comparing the diffusion coefficient of the components from the metal-ion free blank with precursor solution A.

4.2.2 Solution B

Solution B is an Al precursor where malonic acid is selected as chelating agent. To obtain a stable precursor solution a 1:3 ratio of $Al(NO_3)_3.9H_2O$ (Sigma Aldrich, 98%) and malonic acid ($CH_2(COOH)_2$, Sigma Aldrich, 99%) was used. In 8 mL water 0.01 mol of $Al(NO_3)_3.9H_2O$ and 0.03 mol of malonic acid were dissolved and stirred for 30 minutes. The pH was raised with ethanolamine ($HOCH_2CH_2NH_2$, Sigma Aldrich, 99%) till a clear, colourless solution was obtained at pH 9. Finally, the pH was adapted with formic acid (HCOOH, Acros Organics, 98%) till 7 and a clear 0.5 mol L^{-1} Al precursor was synthesised.

Chemical analysis of solution B

Also here, the chelating effect of the used chemicals is analysed by FTIR spectroscopy by comparing metal-ion free blanks with the precursor solution after drying the samples at 75°C for 2h. A clear peak shift around 1550-1590 and 690-750 cm^{-1} is visible and two new vibration modes around 950 cm^{-1} are observed.

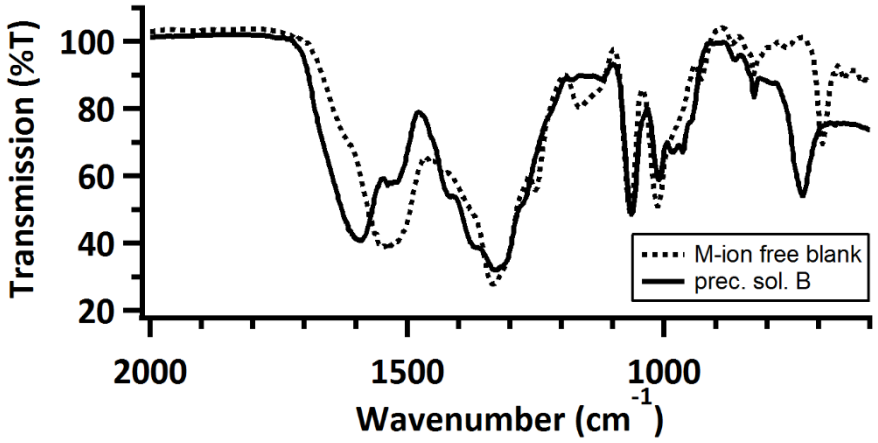

Figure 4.7 FTIR measurement of precursor solution B (solid line) and metal-ion free blank (dashed line).

An overview of all assigned peaks can be found in table 4.4 [21-27]. The peak located at 1538 cm^{-1} in the metal-ion free blank can be assigned to the ν_a (COO) of malonic acid and formic acid while this peak is partially shifted towards 1592 cm^{-1} in solution B. The large peak at 1334 cm^{-1}, due to the vibration mode of nitrate ions, makes it hard to locate the symmetric vibration of the carboxyl functions of malonic acid. However, a shoulder at 1308 cm^{-1} can be observed for solution B. This can be the shift of the ν_s (COO) of malonic acid due to complexation. The appearance of the Al-OH vibration at 964 cm^{-1} makes it obvious that the formed complex will contain some hydroxide groups or water while the carboxyl groups are chelating to prevent the complete hydroxylation of the aluminium ions. Questioning which of the 2 components is inducing the peak shift around 1535-1590 cm^{-1}, other parts of the spectra are studied. For example, one of the characteristic peaks of malonic acid around 692 cm^{-1} (ρ_r (COO)) in the blank shifted towards 732 cm^{-1} for solution B, indicating that malonic acid is chelating with aluminum ions.

Most likely, malonic acid will coordinate with the free aluminum ions in an unidentate configuration. The symmetric stretch of the carboxyl group is most likely situated around 1308 cm^{-1}. Together with the blue shift of the asymmetric stretch of the carbonyl group, a larger difference between the asymmetric and symmetric vibration compared to ionic complexes is observed, respectively 282 cm^{-1} for solution B and 204 cm^{-1} for the blank.

Table 4.4 Overview of the FTIR spectra: peak assignment according to the specific vibration of the IR active groups.

Vibration mode	Metal-ion free blank (cm^{-1})	Solution B (cm^{-1})
ν_a (COO) malonic acid	1538	1592
ν_a (COO) formic acid	1538	1538
δ (CH_2) malonic acid	1430sh	1416sh
δ (CH) formic acid	1372sh	1372
ν_s (COO) formic acid and ν (NO_3^-)	1334	1332
ν_s (COO) malonic acid	1334	1308sh
ρ_r (CH_2) malonic acid and ethanolamine	1250	1274
ν_a (C-C) malonic acid and δ (C-O) ethanolamine	1166	/
ν (C-O) ethanolamine	1066	1064
ν (C-N) ethanolamine	1014	1010
ν_s (C-C) malonic acid	976sh	984
ν (Al-OH)	/	964
δ (CH_2) malonic acid	928	948sh
ν (C-C) ethanolamine	868	862
δ (ONO)	826	826
δ (COO) formic acid	762	/
ρ_r (COO) malonic acid	692	732

These measurements confirm that a stable Al precursor solution is obtained with malonic acid as chelating component. The formed complexes contain also hydroxyl groups or water molecules which is confirmed by the ν (Al-OH).

4.2.3 Solution C

Solution C is an Al precursor solution where malonic acid is selected as chelating agent but another Al precursor is selected, namely $AlCl_3.6H_2O$. To obtain a stable precursor solution a 1:3 ratio of $AlCl_3.6H_2O$ (Sigma Aldrich, 99%) and malonic acid ($CH_2(COOH)_2$, Sigma Aldrich, 99%) was dissolved in 8 mL water and stirred for 30 minutes. The pH was raised with ethanolamine ($HOCH_2CH_2NH_2$, Sigma Aldrich, 99%) till a clear, colourless solution was obtained at pH9. Finally, the pH was adapted with formic acid (HCOOH, Acros Organics, 98%) till 7 and a clear 0.5 mol L^{-1} Al precursor was synthesised.

Chemical analysis of solution C

Apart from the use of chlorides instead of nitrates, the chemical analysis is similar to the one of solution B.

4.2.4 Solution D

Solution D is an Al precursor where citric acid is selected as chelating agent. To obtain a stable precursor solution a 1:1 ratio of $Al(NO_3)_3.9H_2O$ (Sigma Aldrich, 98%) and citric acid monohydrate ($C_6H_8O_7.H_2O$, Carl Roth, 99.5%) was dissolved in 8 mL water and stirred for 30 minutes. The pH was raised with ethanolamine ($HOCH_2CH_2NH_2$, Sigma Aldrich, 99%) till a clear, colourless solution was obtained at pH 9. Finally, the pH was adapted with formic acid (CH_2O_2, Acros Organics, 98%) till 7 and a clear 0.5 mol L^{-1} Al precursor was synthesised.

Chemical analysis of solution D

By comparing the FTIR spectra of the metal-ion free blank and the precursor solution D (figure 4.8), an attempt is made to pinpoint the chelating component. The sample preparation is similar as the other precursor solutions as both were dried in the furnace at 75°C during 2h.

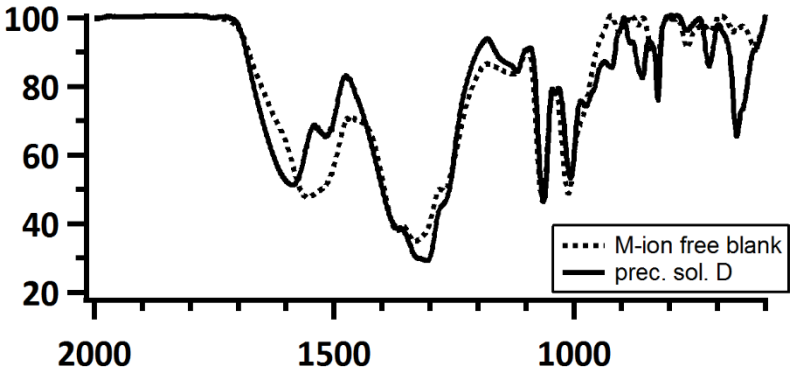

Figure 4.8 FTIR measurement of precursor solution D (solid line) and metal-ion free blank (dashed line).

An overview of the assigned peaks is represented in table 4.5 [21-23, 26-32]. The ν_a (COO) stretch of the citric acid is located at 1557 cm^{-1} for the metal-ion free blank and at 1582 cm^{-1} for precursor solution D. The ν_s (COO), normally located around 1400 cm^{-1}, can't be distinguished in both spectra which makes it hard to assign the type of coordination and to confirm if citric acid is even chelating. The peak at 1518 cm^{-1} can be assigned to the ν_a (COO) of formic acid or the coupling between the carbonyl group and the protonated amine group of ethanolamine. A closer look to the fingerprint region of these spectra can help to create an understanding of the nature of the complexes. At 974 cm^{-1} a peak appears, which can again be attributed to the Al-OH stretch. However, in this region a shoulder at 981 cm^{-1} in the metal-ion free blank is noticed. It is believed that this shoulder is the contribution of the ν (C-C) of citric acid. The possibility exist that this shoulder gained intensity due to the chelating behaviour of citric acid or it is still present in the spectrum as the shoulder is masked by the presence of the ν (Al-OH).

It is also noticed that the FTIR spectrum of solution D has 3 more intense peaks in the region between 900 and 600 cm^{-1} compared the metal-ion free blank. The shoulder at 837 cm^{-1} and the peak at 661 cm^{-1} in the blank are shifted to larger wavenumbers. According to Tarte [28], the vibrations of the tetrahedral AlO_4 fit those intense peaks (661, 647, and 856 cm^{-1}). To obtain a tetrahedral Al complex, the hydroxyl group of citric acid or another molecule such as water or hydroxyl group should also be chelating. The presence of a hydroxyl or water

molecule in the inner coordination sphere can explain the Al-OH vibration at 974 cm^{-1}. The δ (COO) of citric acid at 837 and 661 cm^{-1} are shifted. Those can be located at the position of one of the Al-O vibrations. The first deformation peak is overruled by the Al-O vibration at 856 cm^{-1} while a shoulder at 690 cm^{-1} can be noticed. In conclusion, it is hard to determine the exact composition of the complex due to a lack of fine structure in the region of interest. But the shifting vibrations and deformation of the carboxyl groups allow to assume that citric acid is chelating.

Table 4.5 Overview of the FTIR spectra: peak assignment according to the specific vibration of the IR active groups.

Vibration mode	**Metal-ion free blank (cm^{-1})**	**Solution D (cm^{-1})**
ν_a (COO) citric acid	1557	1582
ν_a (COO) formic acid or ν_a (COO^-/N^+H_3R)	1518sh	1518
δ (CH) formic acid	1371	1371
ν_s (COO) formic acid and ν (NO_3^-)	1333	1327
δ (OH) citric acid	1308sh	1305
ρ_r (CH_2) ethanolamine	1272sh	1272sh
δ (C-O) citric acid and δ (C-O)	1135	1119
ν (C-O) ethanolamine	1064	1064
ν (C-N) ethanolamine	1013	1008
ν (C-C) citric acid or ν (Al-OH)	981sh	974
δ (CH_2)	940	923
δ (C-C) citric acid	907	906sh
δ (CH_2)	894	884
ν (C-C) ethanolamine	865	867sh
δ (COO) citric acid and ν (Al-O)	837sh	856

δ (ONO)	826	825
δ (COO) formic acid	763	765
δ (CH_2) citric acid	715	718
δ (COO) citric acid	668	690sh
ν (Al-O)	/	661
ν (Al-O)	/	647sh
π (CH) citric acid	626	620sh

4.2.5 Solution E

Solution E is very much alike to solution D but again aluminium chlorides are used instead of aluminium nitrates. To obtain a stable precursor solution a 1:1 ratio of $AlCl_3.6H_2O$ (Sigma Aldrich, 99%) and citric acid monohydrate ($C_6H_8O_7.H_2O$, Carl Roth, 99.5%) was dissolved in 8 mL water and stirred for 30 minutes. The pH was raised with ethanolamine ($HOCH_2CH_2NH_2$, Sigma Aldrich, 99%) till a clear, colourless solution was obtained at pH 9. Finally, the pH was adapted with formic acid (HCOOH, Acros Organics, 98%) till 7 and a clear 0.5 mol L^{-1} Al precursor was synthesised.

Chemical analysis of solution E

Apart from the use of chlorides instead of nitrates, the chemical analysis is similar to the one of solution D.

4.2.6 Solution F

Solution F is a concentrated version of solution A. Zinc acetate was dissolved in 10 mL water. The pH was elevated till 10.7 by the addition of 4 mL of ethanolamine ($NH_2CH_2CH_2OH$, Sigma Aldrich, 99%). Afterwards, the pH was adapted with formic acid (HCOOH, Acros Organics, 98%). At the end, the precursor solution was diluted till 20 mL. Finally, a 1 mol L^{-1} zinc acetate precursor solution is obtained.

Chemical analysis of solution F

Solution F contains the same components as solution A which makes them chemically identical.

4.2.7 Other solutions

During this work, many other precursor solutions were formulated. Stable solutions of zinc acetates and/or aluminium nitrates with ethylenediamine, ethylenediamintetraacetic acid, nitrilotriacetic acid, iminodiacetic acid and acetylactone could be achieved.

Unfortunately, these precursor formulations had several disadvantages which made the preparation of high quality AZO thin films impossible. For example, the reproducibility of some precursor solutions was not good enough, others resulted in highly exothermic reactions that lead to large pinholes in the thin films. The precursors containing iminodiacetic acid resulted in a thin film with bad adhesion and low transmittance in the visible range of the electromagnetic spectrum. Figure 4.9 illustrates one of those layers before and after a scotch tape peeling test. One can clearly see that a part of the film is removed by this peeling test, indicating that these solutions are not suited for the deposition of dense AZO thin films. Therefore, these precursor solutions were not studied in detail.

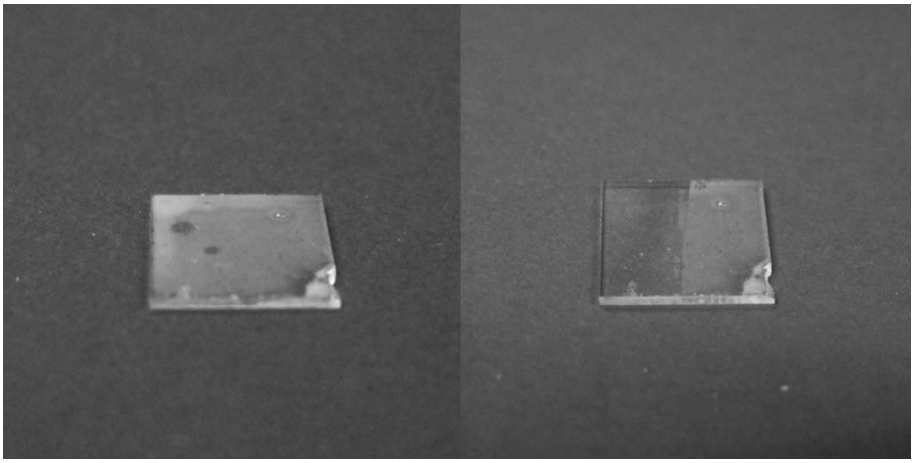

Figure 4.9 Pictures of thin film produced by an iminodiacetic acid precursor. Left: before scotch tape peeling test. Right: after scotch tape peeling test.

4.2.8 AZO starting precursor solutions

Once stable Al and Zn precursor solutions were prepared, they were mixed to obtain a certain dopant concentration. The exact amount of Al precursor solution added to the Zn precursor solution was determined by the desired dopant concentration and can be calculated from eq. 4.1. The final Al doped ZnO precursor solution was named according to the 2 precursor solutions mixed and by the final dopant concentration. For example, solution A3%B is containing precursor solution A and B in a ratio that allowed us to produce 3% Al doped ZnO. An overview of the solutions can be found in the appendix.

Precursor solution selection

By combining the diverse Al precursor solutions (solution B till E) with the zinc precursor solution (solution A) 4 types of AZO precursor solutions were obtained. However, not every precursor solution generated AZO thin films with the proper electrical properties. We noticed an influence of the used precursor salts and chelating agents.

Influence of the used Al precursor salts on the doping of ZnO

Generally, the AZO inks containing $AlCl_3.6H_2O$ as aluminium source resulted in thin films with inferior electrical properties compared to AZO thin films synthesised with inks containing $Al(NO_3)_3.9H_2O$ as aluminium source. A possible explanation can be found in the thermal decomposition of these Al precursor solutions. The Al precursor solutions were studied by ThermoGravimetric Analysis (TGA) to observe the possible influence of the Al source.

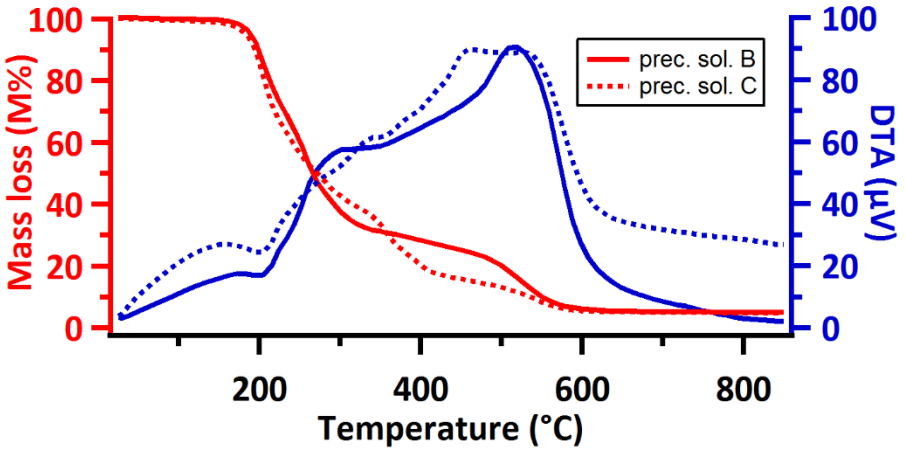

Figure 4.10 TGA of precursor solution B (solid line) and C (dashed line) The red curves represent the mass loss as a function of temperature, while the blue curves represent the differential thermal analysis as a function of temperature.

The thermal decomposition of precursor solution B and C are represented in figure 4.10. It is noticed that the largest differences in the thermal decomposition of both solutions were situated between 300°C and 600°C. Solution B is showing a more gradual mass loss till 500°C, where a final mass loss is observed. Precursor solution C had an additional decomposition step starting around 330°C. The largest difference between solution B and C is the Al precursor, respectively $Al(NO_3)_3.9H_2O$ and $AlCl_3.6H_2O$. It can be suggested that the additional decomposition for solution C between 300°C and 400°C is due to the presence of chlorides in the precursor solution. However, the mass loss can only be assigned accurately when the combustion gasses are analysed by mass spectroscopy. The decomposition can influence the incorporation of Al in the ZnO matrix due to different reaction routes that are followed.

The different decompositions of these inks will also influence the doping of the ZnO. As mentioned in chapter 2, Al can occupy several positions in ZnO. Depending on the position of the dopant, it can contribute to an enhanced electrical conductivity. Therefore, bulk samples of the precursor solution A3%B and A3%C were studied by ^{27}Al MAS NMR after calcination at 500°C for 1h in air (figure 6.11). This technique allows us to differentiate the coordination of the Al species in the ZnO matrix.

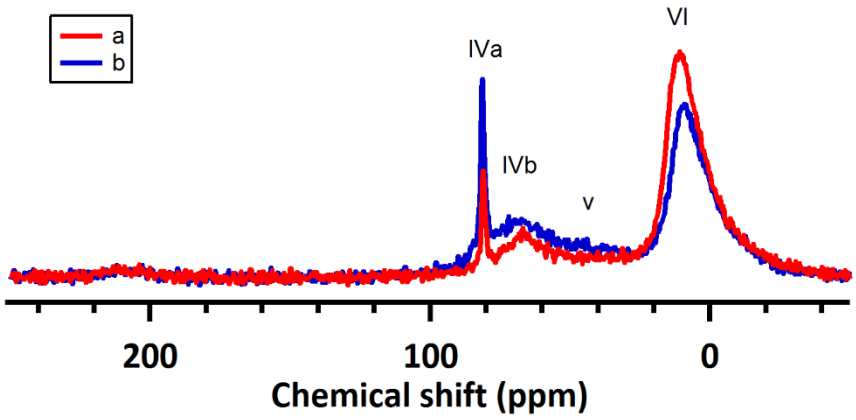

Figure 4.11 1D ^{27}Al MAS NMR spectra of bulk samples obtained by a thermal treatment at 500°C during 1h in air of a) solution A3%C and b) solution A3%B.

Octahedrally coordinated Al is generally seen at 0 ± 15 ppm (VI), while tetrahedral Al is observed at 65 ± 15 ppm (IVa and IVb) [33] and pentahedral Al is observed at 30 ± 15 ppm (V) [34]. We observed a sharp signal at 81 ppm, a much broader signal centred at 69 ppm and 42 ppm and a broad signal with its centre at 10 ppm. The narrow line at 81 ppm does not show any quadrupolar line shape which correlates with a highly symmetrical tetrahedral environment. This indicates a crystalline environment, corresponding with substitutional Al^{3+} ions in crystalline ZnO [34-36]. The broad signal centred at 67 ppm can also be assigned to tetrahedral coordinated Al. Broadened distributions are observed for distorted or amorphous environments which indicates Al occupying empty tetrahedral sites of the ZnO crystal lattice [36]. The signal centred at 42 ppm can be assigned to pentahedral coordination. However, a distorted tetrahedral coordination can't be excluded. Most likely, it will be a combination of both, pentahedral and distorted tetrahedral coordinated Al [36, 37]. As already mentioned at chapter 2 (cfr. 2.3.1), octahedral coordinated Al has a negative influence on the electrical properties, while substitutional Al can act as a carrier provider.

The signals of 1D ^{27}Al MAS NMR spectra were deconvoluted by constructing Gaussian/Lorentzian envelopes at the different peaks. The powders synthesised by using ink A3%B are resulting in 53.3% octahedrally coordinated Al, 20.5% pentahedrally coordinated Al and 26.2% tetrahedrally coordinated Al, where the amount of substitutional Al is 6.6%. Powders synthesised by ink A3%C results in

70.9% octahedrally coordinated Al, 15.5% pentahedrally coordinated Al and 13.6% tetrahedral coordinated Al, where the amount of substitutional Al is 3.6%. The use of a different Al precursor salt clearly affects the distribution of the Al in the ZnO matrix. The use of aluminium chlorides result in more octahedrally coordinated Al sites. These occupied sites can act as electron acceptors reducing the electrical conductivity [35, 38, 39]. Also, the amount of substitutional Al decreases with the use of aluminium chlorides, leading to less charge carriers. This was also observed for precursor solution A3%D (Al nitrate – citrate complex) and A3%E (Al chloride – citrate complex). In both situation the use of Al nitrates as Al precursor salt resulted in more substitutional Al. Therefore, we were convinced to focus on precursor solutions containing $Al(NO_3)_3.9H_2O$ as Al source.

Influence of the chelating agent within the Al complex on the doping of ZnO

Not only different precursor salts influence the decomposition of the precursor solution. As illustrated in figure 4.12, the formed complexes (Al-citrate or Al-malonate) also affect the decomposition of the Al precursor resulting in different amounts of substitutional Al.

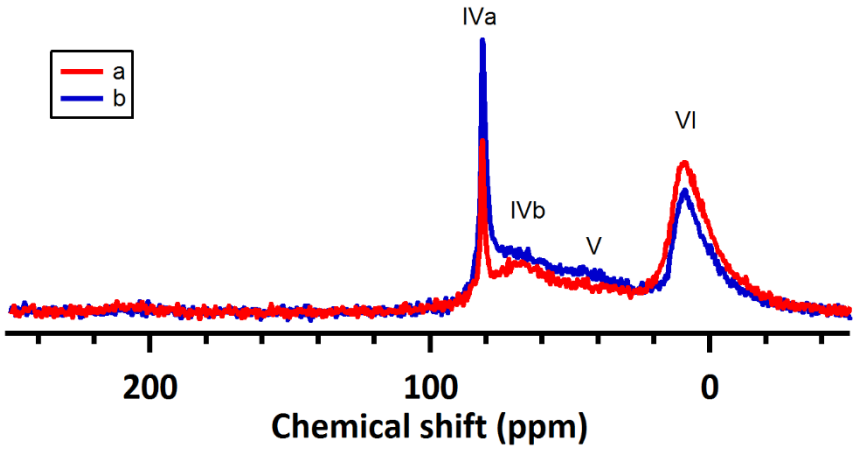

Figure 4.12 1D ^{27}Al MAS NMR spectra of bulk samples obtained by a thermal treatment at 500°C during 1h in air of a) solution A3%B and b) solution A3%D.

Precursor solution A3%D delivers AZO powders where 36.3% of the Al is octahedrally coordinated, 27.0% of the Al is pentahedrally coordinated and 36.7% of the Al is tetrahedrally coordinated. The amount of substitutional Al is 11.7%. Compared to the AZO powders obtained by heating precursor solution

A3%B less octahedrally coordinated Al and more substitutional Al is obtained, respectively 36.3% versus 53.3% and 11.7% versus 6.6%.

Concluding, the selected Al precursor solution influences the distribution of Al in the ZnO matrix. It is noted that aluminium nitrates result in less octahedrally coordinated Al and more substitutional Al compared to aluminium chlorides which positively affects the electrical properties of the material. Next to this, the formed complexes (aluminium malonate or aluminium citrate) also result in different incorporation of the aluminium. By preparing a precursor solution with aluminium nitrate as precursor salt and citric acid as chelating agent, the most promising AZO powders are obtained. Nevertheless, the upcoming chapters will discuss in detail the 2 precursor solutions containing aluminium nitrate and malonic acid or citric acid. If both precursor solutions are showing similar behaviour (e.g. jetting, drying, etc.) only one will be discussed. Highlighting the differences of both precursor solutions will be done by discussing them separately. The precursor solutions containing aluminium chloride will not be further used in this dissertation. Research showed that thin films synthesised by these precursor solutions had a high resistivity which was suggested by the ^{27}Al MAS NMR.

Chemical analysis of solution A3%B

Here, only solution A3%B will be discussed because the other precursor solutions, using e.g. different dopant concentration or other Al precursor solutions, were showing similar behaviour.

Just as for every other precursor solution, the stability is checked. This is done by visually checking for precipitation as a function of time. The shelf life of the solution A3%B was longer than a month. Also, FTIR spectra were recorded. These spectra don't differ from those of solution A as the added quantity of solution B is too small to observe changes in the spectra.

Next to the chemical stability, it is important that the precursor solution was not containing any large particles which could block the opening of the printhead during ink jet printing. A general rule can be set: to avoid blocking of the nozzle, the largest particles should be smaller than 0.01 times the dimension of the printhead opening [40]. Before printing with the 30 µm nozzle, the ink will be filtered with a 0.2 µm PFTE filter. To be sure neither the concentration nor the

composition of the precursor changed, the inks shouldn't contain particles larger than 200 nm. Precursor solution A3%B contains small 'particles' with a mean diameter of 0.72 nm (figure 4.13). Most likely, these corresponds with formed complexes with a hydrodynamic radius of 0.72 nm. These 'particles' will have no influence on blocking of the printhead opening nor will they be filtered off. It is safe to assume this precursor solution is suited for further use in the preparation of Al doped ZnO thin films via ink jet printing.

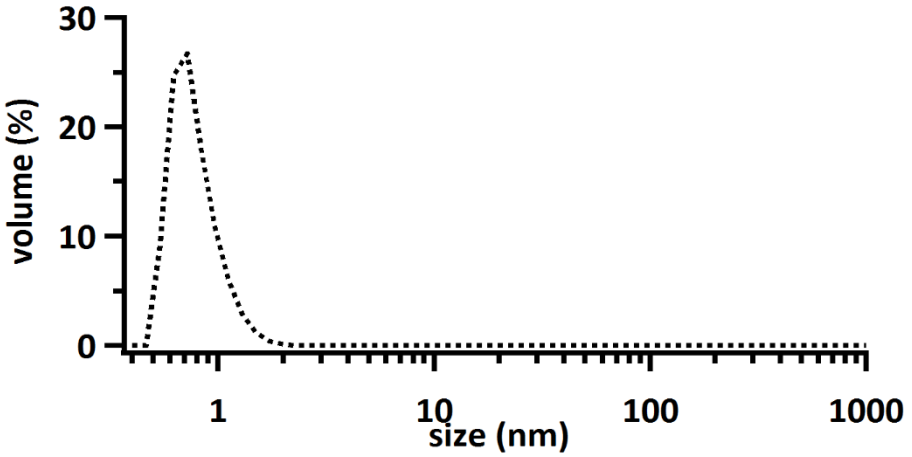

Figure 4.13 Dynamic light scattering measurement of ink A3%B before filtering, where small particles are noticed with a mean diameter of 0.72nm.

4.3 Conclusion

The preparation of a stable precursor solution is the first step towards producing Al doped ZnO thin films through CSD. It is important that the precursor solution shows a high chemical stability at room temperature and elevated temperatures. By adding chelating additives such as malonic acid, citric acid for Al^{3+} ions and formic acid for Zn^{2+} ions stable Al and Zn precursor solutions were obtained. Mixing an Al and a Zn precursor led to the formation of a suited Al doped ZnO starting precursor which can be tested in the following step, namely the coating process. It was concluded that the Al source and the decomposition of the Al precursor solution were the determining factors for the incorporation in the ZnO matrix. The use of $AlCl_3.6H_2O$ yielded more octahedrally coordinated Al which deteriorated the electrical properties. Not only the Al source influenced the incorporation of the Al in AZO. The formed Al-citrate complex is the most promising candidate to produce high quality AZO thin films due to the higher

amount of substitutional Al. In the next experiments we focus on the precursor solutions containing aluminium nitrate as Al source (solution B and D).

4.4 Reference list

1. Arin, M., et al., *Inkjet printing of photocatalytically active TiO2 thin films from water based precursor solutions.* Journal of the European Ceramic Society, 2011. **31**(6): p. 1067-1074.
2. Avci, N., et al., *Characterization of TiO2 powders and thin films prepared by non-aqueous sol-gel techniques.* Journal of Sol-Gel Science and Technology, 2009. **52**(3): p. 424-431.
3. Cloet, V., et al., *Thin La2Zr2O7 films made from a water-based solution.* Journal of Solid State Chemistry, 2009. **182**(1): p. 37-42.
4. Feys, J., et al., *Ink-jet printing of YBa2Cu3O7 superconducting coatings and patterns from aqueous solutions.* Journal of Materials Chemistry, 2012. **22**(9): p. 3717-3726.
5. Penneman, G., et al., *Deposition of CeO2 buffer layers and YBa2Cu3O7-sigma superconducting layers using an aqueous sol-gel method*, in *Euro Ceramics Viii, Pts 1-3*, H. Mandal and L. Ovecoglu, Editors. 2004. p. 501-504.
6. Samyn, P., et al., *Friction, wear and transfer of pure and internally lubricated cast polyamides at various testing scales.* Wear, 2007. **262**(11-12): p. 1433-1449.
7. Schoofs, B., et al., *A water-based sol-gel technique for chemical solution deposition of (RE) Ba2Cu3O7-y (RE = Nd and Y) superconducting thin films.* Superconductor Science & Technology, 2006. **19**(11): p. 1178-1184.
8. Van Driessche, I., et al., *Chemical approach to the deposition of textured CeO2 buffer layers based on sol gel dip coating*, in *Thermec'2003, Pts 1-5*, T. Chandra, J.M. Torralba, and T. Sakai, Editors. 2003. p. 3517-3522.
9. Vermeir, P., et al., *Fluorine-free water-based sol-gel deposition of highly epitaxial YBa2Cu3O7-delta films.* Superconductor Science & Technology, 2009. **22**(7).
10. Vermeir, P., et al., *Elucidation of the Mechanism in Fluorine-Free Prepared YBa2Cu3O7-delta Coatings.* Inorganic Chemistry, 2010. **49**(10): p. 4471-4477.
11. Penneman, G., *Ceramic layers of buffers and YBCO superconductors starting from aueous sol-gel precursors*. 2007, Ghent University: Ghent.
12. Nyquist, R.A., et al., *The handbook of infrared and raman spectra of inorganic compounds and organic salts: Infrared and raman spectral atlas of inorganic compounds and organic salts.* 1997: Academic Press.
13. Hedberg, J., S. Baldelli, and C. Leygraf, *Molecular Structural Information of the Atmospheric Corrosion of Zinc Studied by Vibrational Spectroscopy Techniques II. Two and Three-Dimensional Growth of Reaction Products Induced by Formic and Acetic Acid.* Journal of the Electrochemical Society, 2010. **157**(10): p. C363-C373.
14. Gans, P., *HySS2009: Hyperquad Simulation and Speciation*. 2009, Protonic Sofware: http://www.hyperquad.co.uk/hyss.htm.
15. Filipovic, I., et al., Croat. Chem. Acta, 1970. **42**: p. 541.
16. Persson, H., *The complex formation in the zinc acetate and the proton acetate systems.* Acta Chem. Scand., 1971. **25**: p. 1775-1789.
17. Djurdjevic, P. and J. Bjerrum, *Metal ammmine formation in solution. XXIV. The copper(II)- and some other metal(II)-mono- and diethanolamine systems* Acta Chem.Scand., 1983. **37**: p. 881-890.
18. Martell, A.E. and R.M. Smith, *Critical stability constants - volume 3: Other organic ligands*. 1977: Plenum Press.
19. Martell, A.E. and R.M. Smith, *Critical stability constants - volume 2: Amines*. 1977: Plenum Press.
20. Wang, Y., et al., *Evolution of the zinc compound nanostructures in zinc acetate single-source solution.* Journal of Nanoparticle Research, 2011. **13**(10): p. 5193-5202.

21. Znaidi, L., et al., *Elaboration of ZnO thin films with preferential orientation by a soft chemistry route.* Journal of Sol-Gel Science and Technology, 2003. **26**(1-3): p. 817-821.
22. Nakamoto, K., *Infrared and raman spectra of inorganic and coordination compounds, applications in coordination, organometallic, and bioinorganic chemistry*. 2009: Wiley.
23. Gericke, H.J., *Synthetic, electrochemical and structural aspects of β-diketonato and carboxylate complexes of aluminium*, in *Department of Chemistry, Faculty of Natural and Agricultural Sciences*. 2008, University of the Free State. p. 207.
24. Mathew, V., et al., *Growth and spectral characterization of cobalt malonate crystals.* Optoelectronics and Advanced Materials-Rapid Communications, 2008. **2**(9): p. 561-565.
25. Mathew, V., et al., *Spectral properties of cadmium malonate crystals grown in hydrosilica gel.* Indian Journal of Pure & Applied Physics, 2009. **47**(october 2009): p. 691-695.
26. Pollefeyt, G., et al., *Influence of aqueous precursor chemistry on the growth process of epitaxial SrTiO3 buffer layers.* Inorganic Chemistry, 2014. **53**(10): p. 4913-4921.
27. Jiang, N., et al., *Ethanol amine-assisted solvothermal growth of wurtzite-structured ZnS thin nanorods.* Journal of Alloys and Compounds, 2012. **536**(0): p. 85-90.
28. Tarte, P., *Infra-red spectra of inorganic aluminates and characteristic vibrational frequencies of AlO4 tetrahedra and AlO6 octahedra.* Spectrochimica Acta Part A: Molecular Spectroscopy, 1967. **23**(7): p. 2127-2143.
29. Elbagerma, M.A., et al., *Identification of a new cocrystal of citric acid and paracetamol of pharmaceutical relevance.* Crystengcomm, 2011. **13**(6): p. 1877-1884.
30. Wulandari, P., et al., *Characterization of citrates on gold and silver nanoparticles.* Journal of Colloid and Interface Science, 2015. **438**: p. 244-248.
31. Bertoli, A.C., et al., *Theoretical spectroscopic studies and identification of metal-citrate (Cd and Pb) complexes by ESI-MS in aqueous solution.* Spectrochimica Acta Part a-Molecular and Biomolecular Spectroscopy, 2015. **137**: p. 271-280.
32. Bichara, L.C., et al., *Vibrational study and force field of the citric acid dimer based on the SQM methodology.* Advances in Physical Chemistry, 2011. **2011**.
33. MacKenzie, K.J.D. and E. Smith, *Multinuclear solid-state nuclear magnetic resonance of inorganic materials*. 2002: Elsevier Science.
34. Noriega, R., et al., *Probing the electrical properties of highly-doped Al:ZnO nanowire ensembles.* Journal of Applied Physics, 2010. **107**(7).
35. Kemmitt, T., B. Ingham, and R. Linklater, *Optimization of sol-gel-formed ZnO:Al processing parameters by observation of Dopant Ion location using solid-state Al-27 NMR spectrometry.* Journal of Physical Chemistry C, 2011. **115**(30): p. 15031-15039.
36. Avadhut, Y.S., et al., *Structural investigation of aluminium doped ZnO nanoparticles by solid-state NMR spectroscopy.* Physical Chemistry Chemical Physics, 2012. **14**(33): p. 11610-11625.
37. Damm, H., et al., *Factors Influencing the Conductivity of Aqueous Sol(ution)-Gel-Processed Al-Doped ZnO Films.* Chemistry of Materials, 2014. **26**(20): p. 5839-5851.
38. Kelchtermans, A., et al., *Relation between synthesis conditions, dopant position and charge carriers in aluminium-doped ZnO nanoparticles.* Rsc Advances, 2013. **3**(35): p. 15254-15262.
39. Serier, H., M. Gaudon, and M. Menetrier, *Al-doped ZnO powdered materials: Al solubility limit and IR absorption properties.* Solid State Sciences, 2009. **11**(7): p. 1192-1197.
40. Dorey, R.A., *Ceramic thick films for MEMS and microdevices*. 2011: William Andrew.

Chapter 5 - Conversion from precursor solution to ink

This chapter deals with the transformation of a stable Al doped ZnO precursor solution towards an Al doped ZnO ink. We studied the ink's properties in terms of the wetting of the substrate and the jetting of discrete droplets. If a stable precursor solution is obtained, its physical properties should match specific characteristics to allow proper droplet formation. The droplet formation in a DOD printer is rather complex and physics and fluid mechanics play an important role in the generation of discrete droplets. Next to its capacity to jet discrete droplets, the ink should also show a good wetting of the substrate. Bad wetting of the substrate can result in inhomogeneous thin films or uncovered areas. Hence, the cleaning of the substrates and the ink's capacity to wet a surface is crucial for the formation of homogeneous thin films.

5.1 Physical properties of the ink

Ink properties such as viscosity, surface tension and density are of great importance during the printing process. According to Fromm [1], the printability of inks can be estimated by the inverse of the Ohnesorge number (Oh^{-1}) which is an appropriate grouping of physical constants to describe the drop formation. This dimensionless number is independent of the drop velocity and relates the viscous force to the inertial and surface tension forces. In fact, *Oh i*s the ratio of the square of the Weber number (*We*) and the Reynolds number (*Re*), where *We* is the ratio between the inertial forces and the surface tension, while *Re* is the ratio between the inertial forces and the viscous forces:

$$Re = \frac{v\rho\alpha}{\eta},\ We = \frac{v^2\rho\alpha}{\gamma},\ Oh = \frac{\sqrt{We}}{Re} = \frac{\eta}{\sqrt{\rho\gamma\alpha}} \qquad \text{Eq.5.1}$$

Where γ (J m^{-2}), ρ (kg m^{-3}), v (m s^{-1}), η (Pa s) are respectively the surface tension, the density, velocity and the viscosity of the ink, while α (m) is the diameter of the nozzle opening. Fromm [1] predicted that when Oh^{-1} reaches values higher than 2, drop formation in DOD systems is possible. Reis and Derby [2, 3] fine-tuned this prediction. The inverse of the Ohnesorge number should have a value between 1 and 10 to eject a stable droplet without any satellite droplet formation. The lower limit is set by the ink's viscosity. The viscous forces become dominant and prevent the ejection of drops. The upper limit is set by the formation of unwanted satellite droplets. In reality, systems with values of Oh^{-1} higher than 10 are also printable because the formation of satellite droplets shouldn't necessary result in two single droplets. Jang *et al.* [4] redefined the limit of Oh^{-1} by taking specific characteristics of printing into account. The inverse of the Ohnesorge number has to have a value between 4 and 14. Below 4, the positional accuracy is degraded due to long lifetime of the droplet's tail. Above 14, it's impossible to form a single droplet. Between 10 and 14 it's possible to obtain single droplets when the formed satellite drops have a velocity higher than the primary droplet. Due to the difference in speed between satellite and primary drop they still can recombine to a single droplet (figure 5.1).

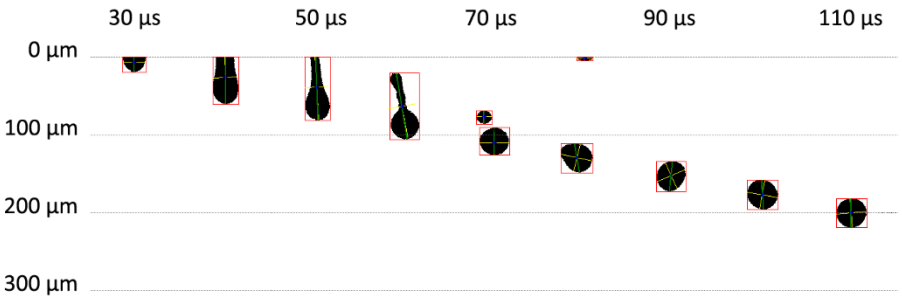

Figure 5.1 Droplet visualisation with a time interval of 10 µs of ink A3%B, using a 30 µm MicroFab nozzle fired at 14 V where the satellite drop merges with the main droplet around 65 µs.

High shear rates at the nozzle orifice are reached during drop ejection. The shear rates can get up to 10^5 - 10^6 s^{-1} [1, 2, 5]. It's important to take these high shear rates into account when the jettability of an ink is predicted by its physical properties. Especially, the influence of the shear rates on the viscosity is of great importance. Depending on the chemical composition of the ink, Newtonian or non-Newtonian behaviour can be distinguished. A Newtonian fluid's shear rate is proportional to the shear stress. This proportionality constant equals the viscosity. A change in viscosity at a varying shear rate is a typical non-Newtonian property. For the latter, shear thickening or thinning can appear. More specific, the viscosity of the ink will increase with increasing shear rates or the viscosity of the ink will decrease with increasing shear rates. It is important to create an understanding in the ink's behaviour at those high shear rates to predict its printability. At the lower limit of the Oh^{-1}, shear thickening can prevent droplet formation while shear thinning at the upper limit of Oh^{-1} can induce satellite droplets. All our inks are showing shear thickening (table 5.1 and figure 5.2). However, jetting is still possible. As demonstrated in table 5.1, the value for Oh^{-1} is decreasing from 11 to 8.84 for an increasing shear rate, resulting in a perfectly jettable ink.

Table 5.1 Fluid properties of ink A3%B with 10 V% ethanol and the calculation of Oh^{-1} to predict the printability. The used orifice diameter (α) equals 30 µm.

Shear rate (s^{-1})	Viscosity η (Pa s)	Density ρ (kg m^{-3})	Surface tension γ (J m^{-2})	Oh^{-1}
13637	3.67 x 10^{-3}	1109	48.6 x 10^{-3}	11.00
45268	4.55 x 10^{-3}	1109	48.6 x 10^{-3}	8.84

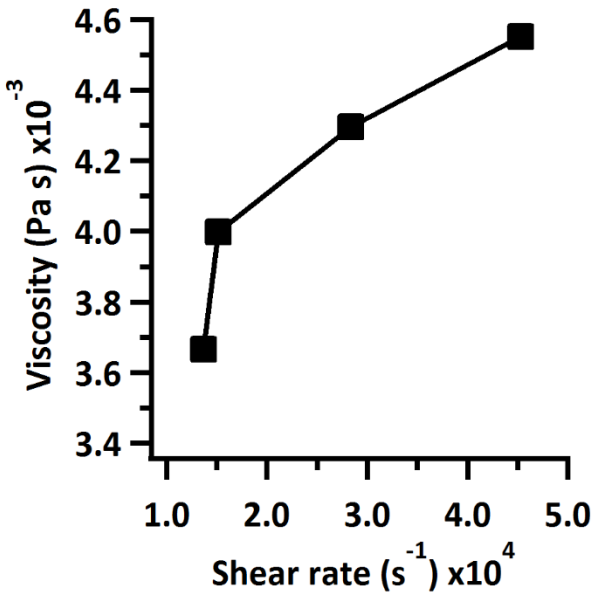

Figure 5.2 Viscosity (at 22°C) as a function of the shear rate for ink A3%B with 10 V% ethanol obtained through double plated rheology measurements with a plate diameter of 60mm.

5.1.1 Droplet formation

By combining all knowledge about the physical properties of the ink and by applying a proper deformation at the cavity of the nozzle, discrete droplets can be formed. The used MicroFab nozzle with a orifice diameter of 30 µm has an piezoelectric actuator. This piezoelectric filament will be deformed by a bipolar waveform defined by a maximum applied voltage, a ramp time to reach the maximum voltage and a dwell time where the maximum voltage is maintained (figure 5.3).

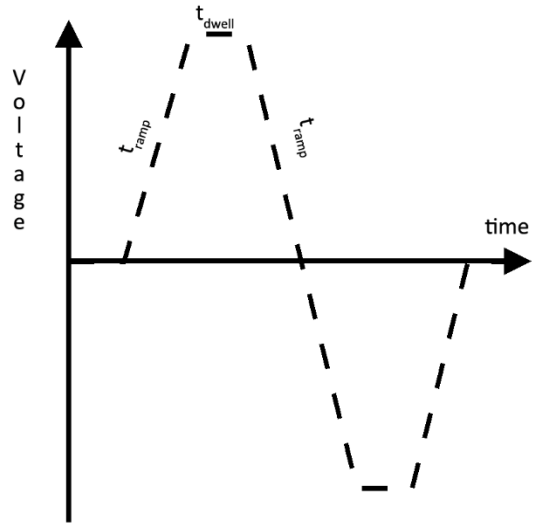

Figure 5.3 A bipolar waveform applied to the piezoelectric filament inside the MicroFab printhead.

Each type of ink has its own specific bipolar waveform to jet drops. Because we opted to use one Zn precursor solution and add small amounts of concentrated Al precursor solutions, the jettability did not change substantially for the different AZO inks. The common used waveform has a maximum voltage of 14 V, a dwell time of 4 µs and a ramp time of 3.5 µs.

As illustrated in table 5.2, the addition of ethanol positively influences the Oh^{-1}. However, we should remark that the ink with 0 v% ethanol also produced discrete droplets after the recombination of the satellite droplet with the main droplet (figure 5.1). At first sight, this ink wouldn't be jettable due to its high Oh^{-1}, respectively 15.9. This can be explained by the already mentioned shear thickening. We tried to take this into account by following the viscosity as a function of the shear rate. The reached shear rates during the rheology measurements (≈ 45000 s^{-1}) are still smaller than those reached during the printing process. Shear thickening or shear thinning make it hard to predict the exact viscosity at the moment droplets are jetted. Therefore, we can only remark that the inverse of the Ohnesorge number is an estimation of the ink's jetting behaviour. It can be used to get a first insight towards the ink's printability.

Even if an ink wouldn't be able to jet single droplets additives can be added to improve jetting. Increasing the viscosity and/or decreasing the surface tension can help the jetting of discrete droplets. The additive should be compatible with the ink and should not influence the formed complexes nor thermal process. In this case, ethanol is suggested as additive. As observed, the viscosity gain of the inks goes along with an increasing amount of ethanol, while the surface tension of the inks is decreasing. Finally, the inverse of the Ohnesorge number is positively influenced and reaches values below 10 for the ink with 10 v% of ethanol (table 5.2).

Table 5.2 Physical ink properties and the inverse of the Ohnesorge number as a function of ink A3%B and its ethanol content. The represented viscosity is measured at a shear rate of 45000 s^{-1}.

Ink	v% ethanol	Surface tension γ ($J\ m^{-2}$)	Density P ($kg\ m^{-3}$)	Viscosity η (Pa s)	Oh^{-1}
A3%B	0	69.0×10^{-3}	1128	3.03×10^{-3}	15.9
A3%B2.5	2.5	62.6×10^{-3}	1122	3.20×10^{-3}	14.3
A3%B5	5	57.4×10^{-3}	1116	3.52×10^{-3}	12.5
A3%B10	10	48.6×10^{-3}	1109	4.55×10^{-3}	8.84

This can be explained by looking to the behaviour of water-ethanol mixtures which show similar behaviour as the mixture of the aqueous ink and ethanol. By mixing water and ethanol a balance should be found between the hydrophobic and hydrogen bonding interactions. The hydrogen bonding interactions involve the hydroxyl-groups of ethanol and water while the hydrophobic interactions are focussed on the alkyl group of ethanol [6]. The viscosity of the water-ethanol mixtures is increasing while the surface tension is decreasing [7, 8]. Many researchers tried to explain the observed phenomena [6, 9-12]. Davis *et al.* [12] found a significantly enhanced hydrogen-bond network around the hydrophobic groups of alcohols, meaning it is more ordered than in bulk water. Ethyl and ethylene groups are the ideal templates to form a water network around. This leads to a locally more enhanced tetrahedral order. This structural behaviour influences the viscosity positively, but doesn't explain the observed trend of the

surface tension. Compared to the bulk, an excess of ethanol at the vapour/liquid interface is noticed [13]. These ethanol molecules are oriented with their alkyl groups pointing out of the solution, resulting in a decrease of the number of water molecules bound compared to the bulk. This leads to a decrease of the surface tension.

The jetting behaviour of the ink A3%B10 is represented in figure 5.4 and figure 5.5. Starting at 30 µs after actuation, a liquid filament is formed. After 50 µs the liquid column breaks off, resulting in a droplet with tail. Finally, the tail merges with the droplet and satellite droplets are prevented, leading to a single droplet with a volume of 24 pL, a droplet diameter of 37 µm and a velocity of 2.29 m/s. One can notice the deformation of the liquid meniscus at the orifice at 70 and 80 µs after jetting. This is due to wave propagation inside the printhead caused by the deformation of the piezoelectric filament. This wave will travel in the printhead and will be reflected. At the moment the piezoelectric filament returns to its original position, a second pressure wave will be created. The second wave will interact with the first one, leading to the deformation of the liquid meniscus when it reaches the nozzle end. If this new pressure wave would have a kinetic energy larger than needed to form a droplet, another droplet would be ejected [2, 14].

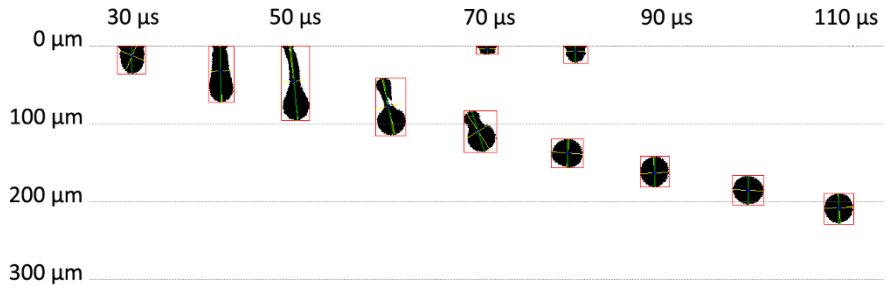

Figure 5.4 Droplet visualisation with a time interval of 10 µs of ink A3%B10, using a 30 µm MicroFab nozzle fired at 14 V with a dwell and ramp time of 4 and 3.5 µs.

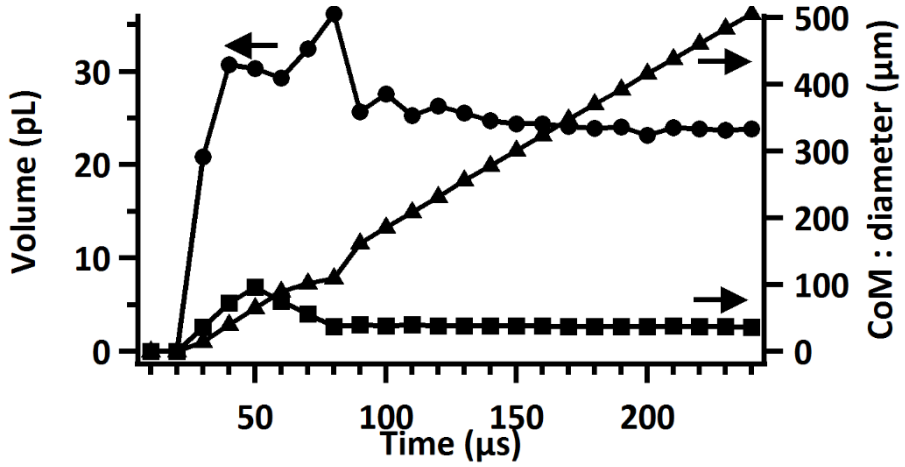

Figure 5.5 Jetting analysis of ink A3%B10. Drop volume (●), drop diameter (■) and the vertically displacement of the centre of mass (▲) are shown as a function of time.

5.2 Droplet – substrate interaction

Obtaining a jettable ink is the first issue that had to be solved to produce ink jet printed AZO thin films. After jetting stable droplets, they were deposited on a substrate. Therefore it is important to gather knowledge about the droplet-substrate interaction. In this research, complete substrate coverage and patterning will be pursued. Thin films are obtained by positioning the droplets with sufficient overlap in *x* and *y* direction. Due to the high degree of overlap needed to deposit thin films with adequate thickness, the position of the droplets is less strict than for patterning. Well defined patterns desire overlap in specific directions which makes the position of the droplets more critical. Additionally, the droplet size after impact will define the maximum feasible resolution.

5.2.1 Droplet impact and spreading

At the moment a droplet impacts on a substrate, it will deform and spread out till an equilibrium sessile drop configuration is obtained. The behaviour of droplets upon impact will be controlled by a number of forces, e.g. inertial, capillary and gravitational forces. Just as with droplet formation the dimensionless numbers such as *We*, *Re* and *Oh* play an important role. Next to this, the Bond number (B_0) should be considered:

$$B_0 = \frac{\rho g d^2}{\gamma} \qquad \text{Eq.5.2}$$

Where *d* is the diameter of the droplet, ρ the density, γ the surface tension and *g* the acceleration of gravity when gravitational forces are included. If the bond number is very small (B_0 <<1) the gravitational contribution can be neglected [15]. As shown in table 5.3, the gravitational contribution can be neglected in the following discussion.

Table 5.3 Calculation of the Bond number for the ink A3%B10 when jetted with a 30 μm MicroFab nozzle.

Ink	Surface tension γ (J m^{-2})	Density ρ (kg m^{-3})	Droplet diameter d (m)	Bond number B_0
A3%B10	48.6 x 10^{-3}	1109	37 x 10^{-6}	3.06 x 10^{-4}

Schiaffino and Sonin [16] studied the impact of relatively low Weber number droplets on solid surfaces. Although their studies considered droplets solidifying after impact, the initial stages after impact should be the same. Droplet behaviour after impact can be divided in two regimes; i.e. an impact driven and a capillary driven regime (figure 5.6). At the impact driven regime, the inertial forces dominate the process. At the capillary driven regime the initial droplet velocity is unimportant. It is estimated that the droplet deformation process occurs over a timescale of μs while the capillary spreading will occur over a couple of ms [17]. Upon impact, the kinetic energy will deform the droplet while some energy is absorbed by viscous dissipation [18]. This defines the maximum spreading of the droplet and its behaviour in the coming stages. If a droplet has a velocity which is too high for its physical properties, droplet splashing will occur and the printing resolution will be reduced [17]. At a low droplet velocity a large rebounce can take place, which can result in a '*jumping*' droplet [19]. A droplet velocity between those boundaries results in a droplet reaching its maximum spreading, recoiling due to surface tension forces and undergoing damped oscillation. Meanwhile the process of capillary spreading will occur, leading to a droplet in equilibrium conditions [18].

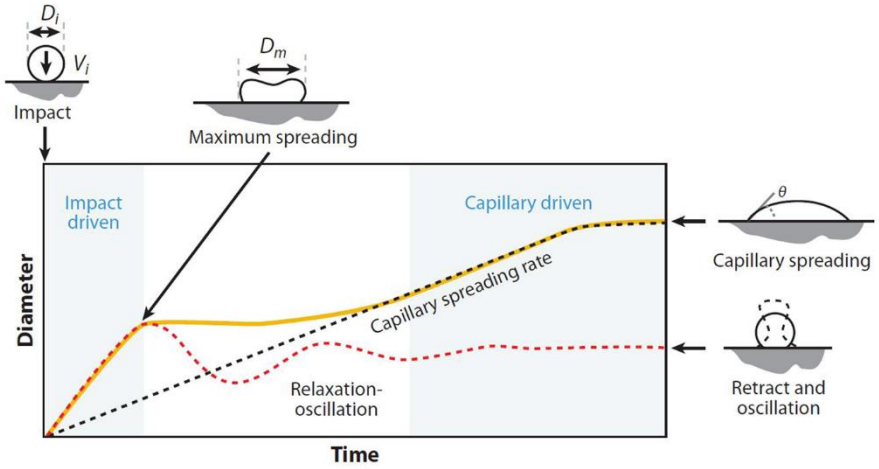

Figure 5.6 Schematic illustration of droplet's behaviour upon impact with a substrate. The initial impact is followed by a sequence of damped oscillations before the capillary regime is entered where the droplet strives to an equilibrium contact angle θ [15].

The threshold velocity for splashing is experimentally determined by Stow and Hadfield [20]. They introduced the following equation:

$$K = We^{1/2}\ Re^{1/4} > f(R) \qquad \text{Eq.5.3}$$

Where *f(R)* is a function of the surface roughness of the substrate. When K reaches a value higher than *f(R)* splashing will occur. Flat surfaces have a value for *f(R)* of 50 – 60. This boundary defines a region of *We* and *Re* within which DOD ink jet printing is possible. Ink A3%B10 has a value for K of 4.49 when we consider a droplet diameter of 37 µm and a velocity of 2.29 m/s as mention above. For these specific ink parameters, the velocity can go up to 17 m/s before splashing will occur. Therefore, we can conclude that splashing will not be of any concern during the printing experiments.

5.2.2 Wetting behaviour of the ink with the substrate

The impact of the droplets on the substrate ends with a capillary regime where the droplet in equilibrium is obtained. This equilibrium and its characteristic contact angle θ plays an important role in wetting the substrate. Producing homogeneous thin films and patterns relies on the wetting of the substrate. This and the coalescence of the droplets are necessary for thin film processing.

Otherwise, inhomogeneous thin films or a large liquid droplet can be formed on the substrate.

Wetting of droplets on a solid surface

To have a better view on wetting of droplets on a surface one can have a look at Young's equation [21]:

$$\gamma_{sl} = \gamma_{sv} - \gamma_{lv} \cos\theta \qquad \text{Eq.5.4}$$

A droplet on a solid surface will form a spherical cap. This spherical cap is a result of the balance between the surface free energy of the substrate (γ_{sv}), the interfacial tension between the solid and liquid surface (γ_{sl}), the surface tension of the liquid (γ_{lv}) and the contact angle (θ) of the droplet at the solid-liquid interface. Depending on the contact angle 3 regimes can be distinguished: (1) Complete wetting where the contact angle reaches 0°. It's more beneficial to enlarge the liquid-substrate interface than maintaining the liquid-vapour interface. Meaning, the surface free energy of the substrate is larger than the interfacial energy between the substrate and liquid. (2) If a contact angle reaches an angle between 0 and 90° partial wetting is obtained. This finite contact angle is obtained when the surface free energy of the substrate is smaller than the sum of the surface tension of the liquid and the interfacial energy of the liquid with the substrate. (3) Droplets in the dewetting regime have a contact angle larger than 90°. The interfacial energy between the substrate and the liquid has a higher value than the surface free energy of the substrate. Meaning, the formation of the liquid-substrate interface is less favourable [22].

To understand the wetting of the substrate, one should take a closer look at the surface energies of the substrate and the ink. It is common knowledge that cleaning and modifying the substrate surface has a large impact on its surface energy. Also, the ink chemistry and its components will influence the surface tension of the ink. By controlling both, the wetting of the ink on the substrate can be tuned to the desired contact angle. Because the interfacial energies are the result of several intermolecular forces (van der Waals forces, Lewis acid-base-interactions, hydrogen-bonding and dipole/dipole interactions), the total interfacial energy can be seen as the sum of interfacial energies of these forces.

Good and Girifalco [23, 24] defined liquids which are only capable of having van der Waals interactions as 'dispersive' where all the other interactions are defined as 'polar'. So, the interfacial energy can be divided in a polar (γ^p) and dispersive (γ^d) component:

$$\gamma = \gamma^p + \gamma^d \qquad \text{Eq.5.5}$$

Using the polar and dispersive component, wetting of a substrate can be visualised by a wetting envelope. A wetting envelope is a graphical design of the wetting of a substrate based on Owens-Wendt method [25].

$$\frac{\gamma_l(\cos\theta + 1)}{2\sqrt{\gamma_l^d}} = \sqrt{\gamma_s^p}\sqrt{\frac{\gamma_l^p}{\gamma_l^d}} + \sqrt{\gamma_s^d} \qquad \text{Eq.5.6}$$

The surface energy's polar and dispersive component of the substrate are determined by contact angle measurements of solvents with well-known surface tensions. When both components of substrate's surface energy are determined by solving eq. 5.6, a reversed Owens-Wendt method is applied. Here, the polar component of a liquid is plotted as a function of the dispersive component for a fixed contact angle on a known substrate. This results in a curve for which a liquid with a given polar and dispersive component of its surface tension will have a fixed contact angle. Every liquid for which the polar and dispersive component of the surface tension falls within the curve will have contact angle smaller than the fixed one. Every liquid which falls out the curve will have a contact angle larger than the fixed one [26].

Influence of substrate cleaning and ink additives on the wetting of the ink with substrate

A wetting envelope can be used to predict the wetting of diverse liquids on the substrate or the wettability of a liquid for different substrates. To remove contamination of the as such delivered substrates a cleaning before use is needed. The wetting properties of the substrate as a function of the cleaning procedure are determined by drafting wetting envelopes for each cleaning method. Three cleaning procedures were selected: (1) The substrates were degreased with isopropanol followed by an ultrasonic treatment for 60 min in

isopropanol. Afterwards, they were dried with an air flow. (2) The substrates were degreased with isopropanol followed by an ultrasonic treatment for 60 min in isopropanol and dried on a hotplate at 450°C during 5 min. (3) The substrates were degreased with isopropanol followed by an ultrasonic treatment for 60 min in isopropanol. Next, they were rinsed with demineralised water and soaked for 1 h in a H_2SO_4:H_2O_2 solution (a 3:1 mixture). Afterwards, the substrates were rinsed with demineralised water and soaked in a 3 mol L^{-1} NaOH solution for 1 h. At the end they were rinsed with a 3 v% HCl solution, demineralised water and isopropanol before dried with an air flow [27].

The wetting envelope for each cleaning method will be determined by measuring the contact angles of 2 liquids on the substrate. Solving eq. 5.6 results in the polar and the dispersive component of the substrate's surface energy. An overview of the contact angle of multiple liquids on the cleaned substrates is given in table 5.4.

Table 5.4 Contact angle measurements on the different cleaned substrates with a broad selection of liquids.

	Cleaning 1	Cleaning 2	Cleaning 3
Contact angle Diiodomethane (°)	64.4	41.2	40.0
Contact angle Water (°)	67.3	14	<5
Contact angle Ethylene glycol (°)	47.3	42.1	<5
Contact angle Glycerol (°)	60.5	21.6	20.0
Contact angle Formamide (°)	47.8	18.1	<5
Contact angle Acetic acid (°)	17.1	<5	<5
Contact angle n-Dodecane (°)	<5	7	<5

Remark: Contact angles smaller than 5° can't be measured accurately. Therefore, it isn't possible to assign an specific contact angle. If these measurements are further used to calculate the substrate's surface tension, a contact angle of 5° will be estimated.

The polar and dispersive component of the substrate's surface energy were solved for 2 different systems, diiodomethane and water and diiodomethane and glycerol respectively (table 5.5). Making use of the data collected by Ström *et al.* [28] equation 5.6 is solved. Especially, for cleaning method 2 and 3 remarkable differences between the two datasets are observed. The wetting envelopes for cleaning method 3 (contact angle of 0°) determined by both systems are plotted (figure 5.7).

Table 5.5 Calculated surface tension of the cleaned substrates by Owens-Wendt method.

	Diiodomethane and water			Diiodomethane and glycerol		
	γ_{tot} (mN/m)	γ^p (mN/m)	γ^d (mN/m)	γ_{tot} (mN/m)	γ^p (mN/m)	γ^d (mN/m)
Cleaning 1	35.01	11.72	23.29	36.07	10.02	26.05
Cleaning 2	76.69	44.31	32.38	59.30	20.76	38.54
Cleaning 3	79.07	46.28	32.79	60.07	20.40	39.61

Depending on the selected liquids to calculate the wetting envelope (table 5.5), a different wetting behaviour of ink A3%B on the substrate cleaned by cleaning method 3 was predicted (figure 5.7). This is due the large difference in the total surface tension calculated for both systems, respectively 79.07 mN/m and 60.07 mN/m.

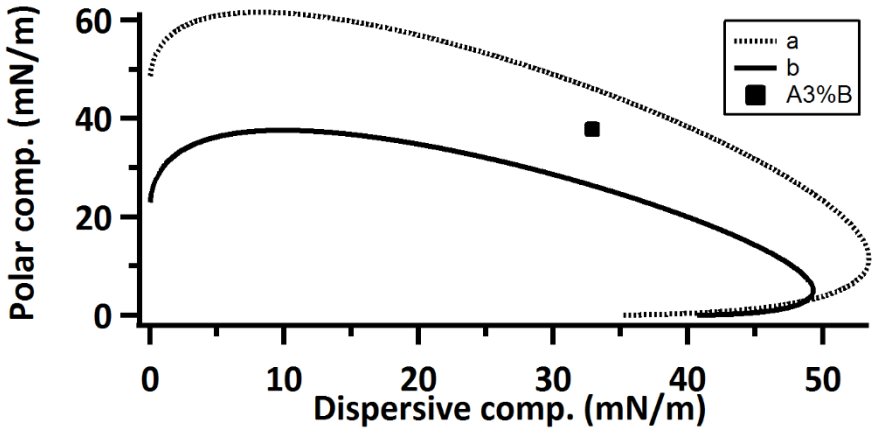

Figure 5.7 Wetting envelope for cleaning method 3 and a contact angle of 0°. a) Contact angles using diiodomethane and water. b) Contact angles using diiodomethane and glycerol. Where (■) represents the polar and dispersive component of ink A3%B's surface tension.

Similar behaviour was observed for cleaning method 2. Cleaning method 2 resulted in similar surface tensions as cleaning method 3 based on the same selection of liquids used to solve eq. 5.6. However, the large deviation between both wetting envelopes/surface tensions depending on the selected couple of

liquids to solve eq. 5.6 is typical of the Owens-Wendt method. Owens and Wendt divided the total surface tension in two components depending on the nature of the possible interactions (polar or dispersive). The large polar component of the surface tension of the liquid as substrate results in dominant polar interactions which overrule the dispersive interactions and 'false' information is collected [29]. Van Oss *et al*. [30] defined the polar component as a combination of electron acceptor-donor interactions, where the polar component is represented as follows:

$$\gamma^p = 2\sqrt{\gamma^+\gamma^-} \qquad \text{Eq.5.7}$$

Where γ^+ represents the acid component and γ^- the basic component. Based on these electron acceptor-donor interaction, the adhesion and cohesion of a liquid on a solid polar surface is enhanced. These interactions make it impossible to predict the wetting of polar surfaces via the Owens-Wendt model and wetting envelopes. However, the Owens-Wendt model is still suited for moderate polar surfaces such as polymers and the glass substrates cleaned by cleaning method 1 [31].

Because an overall model for the wetting of the substrates can't be plotted, the contact angles of several inks are measured for the different cleaning methods (table 5.6)

Table 5.6 Contact angle measurements for ink A3%B with a varying ethanol content (0-10 v% ethanol)

	Contact angle A3%B (°)	**Contact angle A3%B2.5 (°)**	**Contact angle A3%B5 (°)**	**Contact angle A3%B10 (°)**
Cleaning 1	70.1	66.8	65.9	62.2
Cleaning 2	41.5	37	34.2	33.1
Cleaning 3	12.1	7.5	5	<5

It is ascertained that the inks were more capable to wet the substrates cleaned by cleaning method 3. Most likely, the cleaning modified the surface. According to Hau *et al*. [27] hydroxyl groups are formed on the glass surface, resulting in a

more hydrophilic surface and an improved wetting for water based inks. Another general trend is the decreasing contact angle with an increasing quantity of ethanol in the ink. This is mainly due to a decreasing total surface tension of the ink with an increasing ethanol concentration (table 5.2).

The contact angle of ink A3%B10 on a glass substrate cleaned by cleaning method 3 could not be measured by the contact angle setup. By jetting single droplets on the substrate, the footprint of the droplet can be used to calculate the contact angle. The footprint of a droplet on a substrate can be deduced from the following equation [2, 15]:

$$d_{con} = \sqrt[3]{\frac{8}{\tan\frac{\theta_{eqm}}{2}\left(3+\tan^2\frac{\theta_{eqm}}{2}\right)}} * d_0 \qquad \text{Eq.5.8}$$

Where d_{con} is the contact diameter, d_0 the diameter of the droplet in flight, and θ_{eqm} the contact angle at equilibrium.

The contact diameter was measured by optical profilometry. A contact diameter of 158-162 µm was obtained. Coupled with a droplet diameter in flight of 37 µm, equation 5.4 can be solved and a contact angle of 3.5-4° was calculated.

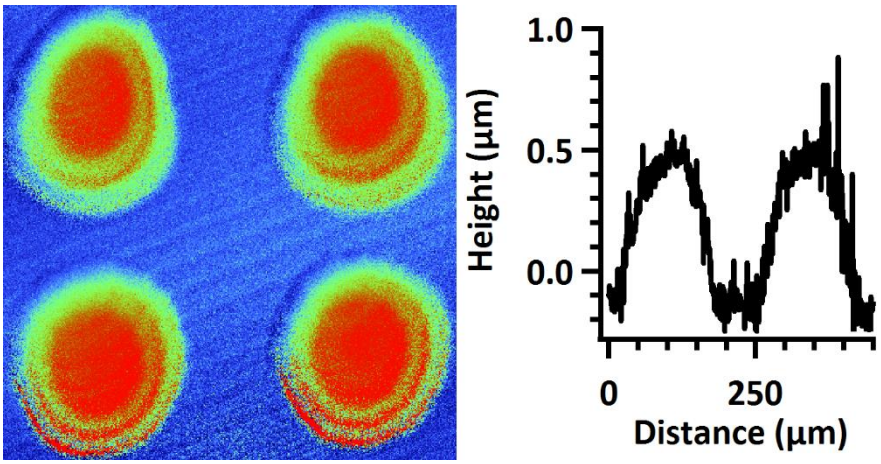

Figure 5.8 Optical profilometry measurement of single droplets printed with ink A3%B10 on a glass substrate cleaned by cleaning method 3.

Finally, the substrate and ink modification led to a good wetting system which allowed the deposition of homogenous thin wet films. Ink jet printing tests were

showing that only ink A%3B10 printed on a substrate cleaned by cleaning method 3 resulted in homogeneous printed wet films. Large liquid fronts at the end of the substrate or concentrated drop of ink were obtained when thin films were printed with other combinations of ink and/or substrate cleaning methods (figure 5.9). To print homogenous thin films with sufficient thickness, the line and drop spacing was fixed at 50 µm. This was resulting in a droplet overlap of ± 70%.

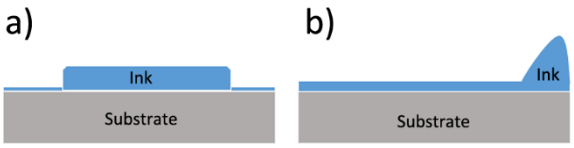

Figure 5. 9 Schematic of prints obtained with ink and/or substrate cleaning methods deviating from ink A3%B10 and cleaning method 3: a) The ink is concentrated at the middle of the substrate. b) A large liquid front is formed at the end of the substrate.

5.3 Conclusion

The precursor solutions prepared in the previous chapter were transformed to printable inks by adjusting the physical constants of the inks. A jettable ink was obtained by the addition of ethanol which influenced the viscosity and surface tension. The positive influence on these physical parameters allowed the jetting of the ink without the formation of satellite droplets. An average printed droplet had a volume of 24 pL, a diameter of 37 µm and a velocity of 2.29 m/s. After obtaining a printable ink, the droplet-substrate interaction was studied. The modification of the substrate surface, based on various cleaning methods, taught us that the determination of the substrates surface tension coupled with wetting envelopes based on the Owens-Wendt method was not valid for polar substrates. Therefore, the ink-substrate interactions were only studied as a function of the contact angle. The printing of homogeneous films was only possible when a contact angle lower than 5° was obtained. Finally, the thin films were printed with a drop and line spacing of 50 µm.

5.4 Reference list

1. Fromm, J.E., *Numerical-calculation of the fluid-dynamics of drop-on-demand jets.* Ibm Journal of Research and Development, 1984. **28**(3): p. 322-333.
2. Reis, N., C. Ainsley, and B. Derby, *Ink-jet delivery of particle suspensions by piezoelectric droplet ejectors.* Journal of Applied Physics, 2005. **97**(9).
3. Reis, N. and B. Derby, *Ink jet deposition of ceramic suspensions: Modelling and experiments of droplet formation*, in *Solid Freeform and Additive Fabrication-2000*, S.C. Danforth, D. Dimos, and F.B. Prinz, Editors. 2000, Materials Research Society: Warrendale. p. 117-122.
4. Jang, D., D. Kim, and J. Moon, *Influence of fluid physical properties on ink-jet printability.* Langmuir, 2009. **25**(5): p. 2629-2635.
5. Lee, T.-M., et al., *Drop-on-demand solder droplet jetting system for fabricating microstructure.* Ieee Transactions on Electronics Packaging Manufacturing, 2008. **31**(3): p. 202-210.
6. Juurinen, I., et al., *Measurement of rwo solvation regimes in water-ethanol mixtures using X-ray Compton scattering.* Physical Review Letters, 2011. **107**(19): p. 197401.
7. Khattab, I.S., et al., *Density, viscosity, and surface tension of water plus ethanol mixtures from 293 to 323 K.* Korean Journal of Chemical Engineering, 2012. **29**(6): p. 812-817.
8. Biscay, F., A. Ghoufi, and P. Malfreyt, *Surface tension of water-alcohol mixtures from Monte Carlo simulations.* Journal of Chemical Physics, 2011. **134**(4).
9. Pradhan, T., P. Ghoshal, and R. Biswas, *Structural transition in alcohol-water binary mixtures: A spectroscopic study.* Journal of Chemical Sciences, 2008. **120**(2): p. 275-287.
10. Cipiciani, A., G. Onori, and G. Savelli, *Structural-properties of water-ethanol mixtures - A correlation with the formation of micellar aggregates.* Chemical Physics Letters, 1988. **143**(5): p. 505-509.
11. Frank, H.S. and M.W. Evans, *Free volume and entropy in condensed systems III. Entropy in binary liquid mixtures; partial molal entropy in dilute solutions; structure and thermodynamics in aqueous electrolytes.* The Journal of Chemical Physics, 1945. **13**(11): p. 507-532.
12. Davis, J.G., et al., *Water structural transformation at molecular hydrophobic interfaces.* Nature, 2012. **491**(7425): p. 582-585.
13. Tarek, M., D.J. Tobias, and M.L. Klein, *Molecular dynamics investigation of an ethanol-water solution.* Physica A: Statistical Mechanics and its Applications, 1996. **231**(1–3): p. 117-122.
14. Bogy, D.B. and F.E. Talke, *Experimental and theroetical-study of wave-propagation phenomena in drop-on-demand ink jet devices.* Ibm Journal of Research and Development, 1984. **28**(3): p. 314-321.
15. Derby, B., *Inkjet printing of functional and structural materials: fluid property requirements, feature stability, and resolution*, in *Annual Review of Materials Research, Vol 40*, D.R. Clarke, M. Ruhle, and F. Zok, Editors. 2010. p. 395-414.
16. Schiaffino, S. and A.A. Sonin, *Formation and stability of liquid and molten beads on a solid surface.* Journal of Fluid Mechanics, 1997. **343**: p. 95-110.
17. Yarin, A.L., *Drop impact dynamics: splashing, spreading, receding, bouncing*, in *Annual Review of Fluid Mechanics*. 2006, Annual Reviews: Palo Alto. p. 159-192.
18. Derby, B., *Inkjet printing ceramics: From drops to solid.* Journal of the European Ceramic Society, 2011. **31**(14): p. 2543-2550.
19. Fukai, J., et al., *Wetting effect on the spreading of a liquid droplet colliding with a flat surface: experiment and modeling.* Physics of Fluids, 1995. **7**(2): p. 236-247.

20. Stow, C.D. and M.G. Hadfield, *An experimental investigation of fluid-flow resulting from the impact of water drop with an unyielding dry surface.* Proceedings of the Royal Society of London Series a-Mathematical Physical and Engineering Sciences, 1981. **373**(1755): p. 419-441.
21. Young, T., *An essay on the cohesion of fluids*. 1804: publisher not identified.
22. Bonn, D., et al., *Wetting and spreading.* Reviews of Modern Physics, 2009. **81**(2): p. 739-805.
23. Good, R.J. and L.A. Girifalco, *A theory for estimation of surface and interfacial energies. III. Estimation of surface energties of solid from contact angle.* The Journal of Physical Chemistry, 1960. **64**(5): p. 561-565.
24. Girifalco, L.A. and R.J. Good, *A theory for the estimation of surface and interfacial energies. I. Derivation and application to interfacial tension.* The Journal of Physical Chemistry, 1957. **61**(7): p. 904-909.
25. Owens, D.K. and R.C. Wendt, *Estimation of the surface free energy of polymers.* Journal of Applied Polymer Science, 1969. **13**(8): p. 1741-1747.
26. Feigl, M., et al., *Improved wetting of bare and pre-coated steels by aqueous alumina sols for optimum coating success.* Journal of Sol-Gel Science and Technology, 2010. **55**(2): p. 191-198.
27. Hau, W.L.W., et al., *Surface-chemistry technology for microfluidics.* Journal of Micromechanics and Microengineering, 2003. **13**(2): p. 272-278.
28. Ström, G., M. Fredriksson, and P. Stenius, *Contact angles, work of adhesion, and interfacial tensions at a dissolving Hydrocarbon surface.* Journal of Colloid and Interface Science, 1987. **119**(2): p. 352-361.
29. Chhatre, S.S., et al., *Fluoroalkylated silicon-containing surfaces–estimation of solid-surface energy.* ACS Applied Materials & Interfaces, 2010. **2**(12): p. 3544-3554.
30. Van Oss, C.J., M.K. Chaudhury, and R.J. Good, *Interfacial Lifshitz-van der Waals and polar interactions in macroscopic systems.* Chemical Reviews, 1988. **88**(6): p. 927-941.
31. Rulison, C., *So you want to measure surface enegry?* , in *Krüss technical note #306*. Krüss GmbH: Hamburg.

Chapter 6 – From wet film to transparent conductive oxide

The previous chapters dealt with the formation of an ink. Firstly, the chemical stability of the ink was investigated followed by the printability and the wetting of the ink on the glass substrate. This chapter will focus on the process steps after the deposition of a wet film on the substrate. This wet film containing stabilised ions will be transformed in an AZO thin film via an optimised thermal process. A thermal oxidation will take place followed by an activation of the electrical properties.

6.1 Thermal processing of the wet film

Once the ink is deposited on the substrate with a drop and line spacing of 50 µm, the wet thin film has to be transformed into an AZO thin film. Thermal processing will decompose the precursor, remove any organics, form the desired oxide phase, induce crystallisation and control the charge carrier concentration [1]. Generally, CSD processed AZO thin films involve a thermal treatment consisting of an oxidation and a post-annealing step. The first step allows the formation of the desired crystalline oxide (AZO) and will remove solvents and organic additives by making use of an O_2-rich atmosphere. Therefore, this step will be further discussed as a thermal oxidation. A second thermal treatment is required for the *activation* of the AZO coating [1-6]. Further on, this will be discussed as the thermal activation of AZO thin films.

A general approach was used as follows: after ink jet printing, the wet coating was immediately dried on a hotplate with a static air flow. Once the coating was dried, it was transported into a tube furnace with a controlled flow and a fine-tuned thermal process. The selected atmosphere for this process will be a 200 ppm O_2 in N_2 flow of 200 mL/min. Depending on the optimal processing parameters a dry or wet atmosphere was selected. Once the samples were cooled to room temperature, a post-annealing followed in an Ar/5% H_2 atmosphere with a flow of 200 mL/min.

6.2 Thermal analysis of the ink

The thermal oxidation is crucial towards the final properties of the AZO thin film. During this thermal treatment the stabilised Zn^{2+} and Al^{3+} ions are oxidised to the desired phase, Al doped ZnO. However not only the formation of AZO takes place, the morphology and crystal growth as well as the opto-electrical properties of these thin films are enormously influenced by the selected heat treatment. Studying the behaviour of the ink A3%B as a function of temperature will help to draft a thermal process. Insights were gained by coupling a ThermoGravimetric Analysis (TGA) of the ink with FTIR and NMR spectroscopy.

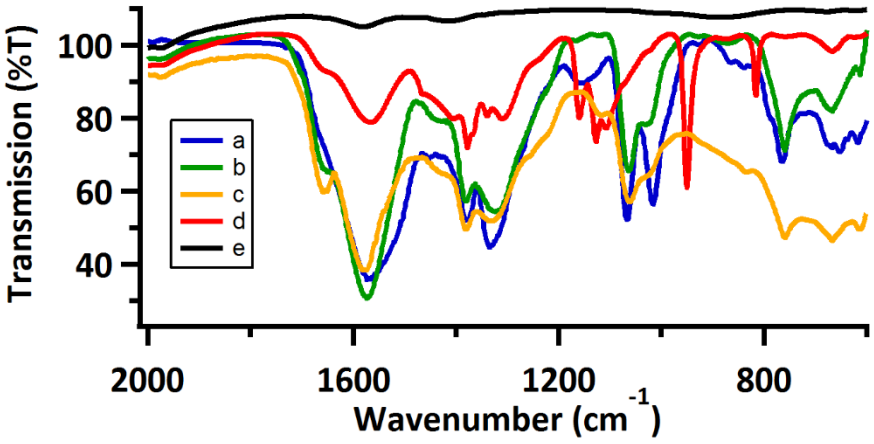

Figure 6.1 FTIR as a function of temperature on ink A3%B. a) Dried at 90°C for 10 minutes, b) dried at 120°C for 10 minutes, c) dried at 150°C for 10 minutes, d) dried at 200°C for 10 minutes and e) dried at 250°C for 10 minutes.

FTIR spectroscopy was performed on freshly printed thin films that are gradually dried on a hotplate. The desired temperature was maintained for 10 minutes. As illustrated in figure 6.1, new components are formed during heating. Compared to the FTIR spectra of sample a (dried at 90°C), new vibration modes at 1650 and 1242 cm^{-1} are noticed for sample b, c and d. According to literature, the peak at 1650 cm^{-1} can be assigned to the amine bending mode of ethanolamine (1648 cm^{-1}) [7] or the vibration mode of surface trapped or adsorbed water (1658 cm^{-1}) [8]. However, the increasing intensity of this peak with increasing temperature (up till 200°C) suggests that adsorbed water can be excluded. Although ethanolamine is present in high concentration, the bending mode of this amine was not visible at low temperatures. At increased temperature other modes of the amine group (e.g. the mode at 1010 cm^{-1}) are reduced. Next to ethanolamine, the IR active modes of formic acid and zinc acetate such as the ν_a and δ (COO) of formic acid at 1585cm^{-1} and 762cm^{-1} and ν_a (COO) of zinc acetate at 1585 cm^{-1} are decreasing as a function of temperature. This can be a result of the thermal removal of the components. Concluding, the decomposition of products can take place resulting in new components or a new component might be formed during the heating of the ink while others are thermally removed.

The ongoing chemical reaction during heating was also studied by 1D proton NMR. We noticed that the contribution of solution B (the Al-source) to the

formation of the new component could be neglected. To avoid interference of non-reacting chemicals such as malonic acid, only precursor solution A (Zn precursor solution) was studied. By comparing 1D proton NMR measurements of the solution A before and after heating at 120°C for 1h (figure 6.1 and figure 6.2), an insight of the chemical reaction happening during heating can be obtained. Before heating all components as mixed in the solution are observed at the NMR spectrum, while after heating signals of 2 additional components are observed, respectively N-(2-hydroxyethyl)acetamide and N-(2-hydroxyethyl)formamide. By integration of the peaks the yield of the amide formation was calculated. Eighty-five percent of the formic acid had reacted in to the corresponding amide, while 13% of the acetic acid was converted to the corresponding amide. This result lies within the expectations. The HySS-2009 software used to calculate the formed complexes predicted that more than 70% of the Zn would form a zinc formate complex (cfr. 4.2.1), resulting in more formic acid than acetic acid that could be subjected to a nucleophilic attack by the amine group of free ethanolamine. When a metal-ion free blank was heated the formation of amides was not observed. Concluding, free acetic acid or formic acid do not react with ethanolamine to their corresponding amide but the chelating acetic acid and formic acid do. In line with the observation of Yang *et al.* [9] for oleylamine and zinc acetate, we suggest the following reaction mechanism. The amine group of the ethanolamine will attack the electron deficient carbon of the acetate or formate group which undergoes a nucleophilic addition to yield the corresponding amide.

Knowing the identity of the formed components, the peaks appearing at the FTIR spectra at 1650 cm^{-1} and 1242 cm^{-1} can now be assigned to the ν (CO) and δ (NH) of the formed amides [10].

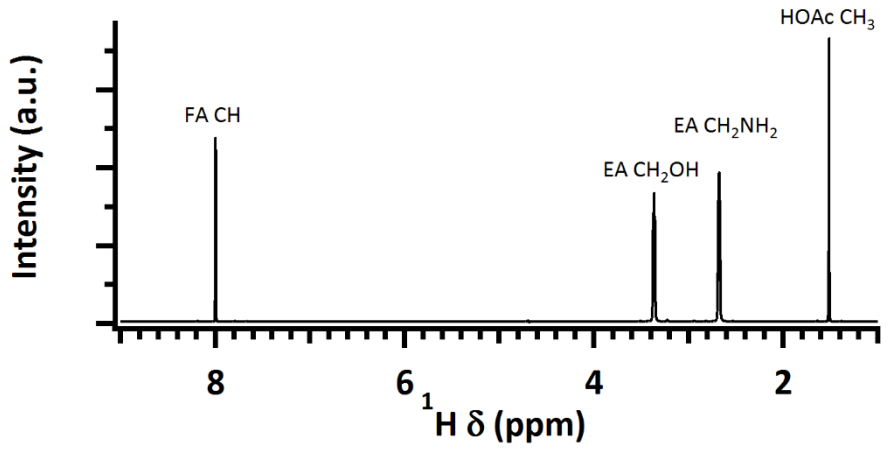

Figure 6.2 1D proton NMR spectrum of solution A before heating.

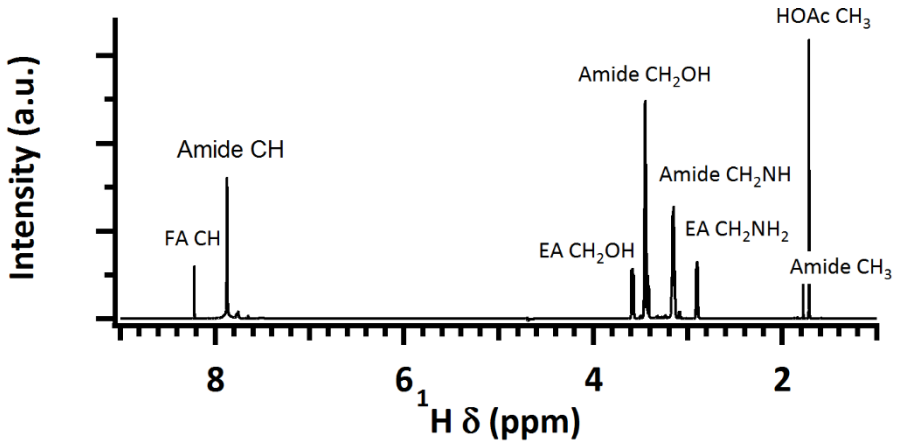

Figure 6.3 1D proton NMR spectrum of solution A after heating at 120°C for 1h.

FTIR spectroscopy learned us that most of the organics are decomposed or removed at 250°C. More detailed information about the thermal decomposition of the ink can be obtained by TGA. By drying the ink at 75°C prior to the measurement, a better resolution was obtained. The TGA of the ink shows 3 major weight losses (figure 6.4). First, a mass loss is starting around 150°C, followed by a mass loss starting around 250°C and finally a mass loss starting at 400°C. The mass loss observed before 150°C is the loss of volatile solvents such as water and non-reacting components such as formic acid, while the mass loss starting at 150°C is due to the evaporation of ethanolamine, which has a boiling point of 170°C, and the formed amides, which have boiling points around 155°C.

The mass loss around 250°C can be ascribed to the decomposition of the Zn complex. Zinc acetate and zinc formate decompose around 250°C [11, 12]. The mass loss starting at 400°C can be ascribed to the decomposition of remaining carbon compounds.

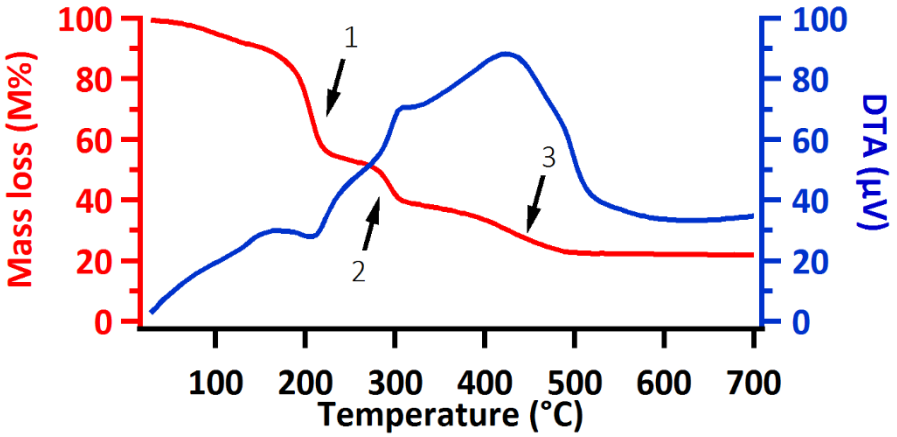

Figure 6.4 Thermogravimetric analysis of ink A3%B after drying at 75°C to evaporate most water. The sample was heated at 10°C/min with an airflow of 120 mL/min.

6.3 Optimising the thermal oxidation of AZO thin films

Based on the thermal analysis of the ink an oxidative thermal process was developed. The freshly deposited thin films were dried for 10 minutes on a preheated hotplate under static air before being transferred into a tube furnace. A constant heating rate of 10°C/min was maintained from room temperature till 250°C. After holding this temperature for 60 minutes, heating continued till 500°C at a heating rate of 10°C/min. This temperature was held for 60 minutes before cooling. A dry or wet 200 ppm O_2 in N_2 atmosphere was directed into the tube furnace with a flow rate of 200 mL/min. A wet 200 ppm O_2 in N_2 atmosphere was obtained by bubbling it through 2 glass bottles containing water before being directed into the furnace. The oxidative thermal treatment was followed by a thermal activation at 450°C during 30 minutes in a dry Ar/5% H_2 atmosphere with a flow rate of 200 mL/min.

Faster or slower heating rates resulted in more porous thin films. However, this will not be discussed in detail. The best results are obtained by heating at 10°C/min. The final temperature of the oxidative thermal treatment was experimentally optimised. Small variations were observed between 450°C and

600°C. Samples treated at 500°C ended up with better opto-electrical properties.

6.3.1 Drying of freshly deposited wet thin films

After deposition, the wet films were dried on a preheated hotplate under a static air flow. The FTIR spectra as a function of temperature show a large influence of the drying temperature on the amorphous (organic) fraction of the thin film (figure 6.1). A changing amorphous fraction can influence the crystallisation process and influence the final morphology of the thin film (cfr. chapter 3). High drying temperatures such as 300°C can induce the simultaneous evaporation and decomposition of the precursor. Medium drying temperatures between 200°C and 250°C force the volatile components (water, ethanolamine, non-reacted formic acid) out of the wet film at high rates. The films will undergo a flash evaporation. At low drying temperatures(< 200°C), the ethanolamine will not be evaporated and can react with the formed Zn complexes leading to the formation of the corresponding amides. This makes it clear that depending on the drying temperature the amorphous fraction of the thin film is changing. This will influence the structural parameters of the AZO coatings.

Influence of the drying temperature on the structural and electrical properties of AZO thin films

As illustrated in table 6.1, the drying temperature has a large influence on the resistivity of the AZO thin film. An optimal drying temperature was found at 120°C (sample b). We believe that the thin film morphology (figure 6.6) and crystal growth (figure 6.5) have a major influence on the changing electrical properties.

Depending on the drying temperature the morphology of the AZO thin film is altered from microcracking (sample a) to a more densified structure (sample b and c), to less connected 'isles' of AZO (sample d and e), to a grainy structure where the small grains are loosely stacked on each other (sample f). The thin films show a uniaxial texture along the *c*-axis for the samples dried at 90 till 250°C. Samples dried at 300°C have a polycrystalline growth. The strong preferred orientation is due to a self-ordering mechanism. As discussed in chapter 3 (ref. 3.2.1), the self-ordering mechanism is a result of the pursuit to a minimal surface energy.

Table 6.1 The resistivity of AZO thin films prepared at different drying temperature before the oxidative thermal treatment took place. All samples were thermally activated at 450°C during 30 minutes in a Ar/5% H_2 atmosphere.

Sample	Drying temperature °C	Resistivity Ω cm
a	90	5.67×10^{-1}
b	120	1.91×10^{-1}
c	150	2.44×10^{-1}
d	200	3.93×10^{-1}
e	250	4.84×10^{2}
f	300	7.74×10^{2}

Sample f (dried at 300°C) has an inferior resistivity. The morphology of this film exists out of small, loosely stacked grains which enhances grain boundary scattering. The X-ray diffractogram shows us reflections of ZnO at 31.79°, 34.36° and 36.20° (JCPDS 89-7102) and most likely Al_2O_3 at 38.10° (JCPDS 85-1337). The polycrystalline nature of the AZO film will increase the number of defects and stacking faults at the grain boundaries [13]. The reflection of Al_2O_3 even indicates that the doping of the ZnO matrix isn't successful and a secondary phase is formed. Segregation of this secondary phase at the grain boundaries will occur and this will hamper the mobility of the charge carriers [14]. It also indicates that the amount of charge carriers is reduced due to the negligible substitutional doping of Al. All this is a consequence of the high drying temperature. The evaporation of the solvents and additives and the decomposition of the complexes will occur simultaneously. This may result in many ZnO nucleation sites and a final morphology with small grains. The high drying temperature also favours the formation of Al_2O_3 instead of the substitution in the ZnO matrix. The evaporation and decomposition of the precursors at the same time can induce different reaction paths which in this case introduces Al_2O_3 nuclei.

The morphology of samples e (dried at 250°C) and d (dried at 200°C) did not differ a lot. However, the resistivity of sample d is a factor 1000 smaller than the one of sample e. Mainly, this can be attributed to the weak crystallinity of

sample e. Similar to sample f, a small fraction of the dopant may have formed a secondary phase due to the high drying temperature. However, XRD measurements couldn't confirm the presence of the secondary phase (Al_2O_3) due to the low concentration.

Sample a (dried at 90°C) has a resistivity that is 3 times as high as sample b (dried at 120°C). The morphology of sample a shows microcracks which limit the conduction pathways of the free charge carriers as air is a good insulator. The drying step may induce these microcracks. Samples dried at 90°C have a large fraction of the non-chelating additives (formic acid and ethanolamine) still present inside the thin film as confirmed by the FTIR measurements (figure 6.5). During the thermal treatment in the tube furnace the remaining additives will be removed too fast, resulting in strain and stress which later on can be released through crack formation. However, drying at higher temperatures (120°C – 150°C) prevented this. At these temperatures ethanolamine will already be partially removed and crack formation will be avoided.

Sample c (dried at 150°C) had electrical properties close to those of sample b. Similar morphologies and preferential growth of the crystals (high intensity of the (002)-reflection) were obtained. Nevertheless, sample b showed areas which are more densified, resulting in better electrical properties.

Summarising, the drying temperature clearly influenced the morphology, crystal growth and electrical properties of these AZO thin films as the amorphous fraction of the thin film is changing with the drying temperature. High drying temperatures (300°C) resulted in a flash evaporation of the unreacted components together with the decomposition of the formed complexes. This led to the formation of unwanted secondary phases (Al_2O_3), while drying at lower temperatures (200 – 250°C) only resulted in the flash evaporation of the unreacted components. Drying at 90°C led to the formation of microcracks and an optimum was found when the samples were dried at 120°C.

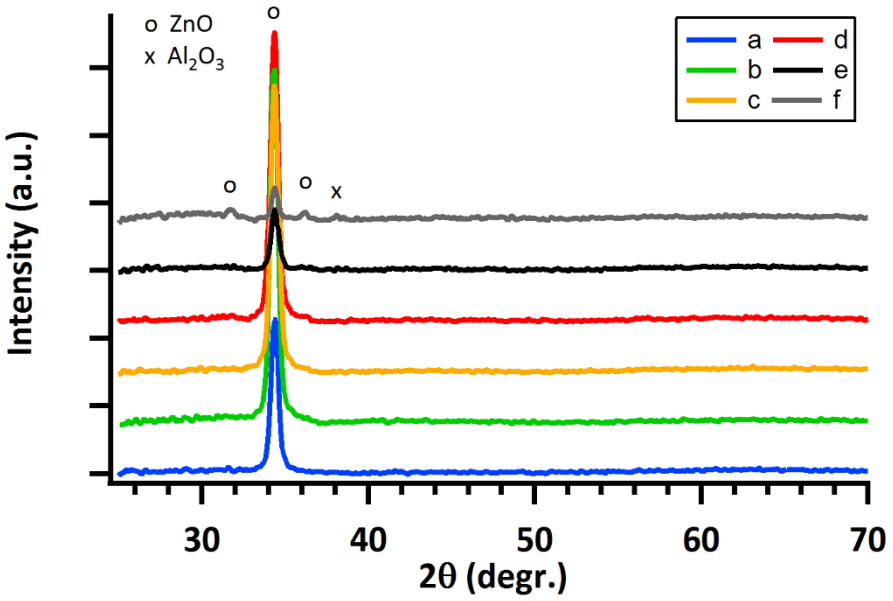

Figure 6.5 XRD measurements as a function of the drying temperature: a) dried at 90°C, b) dried at 120°C, c) dried at 150°C, d) dried at 200°C, e) dried at 250°C and f) dried at 300°C. Each sample was dried for 10 minutes on a hotplate set on the desired temperature.

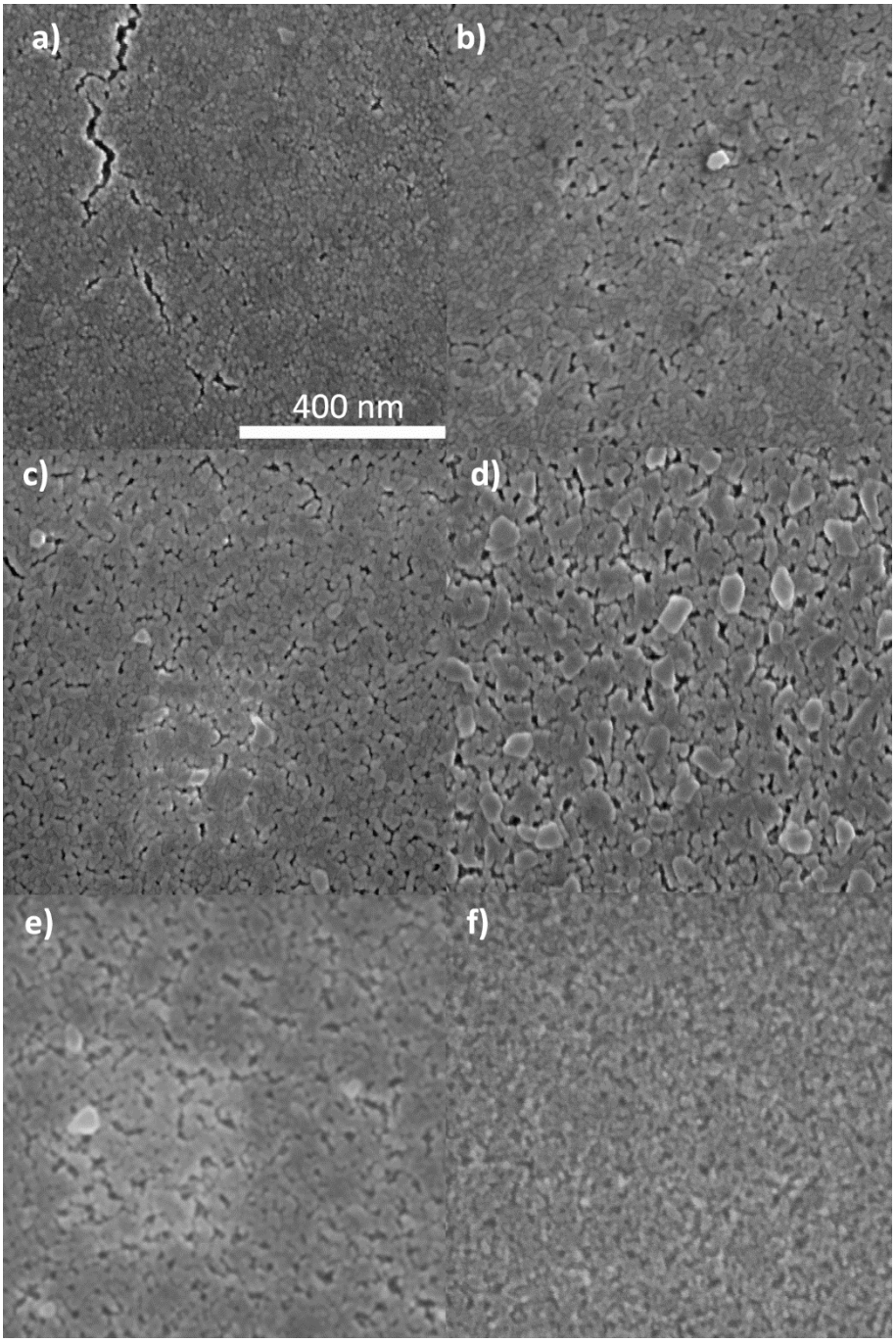

Figure 6.6 SEM images of AZO thin films dried on different temperatures: a) dried at 90°C for 10 minutes, b) dried at 120°C for 10 minutes, c) dried at 150°C for 10 minutes, d) samples dried at 200°C for 10 minutes, e) dried at 250°C for 10 minutes and f) dried at 300°C for 10 minutes.

6.3.2 Wet versus dry processing of AZO thin films

The humidity of the processing atmosphere of metal oxide thin films has been a topic of many research projects. The morphology [15-17], preferred orientation of the crystal growth [18], reaction routes [19-21] and number of trapped states [22] may alter by varying the humidity of the processing atmosphere. The influence of the humidity on the processing atmosphere is too large to ignore. Therefore, the humidity of the processing atmosphere was investigated. All the samples were dried after deposition on a preheated hotplate at 120°C during 10 minutes. The humidity of the processing atmosphere was controlled by bubbling the gas through 2 glass bottles filled with water which were placed in a temperature controlled water bath. By controlling the water temperature, the amount of water vapour carried with atmosphere was controlled. The experiments were performed in a tube furnace as described earlier. However, a varying humidity of the atmosphere was tested by using dry atmosphere or bubbling the atmosphere through glass bottles containing water at 10°C, 20°C and 30°C.

Because both types of ink (A3%B10 and A3%D10) reacted differently on the humidity of the used processing atmosphere, they are discussed separately. Ink A3%D is containing citric acid as stabiliser for the Al^{3+} ions , while ink A3%B is containing malonic acid to stabilise the Al^{3+} ions.

Influence of wet atmosphere on AZO coatings obtained via Ink A3%B10

The varying water vapour partial pressure in the annealing atmosphere has an effect on the electrical properties. A minimal resistivity is obtained with a water vapour enriched atmosphere at 20°C (table 6.2). All this may be a result of the changing structural properties of the AZO thin films or compositional changes in the crystal structure.

Table 6.2 The resistivity as a function of the gas atmosphere bubbled through water at different temperatures.

Sample	Water temperature °C	Resistivity Ω cm	Carrier density cm^{-3}	Mobility $cm^2 V^{-1} s^{-1}$
a	dry	1.91×10^{-1}	6.51×10^{18}	4.98
b	10	9.61×10^{-2}	/	/
c	20	2.54×10^{-2}	2.23×10^{19}	11.00
d	30	2.64×10^{-1}	/	/

Changing structural properties of AZO thin films by wet processing

As illustrated in figure 6.7, the top morphology changed with varying water vapour enriched atmospheres. Generally, larger grains are observed. This is in line with the observation of Nakada *et al*. [15] where grain growth is induced by water vapour, although a densification of the morphology is not observed as suggested by Hung *et al*. [16]. However, the opposite behaviour is observed for the atmosphere bubbled through water at 30°C (sample d). Compared to a dry annealed layer (sample a), a more porous/less connected morphology was observed, while sample c has large grains and a denser structure.

A look at the diffractograms of these thin films (figure 6.8) taught us that the intensity of the (002)-reflection is positively influenced by the water vapour in the processing atmosphere, except for the sample prepared with a gas atmosphere bubbled through water at 30°C (sample d). The XRD spectrum of sample d even shows (100), and (101)-reflections (31.79° and 36.20° (JCPDS 89-7102)), however small (100) and (101)-reflections in the XRD spectrum of sample c are also noticed. It is believed that a more intense preferential growth along the *c*-axis will reduce the number of defects and stacking faults at the grain boundaries which is reducing grain boundary scattering. This will result in a higher conductivity of the AZO thin film due to a reduced mobility. Comparing sample a (dry processed) with sample c, a higher mobility of the charge carriers is obtained with a more prominent growth along the *c*-axis (table 6.2).

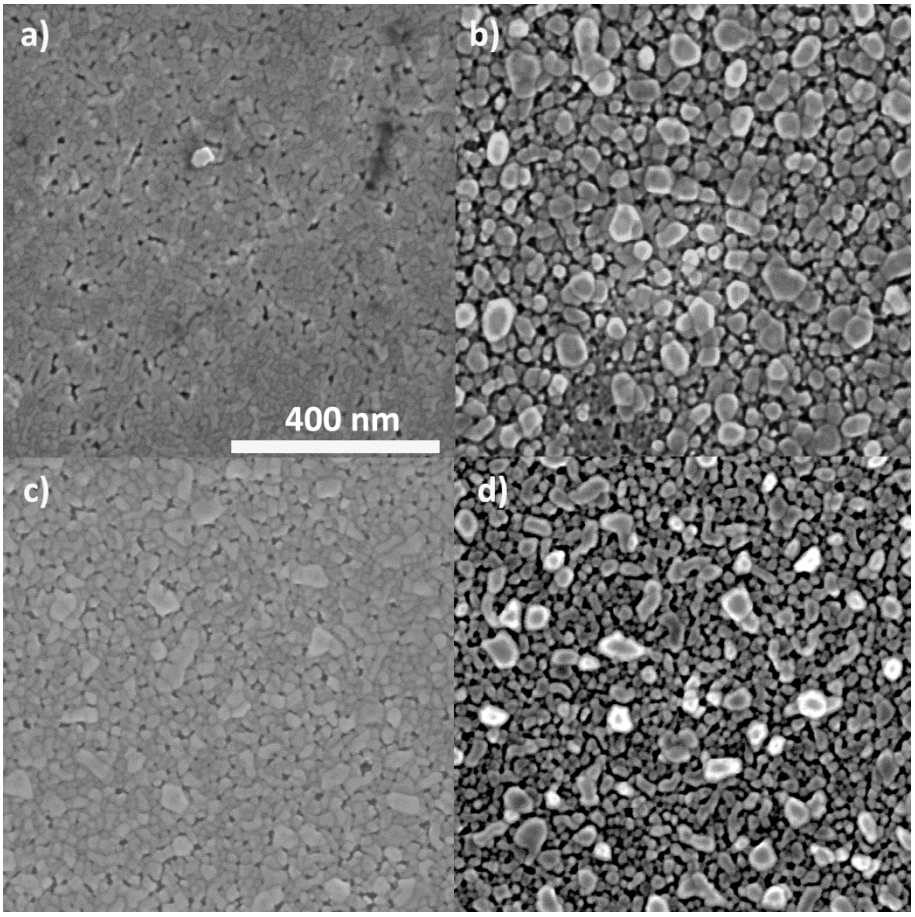

Figure 6.7 SEM images of AZO thin films oxidative treated with the gas atmosphere bubbled through water at different temperatures: a) dry, b) water at 10°C, c) water at 20°C and d) water at 30°C.

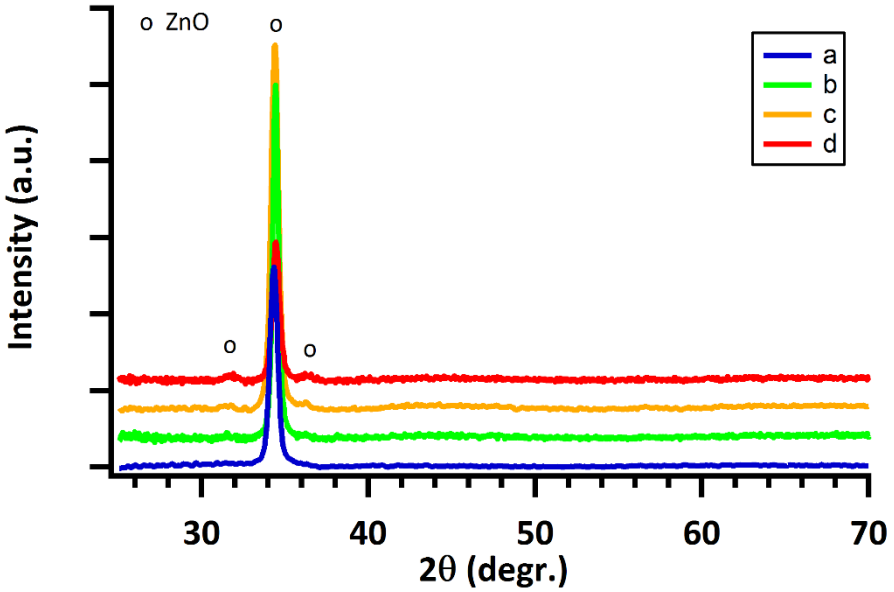

Figure 6.8 XRD measurements of AZO thin films undergoing a thermal oxidation with a gas atmosphere bubbled through water at different temperatures: a) dry, b) water at 10°C, c) water at 20°C and d) water at 30°C.

Altogether, samples prepared with 200 ppm O_2 in N_2 bubbled through water at 20°C are showing the best electrical properties, coupled with a more or less dense top morphology and a high intensity of the (002)-reflection. Nevertheless, the polycrystalline nature was visible due to small reflections located at the 31.79° and 36.20°).

Compositional changes in the crystal structure due to wet processing

To study the influence of the dry and wet thermal process on Al incorporation in the ZnO matrix, AZO powders were synthesised in dry or wet air at 500°C and analysed by solid state Al NMR (figure 6.9). The wet processed AZO powders were synthesised by bubbling air through 2 glass bottles at 20°C. The deconvolution of the spectra led to the following results: the wet processed AZO powders contain more tetrahedrally coordinated Al (38.44 versus 26.2%), more pentahedrally coordinated Al (38.66 versus 20.50%) and more substitutional Al (9.00 versus 6.60%), while containing less octahedrally coordinated Al (22.40 versus 53.30%). So, more charge carriers can be generated as more Al is incorporated in the crystal lattice of ZnO and less electron acceptor sites are generated because Al occupies less octahedral sites. Hall measurements of

sample a and c confirmed the presence of more charge carriers, respectively 6.5 x 10^{18} and 2.2 x 10^{19} cm^{-3} for sample a and c.

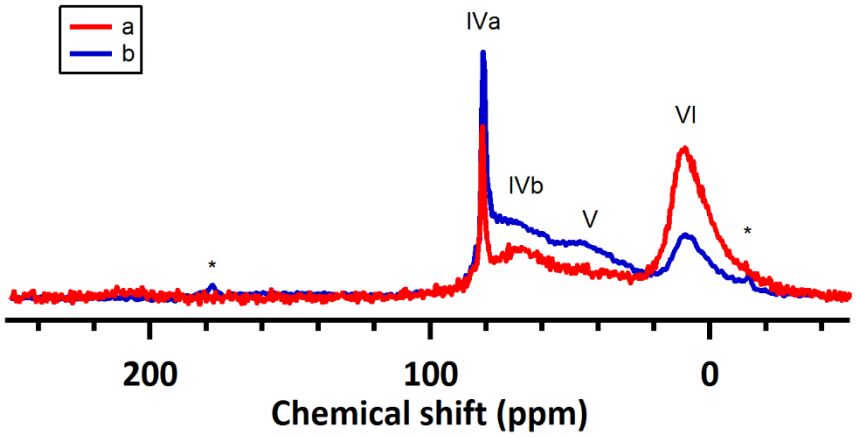

Figure 6.9 1D ^{27}Al MAS NMR spectra of bulk samples obtained by heating ink A3%B in a) dry air and b) wet air at 500°C for 1h, where * marks spinning sidebands.

Not only the preferred growth of the crystals, morphology and the incorporation of the Al in the ZnO matrix changed by switching from dry to wet processing atmosphere. Also, the electrical properties are positively influenced, when the atmosphere is bubbled through 2 glass bottles containing water at 20°C. Everything is insinuating that the humidity of the processing atmosphere affects the formation of Al doped ZnO. A change in humidity can influence hydrolysis and condensation reactions going on during the thermal process [23]. Also, the absorption and easier breakup of water vapour at the surface of the thin film can accelerate the kinetics of the oxidation [24]. This can induce another reaction route or faster decomposition of the precursor leading to a thin film with improved properties. But introduction of too much water vapour in the processing atmosphere can enhance the hydrolysis and condensation reactions and/or the kinetics of the oxidation even more. This can lead to an uncontrolled reaction route resulting in AZO coatings with poorer properties, e.g. sample d.

Influence of wet atmosphere on AZO coatings obtained via ink A3%D10

The water vapour partial pressure of the processing atmosphere has a completely different effect on the final properties of the AZO thin films prepared with ink A3%D10. Here, a minimal resistivity is obtained with a dry processing atmosphere (table 6.3). Not only the electrical properties are affected by changing the water vapour partial pressure of the processing atmosphere. Also the morphology (figure 6.11) and crystal growth (figure 6.10) altered.

Table 6.3 The resistivity as a function of the gas atmosphere bubbled through water at different temperatures.

Sample	Water temperature °C	Resistivity Ω cm	Carrier density cm^{-3}	Mobility $cm^2 V^{-1} s^{-1}$
a	dry	2.42×10^{-2}	2.31×10^{19}	11.23
b	10	1.51×10^{-1}	/	/
c	20	1.23×10^{0}	1.70×10^{18}	3.00
d	30	3.51×10^{0}	/	/

The higher the water vapour partial pressure, the more preferential growth of the *c*-axis is obtained. Dry processed samples (sample a) show the polycrystalline nature of the AZO film by clear reflections at 31.78°, 34.44° and 36.16°, respectively (100), (002) and (101)-reflections. Wet processed samples (sample b, c and d) have a more intense (002)-reflection with increasing water temperature while the other reflections can be neglected.

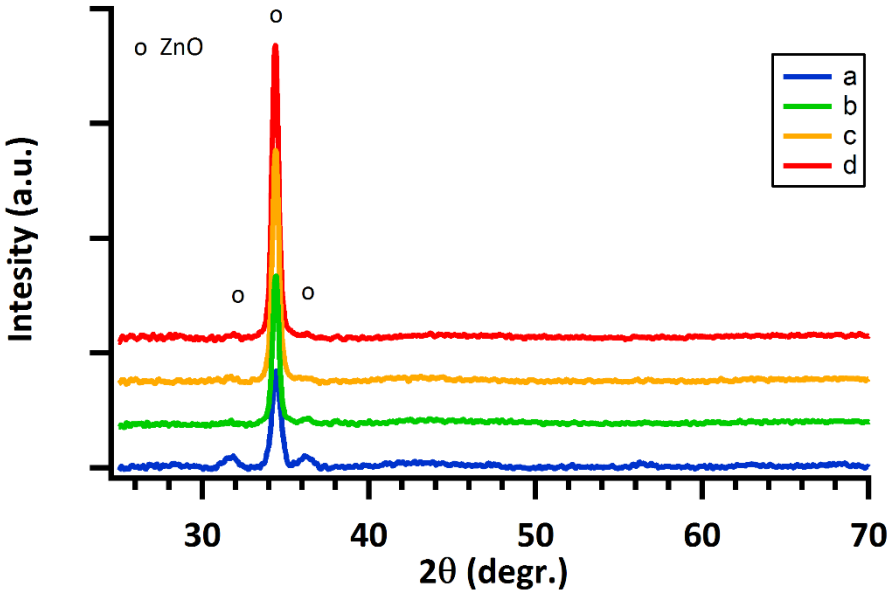

Figure 6.10 XRD measurements of AZO thin films undergoing a thermal oxidation with a gas atmosphere bubbled through water at different temperatures: a) dry, b) water at 10°C, c) water at 20°C and d) water at 30°C.

Not only a change in crystal growth is noticed, the morphology of the AZO thin films is affected as well. The dry processed AZO thin film (sample a) has a dense top morphology with fine grains, while the wet processed samples have in general larger grains. Sample b has a morphology in-between sample a and sample c. Some parts of the sample still contain the morphology of sample a, while other parts show the same morphology of sample c. This suggest that the amount of water in the atmosphere was not high enough to influence the morphology completely. This also indicates that water is reacting at the top of the film. A higher water vapour partial pressure led to a completely homogenous surface morphology, as sample d shows the more densified top morphology.

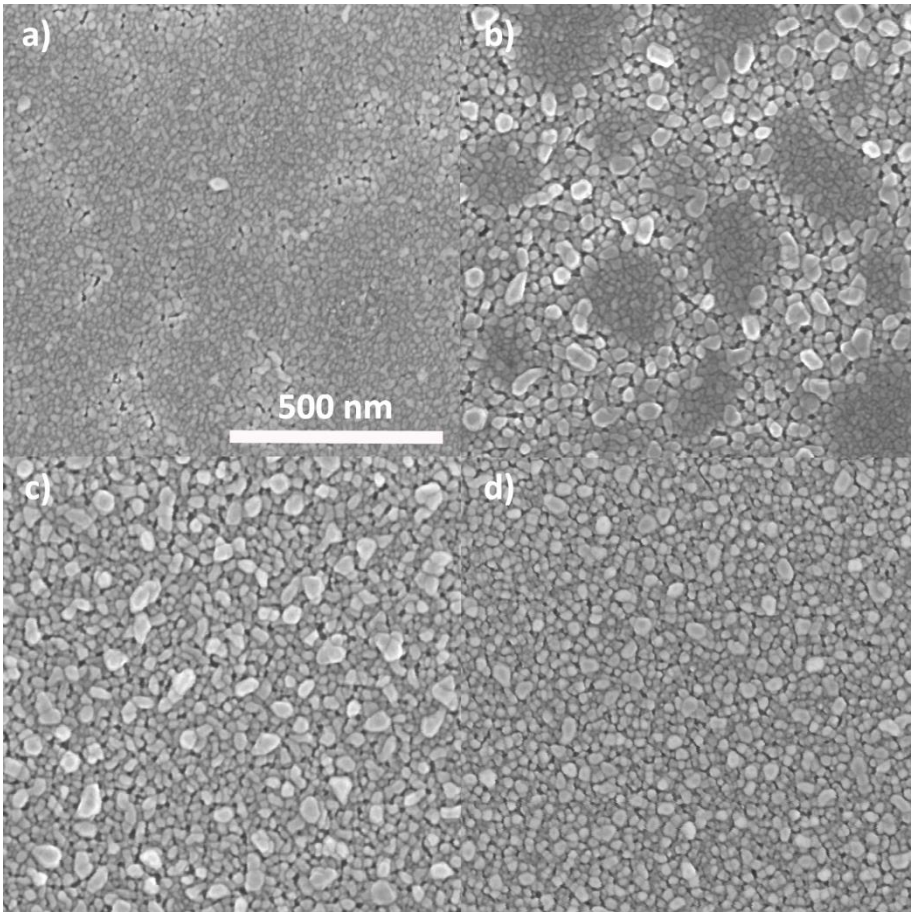

Figure 6.11 SEM images of AZO thin films oxidative treated with the gas atmosphere bubbled through water at different temperatures: a) dry, b) water at 10°C, c) water at 20°C and d) water at 30°C.

Based on the XRD data and the morphology, one would suggest that sample d should have the lowest resistivity. A more prominent preferential growth along the *c*-axis and a dense top morphology is observed. Nevertheless, the dry processed sample has the lowest resistivity. This can only mean that the water vapour partial pressure of the processing atmosphere has a big influence on the number of free charge carriers generated by doping with Al. Most likely wet processing of the ink will result in more octahedrally coordinated and less substitutional Al. This can be confirmed by comparing the carrier density of a dry and wet processed sample. The dry processed sample (sample a) has a higher carrier density, respectively 2.31 x 10^{19} for sample a and 1.70 x 10^{18} for sample c.

Finally, wet processing positively affected the electrical properties of the AZO thin films synthesised by ink A3%B10, containing aluminium malonate complexes. A negative influence was noticed for ink A3%D10 containing aluminium citrate complexes. As suggested, the use of water vapour can affect the reaction route and kinetics which leads to optimum reaction conditions. These conditions will differ for each precursor solution. Therefore, it is important to create a better understanding of the effect of water vapour in the processing atmosphere for each precursor.

6.4 Thermal activation of AZO thin films

The oxidative removal of the organics, the oxide formation and crystallisation are part of a consecutive process before the thermal activation. Nevertheless, a proper thermal activation of the AZO layers is needed to study the parameter variation of the oxidative thermal process and ink. A thermal activation enhances the electrical properties of the AZO coatings. The thin films can be heated in inert or reducing atmospheres in order to create more charge carriers. Thermal treatments in vacuum [25, 26], N_2 [27] and forming gas (5% H_2 in N_2 or Ar) [28-31] are frequently applied to activate the AZO thin films. The activation by annealing in forming gas is an attractive, efficient and cost-effective method. The thermal activation in vacuum isn't preferred because this thesis wants to suggest an atmospheric deposition technique as alternative for the many vacuum deposition techniques of AZO. The N_2 annealing is more intensive as higher temperatures and longer reaction times are required to obtain similar results. The activation in forming gas is more attractive due to the reduced temperatures and reaction times.

According to Chang *et al*. [32] and Oh *et al*. [33] the thermal activation of the AZO thin films is nothing more than the removal of adsorbed oxygen at the grain boundaries and surface. Oxygen can adsorb at high temperatures during the oxidative thermal treatment as illustrated by eq. 6.1 [34, 35].

$$O_{2\,(g)} + 2\,e^- \rightarrow 2\,O^-_{(ads)} \qquad \text{Eq.6.1}$$

The presence of these species increases the number of trapping states at the grain boundaries and the surface. These trapping states can trap the free carriers from the bulk and reduce the overall electrical conductivity. Near the grain boundaries band bending will occur and a depletion region will be formed.

This region can be visualised as two back-to-back Schottky barriers, where the potential barriers created by the charged states inhibit the passage of free carriers to a neighbouring grain [32, 33].

However, the electrical properties are not only enhanced by the removal of the adsorbed oxygen species. The annealing in forming gas improves the Al substitution [4, 36] and the formation of more oxygen vacancies [32] (eq. 6.2).

$$Al_2O_3 \xrightarrow{ZnO} 2\,Al_{zn}^{\circ} + 2\,O_{(o)} + \frac{1}{2}O_{2\,(g)} + 2\,e^- \qquad \text{Eq.6.2}$$

Also, the thermal activation of the AZO thin film in H_2-rich environment can lead to the incorporation of hydrogen as electron donor. During the removal of the adsorbed oxygen, hydrogen can be incorporated in the ZnO as suggested by eq. 6.2 [4].

$$ZnO_{(1+x)} + \left(x + \frac{y}{2}\right)H_2 \rightarrow H_yZnO + x\,H_2O \text{ with } (y)\,e_{cb}^- \qquad \text{Eq.6.2}$$

Summarising, the thermal activation enhances the electrical conductivity of AZO coatings by multiple contributions: (1) The adsorbed oxygen at the grain boundaries, which could trap free carriers, is desorbed. (2) The Al substitution in the ZnO matrix is improved, leading to more charge carriers. (3) The use of a hydrogen atmosphere can lead to additional shallow donors, namely hydrogen. (4) More oxygen vacancies are formed, which also have a positive influence on the electrical properties, cfr. 2.3.1.

Nevertheless, a thermal treatment in Ar/5% H_2 at too high temperatures will completely remove the film by hydrogen etching. For example, when a synthesised AZO thin film was thermally activated at 600°C during 30 minutes in an Ar/5% H_2 atmosphere the AZO thin film was completely removed. EDS (Energy Dispersive X-ray Spectroscopy) measurements before and after the thermal activation at 600°C illustrate the removal of the AZO layer (figure 6.12). Before the thermal activation in forming gas the K_α line of Zn around 8.6 keV was visible. Afterwards, the signal of the K_α line was not detected, implying a solid-gas reaction between ZnO and H_2 took place [37] (eq. 6.4) which had removed the AZO layer.

$$ZnO_{(s)} + H_{2\,(g)} \rightarrow Zn_{(g)} + H_2O_{(g)} \qquad \text{Eq.6.4}$$

Lew *et al*. [38] discussed the kinetics of the ZnO reduction by heating in a H_2-rich atmosphere. Reduction rates of 10^{-9} mol cm^{-2} s^{-1} at 600°C are obtained when the samples are heated in a 10% H_2 in N_2 atmosphere. At these reduction rates it would only take 10 minutes to remove a 80 nm thick ZnO layer.

Concluding, optimising the thermal activation in H_2-rich atmosphere is balancing between the enhancement of the electrical properties and avoiding the reduction of ZnO.

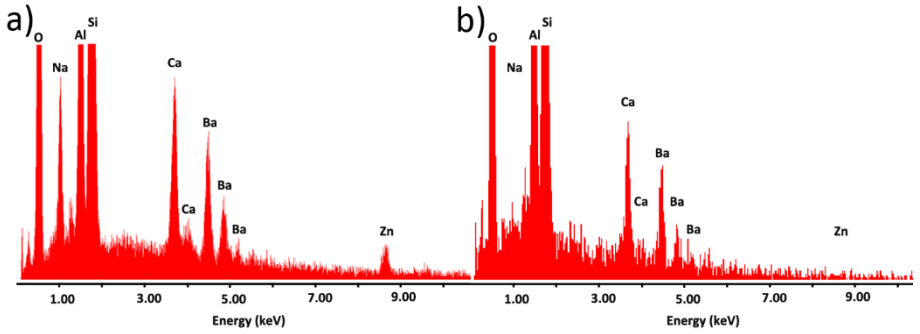

Figure 6.12 Energy dispersive X-ray spectroscopy measurement of a) an AZO thin film before the thermal activation at 600°C and b) an AZO thin film after the thermal activation at 600°C.

6.4.1 Influence of the thermal activation on the electrical and structural properties of AZO thin films

To study the effect of thermal activation on the synthesised AZO thin films the oxidative thermal treatment and selected ink were unvaried. The experiments were performed with ink A3%B10. The zinc precursor solution (solution A) was combined with the $Al(NO_3)_3$-malonic acid precursor solution (solution B) and 10 v% of ethanol was added to improve the jetting and wetting quality of the ink. After deposition of the wet film, the samples were dried for 10 minutes at 120°C and inserted in a preheated tube furnace at 500°C. The samples were treated during 1h at 500°C before the furnace was cooled to room temperature. A 200 mL/min gas flow of 200 ppm O_2 in N_2 atmosphere was bubbled through 2 glass bottles containing water at 20°C before being directed into the furnace. The oxidative treatment was followed by the thermal activation of the samples. The tube furnace was evacuated and filled with Ar/5% H_2. This process was repeated 3 times before the tube furnace was heated at 10°C/min to the setpoint. The setpoint was held for 30 minutes before cooling. A dry Ar/5% H_2 atmosphere

was directed in the tube furnace with a flow of 200 mL/min. The samples were cooled to room temperature under an Ar/5% H_2 atmosphere.

Table 6.4 illustrates that the electrical properties of the AZO thin films are affected by the temperature at which the thermal activation took place. Comparing samples before and after the thermal activation, the sheet resistance decreased dramatically. However, a more intensive thermal treatment (550°C) produced samples with a too high sheet resistance that falls out of measuring range of the four point probe resistivity analyser. An optimum is observed for the thermal activation at 450°C.

Table 6.4 The sheet resistance as a function of the thermal activation. The samples were treated at 400°C, 450°, 500°C and 550°C for 30 minutes in Ar/5% H_2

Sample	Thermal activation (°C)	Sheet resistance (Ohm/square)
a	No thermal activation	2×10^6
b	400	9.54×10^3
c	450	7.54×10^3
d	500	8.37×10^4
e	550	/

The morphology of the AZO thin films changed as a function of the thermal activation (figure 6.13). Before the thermal treatment in Ar/5% H_2, the AZO thin film has a dense surface morphology. The thermal activation resulted in etching of the AZO thin films. At increasing temperatures the H_2-etching is getting more and more visible. The thermal activation at 400 and 450°C resulted in thin films with marks of the H_2-etching. The H_2-etching completely destroyed the surface morphology at 500 and 550°C. The grains are getting smaller due to the etching. The hydrogen reacts with the AZO resulting in metallic zinc and water vapour (eq. 6.2). The metallic zinc evaporates and the AZO grains are etched away till nothing is left. Although sample b and c did not suffer enormously from the hydrogen etching, the morphology changed. Grains are less connected and some small grains are etched away. Sample b has more or less the same morphology as sample a which is not thermally activated, while sample c shows

larger grains compared to sample a and b. Grain growth by an additional annealing in hydrogen is also observed by Ghosh *et al*. [39] and Choi *et al*. [40]. It is believed that the decrease of defects at the grain boundaries (desorption of oxygen) results in grain growth or grain agglomeration. Baik *et al*. [41] noticed that grain growth is enhanced by etching the smaller grains between large grains. This is also observed for sample c. Smaller grains are etched away, while the initially larger grains are growing.

A preferential growth of the *c*-axis is observed by X-ray diffraction measurements (figure 6.14). The intensity of this reflection is reduced after the thermal activation. The reflections of sample e have low intensity, mainly due to the hydrogen etching. The reduced intensities of the (002)-reflection of samples b, c and d can be explained by multiple events: (1) The improved Al^{3+} substitution in the ZnO matrix leads to a higher effective dopant concentration. The introduction of Al as dopant can induce stresses due to the large difference in ionic size of both, respectively 0.074 nm for Zn^{2+} and 0.054 nm for Al^{3+}. Higher dopant concentration can deteriorate the crystallinity of these thin films [42]. (2) Hydrogen removes the adsorbed oxygen, altering the morphology in a different way because smaller grains are etched away.

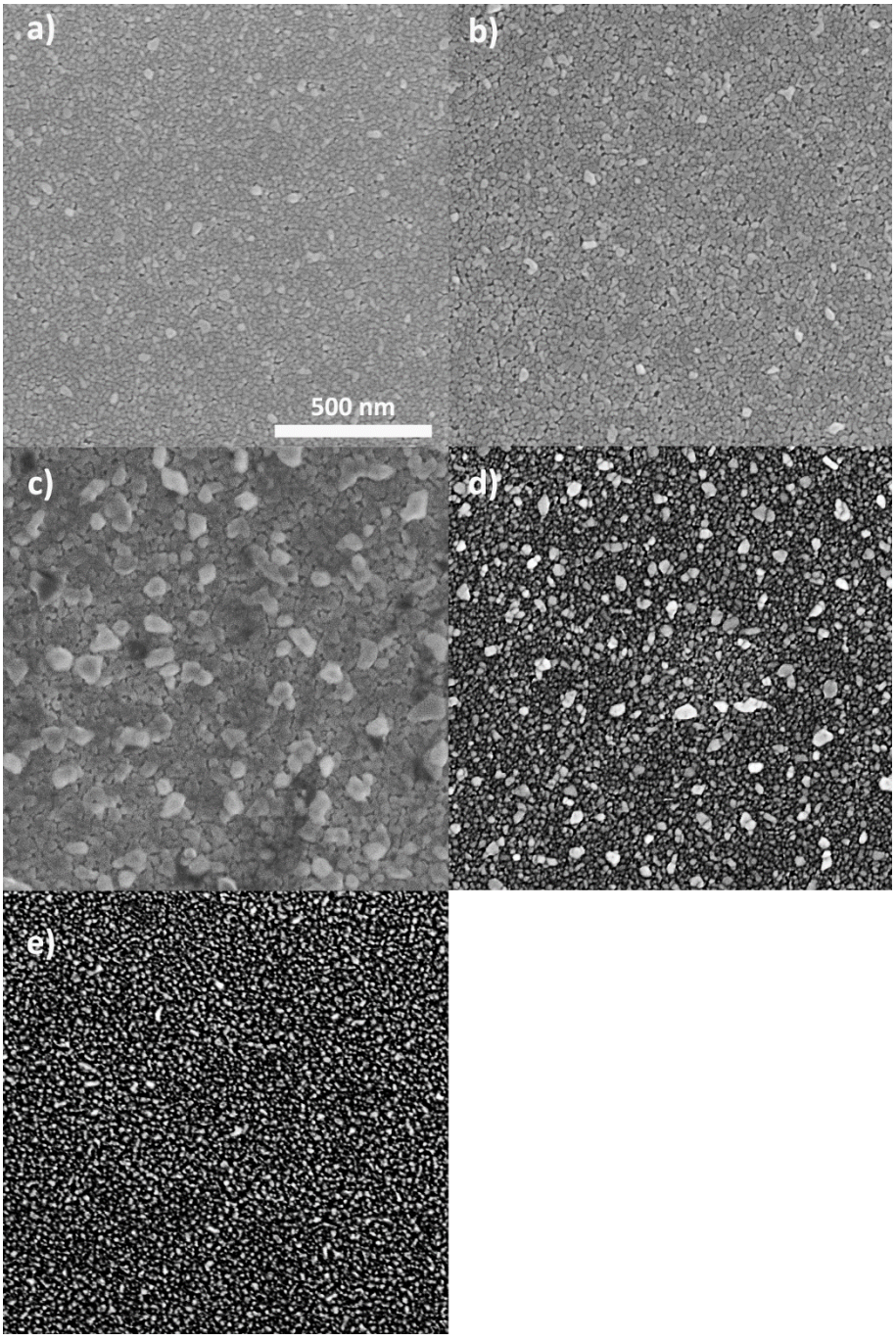

Figure 6.13 SEM images of samples prepared with ink A3%B10. All had a different thermal activation treatment in Ar/5% H_2: a) didn't undergo a thermal activation, b) treated for 30 minutes at 400°C, c) treated for 30 minutes at 450°C, d) treated for 30 minutes at 500°C and e) treated at 550°C for 30 minutes.

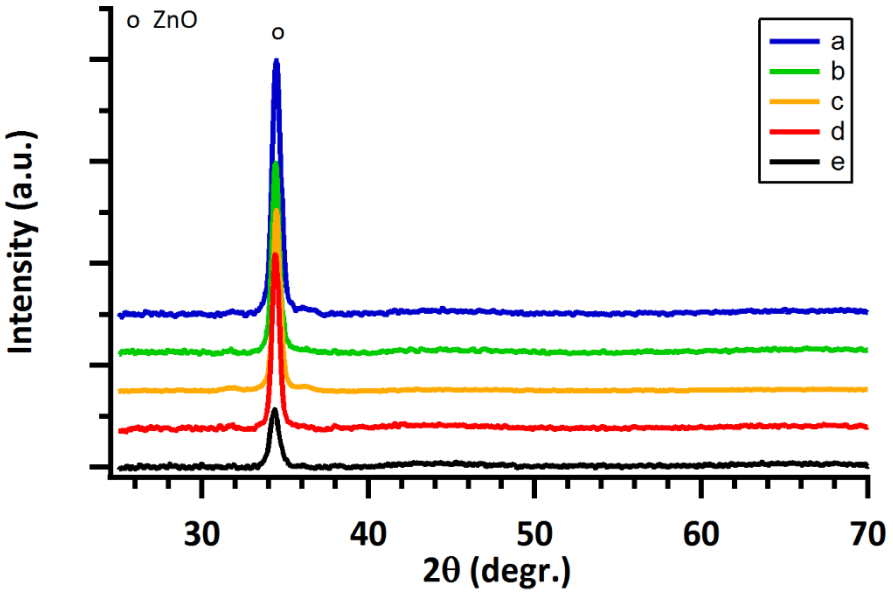

Figure 6.14 XRD measurements of samples prepared with ink A3%B10. All had a different thermal activation treatment in Ar/5% H_2: a) didn't undergo a thermal activation, b) treated for 30minutes at 400°C, c) treated for 30 minutes at 450°C, d) treated for 30 minutes at 500°C and e) treated at 550°C for 30 minutes.

6.4.2 Compositional changes due to the thermal activation of AZO

The thermal activation will not only change the structural properties, also compositional changes may occur. The influence of the thermal activation on the composition of AZO was studied by analysing AZO powders samples with the help of X-ray Photoelectron Spectroscopy (XPS) and ^{27}Al MAS NMR. Prior to the thermal activation at 450°C during 30 minutes, the precursor solution A3%B10 was thermally oxidised at 500°C during 1h.

To exclude the contribution of metallic Zn to the conduction of thermally activated AZO, XPS data are collected (figure 6.15 and figure 6.16). The Zn $2p_{3/2}$ is selected to detect metallic Zn since this peak is strong and narrow enough to detect any asymmetry [43]. Sample a, AZO powder before thermal activation, shows a good fit with a Gaussian/Lorentzian distribution. The maximum of the fit is obtained at 1021.7 eV. Sample b, AZO powder that is thermally activated, shows an asymmetric peak shape. Fitting 2 distributions resulted in a fit, with maxima at 1021.5 and 1023.4 eV. The signal positioned at around 1021.7 eV is assigned to ZnO while the signal at 1023.4 eV can most likely be assigned to

$Zn(OH)_2$ [44]. However, Chen *et al*. [45] observed an asymmetric behaviour of the Zn $2p_{3/2}$ line for oxygen deficient ZnO. The information of the Zn LMM auger lines can help to distinguish deferent Zn species. The shape of the Zn LMM Auger lines with a maximum at 989.8 eV points towards the presence of one Zn component. Also, FTIR spectra do not indicate any sign of hydroxide groups, suggesting the signal at 1023.4 eV could be due to contamination of the sample or a result of oxygen deficient ZnO. The position of Zn LMM Auger lines combined with position of the Zn $2p_{3/2}$ lines indicate a prominent Zn^{2+} state according to the Wagner plot [46]. No asymmetry due to the presence of metallic Zn could be detected, indicating that Zn isn't present in the AZO powders after the thermal activation.

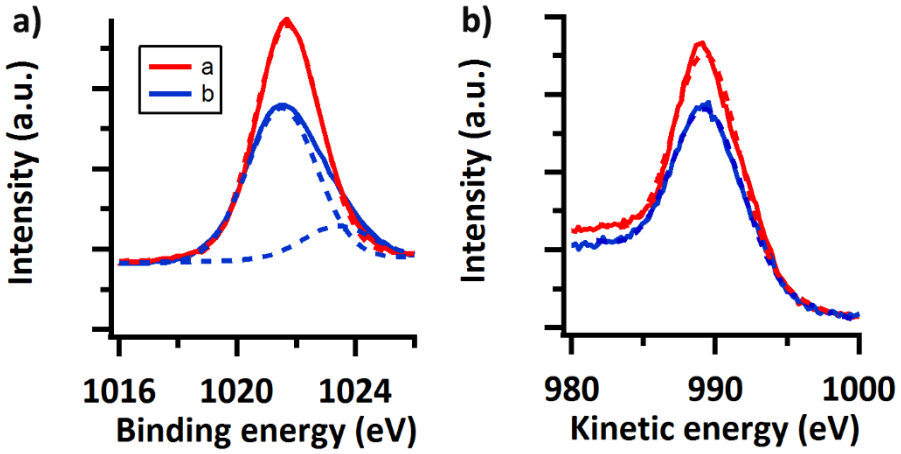

Figure 6.15 XPS analysis of AZO powders before (sample a, red line) and after (sample b, blue line) thermal activation of the samples. Figure a shows the binding energies of Zn $2p_{3/2}$ core levels, where the dashed lines represent Gaussian/Lorentzian fitted components. Figure b shows the Zn LMM Auger spectrum, where the dashed lines represent Gaussian/Lorentzian fits.

The O 1s spectra for both samples consist out of 2 features as shown in figure 6.16. The fit centred at 530 eV is due to the appearance of O^{2-} ions in ZnO, while at 531.4 eV O^{2-} ions with oxygen vacancies as neighbour are detected. No adsorbed oxygen molecules or water could be found at 532.4 eV, indicating a minimal amount of adsorbed oxygen at the AZO grain boundaries [47]. Thermally activating AZO powders resulted in a relative more intense signal at 531.4 eV, meaning that relatively more O^{2-} ions are nearby oxygen vacancies. This is indirectly indicating a higher amount of oxygen vacancies present after the thermal activation, which is confirming the hypothesis that more oxygen

vacancies are formed during the thermal activation. A large amount of oxygen vacancies can lead to oxygen deficient ZnO which can explain the asymmetric behaviour of the Zn $2p_{3/2}$ signal.

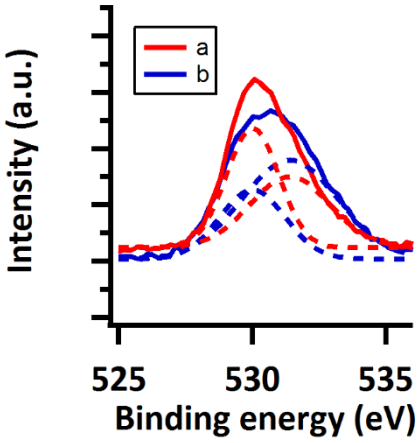

Figure 6.16 XPS analysis of AZO before (sample a, red line) and after (sample b, blue line) thermal activation. The figure shows the binding energies of O 1s.

The 1D ^{27}Al MAS NMR spectra reveals the effect of the thermal activation on the incorporation of Al in the ZnO matrix (figure 6.17). Comparing AZO powders before and after the thermal activation showed us that more pentahedrally (38.71 versus 20.5%) and tetrahedrally coordinated Al (45.82 versus 26.20%) is present, while less substitutional (3.98 versus 6.60%) and octahedrally coordinated Al (15.47 versus 53.3%) is present. The higher content of tetrahedrally coordinated Al as a result of the thermal activation can lead to a more substitutional Al. However, the deconvolution of the spectrum doesn't confirm a more intense signal at 81 ppm. The incorporated Al can become metallic due to the thermal activation [48, 49]. The corresponding Knight shift is slightly visible in the spectrum after thermal activation. This is a shift in NMR frequency due to metallic environment around the atom of interest[50]. Also, as more oxygen vacancies are present, the distortion of the tetrahedral coordination can take place, leading to an increased signal around 67 and 42 ppm. This all makes it hard to confirm the improved incorporation of the Al in the ZnO matrix. Nevertheless, it cannot be excluded as well. The higher content of pentahedrally coordinated Al can also be a result of the larger number of oxygen vacancies present in the powder which explains the decreasing number of octahedrally coordinated Al.

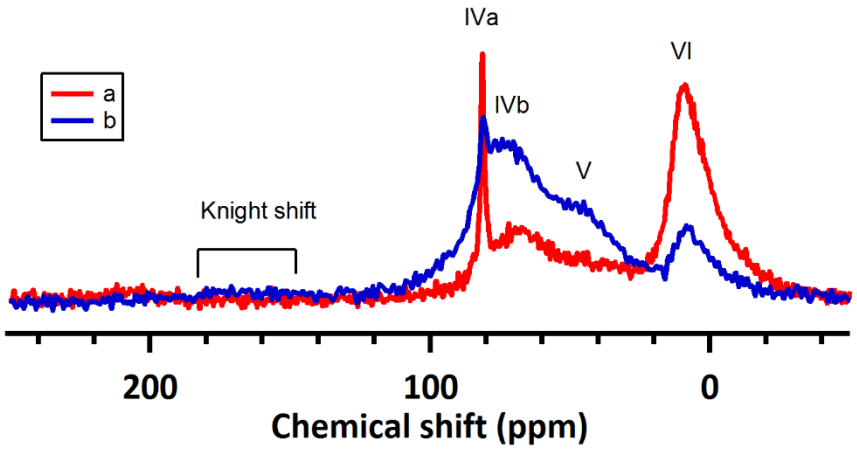

Figure 6.17 1D ^{27}Al MAS NMR spectra of bulk samples obtained by a thermal treatment of a) solution A3%B before the thermal activation and b) solution A3%B after thermal activation.

Summarising, a thermal activation helps to improve the electrical properties. The desorption of adsorbed oxygen will take place which is decreasing the number of trapping states. More oxygen vacancies are created. This can have a positive influence on the number of charge carriers as discussed in chapter 2. More tetrahedrally coordinated Al is present in the AZO powders after thermal activation and a small Knight shift is observed. This suggests an improved incorporation of the Al in the ZnO matrix. Also, less octahedrally coordinated Al is observed, which reduces the number of electron acceptor sites. This results in more contributing Al sites to the improved conductivity. Nevertheless, the thermal activation should happen at a controlled temperature because the reduction of ZnO will occur at high temperature.

6.5 Conclusion

The studied parameters of the thermal process affect the structural, chemical and physical properties of the AZO thin films. During the thermal oxidation of the freshly deposited thin film, the tuning of diverse parameters helped us to optimise the thermal oxidation process. It was noted that 2 specific parameters, the drying of the thin film and the humidity of the processing atmosphere largely affected final properties of the AZO thin films. An optimal drying temperature of 120°C was found for both precursors, while humidity of the processing atmosphere affected both inks differently. For ink A3%B10, the best electrical properties are obtained when the atmosphere was bubbled through 2 water

bottles at 20°C, while ink A3%D10 showed the best electrical properties when the wet film was processed in a dry atmosphere.

The thermal activation of the AZO thin films in a H_2-rich atmosphere is balancing between two competing events. First, there are events which positively influence resistivity of the AZO thin film such as the removal of adsorbed O_2, better substitution of Al in the ZnO matrix etc.. Secondly, hydrogen etching is demolishing the formed AZO because it reacts with the ZnO, forming metallic Zn and water vapour. This can lead to a complete removal of the AZO thin film. For thin films treated for 30 minutes at 450°C in Ar/5% H_2 an optimum is found.

6.6 Reference list

1. Pasquarelli, R.M., D.S. Ginley, and R. O'Hayre, *Solution processing of transparent conductors: from flask to film.* Chemical Society Reviews, 2011. **40**(11): p. 5406-5441.
2. Rydzek, M., et al., *Comparative study of sol-gel derived tin-doped indium- and aluminum-doped zinc-oxide coatings for electrical conducting and low-emitting surfaces.* Progress in Organic Coatings, 2011. **70**(4): p. 369-375.
3. Lin, K.-m., Y.-Y. Chen, and K.-Y. Chou, *Solution derived Al-doped zinc oxide films: doping effect, microstructure and electrical property.* Journal of Sol-Gel Science and Technology, 2009. **49**(2): p. 238-242.
4. Damm, H., et al., *Factors Influencing the Conductivity of Aqueous Sol(ution)-Gel-Processed Al-Doped ZnO Films.* Chemistry of Materials, 2014. **26**(20): p. 5839-5851.
5. Schuler, T. and M.A. Aegerter, *Optical, electrical and structural properties of sol gel ZnO : Al coatings.* Thin Solid Films, 1999. **351**(1-2): p. 125-131.
6. Ohyama, M., H. Kozuka, and T. Yoko, *Sol-gel preparation of transparent and conductive aluminum-doped zinc oxide films with highly preferential crystal orientation.* Journal of the American Ceramic Society, 1998. **81**(6): p. 1622-1632.
7. Han, K.J., et al., *Effect of annealing temperature on the conduction mechanism for a sol-gel driven ZnO Schottky diode.* Journal of Physics D-Applied Physics, 2009. **42**(12).
8. Mondal, C., et al., *Fabrication of a ZnO nanocolumnar thin film on a glass slide and its reversible switching from a superhydrophobic to a superhydrophilic state.* Rsc Advances, 2013. **3**(17): p. 5937-5944.
9. Yang, H.-J., S.-Y. He, and H.-Y. Tuan, *Simultaneous axial screw dislocation-mediated growth and radial layer-by-layer deposition for controlled synthesis of asymmetric axial ZnO nanospindles.* Nanoscale, 2014. **6**(15): p. 9034-9042.
10. Diem, M., *Introduction to modern vibrational spectroscpoy* ed. A.W.-I. publication. 1993, United States of America: John Wiley & sons
11. Ghule, A.V., et al., *In situ thermo-TOF-SIMS study of thermal decomposition of zinc acetate dihydrate.* Journal of Mass Spectrometry, 2004. **39**(10): p. 1202-1208.
12. Gyoryova, K., V. Balek, and V. Zelenak, *Thermal-stability of zinc formate complex-compounds containing urea, thiourea and caffeine.* Thermochimica Acta, 1994. **234**: p. 221-232.
13. Maejima, K., et al., *Correlation between Electrical Properties and Crystal c-Axis Orientation of Zinc Oxide Transparent Conducting Films.* Japanese Journal of Applied Physics, 2012. **51**(10).
14. Chen, M., et al., *Intrinsic limit of electrical properties of transparent conductive oxide films.* Journal of Physics D-Applied Physics, 2000. **33**(20): p. 2538-2548.
15. Nakada, T., Y. Ohkubo, and A. Kunioka, *Eeffect of water-vapor on the growth of textured ZnO-based films for solar-cells by DC-magnetron sputtering.* Japanese Journal of Applied Physics Part 1-Regular Papers Short Notes & Review Papers, 1991. **30**(12A): p. 3344-3348.
16. Hung, S.C., et al., *Investigation of arsenic-doped ZnO thin films grown on Si substrate by atmospheric-pressure metal-organic chemical vapor deposition.* Physica Status Solidi a-Applications and Materials Science, 2012. **209**(6): p. 1053-1058.
17. Pollefeyt, G., et al., *Influence of aqueous precursor chemistry on the growth process of epitaxial SrTiO3 buffer layers.* Inorganic Chemistry, 2014. **53**(10): p. 4913-4921.
18. Sathyamurthy, S., et al., *Effect of relative humidity on the crystallization of sol-gel lanthanum zirconium oxide films.* Chemistry of Materials, 2006. **18**(25): p. 5829-5831.
19. Lei, L., et al., *Water-vapor-controlled reaction for fabrication of YBCO films by fluorine-free sol-gel process.* Ieee Transactions on Applied Superconductivity, 2010. **20**(5): p. 2286-2293.

20. Arii, T. and A. Kishi, *The effect of humidity on thermal process of zinc acetate.* Thermochimica Acta, 2003. **400**(1-2): p. 175-185.
21. Kozawa, T., et al., *Effect of water vapor on the thermal decomposition process of zinc hydroxide chloride and crystal growth of zinc oxide.* Journal of Solid State Chemistry, 2011. **184**(3): p. 589-596.
22. Nomura, K., et al., *Defect passivation and homogenization of amorphous oxide thin-film transistor by wet O(2) annealing.* Applied Physics Letters, 2008. **93**(19).
23. Crepaldi, E.L., et al., *Controlled formation of highly organized mesoporous titania thin films: From mesostructured hybrids to mesoporous nanoanatase TiO2.* Journal of the American Chemical Society, 2003. **125**(32): p. 9770-9786.
24. Chen, R., et al., *Growth mechanism of ZnO nanostructures in wet-oxidation process.* Thin Solid Films, 2011. **519**(6): p. 1837-1844.
25. Tang, W. and D.C. Cameron, *Aluminium-doped zinc-oxide transparent conductors deposited by the sol-gel process.* Thin Solid Films, 1994. **238**(1): p. 83-87.
26. Li, J., et al., *Preparation and characterization of Al doped ZnO thin films by sol-gel process.* Journal of Alloys and Compounds, 2012. **542**: p. 151-156.
27. Ohya, Y., H. Saiki, and Y. Takahashi, *Preparation of transparent, electrically conducting ZnO film from zinc acetate and alkoxide.* Journal of Materials Science, 1994. **29**(15): p. 4099-4103.
28. Isago, T., et al., *Preparation of transparent and conductive ZnO thin films by applying a solution of zinc alkoxide.* Journal of the Ceramic Society of Japan, 1996. **104**(11): p. 1052-1055.
29. Zhang, X.L., et al., *Effect of thermal annealing on the structural, electrical and optical properties of Al-Ni co-doped ZnO thin films prepared using a sol-gel method.* Surface & Coatings Technology, 2015. **261**: p. 149-155.
30. Yao, P.C., et al., *Optical and electrical characteristics of Al-doped ZnO thin films prepared by aqueous phase deposition.* Applied Surface Science, 2010. **257**(5): p. 1441-1448.
31. Nehmann, J.B., et al., *Aluminum-doped zinc oxide sol-gel thin films: Influence of the sol's water content on the resistivity.* Thin Solid Films, 2014. **556**: p. 168-173.
32. Chang, J.F., W.C. Lin, and M.H. Hon, *Effects of post-annealing on the structure and properties of Al-doped zinc oxide films.* Applied Surface Science, 2001. **183**(1-2): p. 18-25.
33. Oh, B.Y., et al., *Post-annealing of Al-doped ZnO films in hydrogen atmosphere.* Journal of Crystal Growth, 2005. **281**(2-4): p. 475-480.
34. Morrison, S.R., *Selectivity in semiconductor gas sensors.* Sensors and Actuators, 1987. **12**(4): p. 425-440.
35. Papadopoulos, C.A. and J.N. Avaritsiotis, *A model for the gas sensing properties of tin oxide thin films with surface catalysts.* Sensors and Actuators B: Chemical, 1995. **28**(3): p. 201-210.
36. Addonizio, M.L., et al., *Transport mechanisms of RF sputtered Al-doped ZnO films by H2 process gas dilution.* Thin Solid Films, 1999. **349**(1-2): p. 93-99.
37. Gioia, F., G. Mura, and A. Viola, *Experimental study of the direct reduction of sinterized zinc oxide by hydrogen.* Chemical Engineering Science, 1977. **32**(11): p. 1401-1409.
38. Lew, S., A.F. Sarofim, and M. Flytzani-Stephanopoulos, *The reduction of zinc titanate and zinc oxide solids.* Chemical Engineering Science, 1992. **47**(6): p. 1421-1431.
39. Ghosh, S., et al., *Microstructure of ZnO films produced by reactive DC sputtering technique.* Journal of Crystal Growth, 1991. **108**(3–4): p. 534-540.
40. Choi, S.-y., K. Choi, and S.J. Kim, *Rapid thermal annealing effects on the electrical and structural properties of the AZO thin film deposited at a room temperature.* .

International Journal of Advanced Research in Electrical, Electronics and Instrumentation Engineering, 2013. **2**(12): p. 9.
41. Baik, S.J., et al., *Highly textured and conductive undoped ZnO film using hydrogen post-treatment.* Applied Physics Letters, 1997. **70**(26): p. 3516-3518.
42. Xu, Z.Q., et al., *Al-doping effects on structure, electrical and optical properties of c-axis-orientated ZnO : Al thin films.* Materials Science in Semiconductor Processing, 2006. **9**(1-3): p. 132-135.
43. Islam, M.N., et al., *XPS and X-ray diffraction studies of aluminum-doped zinc oxide transparent conducting films.* Thin Solid Films, 1996. **280**(1-2): p. 20-25.
44. Bai, S., et al., *Quantum-sized ZnO nanoparticles: synthesis, characterization and sensing properties for NO2.* Journal of Materials Chemistry, 2011. **21**(33): p. 12288-12294.
45. Chen, M., et al., *X-ray photoelectron spectroscopy and auger electron spectroscopy studies of Al-doped ZnO films.* Applied Surface Science, 2000. **158**(1-2): p. 134-140.
46. Wagner, C.D. and G.E. Muilenberg, *Handbook of x-ray photoelectron spectroscopy : a reference book of standard data for use in x-ray photoelectron spectroscopy*. 1979, Eden Prairie, Minn.: Physical Electronics Division, Perkin-Elmer Corp.
47. Zhang, X., et al., *Effect of aspect ratio and surface defects on the photocatalytic activity of ZnO nanorods.* Scientific Reports, 2014. **4**.
48. Avadhut, Y.S., et al., *Structural investigation of aluminium doped ZnO nanoparticles by solid-state NMR spectroscopy.* Physical Chemistry Chemical Physics, 2012. **14**(33): p. 11610-11625.
49. Noriega, R., et al., *Probing the electrical properties of highly-doped Al:ZnO nanowire ensembles.* Journal of Applied Physics, 2010. **107**(7).
50. Knight, W.D. and S.-I. Kobayashi, *Knight shift*, in *eMagRes*. 2007, John Wiley & Sons, Ltd.

Chapter 7 – Tuning the opto-electrical properties of AZO thin films

As illustrated in the previous chapter, the thermal process has a big influence on the crystal growth, morphology and resistivity of the synthesised AZO thin films. However, these experiments were performed with a fixed dopant concentration, respectively 3 at% Al doped ZnO. Varying the dopant concentration will affect the charge carriers concentration. Hence, the opto-electrical properties of these AZO thin films will be altered depending on the dopant concentration. For each ink the most suited thermal process is selected according to the results in chapter 6, followed by an investigation of the influence of the dopant concentration. In order to study the effect of the aluminium concentration on the microstructural and opto-electrical properties, samples were prepared with varying concentrations of aluminium (0, 1 , 2, 3 and 4 at%).

7.1 Influence of Al doping on the structural and opto-electrical properties of ZnO thin films

As mentioned in chapter 2, doping of ZnO can influence the final properties of the matter, e.g. ferromagnetic properties by doping with Co, low conductive thin films by doping with Na or Li, high conductive thin films by doping with Al or Ga, etc.. Doping of ZnO does not only affect the electrical properties, the morphology and optical properties of these thin films change as well [1-3].

Doping of ZnO with Al is known for its disturbed grain growth. Kuo and Zhang *et al*. [1, 3] noticed a decrease in average particle size with increasing dopant concentration. The inhibition of grain growth can be ascribed to compression stresses by doping. These stresses are induced by the difference in ionic radii between Zn^{2+} and Al^{3+} ions, respectively 0.074 and 0.054 nm [1, 3]. Also, if the solubility limit is reached the formation of $ZnAl_2O_4$ particles reduces the grain growth of AZO. The $ZnAl_2O_4$ particles pin the AZO grain boundaries and reduce their mobility. Both are contributing to an increased grain growth activation energy [4, 5]. We also observed the reduced grain size of AZO powders which were studied by XRD and Rietveld refinement (figure 7.1). The increasing dopant concentration led to the decrease in grain size, respectively from 63 nm for pure ZnO to 13 nm for 5 at% AZO. Not only the grain size is reduced by doping with Al, the morphology of the thin films changes as well. As illustrated in figure 7.2, a more densified top morphology is obtained by Al doping.

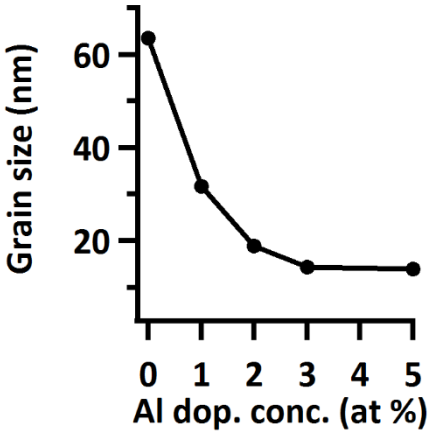

Figure 7.1 Crystallite size of bulk AZO powders synthesized via ink Ax%B10 as a function of the dopant concentration.

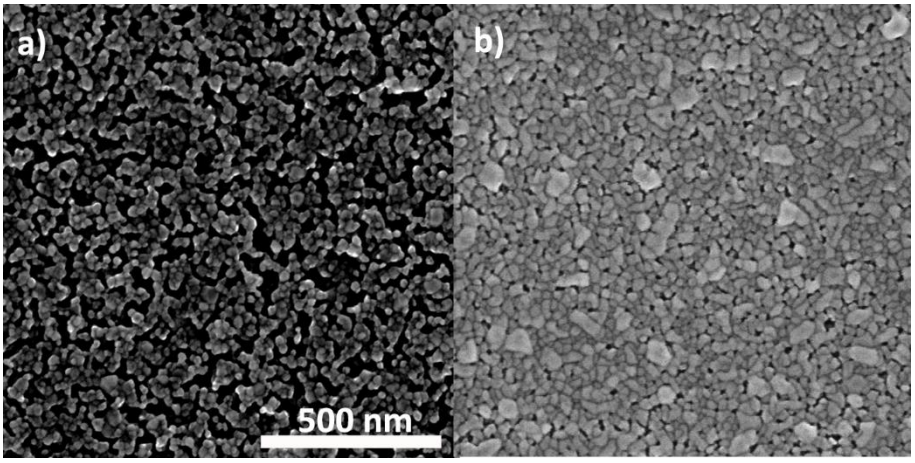

Figure 7.2 SEM image of fully processed ZnO and 3 at% AZO, respectively obtained by ink A10 and A3%B10.

Next to the effect of doping on the morphology, the optical properties change as well. Doping of ZnO will affect the optical absorption edge [2]. The shift in the optical absorption edge is dominated by two competing effects, namely band gap narrowing and Burstein-Moss band-filling effect [6, 7]. Band gap narrowing occurs when the synthesised AZO meets Mott's criterion which is set at a carrier concentration of 6 x 10^{18} cm^{-3} [8]. In that case, the donor states merge with the conduction band. The change in nature and strength of the interaction potentials between the donors and matrix shift the valence and conduction band towards each other, resulting in band gap narrowing [9]. The Burstein-Moss effect positively shifts the optical absorption edge with increasing carrier concentration. For heavily doped ZnO the lower states in the conduction band are occupied. When an electron is excited from the top of the valence band additional energy is needed to excite the electron to the higher, unoccupied levels of the conduction band. Overall, a blue shift of the optical absorption edge is noticed.

The optical band gap, E_g, can be determined by a Tauc plot, making use of the absorption coefficient, α, and the following relation [10]:

$$\alpha h\upsilon \approx (h\upsilon - E_g)^{1/2} \qquad \text{Eq.7.1}$$

where the absorption coefficient is obtained from the transmittance data (α = (1/d)ln(1/T)), and d and T are the thickness and transmittance of the films. The

optical band gap can be obtained by extrapolating the Tauc plot towards the x-axis [11].

Before continuing the discussion about the influence of the dopant concentration on the opto-electical properties of AZO thin films, we will first discuss a non-doped ZnO thin film synthesised by solution A. This will be a reference for the AZO thin films. The ZnO thin film was synthesised with the optimised thermal process for the deposition of AZO thin film with ink A3%B10. Meaning, a wet oxidative thermal treatment till 500°C followed by a thermal activation at 450°C.

The ZnO thin film has a resistivity of 1.69 Ω cm, a polycrystalline nature as seen in the X-ray diffractogram (figure 7.3), an average optical transmittance in the visible range of the spectrum of 84.28% and an optical band gap of 3.25 eV (figure 7.4).

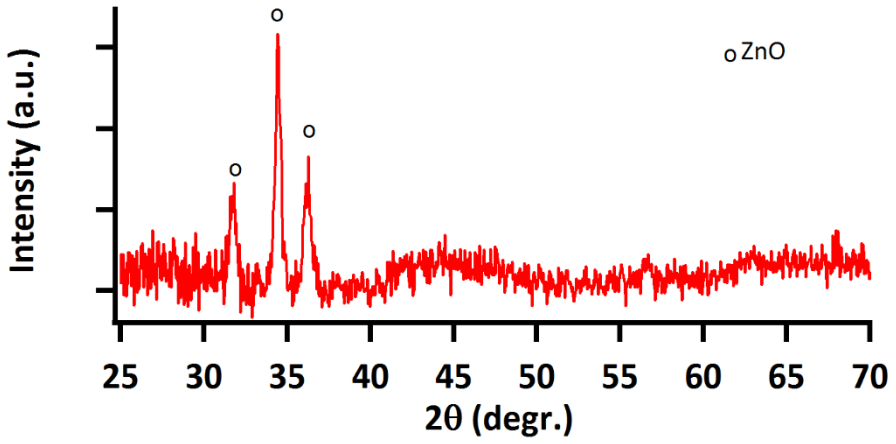

Figure 7.3 XRD measurement of fully processed ZnO. Reflections at 31.83° (100), 34.45° (002) and 36.29° (101) (JCPDS 89-7102).

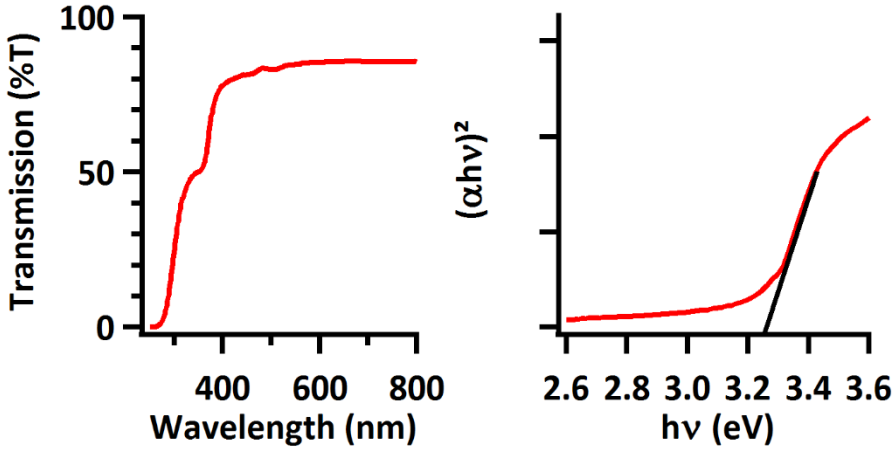

Figure 7.4 Optical properties of the synthesised ZnO thin films. Left: Transmittance obtained from fully processed ZnO thin film. Right: Tauc plot, where $(\alpha h\nu)^2$ is represented as a function of $h\nu$.

7.2 The effect of the dopant concentration on AZO thin films

Not only the dopant concentration will be discussed in the upcoming paragraphs, also the influence of the different Al-precursors. As mentioned in chapter 4, the Al-precursor influences the effectiveness of the Al incorporation in the ZnO matrix. A variation in the starting precursor salt and/or formed complexes results in different amounts of substitutional Al. Generally, aluminium nitrates are more efficient in doping of the ZnO. The use of aluminium nitrates in combination with citric acid resulted in the most efficient doping of ZnO. However, the processing atmosphere has a big influence as well. In the previous chapter, we showed that a wet atmosphere improves the substitutional doping of Al for the aluminium malonate precursor, while a dry atmosphere is favoured for the aluminium citrate precursor. By tuning the processing parameters the resistivities of AZO thin films obtained with different inks are almost identical. Hereby, the 2 types of inks will be studied with diverse Al contents, respectively an ink containing aluminium nitrate and malonic acid (Ax%B10) and an ink containing aluminium nitrate and citric acid (Ax%D10).

7.2.1 Variation of dopant concentration for the ink containing aluminium malonate complexes

The variation of dopant concentration was studied by changing the added amount of Al precursor solution, as discussed in chapter 4. The AZO thin films synthesised from ink Ax%B10 are thermally treated according to the procedure

discussed in the previous chapter. Firstly, the films were dried on a preheated hotplate at 120°C during 10 minutes. Secondly, the films were placed in a tube furnace and subjected to the thermal oxidation step in a wet atmosphere. A heating rate of 10 K/min was maintained during this process, while at 250 and 500°C was held for 60 minutes. The 200 ppm O_2 in N_2 was bubbled through 2 glass bottles with water at 20°C. Finally, the AZO thin films were thermally activated at 450°C for 30 minutes in a Ar/5% H_2 atmosphere.

Opto-electrical properties of the AZO thin films

An optimum in electrical properties of the AZO thin films is noticed at a dopant level of 3 at%, where a resistivity of 2.54 x 10^{-2} Ω cm is obtained (figure 7.5). Up to a dopant concentration of 3 at%, the carrier density is increasing with an increasing dopant concentration. However, once this threshold is exceeded a decrease in the carrier density is observed. A higher dopant concentration can induce more charge carriers if the solubility limit isn't exceeded. In case of a high dopant concentration, one should be aware of segregation of the dopant at the grain boundaries which hampers the charge carrier's mobility [1]. The mobility of the charge carriers is increasing up till a dopant concentration of 3 at% (11 $cm^2\ V^{-1}\ s^{-1}$) . Doping ZnO with 4 at% Al resulted in a dramatic decrease of the carrier mobility (5 $cm^2\ V^{-1}\ s^{-1}$).

The optical transmittance of the fully processed thin films is represented in figure 7.6. All of the films exhibit a transmission higher than 90% in the visible range of the spectrum with a sharp absorption edge around 385 nm. The absorption edges shift towards shorter wavelengths by increasing the dopant concentration. A Tauc plot was used to estimate the band gap of these materials. In case of 1 at% dopant concentration the band gap reaches 3.27 eV while thin films with a dopant concentration of 2, 3 and 4 at% have a band gap of 3.29, 3.32 and 3.34 eV. The blue shift in the absorption onset of Al doped ZnO thin films compared to ZnO is commonly associated with the increase of carrier concentration blocking the lowest states of the conduction band, as described by Burstein [6] and Moss [7], resulting in a higher optical absorption edge.

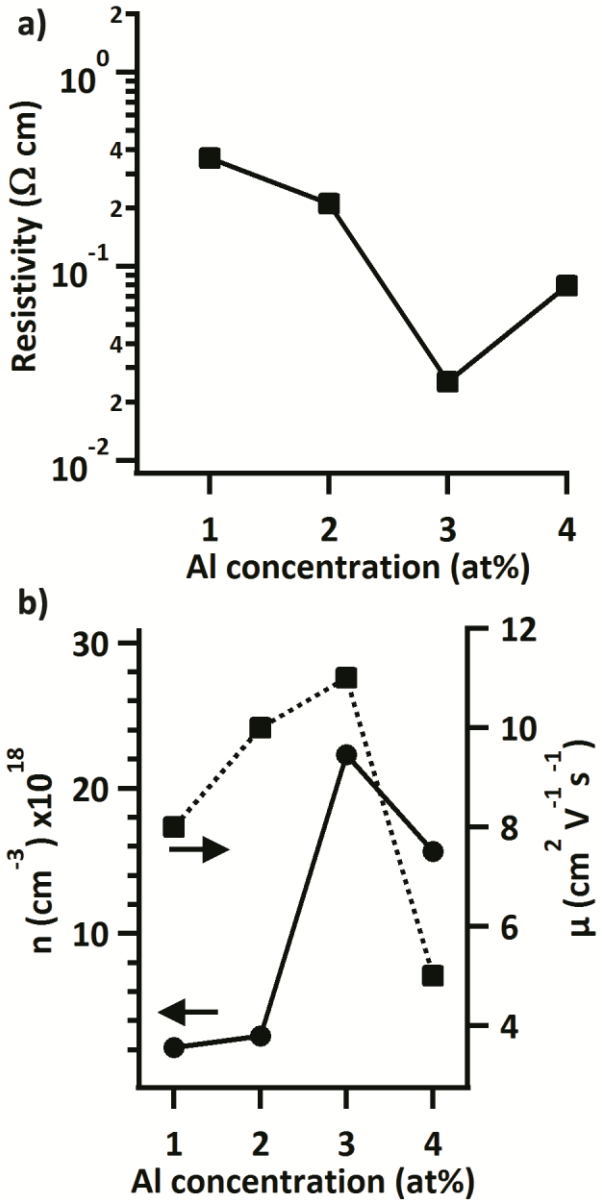

Figure 7.5 Electrical properties of fully processed AZO thin films obtained by ink Ax%B10, a) the resistivity as a function of the dopant concentration and b) carrier concentration and carrier mobility as a function of the dopant concentration.

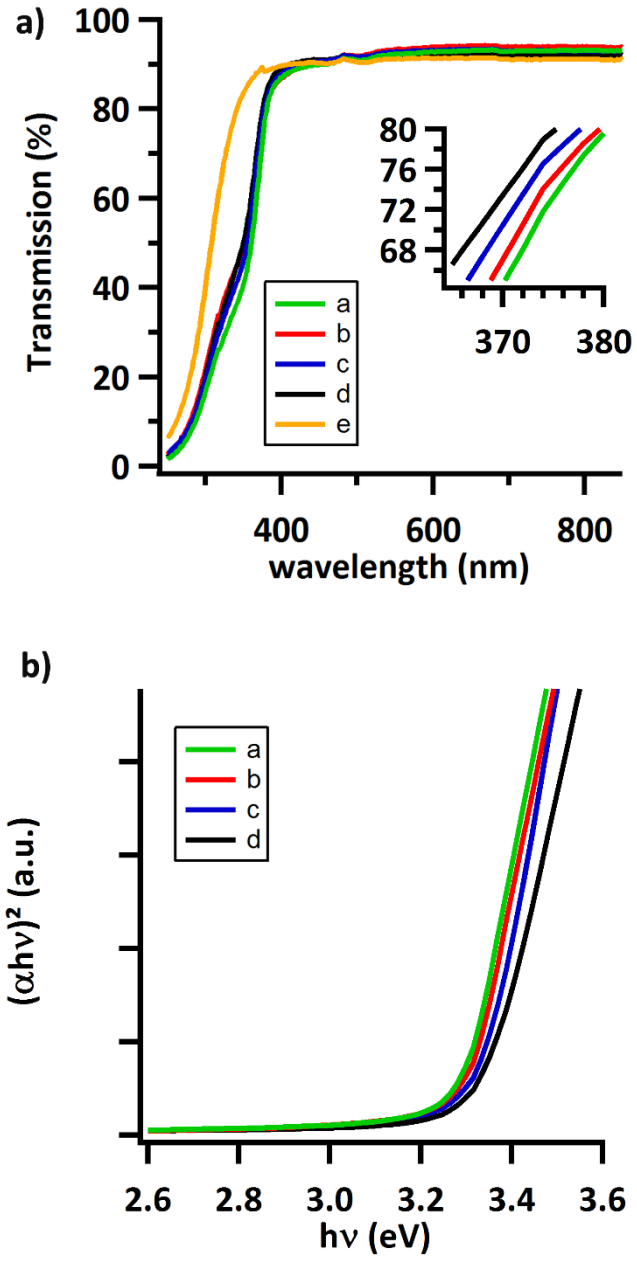

Figure 7.6 Optical properties of fully processed AZO thin films with different dopant concentrations with a) 1 at%, b) 2 at%, c) 3 at%, d) 4 at% AZO and f) uncoated glass substrate. Top: Transmittance obtained from fully processed AZO coatings. The inset shows a more detailed view of the transmittance spectra between 365 and 380 nm. Bottom: Tauc plot, where $(\alpha h\nu)^2$ is represented as a function of $h\nu$.

Structural properties of the AZO thin films

Based on the X-ray diffractograms (figure 7.7), one should expect low resistive coatings for a dopant concentration of 2 at%. The strong preferential growth along the *c*-axis would suggest a possible candidate for good electrical conductivity at 2 at% AZO. However, a higher dopant concentration (3 at% AZO) can induce more charge carriers if the solubility limit isn't exceeded. An increasing amount of charge carriers doesn't always directly lead to an increased electrical conductivity. The mobility of these charge carriers also plays a vital role in the final electrical properties combined with diverse scattering events such as grain boundary scattering, lattice scattering, ionised-impurity scattering etc. [12].

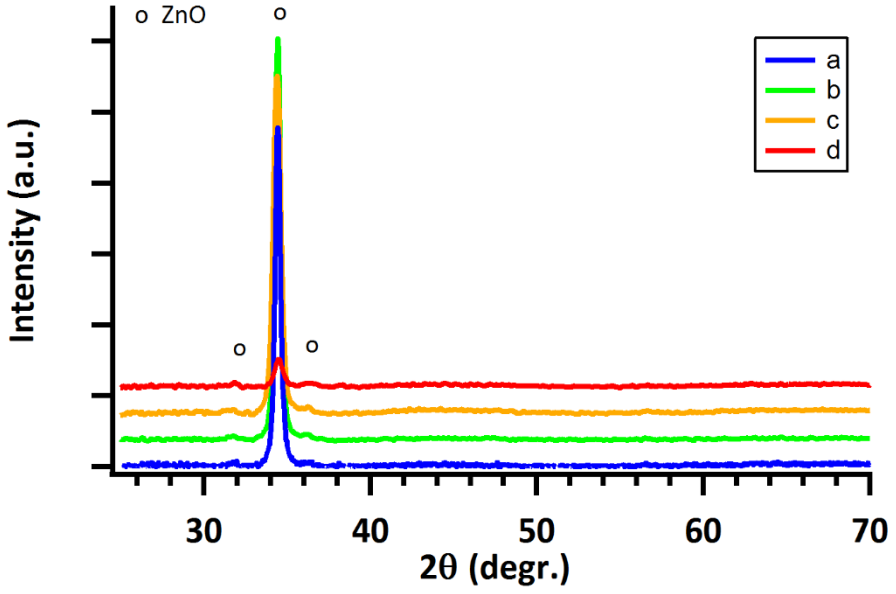

Figure 7.7 XRD measurements of fully processed AZO thin film obtained by printing ink Ax%B10: a) 1 at% AZO, b) 2 at% AZO, c) 3 at% AZO and d) 4 at% AZO.

Compared to the X-ray diffractogram of pure ZnO (figure 7.3), the AZO films are crystalline with a preferential growth along the *c*-axis. No secondary phases are noticeable. All reflections can be assigned to AZO. The reflections at 31.77° (100) and 36.26° (101) are almost negligible compared to the reflection at 34.42° (002) (JCPDS 89-7102), indicating a strong preferential growth along the *c*-axis. However, pole figures did not show any discrete spots. Concluding, no complete

epitaxial growth is present. The films are growing according to a uniaxial orientation.

The strong preferential growth along the *c*-axis reaches an optimum around a doping level of 2 at% and has a minimum at 4 at%. This can be explained by taking two phenomena in to account: (1) Cebulla *et al.* [13] noticed an increase of texturing by doping ZnO with Al, where Al acts as a mineraliser or surfactant. (2) An excess of dopant can induce stresses due to the large difference in ionic size of both, respectively 0.074 nm for Zn^{2+} and 0.054 nm for Al^{3+} [1]. This indicates that a certain amount of dopant helps the texture while an excess of the dopant concentration deteriorates the crystallinity of these thin films.

To understand the relationship between the electrical properties and the crystal growth of these thin films, the full width half maxima (FWHM) of the rocking curves of the (002)-reflection are compared (figure 7.8). The FWHM of these rocking curves are 7.04°, 7.38°, 7.00° and 9.07° for dopant levels of 1, 2, 3 and 4 at% respectively. The FWHM values up till dopant levels of 3 at% are comparable while for 4 at% there is a significant increase. The larger misfit of the uniaxally grown grains may be a result of impurity segregation at the grain boundaries as there is a possibility the solubility limit is exceeded. This larger misfit will induce more defects and dangling bonds at the grain boundaries which reduces the charge carrier's mobility, especially with the more porous morphology (figure 7.9). Concluding, the carrier mobility will mainly be influenced by grain boundary scattering. The effect of ionised impurity scattering is not expected to be dominating because the carrier concentration is far below 10^{21} cm^{-3} where impurity scattering becomes dominant [14].

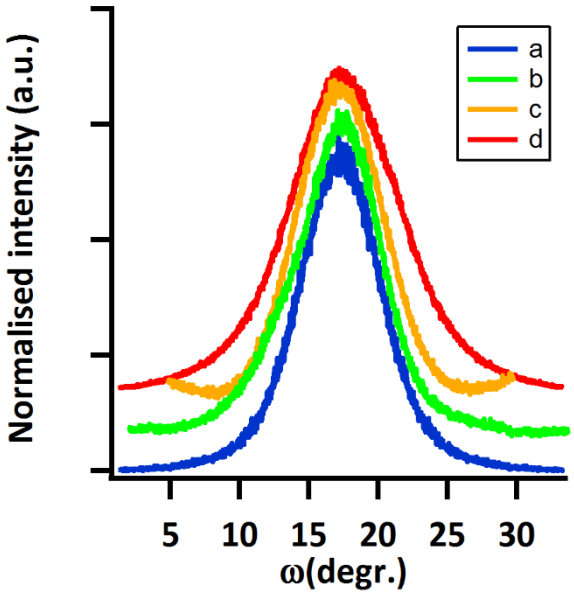

Figure 7.8 Rocking curves of the (002)-reflection: a) 1 at%, b) 2 at%, c) 3 at% and d) 4 at% of AZO thin films. The intensity is normalised on the rocking curve of sample b.

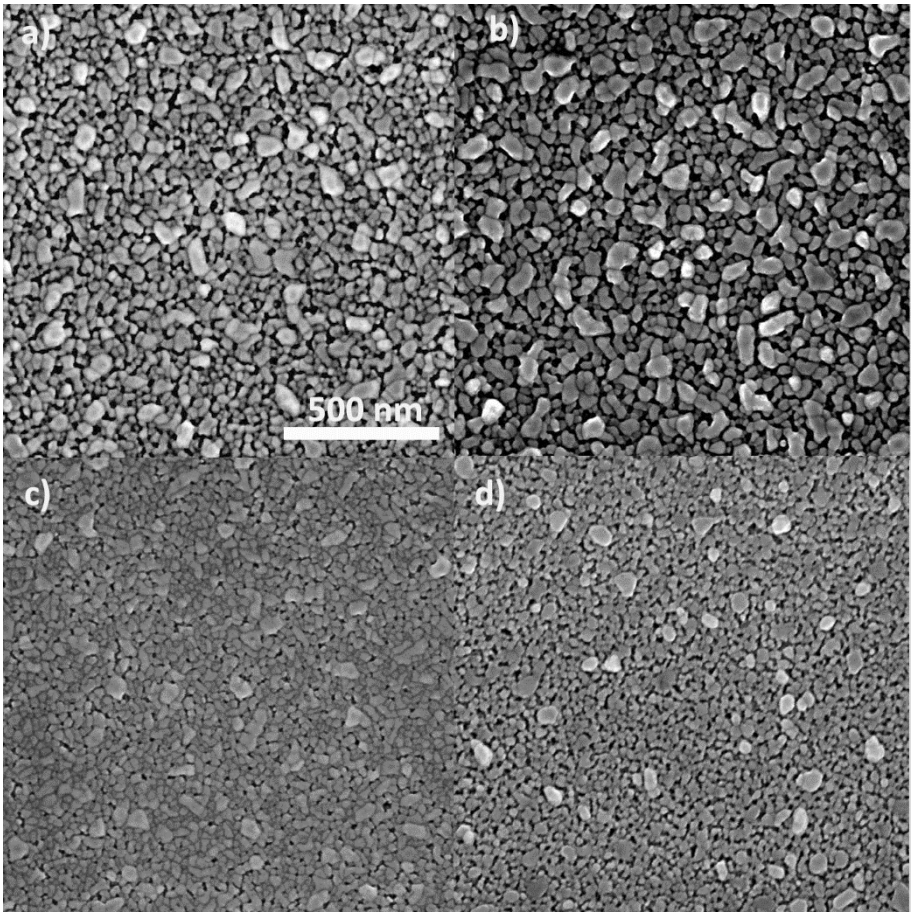

Figure 7.9 SEM images of fully processed AZO thin films with varying dopant concentrations obtained by printing with ink Ax%B10: a) 1 at%, b) 2 at%, c) 3 at% and d) 4 at% of AZO.

The thin films of 3 at% AZO have the most densified morphology. The morphologies of the coatings made of 1 at% and 2 at% AZO show grains that are less connected. The grains of these coatings look loosely stacked while those of 3 at% AZO thin films are more connected and densified. The coating with the lowest FWHM value and a better morphology finally results in the highest mobility (11 $cm^2 V^{-1} s^{-1}$). Coupled with the large number of charge carriers (2.23 x 10^{19} cm^{-3}) obtained due to a higher dopant concentration, it is clear that the lowest resistivity is obtained (2.54 x 10^{-2} Ω cm) for 3 at% AZO thin films.

7.2.2 Variation of dopant concentration for the ink containing aluminium citrate complexes

The AZO thin films synthesised from ink Ax%D10 were thermally treated according to the procedure discussed in the previous chapter. Firstly, the films were dried on a preheated hotplate at 120°C during 10 minutes. Secondly, the films were placed in a tube furnace and subjected to the thermal oxidation step in a dry atmosphere. A heating rate of 10 K/min was maintained during this process, while at 250 and 500°C was held for 60 minutes. Finally, the AZO thin films were thermally activated at 450°C for 30 minutes in a Ar/5% H_2 atmosphere.

Opto-electrical properties of the AZO thin films

Also here, a minimal resistivity is obtained after doping with 3 at% Al (figure 7.10). An AZO thin film was synthesised with resistivity of 2.41 x 10^{-2} Ω cm, a carrier density of 2.31 x 10^{19} cm^{-3} and a carrier mobility of 11.23 cm^2 V^{-1} s^{-1}. Up to a dopant concentration of 3 at%, the carrier density is increasing with an increasing dopant concentration. However, once this threshold is exceeded a decrease in the carrier density is observed. Similar to the earlier discussed AZO thin films, there is a possibility that the solubility limit is exceeded. The mobility of the charge carriers is increasing up to a dopant concentration of 3 at% (11.2 cm^2 V^{-1} s^{-1}). Doping ZnO with 4 at% Al resulted in a dramatic decrease of the carrier mobility (3.7 cm^2 V^{-1} s^{-1}).

The optical transmittance of the fully processed thin films is represented in figure 7.11. The average transmission in the visible range of the spectrum varies between 87 % for sample d and 90% for sample c. Around a wavelength of 390 nm a sharp absorption edge starts to form. As illustrated in the inset of figure 7.11, the absorption edge shifts to shorter wavelength by increasing dopant concentration. In case of 1 at% AZO a band gap of 3.31 eV was extracted while the thin films of 2, 3 and 4 at% AZO have a band gap of 3.32, 3.34 and 3.30 eV. Compared to ZnO (3.25 eV) a blue shift is observed with increasing dopant concentration, also known as the Burstein-Moss effect [6, 7].

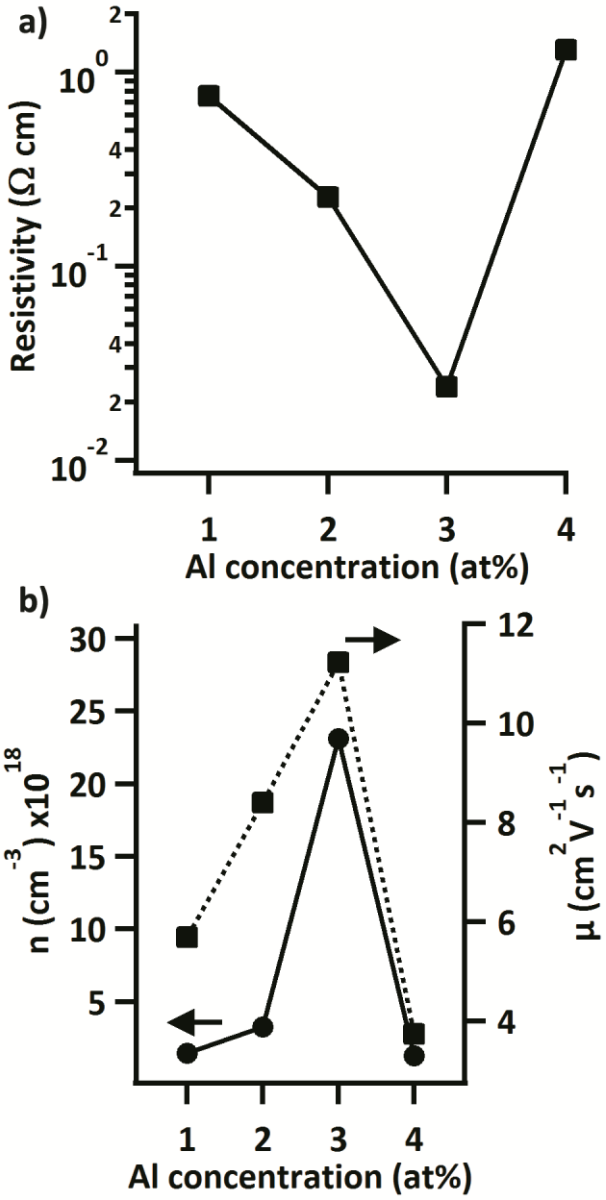

Figure 7.10 Electrical properties of fully processed AZO thin films obtained by ink Ax%D10: a) the resistivity as a function of the dopant concentration and b) the carrier concentration and carrier mobility as a function of the dopant concentration.

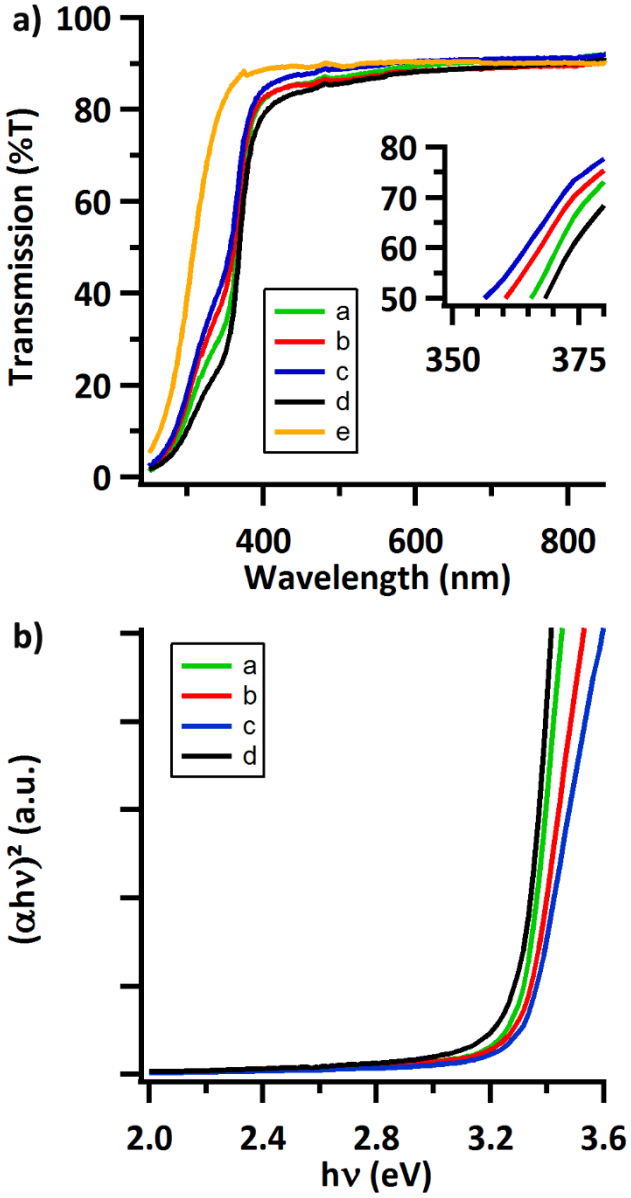

Figure 7.11 Optical properties of fully processed AZO thin films with different dopant concentrations with a) 1 at%, b) 2 at%, c) 3 at%, d) 4 at% AZO and f) uncoated glass substrate. Top: Transmittance obtained from fully processed AZO coatings. The inset shows a more detailed view of the transmittance spectra between 365 and 380 nm. Bottom: Tauc plot, where $(\alpha h\nu)^2$ is represented as a function of $h\nu$.

Structural properties of the AZO thin films

When the surface morphologies of all samples are compared (figure 7.12), one can notice that sample c (3 at% AZO) has the most densified structure. Sample a looks very similar to the non-doped ZnO thin film shown in figure 7.2. An increasing Al content results in more densified films which is in line with the observations of Han *et al*. [4]. However, sample d (4 at% AZO) is showing more microcracks. The densified structure combined with the high dopant concentration of sample c result in the lowest resistivity due to the high mobility and carrier concentration. The low mobility and carrier concentration for sample d can be explained by the presence of the microcracks and by the possibility of exceeding the dopant concentration which can introduce a small amount of secondary phases at the grain boundaries [15].

The XRD measurements of the AZO thin films clearly show the presence of a polycrystalline nature (figure 7.13). One can distinguish the (100), (002) and (101)-reflections of ZnO, respectively at 31.69°, 34.44° and 36.20°. Still, a slightly preferential growth along the *c*-axis is observed, although this preferential growth is less dominant compared to the AZO thin films produced with ink Ax%B10. Moreover, the intensity of the (002)-reflection is decreasing with an increasing dopant concentration. This indicates that an increasing dopant concentration deteriorates crystallinity. A higher dopant concentration can induce the formation of stresses due to the difference in ionic radius of Zn^{2+} and Al^{3+} [1, 16], indicating the role of Al as mineraliser at a different dopant concentration as for the ink Ax%B10. Nevertheless, good conductive AZO thin film is obtained by doping with 3 at% Al. Most likely, the combination of dopant concentration and morphology are more dominant compared to the preferential crystal growth of these thin films.

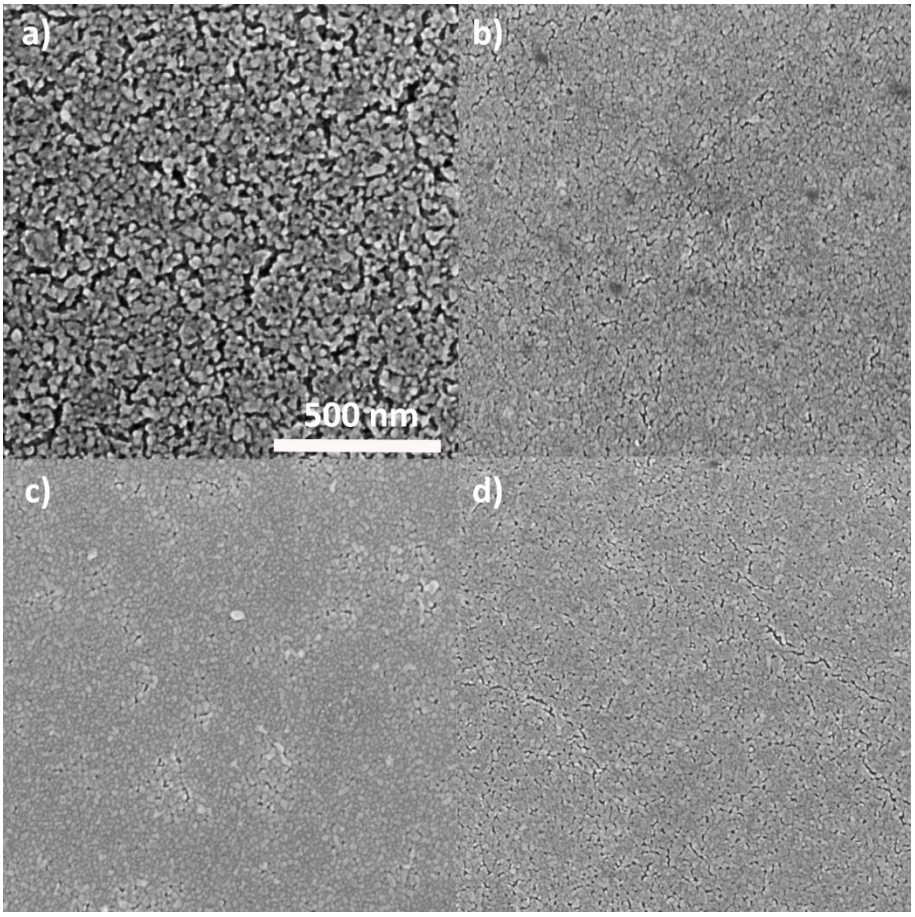

Figure 7.12 SEM images of fully processed AZO thin films with varying dopant concentrations obtained by printing with ink Ax%D10: a) 1 at%, b) 2 at%, c) 3 at% and d) 4 at% of AZO.

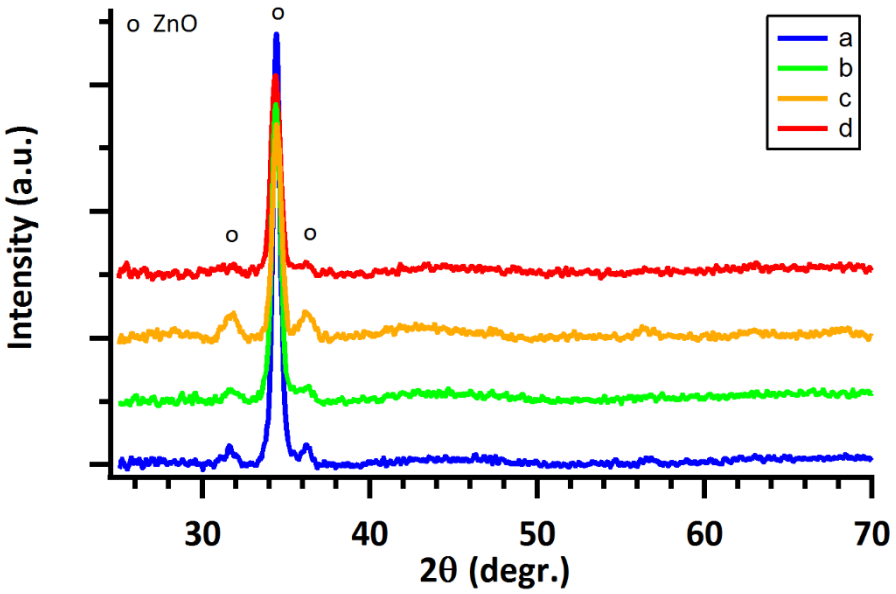

Figure 7.13 XRD measurements of fully processed AZO thin film obtained by printing with ink Ax%D10: a) 1 at% AZO, b) 2 at% AZO, c) 3 at% AZO and d) 4 at% AZO.

7.3 Comparison of AZO thin films synthesised by inks A3%B10 and A3%D10

Previous paragraphs discussed the opto-electrical and structural properties of AZO thin films synthesised by 2 different inks. Both inks are containing the same Zn precursor solution, but different Al precursor solutions were added to obtain a well-defined dopant concentration. Ink A3%B10 is containing Al-malonate complexes, while ink A3%D10 is containing Al-citrate complexes. As discussed in chapter 6, both inks require different processing conditions. The ink A3%B10 requires processing in a wet 200 ppm O_2 in N_2 atmosphere, while ink A3%D10 requires processing in a dry 200 ppm O_2 in N_2 atmosphere. Finally, the fully processed AZO thin films have almost identical opto-electrical properties, although they are having a completely different morphology and crystal growth, both exhibit a minimal resistivity by doping with 3 at% Al. This led to almost identical resistivity, carrier mobility and carrier density, respectively 2.54×10^{-2} Ω cm, 2.23×10^{19} cm^{-3} and 11 $cm^2 V^{-1} s^{-1}$ for ink A3%B10 and 2.41×10^{-2} Ω cm, 2.31×10^{19} cm^{-3} and 11.23 $cm^2 V^{-1} s^{-1}$ for ink A3%D10. The average transmittance obtained in the visual region of the spectrum slightly differ, respectively 92% for ink A3%B10 and 90% for ink A3%D10.

As illustrated in figure 7.14, the thin films obtained by the different inks have different structural properties. The samples synthesised with ink A3%B10 have a more intense (002)-reflection, while the samples synthesised with ink A3%D10 have more prominent (100) and (110)-reflections in the diffractogram. The morphology of coatings synthesised with ink A3%B10 shows larger grains at the surface compared to the coatings synthesised with ink A3%D10, while the latter show a more densified morphology.

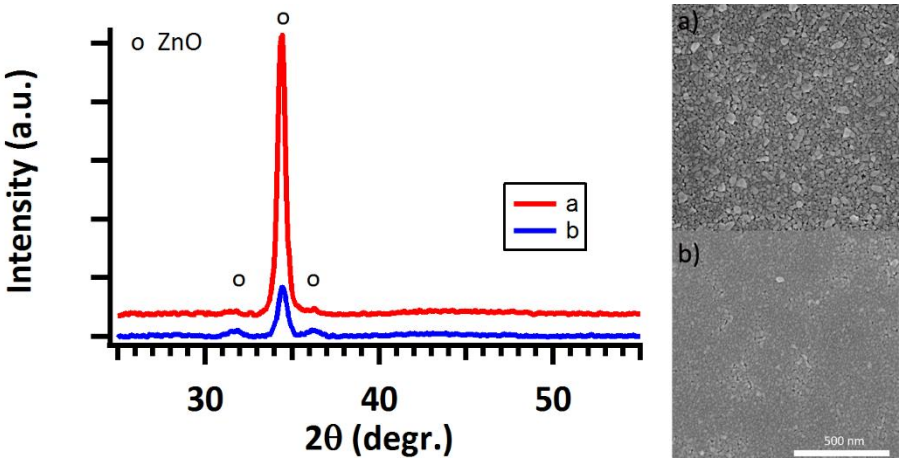

Figure 7.14 XRD measurements and SEM images of AZO coatings obtained by different inks: a) 3at% AZO synthesized with ink A3%B10 and b) 3 at% AZO synthesised with ink A3%D10.

7.3.1 Compositional analysis of AZO powders synthesised from both inks

When the AZO powders prepared from these inks, are compared by solid state Al NMR, one can notice a more intense signal at 81 ppm and 8 ppm for sample b (figure 7.15). This results in more substitutional Al (11.70 versus 9.00%) and octahedrally coordinated Al (36.30 versus 22.40%). The higher amount of incorporated Al in the ZnO matrix will be balanced by more occupied octahedral sites which act as electron acceptors [15, 17, 18]. If a certain amount of the dopant forms it corresponding oxide (Al_2O_3), a more intense signal of octahedrally coordinated Al is possible without resulting in more electron acceptor sites in the ZnO matrix. But these impurities would enhance grain boundary scattering and limit the mobility of the charge carriers. Considering the structural and compositional properties of these thin films, it is not clear why they have similar electrical properties.

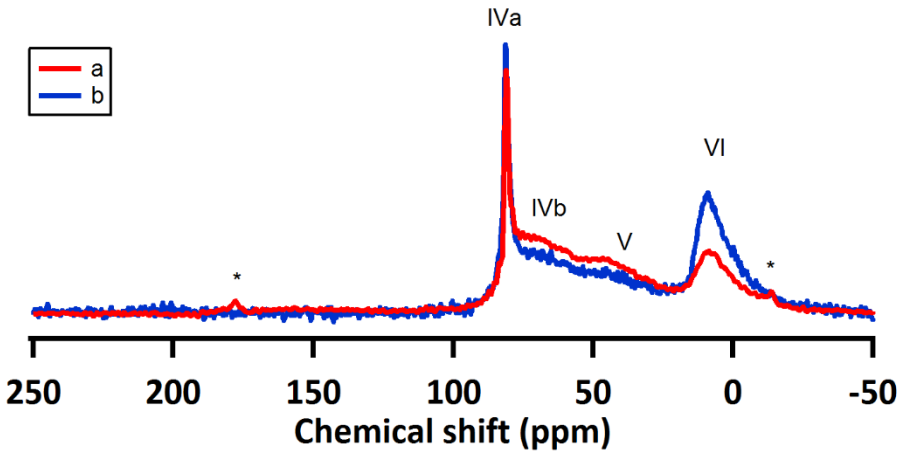

Figure 7.15 1D ^{27}Al MAS NMR spectra of AZO powders synthesised by a) heating ink A3%B10 in wet air and b) heating ink A3%D10 in dry air, where * mark spinning sidebands.

7.3.2 A more in depth structural analysis of the AZO thin films synthesised by both inks

To create a better understanding of the similar electrical properties of these thin films, a more in depth study is necessary. The porosity of these AZO coatings was studied by a cross-sectional SEM image (figure 7.16). One can distinguish 3 type of materials in these images, namely the glass substrate, the AZO layer and platinum which is used as protective layer during the cutting of the cross-section. Both films have a thickness around 80 nm, respectively 85 nm for sample a and 77 nm for sample b. As can be observed, sample b has a sporadic pinhole. It also looks more porous. The grayscale in the thin film points out a porous structure. Sample a looks more dense. However, a slight contrast can be observed, which may indicate a minor porosity. The more porous structure of sample b might be assigned to the combination of aluminium nitrate and citric acid. Metal nitrates combined with citric acid result in an auto-combustion reaction releasing various gasses (H_2O, N_2 and CO_2) ending up with a more porous structure [19, 20].

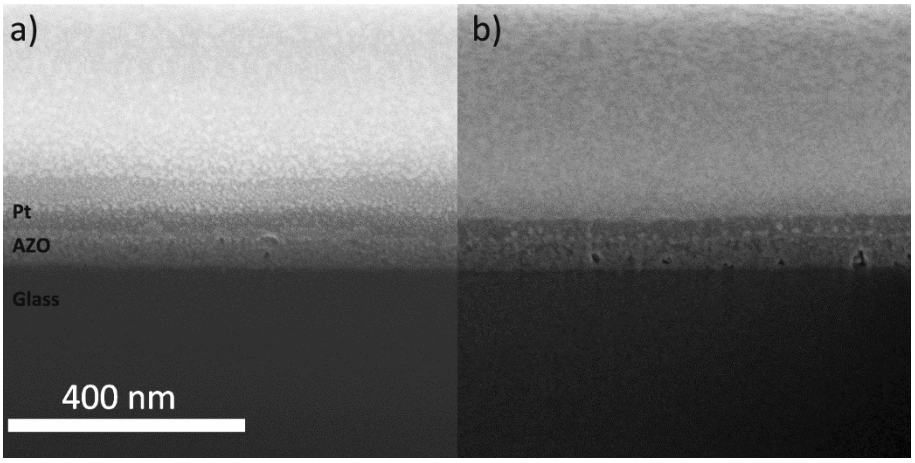

Figure 7.16 Cross-sectional view of the samples with the best electrical properties of both inks: a) 3 at% AZO synthisised with ink A3%B10 and b) 3 at% AZO synthesised with ink A3%D10.

A more in depth study of both thin films was performed by Transition Electron Microscopy (TEM). This allowed us to have a more detailed view on the morphology, crystallinity of the films and the distribution of the Al through the film. The TEM analysis of sample a (ink A3%B10) is represented in figure 7.17. As discussed in chapter 3, 3 types of structural parameters can occur, respectively a granular, columnar and layered structure [21]. Here, a granular structure at the substrate/AZO interface is observed while the top region has a columnar structure. In between, a more porous structure is noticed. The presence of Pt dots (black dots) point out the porous structure, while at the substrate/AZO interface a dense region is found. The Selected Area Electron Diffraction (SAED) pattern shows the diffraction rings of the (100) and (101) crystal planes, while only 2 bright spots of the (002) crystal planes are present. This indicate a polycrystalline and oriented matter inside the thin film. A more detailed view of the top region (20 nm) shows a top layer oriented along the *c*-axis, although the region beneath it is polycrystalline. When we consider the X-ray diffractogram of sample a, the (100) and (101)-reflections are not strongly present. A possible explanation can be found in the size of these grains. A grain size of 13 nm for the polycrystalline phase is measured. This is in line with the grain size determined by bulk XRD measurements and Rietveld refinement (figure 7.1). These nanocrystalline grains will broaden the reflections which makes them less visible at low intensities [22].

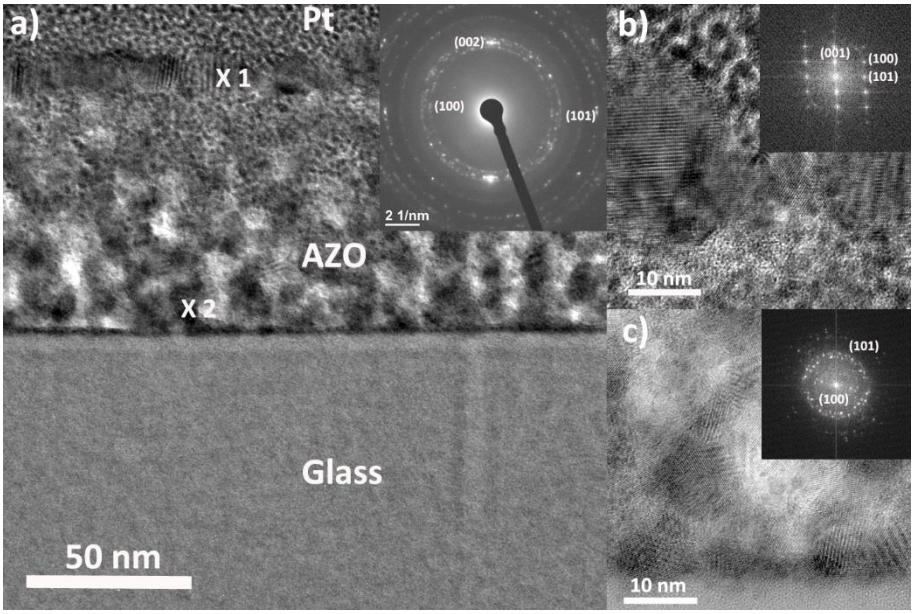

Figure 7.17 TEM analysis of sample a (ink A3%B10): a) An overview of the layer with a diffraction pattern as inset. X 1 and X 2 mark the spots where elemental analysis is performed. b) Top of the AZO layer in more detail with a fourier transformed image as inset. c) A more detailed image of the substrate/AZO interface with a fourier transformed image as inset.

The EDS measurements at spot X 1 and X 2 show a remarkable difference (figure 7.18 and figure 7.19). The top layer does not contain Al or has a low level of it, while the polycrystalline material does.

In this case the preferential growth along the *c*-axis doesn't start at the substrate/AZO interface as suggested by Fujihara *et al*. [23]. A clearly polycrystalline interface is observed. Neither, is it a result of the survival of nuclei at the substrate surface. Otherwise, an oriented grain/lamella would be found in the cross-sectional view. The more porous region between the top and the dense region at the interface can suggest that a phase separation is going on. The EDS measurements can support this. The top layer consists out of ZnO with an Al content below the detection limit, while at the other parts of the film a clear Al signal is visible. Quantitative determination showed that the polycrystalline region contains more or less 4.5 at% Al. In this region, no secondary phase such as Al_2O_3 or $ZnAl_2O_4$ is detected, showing that the Al is incorporated in the ZnO matrix.

No reason can be found for the orientation of the top layer and polycrystalline nature of the matter beneath it. We suggest that 3 at% AZO is a metastable system, resulting in a oriented top layer of ZnO which is containing low contents of Al and a polycrystalline AZO phase below containing 4.5 at% Al. To clarify what is going on during the thermal process and why we are ending up with this kind of morphology, a more in depth study should be considered. A quench study combined with XRD, ^{27}Al MAS NMR, TEM and SEM analysis can help investigate the ongoing process during the thermal treatment.

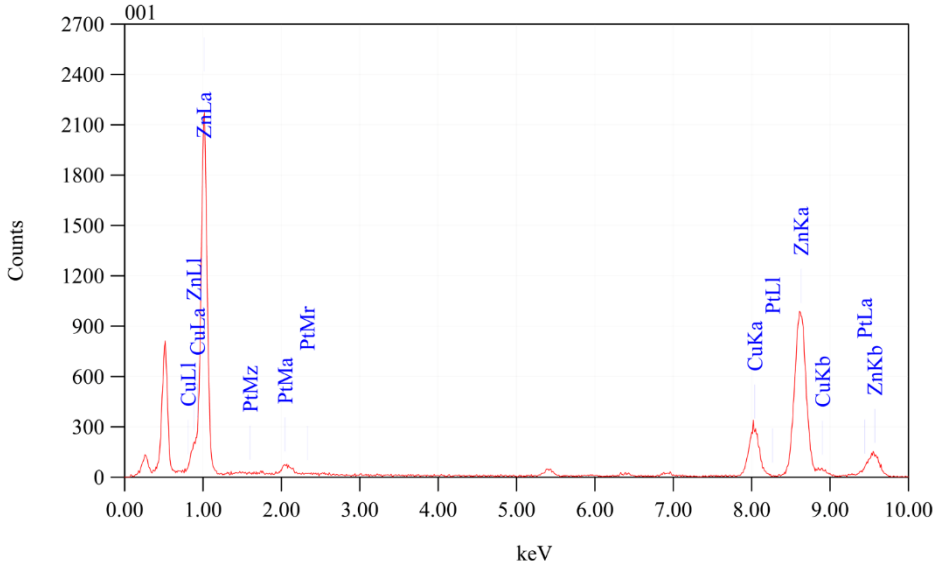

Figure 7.18 EDS spectrum of spot X 1 at the top layer of sample a.

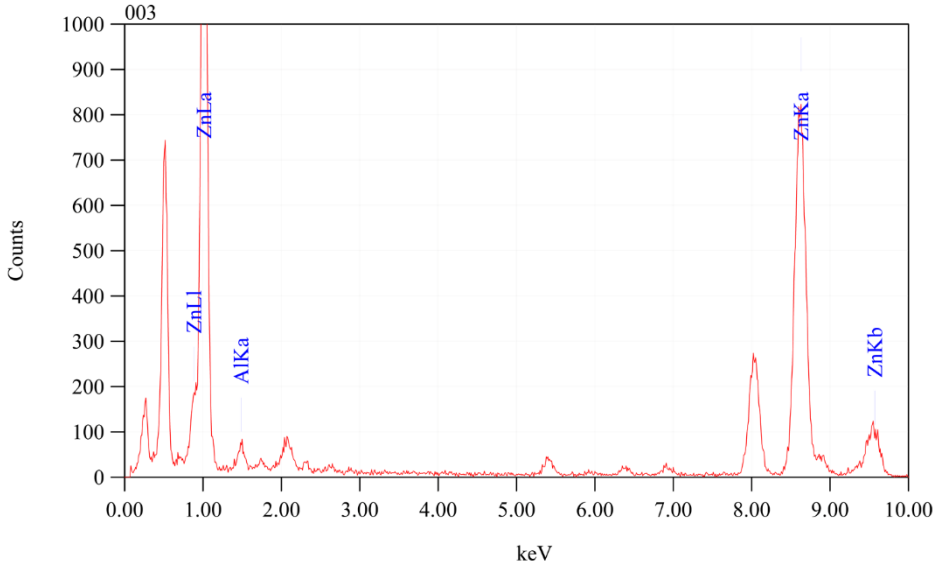

Figure 7.19 EDS spectrum of spot X 2 at the top layer of sample a.

The TEM analysis of sample b (ink A3%D10) shows a similar structure as sample a (figure 7.20). At the substrate interface a dense polycrystalline region is obtained, flowing over in a more porous region containing 4 at% Al. At the top a ZnO *c*-axis oriented layer is observed. As already deduced from the cross-sectional views, sample b is more porous than sample a. Also, the top layer is less thick (15 nm versus 20 nm) which can explain the weaker (002)-reflections in the X-ray diffractogram. According to the fourier transformed images of the top region, a secondary phase is present. However, the origin of this phase is unknown. A more intensive TEM analysis is required to confirm the origin of this secondary phase.

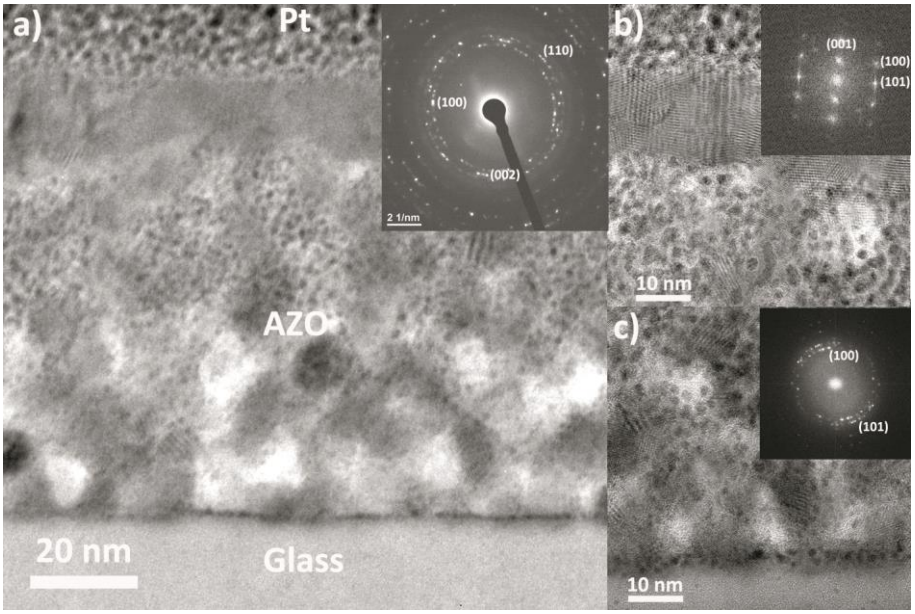

Figure 7.20 TEM analysis of sample b (ink A3%D10): a) An overview of the layer with a diffraction pattern as inset. b) Top of the AZO layer in more detail with a fourier transformed image as inset. c) A more detailed image of the substrate/AZO interface with a fourier transformed image as inset.

The TEM analysis shows a grain size of maximum 15 nm which is enhancing the effect of grain boundary scattering on the carrier mobility [12, 24]. We are also convinced that the top layer of both thin films have a major contribution to the electrical properties. The porous region beneath the top layer will limit the overall contribution of the entire thin film to the electrical properties. Based on this suggestion, one can state that ink A3%D10 is the most promising ink to continue research with. A slightly lower resistivity is obtained, but the top layer of these coatings are thinner. Meaning, this top layer yields to a lower resistivity. Nevertheless, further optimisation is needed to produce a homogenous thin film.

7.4 Conclusion

The initial intention of doping ZnO with Al is decreasing the resistivity and enhancing the optical properties. However, the introduction does not only affect the opto-electrical properties of the coatings. The grain size reduces, the morphology of the coating changes and the X-ray diffractogram shows a prominent growth of the (002)-reflection. Two different inks, where only the Al precursor is varied, were used to study the influence of the dopant

concentration. Both are showing a minimum resistivity at 3 at% Al doped ZnO, respectively 2.54 x 10^{-2} Ω cm for the aluminium malonate and 2.41 x 10^{-2} Ω cm for the aluminium citrate ink. Both are having an average optical transmittance in the visible range of the spectrum of more than 90%. Overall, AZO coatings synthesised with ink A3%D10 are looking the most promising, if further optimisation can lead to a more dense thin film. Nevertheless, the coatings exist out of 3 regions. A dense region at the substrate interface is transitioning in a more porous region. Above this all, a *c*-axis oriented top layer is observed. It is suggested that these thin films are metastable as the top layer is poor in Al and the other regions contain more than 4 at% Al without the formation of any secondary phases. Still, the mechanism behind this feature is unclear. Further research will be needed to investigate what is going on during thermal processing of these films.

7.5 Reference list

1. Kuo, S.Y., et al., *Effects of doping concentration and annealing temperature on properties of highly-oriented al-doped ZnO films.* Journal of Crystal Growth, 2006. **287**(1): p. 78-84.
2. Sim, K.U., et al., *Effects of dopant (Al, Ga, and In) on the characteristics of ZnO thin films prepared by RF magnetron sputtering system.* Current Applied Physics, 2010. **10**(3): p. S463-S467.
3. Zhang, Y., et al., *The solubility and temperature dependence of resistivity for aluminum-doped zinc oxide ceramic.* International Journal of Applied Ceramic Technology, 2012. **9**(2): p. 374-381.
4. Han, J.P., P.Q. Mantas, and A.M.R. Senos, *Densification and grain growth of Al-doped ZnO.* Journal of Materials Research, 2001. **16**(2): p. 459-468.
5. Nunes, S.I. and R.C. Bradt, *Grain-growth of ZnO in ZnO-Bi2O3 ceramics with Al2O3 additions.* Journal of the American Ceramic Society, 1995. **78**(9): p. 2469-2475.
6. Burstein, E., *Anomalous optical absorption limit in InSb.* Physical Review, 1954. **93**(3): p. 632-633.
7. Moss, T.S., *The interpretation of the properties of Indium Antimonide.* Proceedings of the Physical Society. Section B, 1954. **67**(10): p. 775.
8. Schleife, A., et al., *Optical absorption in degenerately doped semiconductors: Mott transition or Mahan excitons?* Physical Review Letters, 2011. **107**(23).
9. Liu, Y.L., Y.F. Li, and H.B. Zeng, *ZnO-based transparent conductive thin films: doping, performance, and processing.* Journal of Nanomaterials, 2013: p. 9.
10. Tauc, J., R. Grigorovici, and A. Vancu, *Optical properties and electronic structure of amorphous germanium.* physica status solidi (b), 1966. **15**(2): p. 627-637.
11. Ilican, S., Y. Caglar, and M. Caglar, *Preparation and characterization of ZnO thin films deposited by sol-gel spin coating method.* Journal of Optoelectronics and Advanced Materials, 2008. **10**(10): p. 2578-2583.
12. Chen, M., et al., *Intrinsic limit of electrical properties of transparent conductive oxide films.* Journal of Physics D-Applied Physics, 2000. **33**(20): p. 2538-2548.
13. Cebulla, R., R. Wendt, and K. Ellmer, *Al-doped zinc oxide films deposited by simultaneous rf and dc excitation of a magnetron plasma: Relationships between plasma parameters and structural and electrical film properties.* Journal of Applied Physics, 1998. **83**(2): p. 1087-1095.
14. Minami, T., *New n-type transparent conducting oxides.* Mrs Bulletin, 2000. **25**(8): p. 38-44.
15. Serier, H., M. Gaudon, and M. Menetrier, *Al-doped ZnO powdered materials: Al solubility limit and IR absorption properties.* Solid State Sciences, 2009. **11**(7): p. 1192-1197.
16. Xu, Z.Q., et al., *Characteristics of Al-doped c-axis orientation ZnO thin films prepared by the sol–gel method.* Materials Research Bulletin, 2006. **41**(2): p. 354-358.
17. Kelchtermans, A., et al., *Relation between synthesis conditions, dopant position and charge carriers in aluminium-doped ZnO nanoparticles.* Rsc Advances, 2013. **3**(35): p. 15254-15262.
18. Kemmitt, T., B. Ingham, and R. Linklater, *Optimization of sol-gel-formed ZnO:Al processing parameters by observation of Dopant Ion location using solid-state Al-27 NMR spectrometry.* Journal of Physical Chemistry C, 2011. **115**(30): p. 15031-15039.
19. Deganello, F., G. Marci, and G. Deganello, *Citrate-nitrate auto-combustion synthesis of perovskite-type nanopowders: A systematic approach.* Journal of the European Ceramic Society, 2009. **29**(3): p. 439-450.

20. Van de Velde, N., et al., *CeO2 buffer layers for HTSC by an aqueous sol-gel method – chemistry and microstructure.* European Journal of Inorganic Chemistry, 2010. **2010**(2): p. 233-241.
21. Schuler, T., et al., *Influence of structure zone model parameters on the electrical properties of ZnO : Al sol-gel coatings.* Thin Solid Films, 2006. **502**(1-2): p. 67-71.
22. Scherrer, P., Göttinger Nachrichten Gesell., 1918. **2**: p. 98.
23. Fujihara, S., C. Sasaki, and T. Kimura, *Crystallization behavior and origin of c-axis orientation in sol-gel-derived ZnO : Li thin films on glass substrates.* Applied Surface Science, 2001. **180**(3-4): p. 341-350.
24. Zhang, D.H. and H.L. Ma, *Scattering mechanisms of charge carriers in transparent conducting oxide films.* Applied Physics a-Materials Science & Processing, 1996. **62**(5): p. 487-492.

Chapter 8 – Printing of Al doped ZnO patterns

Previously, printing of AZO thin films was discussed. Printing of AZO patterns can be interesting matter. This chapter will discuss the deposition of AZO tracks via ink jet printing, where we will focus on the line stability and the deposition of a track. Ink jet printing of patterns can avoid or reduce an etching procedure. Also, a more cost-efficient process can be obtained. Ink jet printing is a direct writing technique that can accurately deposit a pattern. So, no complete thin films need to be deposited first to obtain a pattern.

8.1 Introduction

Most of the TCOs used in devices are patterned, e.g. transparent electrodes in photovoltaic devices [1] and touch screens [2-4]. Top-down lithography techniques are commonly used to obtain patterns [5]. This is an intensive process where well-defined patterns can be obtained. Nevertheless, a low-cost and high throughput direct writing technique is a promising route to produce patterns. Ink jet printing already showed to be a promising candidate for printing metal [6], metal oxide [7] and polymer [8] patterns. The dimensions of the patterns are determined by the resolution of the plotter, the nozzle diameter, the contact angle of the ink on the substrate and the loading of the ink [9, 10]. So, optimising the setup and the ink's physical parameters will improve the resolution.

Printing of thin films was discussed in the previous chapters. There it was noticed that good wetting (contact angle < 5°) and a large droplet overlap were necessary to obtain homogenous thin films. Printing of patterns is more complex. We should consider line stability and drying behaviour. The upcoming paragraphs will discuss these topics.

8.2 Line stability and drying behaviour of patterns

Printing patterns starts by printing a discrete droplet on a substrate where the next droplet will overlap with the previous one to obtain a pattern. If a discrete droplet is printed on a flat substrate with a certain overlap to the previous one both droplets can merge and the following three situations can occur: (1) The contact angle of the first printed droplet is fixed while the contact line is free to move. (2) The contact angle of the first printed droplet is a function of the moving contact line. (3) The contact angle of the first printed droplet is free to change while the contact line is fixed. Only the third situation can lead to a stable fluid line on the substrate, while the first and second situation will undergo a Rayleigh instability [11, 12]. Printing a uniform line goes hand in hand with tuning the droplet spacing. As illustrated in figure 8.1, depending on the droplet spacing different line shapes can be obtained. When the droplet spacing is larger than the droplet footprint, discrete droplets will be observed. However, printing droplets with a certain overlap can result in line formation. At small overlap ratio droplet coalescence is observed but a scalloped structure is shown. By increasing the droplet overlap a uniform line can be printed. Nevertheless, a

large overlap ratio can result in bulging [13]. The initiation of bulging is in relationship to both droplet overlap and the speed at which the line is printed. Duineveld [14] described the mechanism of bulging formation as follows. The competition between possible flow paths when a new droplet interacts with the leading edge of the line can lead to bulging. If the capillary spreading of the droplet is relatively slow, the newly deposited droplet at the front of the liquid train will have a greater curvature at the liquid/air interface than the liquid train. The difference in Laplace pressure will drive the liquid of the newly deposited droplet along the pre-existing liquid train. Controversially, high deposition rates reduce bulging and instead favour spreading of the droplet [15]. Thus, droplet spacing and frequency at which droplets are jetted influence bulge formation.

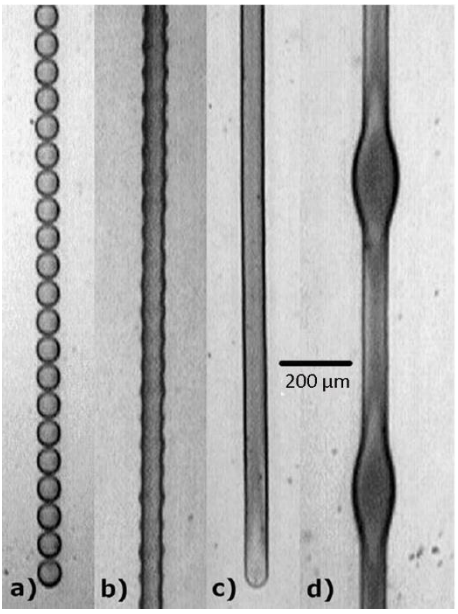

Figure 8.1 The printed line shape is determined by the droplet overlap and coalescence: a) droplet spacing is larger than the footprint of the droplet, resulting in single droplets, b) the droplet overlap is small, obtaining a scalloped structure, c) the droplet overlap is sufficient enough, obtaining a uniform line and d) the droplet overlap is too large, obtaining bulge formation [13].

The solidification of printed lines is accompanied with a large volume change due to the low concentration of the inks. Hereby, the evaporation of the ink is crucial because solute distribution during drying can strongly influence the shape of a printed pattern [15]. As illustrated in figure 8.2 two types of drying can appear: a) coffee staining and b) uniform drying. Coffee staining is a well-known occurring effect [16] and is studied by Deegan *et al*. [17]. Coffee staining

is the outcome of a higher evaporative flux at the edges of a feature (drop or pattern). The evaporation of the solvent at the edges is larger than in the centre of the droplet, resulting in a faster evaporation of the ink. Due to the contact line pinning, the ink is flowing from the centre of the feature to the edges, resulting in the agglomeration of material at the edges. The uniform drying system is observed in n-octane or ethanol where the thermal Marangoni flow counterbalances the coffee-ring effect. The heat transfer by the substrate is higher than at the ink/vapour interface inducing a thermal gradient in the printed feature. The longer conduction path at the centre of the features results in a lower temperature at the top compared to the edges, leading to a surface tension difference. This will lead to a circular flow inside the droplet causing a redistribution of the material [18, 19].

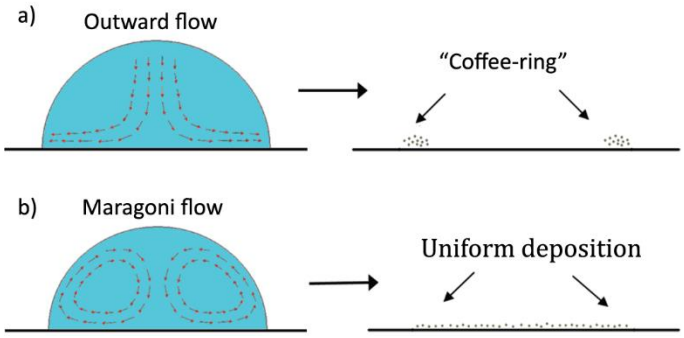

Figure 8.2 Drying behaviour of patterns: a) coffee staining and b) uniform drying. Adapted from [20].

However, the thermal Marangoni flow has not been reported for water [18]. Controlling the evaporation rate of the ink can lead to a more uniform deposition. This can be established by increasing the substrate temperature. This minimises the effect of the outward flow by reducing the drying time [16]. Another approach is making use of complex solvent mixtures with low and high boiling points. This will result in a smaller difference of the evaporation rates at the edges and centre of the feature which is reducing the coffee-ring effect [21, 22].

8.3 Printing of thin AZO patterns

8.3.1 Printing of AZO patterns with ink A3%D

The AZO patterns were printed with a Dimatix Materials Printer (Fujifilm Dimatix Inc., DMP-2831) with cartridges providing orifice diameters of 22 µm. The selected ink is ink A3%D as this is the most promising one. The patterns were printed with ink A3%D containing 0 v% ethanol, as the contact angle is 12° on a cleaned substrate by cleaning method 3 (cfr. chapter 5). The preference for a higher contact angle for printing patterns is based on smaller contact diameters of the droplet with the substrate. This improves the resolution of printing and thicker features can be obtained with only one print. In fact, one could suggest printing of patterns on substrates cleaned by method 1 or 2 but the prints resulted in unconnected droplets or inhomogeneous patterns caused by Rayleigh instability. As illustrated in figure 8.3, no contact line pinning can be observed when the ink is deposited on a glass substrate cleaned by method 2. The spreading of the droplet by adding an additional volume indicates a moving contact line.

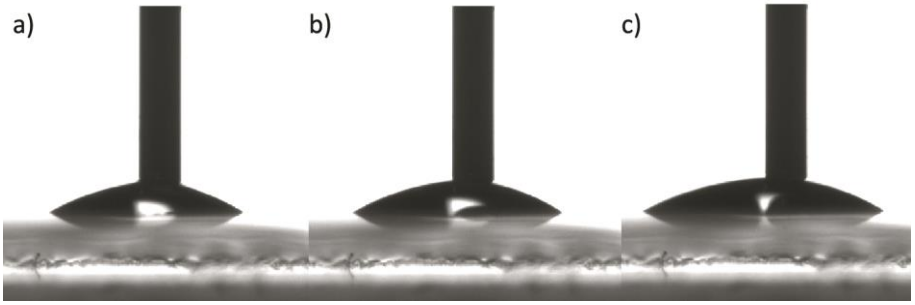

Figure 8.3 Droplet shape analysis of ink A3%D on a glass substrate cleaned by method 2: a) a 1 µL droplet is deposited on the glass substrate, b) 0.25 µL of the ink is added and c) 0.75 µL of the ink is added.

Ink A3%D was printed on a substrate with a controlled temperature of the ink and substrate. To avoid evaporation of the ink, the cartridge temperature was fixed at 28°C. The ink was fired at 9.4 V. The substrate temperature was fixed at 28°C. Printing tracks with diverse overlap ratios led to the formation of bulging or unconnected patterns (figure 8.4). When the droplet spacing is equal to the contact diameter (0% overlap) droplet pairing occurred. Higher overlap ratios (20-30%) result in a harmonic bulging. When 20% overlap is used, bulging is

dominant. Even the bottlenecks between the bulges are unconnected. At higher overlap ratio (30%) more liquid is present, resulting in connected bulges.

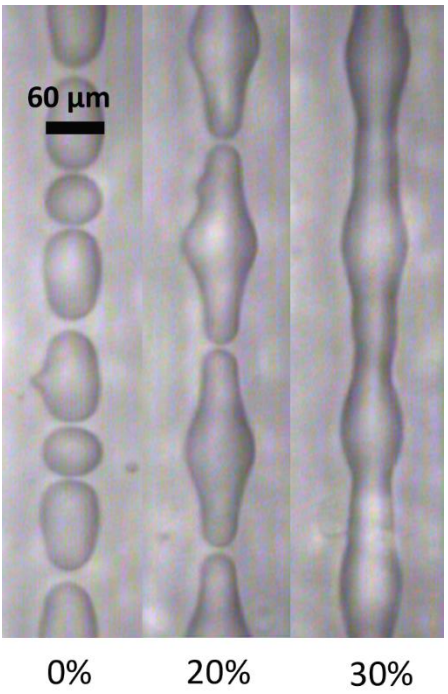

Figure 8.4 Printing of AZO tracks with ink A3%D on a method 3 cleaned substrate. Varying overlap ratios are used. Ink and substrate temperature were fixed at 28°C. The ink was fired at 9.4 V with a frequency of 1 kHz.

Higher printing frequencies still resulted in bulging. This indicates the very slow spreading of the droplet which encourages bulging. As illustrated in figure 8.5, printing on heated substrates can help. Till 20% of droplet overlap, droplet pairing occurs. Tracks are formed starting from overlap ratios of 30%. At 30% overlap, interruption of the track is still possible which can be avoided with higher overlap ratios.

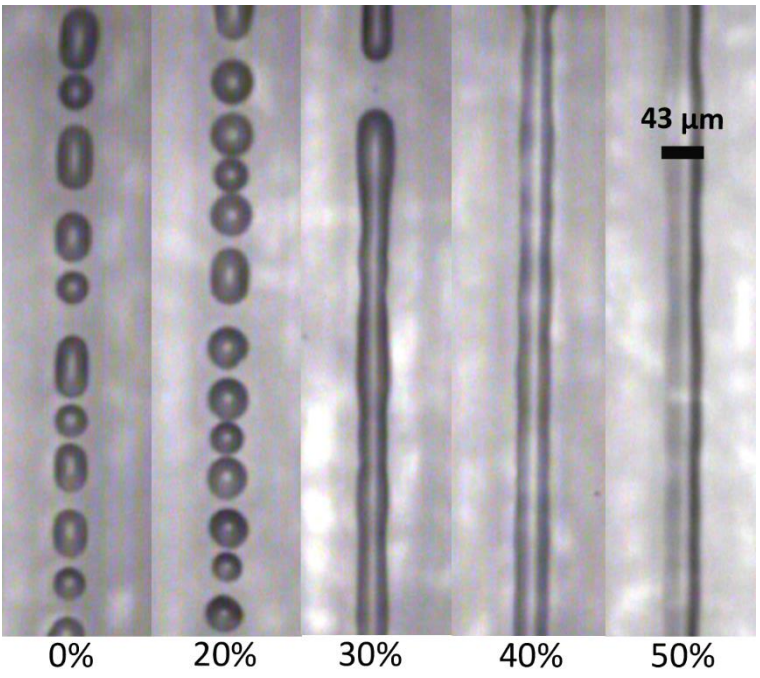

Figure 8.5 Printing of AZO tracks with ink A3%D on a method 3 cleaned substrate. Varying overlap ratios resulted in droplet pairing or the formation of patterns. The temperature of the ink was fixed at 28°C, while the substrate's temperature was 50°C. The ink was fired at 9.4 V with a frequency of 1 kHz.

Printing on a heated substrate (50°C) does not only reduce bulging, the patterns get narrower as well. The contact diameter of the droplet (d_{con}) and thus the contact angle changes with the temperature of the substrate. Using eq. 5.8 the contact angle is calculated (table 8.1). When the droplets are printed on a substrate at 28°C, the calculated contact angle matches the contact angle measured with the drop shape analyser, respectively 12° versus 13°. Because the contact angle couldn't be measured at elevated temperatures with the in-house setup, the calculated data could not be compared with the measured data. However, previous experiments showed that this approach is very accurate. It can be seen that the contact angle increased up to 41° for a substrate at 50°C. This would make it possible to print thicker patterns due to the smaller contact diameter.

The bulging could be reduced by the increased contact angle. A higher contact angle could possibly decrease the capillary spreading of the droplet and helps to avoid bulging. Also, the heated substrate will transfer its heat to the ink droplet,

resulting in a faster evaporation of the volatile components. This will affect the viscosity and impede flow of the ink what can reduce bulging because of the 'fixation' of the droplet at the position of impact.

Table 8.1 Overview of the droplet properties after impact with a substrate heated at 28 or 50°C. The represented contact angles are calculated from the droplet diameter in flight and after impact.

Temperature substrate (°C)	d_0 (µm)	d_{con} (µm)	Contact angle (°)
28	22	63	13
50	22	41	41

Printing with an overlap ratio of 50% results in tracks having a width of 43 µm. Calculations showed us that a fully processed AZO track would result in a height of 35 nm. To compare the properties of the tracks with those of thin films, we were striving to similar thicknesses. Therefore multiple layers were printed without any thermal treatment in between (figure 8.6). By increasing the number of coatings, the tracks also became wider. Double printed tracks maintained their shape, while quadruple printed track had an irregular shape. The broadening of the multiple printed tracks can be explained by the different wetting properties of ink. The wetting of the ink on a bare substrate and the ink with the printed track are different, resulting in ink spreading over the tracks which broadens the final pattern. Another explanation can be found in the fact that the contact line isn't pinned anymore. Maybe a large addition of ink can neutralise the contact line pinning, resulting in spreading of the ink.

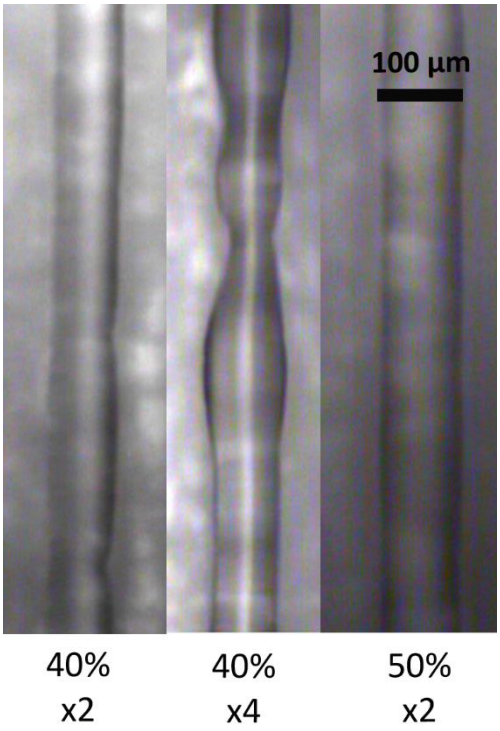

Figure 8.6 Printing of AZO tracks with ink A3%D on a method 3 cleaned substrate. Varying overlap ratios and the number of prints. The temperature of the ink was fixed at 28°C, while the substrate's temperature was 50°C. The ink was fired at 9.4 V with a frequency of 1 kHz.

The double printed tracks with overlap ratios of 40 and 50% were fully processed under the same conditions as the thin films (cfr. chapter 6 & 7). Both AZO tracks have a thickness of 37 nm. The tracks printed with an overlap of 40% have a width of 70 µm while the ones printed with an overlap of 50% have a width of 100 µm (figure 8.7). Attempts to increase thickness by multiple deposition, resulted in irregular and/or interrupted patters which insinuates that the pinning of the contact line doesn't take place when the amount of printed ink increases dramatically.

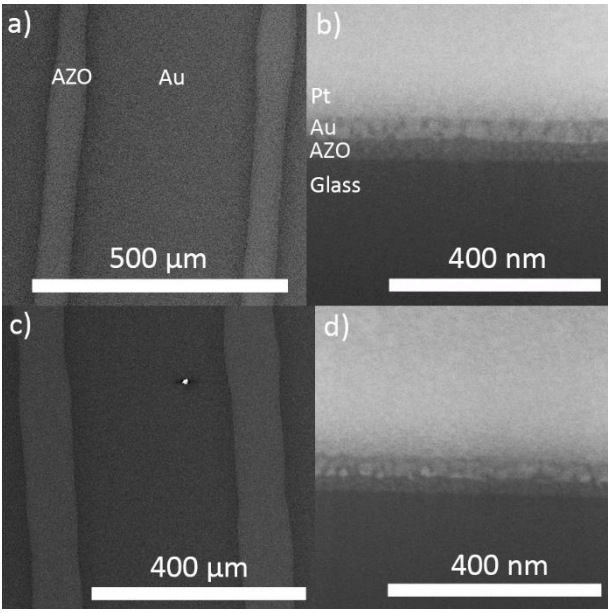

Figure 8.7 SEM images of AZO printed tracks with an overlap ratio of a) & b) 40% double printed and c) & d) 50% double printed.

8.3.2 Printing of AZO patterns with ink F3%D

Thicker patterns may be deposited by increasing loading of the ink. Therefore, an ink was synthesised starting from a Zn precursor solution containing 1 mol L^{-1} Zn^{2+} ions (solution F) which is twice as much as solution A. The temperature of the cartridge was kept at 28°C and the ink was fired at 10.1 V with a frequency of 1 kHz. The most homogeneous patterns printed with ink F3%D were obtained by printing on a heated substrate at 50°C. A double printed track with an overlap ratio of 30% results in a 80 µm wide and 65 nm thick pattern (figure 8.8). A gold coating was sputtered on top of the samples to avoid charging during SEM imaging. This made a close-up of the printed patterns impossible, because the gold coating is covering the AZO pattern and is imaged instead. The cross-sectional view at the centre of a pattern shows a thickness of 65 nm containing multiple pinholes. No sign of an oriented top layer as observed in the thin films is visible.

Profilometry measurements showed no coffee staining and confirmed the width of the track at 80 µm (figure 8.9).

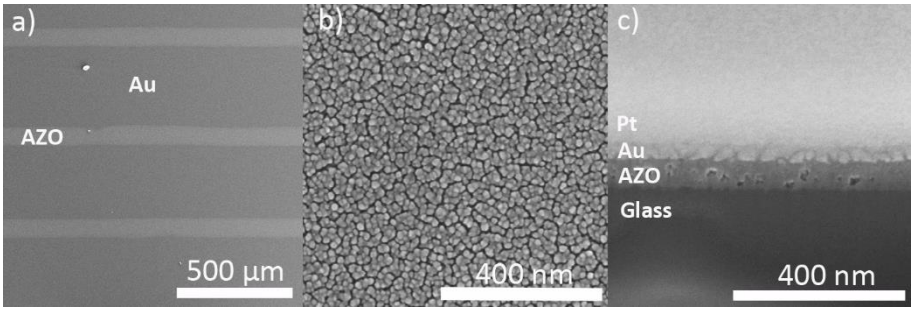

Figure 8.8 SEM images of AZO tracks printed with ink F3%D, fired at 10.1 V with a frequency of 1 kHz. The tracks are double printed with an overlap ratio of 30%: a) overview of the printed tracks, b) close-up of the surface of one track and c) cross-sectional view of one AZO track.

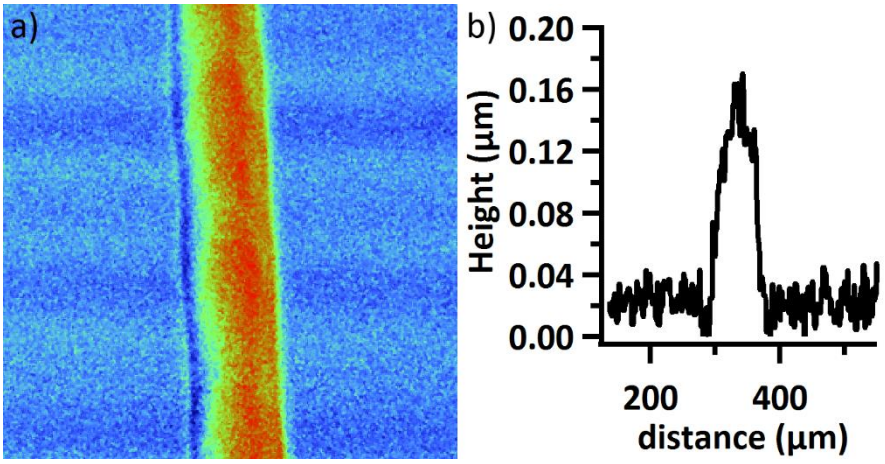

Figure 8.9 Profilometry of a printed AZO track with ink F3%D, fired at 10,1 v with a frequency of 1 kHz. The tracks are double printed with an overlap ratio of 30%: a) image of an AZO track, b) height profile of the printed pattern.

As illustrated in figure 8.10, the sides of the printed AZO patterns aren't perpendicular to the substrate. By cross-sectional imaging it is visualized that the height is gradually increasing. It takes 17 µm before the maximum height of the pattern is obtained. This could be expected from a contact angle of 41° and the broadening of the pattern after the second print. During the second print the ink will spread over the first deposited pattern, resulting in a less steep increase of its slope.

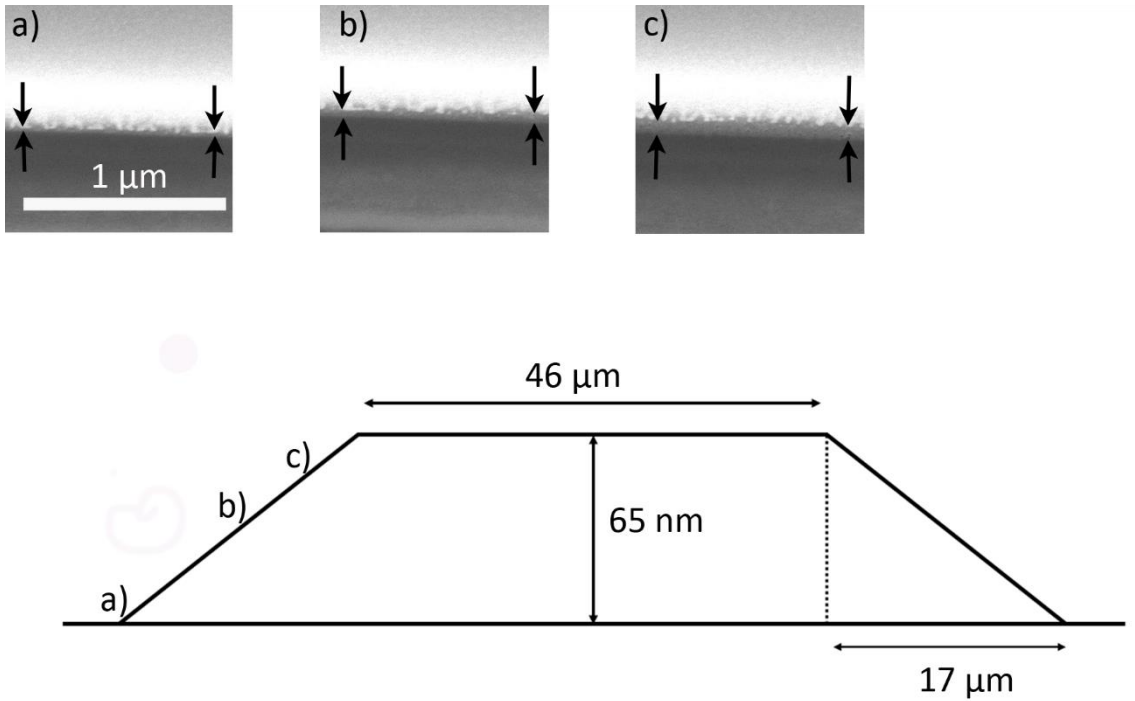

Figure 8.10 Schematic of the printed AZO track with ink F3%D.The cross-sectional views of points a), b) and c) at the sketch are shown above, where the AZO layer is marked by black arrows.

The printed pattern was analysed by XRD and the resistivity is measured but no results could be extracted. The diffractogram doesn't show any reflection and no resistivity could be measured due to a too high resistance. The absence of a oriented top layer can explain the lack of any reflections and the too high resistance. Less matter is present to reflect the X-rays compared to a completely covered substrate. In chapter 7, we already assumed that the top layer has the main contribution to the electrical properties of the thin films which can be confirmed here. Also, one should consider that the presence of defects inside the coating can enormously affect the resistance of the printed patterns. If a defect is present in a thin film, enough matter surrounding it can alter the pathway of the charge carriers. However, defects present in narrow patterns can affect the resistivity enormously as the matter surrounding it is limited.

8.4 Conclusion

Printing of AZO patterns was successful on heated substrates at 50°C. By printing ink A3%D with a droplet overlap ratio of 50% resulted in AZO tracks of 43 µm wide and 35 nm thick. An attempt to increase the thickness by multiple prints failed. Two consecutive prints led to a track with a width of 90 to 100 µm and a thickness of 37 nm. More consecutive prints resulted in irregular shape patterns. Increasing the loading of the ink can increase the amount of material deposited by a single print. Therefore, we printed AZO patterns with a ink containing 1 mol L^{-1} Zn^{2+} ions (ink F3%D). A double printed pattern with a droplet overlap ratio of 30% led to an 80 µm wide and 65 nm thick pattern. XRD measurements did not show any reflections and resistivity measurements couldn't be performed due to the high resistance of the printed patterns.

8.5 Reference list

1. Pasquarelli, R.M., D.S. Ginley, and R. O'Hayre, *Solution processing of transparent conductors: from flask to film.* Chemical Society Reviews, 2011. **40**(11): p. 5406-5441.
2. Kent, J. and A. Ravid, *Projective capacitive touchscreen*. 2001, Google Patents.
3. Hwang, T.-H., et al., *A Highly area-efficient controller for capacitive touch screen panel systems.* Ieee Transactions on Consumer Electronics, 2010. **56**(2): p. 1115-1122.
4. Sleeman, P., et al., *Capacitive Touch Screen with Noise Suppression*. 2010, Google Patents.
5. Zhang, W. and K.M. Krishnan, *Epitaxial patterning of thin-films: conventional lithographies and beyond.* Journal of Micromechanics and Microengineering, 2014. **24**(9).
6. Lee, H.H., K.S. Chou, and K.C. Huang, *Inkjet printing of nanosized silver colloids.* Nanotechnology, 2005. **16**(10): p. 2436-2441.
7. Feys, J., et al., *Ink-jet printing of YBa2Cu3O7 superconducting coatings and patterns from aqueous solutions.* Journal of Materials Chemistry, 2012. **22**(9): p. 3717-3726.
8. Arias, A.C., et al., *All jet-printed polymer thin-film transistor active-matrix backplanes.* Applied Physics Letters, 2004. **85**(15): p. 3304-3306.
9. Smith, P.J., et al., *Direct ink-jet printing and low temperature conversion of conductive silver patterns.* Journal of Materials Science, 2006. **41**(13): p. 4153-4158.
10. Moon, Y., et al., *Effect of contact angle and drop spacing on the bulging frequency of inkjet-printed silver lines on FC-coated glass.* Journal of Mechanical Science and Technology, 2014. **28**(4): p. 1441-1448.
11. Davis, S.H., *Moving contact lines and rivulet instablities.* . Journal of Fluid Mechanics, 1980. **98**(MAY): p. 225-242.
12. Schiaffino, S. and A.A. Sonin, *Formation and stability of liquid and molten beads on a solid surface.* Journal of Fluid Mechanics, 1997. **343**: p. 95-110.
13. Derby, B., *Inkjet printing of functional and structural materials: fluid property requirements, feature stability, and resolution*, in *Annual Review of Materials Research, Vol 40*, D.R. Clarke, M. Ruhle, and F. Zok, Editors. 2010. p. 395-414.
14. Duineveld, P.C., *The stability of ink-jet printed lines of liquid with zero receding contact angle on a homogeneous substrate.* Journal of Fluid Mechanics, 2003. **477**: p. 175-200.
15. Derby, B., *Inkjet printing ceramics: From drops to solid.* Journal of the European Ceramic Society, 2011. **31**(14): p. 2543-2550.
16. Dou, R., et al., *Ink-jet printing of zirconia: Coffee staining and line stability.* Journal of the American Ceramic Society, 2011. **94**(11): p. 3787-3792.
17. Deegan, R.D., et al., *Capillary flow as the cause of ring stains from dried liquid drops.* Nature, 1997. **389**(6653): p. 827-829.
18. Savino, R., D. Paterna, and N. Favaloro, *Buoyancy and Marangoni effects in an evaporating drop.* Journal of Thermophysics and Heat Transfer, 2002. **16**(4): p. 562-574.
19. Hu, H. and R.G. Larson, *Marangoni effect reverses coffee-ring depositions.* Journal of Physical Chemistry B, 2006. **110**(14): p. 7090-7094.
20. Feys, J., *Digitally printed supercondutiong coatings and patterns* in *Department of Inorganic and Physical Chemistry*. 2014, Ghent University Ghent. p. 174.
21. de Gans, B.J. and U.S. Schubert, *Inkjet printing of well-defined polymer dots and arrays.* Langmuir, 2004. **20**(18): p. 7789-7793.
22. Zhang, Y., et al., *Shape changes during the drying of droplets of suspensions.* Langmuir, 2008. **24**(8): p. 3752-3758.

Concluding remarks and future perspectives

The transparent conductive thin film market is growing exponentialy, where ITO is dominating with a market share of more than 90%. However, the high cost and low abundance of indium promote the use of alternative transparent conductive materials. A promising alternative is doped ZnO. When ZnO is doped with Al, In or Ga excellent opto-electrical properties are obtained by vacuum deposition methods. However, atmospheric deposition methods are more attractive when they can provide a scalable and cost-efficient production process. Chemical solution deposition is one of those atmospheric processes what can be used to deposit doped ZnO thin films. By making use of a water based system, a cheap and environmentally friendly solvent is used. Dissolving metal salts in the solvent and stabilising the metal ions with chelating agents result in a precursor solution that can be used for the deposition of TCFs by spin or dip coating. In this dissertation, the option is taken to study the synthesis of Al doped ZnO deposited via ink jet printing. Aluminium is a cheap and abundant doping element Compared to Ga and In. The use of ink jet printing as deposition process allows the deposition of thin films as well as patterns without etching. Next to this, it is a scalable and versatile method what leads to a higher yield of the used precursors by a controlled deposition of the ink. Nowadays, literature makes use of an organic based solution that is deposited by a multiple coating approach with a thermal treatment in between every coating step. The aim of this research was to use a water based ink for the deposition of Al doped ZnO thin films and patterns. Hereby, we strived to a single deposition approach what is beneficial to the scalability of the process.

This research started with the synthesis of an ink which is the combination of an Al and Zn precursor solution. Aluminium chloride and aluminium nitrate were used as Al source. Both were stabilised with malonic acid or citric acid. Zinc acetate was used as Zn source and was stabilised by the addition of formic acid. An AZO precursor solution was synthesised by mixing one of the diverse Al precursors solutions with the Zn precursor solution. Solid state Al NMR showed us that the use of aluminium nitrates is more beneficial for the electrical properties of the AZO. Compared to the aluminium chloride precursor solutions, more substitutional Al and less octahedrally coordinated Al is obtained what is resulting in higher electrical conductivity.

The selected precursor solutions were examined towards printability. The physical parameters of the ink such as density, viscosity and surface tension influence the jetting behaviour of the ink. Unmodified inks show the formation of satellite droplets that merged later on with the main droplet. By adding small amounts of ethanol, the viscosity and surface tension are modified to improve jetting. Now, single droplets are jetted without the formation of any satellite droplets. Not only the jetting of the ink was positively affected by the addition of ethanol. Also, the wetting of the ink with the glass substrate changed as a function of the added ethanol concentration. The contact angle dropped from 12° till less than 5° if 10 v% of ethanol was added. The good wetting of the ink on the substrate allowed the deposition of homogeneous thin films by ink jet printing.

Once a thin film is deposited, it will be subjected to a thermal process. Here, the stabilised metal ions are converted to metal oxides (thermal oxidation). In this stage, the deposited films are dried after deposition on a hotplate and finally treated in a tube furnace till 500°C under a dry or wet 200 ppm O_2 in N_2 atmosphere. It was found that the drying temperature is crucial towards the morphology, crystallinity and the properties of the AZO coating because it is changing the amorphous fraction of the thin film. High drying temperature led to flash evaporation of unreacted components and the decomposition of the formed metal-complexes, leading to the formation of unwanted secondary phases. Low drying temperature allowed the formation of amides during the thermal process. An optimum was found at 120°C. Once the films are dried and placed in the tube furnace, a controlled thermal process is applied till 500°C. It is noted that the humidity of the processing atmosphere affected the final properties of the AZO coatings. Depending on the used ink a dry of wet processing atmosphere positively affected the final properties. In case of the ink Ax%B10 (containing aluminium nitrate and malonic acid) the best results were obtained by bubbling the atmosphere through 2 glass bottles containing water at 20°C, while ink Ax%D10 (containing aluminium nitrate and citric acid) showed the best results by dry processing. The thermal oxidation process was followed by a thermal activation in Ar/5% H_2 at 450°C. During this process multiple events are happening: (1) the adsorbed oxygen is getting desorbed, (2) more oxygen vacancies are created, (3) less octahedral coordinated Al is noted and (4) most likely a higher amount of substitutional Al is obtained. These events are contributing to a decrease of the resistivity by a factor 1000.

The dopant concentration has an influence on the number of generated free carriers. Therefore, the opto-electrical properties of the AZO coatings were monitored as a function of the dopant concentration for both systems (ink Ax%B10 and ink Ax%D10). An optimum was found at 3 at% AZO for both systems, respectively 2.54 x 10^{-2} Ω cm for the aluminium malonate and 2.41 x 10^{-2} Ω cm for the aluminium citrate ink. Both types of AZO coatings have an average optical transmittance in the visual range of the spectrum of more than 90%. However, both have a different top layer morphology and crystallinity, a TEM analysis showed a similar build up. These coatings have a dense region at the interface with the substrate which is gradually evolving in a more porous region. On top of this a dense *c*-axis oriented layer is obtained. It is suggested that these thin films are metastable as the top layer is poor of Al and the other regions contain more than 4 at% Al without the formation of any secondary phases. Still, the mechanism behind it is unclear. Also, it is believed that the top layer has the largest contribution to the electrical properties of these coatings.

In the last chapter, printing of AZO patterns is discussed. Printing of AZO patterns was done by using ink A3%D without the addition of ethanol. By printing on heated substrates (50°C) homogenous prints were obtained and no bulging was present. Printing with a droplet overlap ratio of 40% resulted in 45 µm wide and 35 nm thick tracks. By multiple prints the tracks got wider and maintained their height or irregular shapes were observed if too much ink was deposited. Doubling the concentration of the ink resulted in 80 µm wide and 65 nm thick AZO tracks. No coffee staining was observed. Nevertheless, no resistivity could be measured.

Concluding, we were successful in printing AZO layers and tracks by a single deposition step without any addition a heat treatment in between two or more depositions. The printed thin films have an average thickness of 80 nm. The best results are obtained with a doping concentration of 3 at% Al. We also showed that printing of AZO tracks is possible. The tracks are 80 µm wide and 65 nm thick but need improvements of the electrical properties.

This work showed that chemical solution deposition of AZO thin films by a single coating process can be a promising approach. Combining CSD processing with ink jet printing even allows the deposition of patterns. Nevertheless, further research is necessary. The scope of further research can be as follows: (1) One

can study more in detail the influence of the **precursor chemistry** on the **incorporation of Al in the ZnO matrix and the electrical active sites**. This work showed that the use of precursor salt as chelating agent have a large influence on the doping of ZnO. Expanding the knowledge about the chemistry behind this process can yield to a more efficient doping process. An in-depth study based on the formed complexes and their decomposition will result in a better understanding of the chemistry behind the doping process. Combining Raman and FTIR spectroscopy, solid and liquid ^{27}Al NMR and TGA measurements coupled with mass spectroscopy should help to understand this all. (2) **Understanding** the reason for the **cross-sectional morphology** of the already synthesised thin films can help to lower the resistivity of these films. of t it can only of what happens during the deposition of these AZO thin films. A more homogeneous thin film can improve the overall performance. Most likely, the decomposition of the ink is crucial towards the formation of the present morphology. Therefore, a quench study combined with TEM measurements is advised. These results will lead to a further optimisation of the thermal process or the ink's composition. The influence of the ink chemistry can be studied in more detail, linking the formed complexes to the opto-electrical and structural properties of AZO thin films. Optimising the thermal process can lead to a more controlled decomposition of the ink. This can not only affect the doping of ZnO but also the morphology and crystallinity of the obtained AZO thin films. If further research is insinuating that the high carbon content of during the decomposition of the ink is leading to phase separation, one can select another solvent. In that case, ethanol will be favoured. The precursor will be less sensitive to hydrolysis and less additives need to be added to preserve its stability. (3) More attention can be paid to **printing of complex patterns**. The knowledge build-up about printing of tracks can be transferred. Up till now, only highly resistive AZO track could be printed. An improved ink or thermal process may result in conductive AZO tracks and patterns. Still, more research needs to be performed on printing of complex patterns. Establishing patterns and tracks with steeper edges would be advise. At the moment 40 up to 50% of the printed tracks consist out of a homogeneous, flat region. Steeper edges will increase the resolution of these tracks. Still, other important questions need to be answered: Will patterns existing out of multiple droplets next to each other maintain their shape or will they deform? How will the edges of a complex pattern look like? What is the minimal pitch between 2 patterns?

Samenvatting

De markt van transparant geleidende dunne films is exponentieel groeiend. Indium tin oxide heeft een marktaandeel van meer dan 90%. De hoge kost en lage abundantie van indium stimuleren echter het gebruik van alternatieve transparante, geleidende materialen. Veel belovende alternatieven zijn gedoteerde ZnO materialen. Indien ZnO gedoteerd wordt met Al, In of Ga worden excellente opto-elektrische eigenschappen bekomen bij het gebruik van vacuüm depositiemethodes tijdens het fabricageproces. Depositiemethodes waarbij een atmosferische druk gehandhaafd wordt, zijn aantrekkelijker indien deze deel uitmaken van een schaalbaar en kostenefficiënt proces. De depositie van oplossingen met geschikte precursoren past perfect in dit plaatje. Door gebruik te maken van waterige oplossingen, wordt een goedkoop en milieuvriendelijk solvent aangewend. Verder maakt deze oplossingsmethode gebruik van het oplossen van metaalzouten in het solvent. Om de opgeloste metaalionen te stabiliseren worden chelerende componenten toegevoegd. De finale oplossing kan dan aangewend worden voor de depositie van transparante, geleidende dunne films door een spincoat of dipcoat procedé. Dit werk opteert om de synthese van Al gedoteerd ZnO dunne lagen afgezet via inkjet printen te onderzoeken. In vergelijking met Ga en In is Al een goedkoop en vrij beschikbaar element om te doteren en het gebruik van de inkjet printen als depositie procedé laat het toe om zowel dunne films als patronen af te zetten zonder een additionele etsprocedure. Bovendien is het een schaalbaar en veelzijdig proces wat een gecontroleerde depositie van de inkt toelaat. Dit leidt tot een hogere opbrengst van de gebruikte inkt. Tot op heden maakt de geraadpleegde literatuur vaak gebruik van oplossingen die organische solventen bevatten. Daarnaast wordt een coatingsproces gehanteerd, bestaande uit verschillende depositiestappen met telkens een thermische behandeling tussen deze stappen.

In dit onderzoek wordt er getracht om Al gedoteerde ZnO dunne films of patronen te bekomen door middel van het afzetten van waterige inkten. Daarnaast streven we naar een enkelvoudige depositiestap. Dit zal de schaalbaarheid van het gebruikte procedé ten goede komen. De keuze van een geschikte inkt was de eerste mijlpaal in dit onderzoek. Deze inkt was een mengsel van een Al en Zn precursoroplossing. Als Al-bron werden zowel aluminiumchlorides als aluminiumnitraten aangewend. Beiden werden

gestabiliseerd met behulp van malonzuur en citroenzuur. Als Zn-bron werd zinkacetaat gebruikt. De additie van mierenzuur helpt de Zn^{2+} ionen te stabiliseren. Door één van de Al-precursoroplossingen te mengen met de Zn precursoroplossing werd een Al gedoteerd ZnO precursoroplossing bekomen. Vaste stof NMR toonde aan dat het gebruik van aluminiumnitraten betere elektrische eigenschappen zou opleveren. Ten opzichte van precursoroplossingen met aluminiumchlorides, resulteerde het gebruik van aluminiumnitraten in een hogere percentage aan gesubstitutioneerd Al en een lagere percentage octahedrisch omringd aluminium. Dit leidt tot een hogere elektrische geleidbaarheid.

De geselecteerde precursoroplossingen werden verder onderzocht naar hun printbaarheid. Fysische parameters zoals de dichtheid, viscositeit en oppervlaktespanning beïnvloeden de printbaarheid van de inkt. De niet gemodificeerde precursoroplossingen tonen de vorming van satellietdruppels tijdens het printproces, die in vlucht terug samenkomen met de primaire druppel. Echter, door kleine hoeveelheden ethanol toe te voegen aan de precursoroplossing werd de viscositeit en oppervlaktespanning positief beïnvloed. Nu was het mogelijk om druppels te printen zonder de vorming van satellietdruppels. Naast de verbeterde printbaarheid wordt ook door het toevoegen van ethanol de bevochtiging van het substraat verbeterd. Bij een additie van 10 v% aan ethanol daalde de contacthoek van 12° naar 5°. Deze goede bevochtiging van de inkt met het substraat, leidde tot de depositie van homogene dunne films met behulp van inkjet printen.

Eenmaal een natte film is afgezet op het substraat, wordt deze onderworpen aan een thermisch proces. Tijdens het thermisch proces worden de gestabiliseerde metaal ionen omgezet tot metaaloxides (thermische oxidatie). Eerst worden deze films gedroogd, waarna ze thermisch behandeld worden tot 500°C in een buisoven bij droge of natte atmosfeer (200 ppm O_2 in N_2). De droogtemperatuur bleek een cruciale invloed te hebben op de finale morfologie en kristalliniteit en dus ook op opto-elektrische eigenschappen van de AZO coating. De droogtemperatuur heeft een invloed op de amorfe fractie van de dunne film en beïnvloedt op deze manier de morfologie en kristalliniteit. Hoge droogtemperaturen leidde tot een simultane verdamping van de niet gereageerde componenten en de decompositie van de gevormde metaalcomplexen. Dit leidde tot de formatie van een ongewenste secondaire

fase. Lage droogtemperaturen laten de vorming van amide toe tijdens het droogproces. Een optimale droogtemperatuur werd gevonden bij 120°C. Na het droogproces werden de samples in de buisoven geplaatst waar ze werden onderworpen aan een gecontroleerd thermisch proces. De vochtigheid van de gekozen atmosfeer beïnvloedde de finale eigenschappen van de Al gedoteerd ZnO coating. Afhankelijk van de gebruikte inkt, werden de beste resultaten bekomen met een droge of natte atmosfeer. In het geval van inkt Ax%B10 (bevat aluminiumnitraat en malonzuur) werden de beste resultaten verkregen indien de gekozen atmosfeer door 2 glazen flessen met water op 20°C werd geborreld. Echter, inkt Ax%D10 (bevat aluminiumnitraat en citroenzuur) leverde de beste resultaten indien de coatings met een droge atmosfeer werden behandeld. De thermische oxidatie werd gevolgd door een thermische activatie in een Ar/5% H_2 atmosfeer bij 450°C. Tijdens dit proces deden zich verschillende ontwikkelingen voor: (1) de geadsorbeerde zuurstofmoleculen worden gedesorbeerd, (2) er worden meer zuurstofvacatures gecreëerd, (3) er wordt minder octahedrisch omringd Al waargenomen en (4) hoogstwaarschijnlijk is er meer substitutioneel Al aanwezig in de ZnO matrix. Dit alles draagt bij tot een verlaging van de resistiviteit met een factor 1000.

De dopantconcentratie heeft een invloed op het aantal verkregen vrije ladingsdragers. Hierdoor worden de opto-elektrische eigenschappen van de Al gedoteerd ZnO coatings gevolgd in functie van de dopantconcentratie. Voor beide systemen (inkt Ax%B10 en inkt Ax%D10) werd een optimum gevonden bij een dotering van 3 at%. Een resistiviteit voor coatings gesynthetiseerd uit inkt A3%B10 en A3%D10 zijn bijna identiek, namelijk 2.54 x 10^{-2} Ω cm en 2.41 x 10^{-2} Ω cm. Beide coatings hebben een gemiddelde optische transmissie in het zichtbare deel van het spectrum die groter is dan 90%. De morfologie en kristalliniteit van deze coatings zijn verschillend. TEM analyse toonde echter aan dat een gelijkaardige opbouw aanwezig is. De regio van de coating aan de *interface* met het substraat is dens en polykristallijn. Geleidelijk aan gaat deze regio over in een poreus gedeelte met een dens en *c*-as georiënteerde laag hier bovenop. Dit kan wijzen op een metastabiel systeem, aangezien de toplaag Al arm is, terwijl de andere regio's meer dan 4 at% Al bevatten. Desondanks is het mechanisme achter dit fenomeen niet gekend. We geloven ook dat de toplaag van de coating het grootste aandeel heeft in de verkregen elektrische eigenschappen.

Het laatste hoofdstuk handelt over het printen van patronen uit Al gedoteerd ZnO. De patronen werden geprint met een inkt waaraan geen ethanol werd toegevoegd. Het printen op verwarmde substraten (50°C) leverde homogene patronen op van 45 µm breed en 35 nm dik. Het afzetten van verschillende prints op elkaar leverde bredere, inhomogene patronen op met identieke hoogte. Door de concentratie van de inkt te verdubbelen werden patronen bekomen met een breedte van 80 µm en een dikte van 65 nm. Geen koffievlekeffect kon worden geobserveerd, maar ook kon er geen resistiviteit opgemeten worden.

We kunnen concluderen dat AZO lagen en patronen op een succesvolle manier afgezet zijn in één depositiestap zonder een extra warmtebehandeling tussenin. De geprinte coatings hebben een gemiddelde dikte van 80 nm waarbij de beste resultaten verkregen werden met een dopantconcentratie van 3 at%. Het printen van patronen was succesvol met als resultaat patronen van 80 µm breed en 65 nm dik.

Desalniettemin is progressie nog steeds mogelijk. Hiervoor moet een betere kennis verkregen worden omtrent de volgende zaken: (1) Het doteren van ZnO in fucntie van de precursorchemie. Het belang van de Al-bron en gevormde complexen is reeds aangetoond. Echter, het uitbreiden van de kennis en een meer gedetailleerde studie kan leiden toch een efficiënter proces om ZnO te doteren. (2) Het begrijpen van de processing die leiden tot een dunne film met een inhomogene dwarsdoorsnede kan een oplossing bieden tot dit probleem. Echter, een intense quench-studie gekoppeld met TEM onderzoek zullen noodzakelijk zijn om dit alles te begrijpen. Vervolgens kan er geopteerd worden om in te spelen op het thermisch proces of de gekozen inkt. (3) Het printen van complexe en hoge resolutie patronen is werkpunt. Het reeds verwezenlijkt onderzoek leidde tot patronen met traag oplopende randen. Idealiter zouden deze randen loodrecht moeten oplopen.

Appendix: Experimental methodology

AZO Precursor characteristics

Overview precursor solutions

Precursor solution	Metal salt	Chelating agent	Additives
Solution A	Zinc acetate	Formic acid	Ethanolamine
Solution B	Aluminium nitrate	Malonic acid	Formic acid & ethanolamine
Solution C	Aluminium chloride	Malonic acid	Formic acid & ethanolamine
Solution D	Aluminium nitrate	Citric acid	Formic acid & ethanolamine
Solution E	Aluminium chloride	Citric acid	Formic acid & ethanolamine

The inks are named after their content. For example, ink A3%B10 is containing solution A, an amount of solution B which results in 3 at% Al doped ZnO and 10 v% of ethanol.

Speciation plots of formed complexes

Speciation plots helped us to predict the chelating behaviour of the added chelates as a function of pH. Therefore, Hyss-2009 software [1] was used to generate speciation plots based on complexation constants and compositional details of the precursor solution.

Infrared spectroscopy

Infrared spectroscopy is used to determine the presence of metal-chelates in the aqueous precursor solutions. Each structure absorbs specific energy (resonant frequencies) which is related with the transition energy of the bond or group that vibrates. As shown in chapter 4, these specific vibration modes are used to characterise the presence or interaction with specific molecules. The aqueous precursors solutions are characterised by ATR-FTIR (Perkin Elmer Spectrum 100). Gels of the metal precursors and metal-ion free blanks are measured in open air. The pH was adapted to the final pH of the ink.

Nuclear Magnetic Resonance (NMR) spectroscopy

Liquid NMR measurements are performed to identify the synthesis species and to determine the diffusion coefficient of the components in the precursor solution. By comparing this with the data obtained from the metal-ion free blanks, one can conclude if a component is interacting with the metal ions in precursor solution. The NMR measurements were recorded on a Bruker Avance III Spectrometer operating at a 1H frequency of 500.13 MHz and equipped with a BBI-Z probe. The sample temperature was set to 298.2 K. One dimensional (1D) 1H spectra were acquired using standard pulse sequences from the Bruker library. For the quantitative 1D 1H measurements, 64k data points were sampled with the spectral width set to 16 ppm and a relaxation delay of 30 sec. Diffusion measurements (2D DOSY) were performed using a double stimulated echo sequence for convection compensation and with monopolar gradient pulses. Smoothed rectangle gradient pulse shapes were used throughout. The gradient strength was varied linearly from 2-95% of the probe's maximum value (calibrated at 50.2 G/cm) in 32 or 64 steps, with the gradient pulse duration and diffusion delay optimized to ensure a final attenuation of the signal in the final increment of less than 10% relative to the first increment. 1D spectra were multiplied with an exponential window function. Concentrations were obtained using the Digital ERETIC method.

Fluid characteristics

As shown in chapter 5, fluid characteristics such as density , viscosity and surface tension affect the printability of the ink. The viscosity was measured with a Haake Rheostress RS600 rheometer. A small amount of the ink is placed between 2 plates of 60 mm. The height in between the plates and the pre-set rotation speed cause a certain shear rate in the sample. The torque needed to maintain the shear rate relates to the viscosity. The distance between the plates was varied between 200, 150, 100 and 50 µm which led to shear rates of 13650, 15500, 28400 and 45300 s^{-1}.

The density of the solutions was determined by using a 10 mL glass pycnometer (Duran).

The surface tension of the ink was obtained by making use the pendant drop method measured on a Krüss Drop Shape Analyzer 30. Here, the droplet is generated from a syringe needle with a known diameter. The generated droplet has to be as large as possible for a proper surface tension determination. By using the Young-Laplace model, the characteristic shape and size of the droplet is used to calculate the surface tension. An average value is obtained by performing the experiment multiples time.

Printing devices

The AZO thin films were printed with a computer controlled XY-plotter equipped with a 30 µm orifice of MicroFab Technologies Inc. (MJ-ABP-01). The AZO tracks were printed with a Dimatix Materials Printer (Fujifilm Dimatix Inc., DMP-2831) This setup makes use of disposable cartridges equipped with orifices with a diameter of 9 and 22 µm. During this dissertation a 22 µm orifice is used.

Drop formation visualisation

The jetted droplets are visualized to distinct the effect of the waveform on the droplet formation. The formation of satellite droplets or one single droplet were visualised with a combination of a digital camera (Allied Vision Technologies, Stingray F-125B) equipped with a telecentric zoom lens (ML-Z07545, Moritex) and a strobed collimated LED illumination. The LED is mounted behind the nozzle. Pulsed illumination for 1 µs with a certain delay time after actuating the printhead allowed imaging the printed droplets. A quantitatively analysis of each image series in terms of droplet volume and velocity was performed with custom-written software (Dr. Simon Hopkins, University of Cambridge).

Each waveform was optimized by making use of the droplet visualisation technique. Finally, an optimised waveform allowed printing of single droplets for every ink discussed in chapter 5.

Droplet-substrate interaction

As demonstrated in chapter 5, diverse cleaning method have affected the wetting of the substrates. One of the characteristic parameters to describe the

droplet-substrate interaction is the contact angle. Contact angle measurements are performed on cleaned substrate where 1 µL droplets are dosed through a syringe with known diameter. All contact angles represented in this dissertation are an average of 3 measurement on different substrate. The contact angle measurements are performed on a Krüss Drop Shape Analyzer 30, where the drop shape is capture by camera. Sequentially, a circular or Young-Laplace model is used to fit and retract the contact angle.

The droplet substrate interaction of the printed droplet is studied by optical profilometry (Veeco NT9080). This technique makes use of white light interferometry, where the obtained contrast is matched to the surface height. In this work, optical profilometry is used to determine the shape and size of freshly printed droplets.

Thermal analysis

A thermal analysis is performed to study the physical and chemical changed of the samples as a function of temperature. In this dissertation, the thermogravimetric analysis (TGA) and differential thermal analysis (DTA) are combined to study the decomposition behaviour of the ink or to determine the water content of the starting precursors salt. A TGA curve has the mass loss of the sample plotted as a function of the temperature, whereas a DTA curve has the temperature difference of the sample with a reference sample (Al_2O_3) plotted as a function of the temperature. Combining both data, result in the assignment of a mass loss to a exo- or endothermic event.

The measurements were performed on a Netzsch STA449 F3 Jupiter setup. A small amount of the species (± 10 mg) was subjected to a heating rate of 10 K/min and a 120 mL/min air flow.

AZO thin film and powder characteristics

X-Ray Diffraction (XRD)

The crystallinity and phase composition of AZO thin films and powders were characterised by XRD measurements. A θ-2θ scan was generally used for standard thin film and powder characterisation, whereas rocking curves were to detect the out-of-plane orientation. All XRD analysis of thin films were performed on a Bruker D8 diffractometer (Cu, K_α = 1.5405 Å). The powder

samples were analysed by a Thermo Scientific ARL X' tradiffractometer (Waltham, MA, USA, Cu K_α = 1.5405 Å). The powder samples were side loaded to a special sample holder to reduce preferential orientation effects. TOPAS-Academic V4.1 software [2] was used to perform Rietveld refinement.

1D ^{27}Al NMR

Solid state Al NMR measurements are performed to identify the exact coordination of the Al species inside the ZnO matrix. The spectra were recorded on a Bruker Avance400 spectrometer, using a 4 mm MAS probehead and a spinning frequency of 10 kHz. The length and power level of the rf-pulses were carefully optimised on the sample itself. To collected data are an accumulation of 1536 scans with a recycle delay of 5s.

X-ray Photoelectron Spectroscopy (XPS)

All measurements were recorded on a X-ray photoelectron spectroscopy S-Probe XPS spectrometer with monochromated Al (1486 eV) exciting radiation from Surface Science Instruments (VG). The samples were attached to the sample holder by conducting carbon tape. As severe charging of the sample is observed a nickel grid was used, placed 2 mm above the sample. A low energy electron flood gun 3 eV was used as a neutralizer. Calibration of the spectra was performed by looking to the carbon signal at 284.6 EV.

Focussed Ion Beam – Scanning Electron Microscopy (FIB-SEM)

The analysis of the microstructure such as surface morphology, layer thickness and porosity was performed by FIB-SEM. The layer thickness was studied by cross sectional imaging. Therefore, the area of interest was first covered with electron-beam deposited Pt of 17 x 1.7 x 0.2 µm (2.0 kV, 0.84 nA) and ion-beam deposited Pt of 15 x 2 x 0.3 µm (30.0 kV, 100 pA). Secondly, the cross section was made by cutting an area of 13 x 4 x 2 µm (30.0 kV, 3 nA). As last, the cross-section was cleaned to obtain high quality images through SEM (30.0 kV, 0.3 nA). In this dissertation, a FEI nova 600 Nanolab DualBeam was used to perform FIB-SEM work.

Transmission Electron Microscopy (TEM)

In order to study the morphology of the layer more in detail, TEM analysis is used. TEM imaging happens with accelerating voltages of 80 – 300 kV, meaning that electrons exhibit wavelengths which allow atomic resolution imaging. As the technique is based on the transmission and interaction of the electron beam with matter, an extremely thin species should be obtained. A 100 nm thick lamella of the sample is obtained by the FIB *in situ* lift out procedure [3].

In this work, the samples were analysed by making use of multiple TEM-modes such as high resolution TEM, Selected Area Electron Diffraction (SAED) and Scanning Transmission Electron Microscopy (STEM) combined with Energy Dispersive X-ray Spectroscopy (EDS). Crystallographic information is collected by high resolution TEM and SAED, while chemical information is collected by the combination of STEM and EDX. The measurements were performed on a JEOL 2200 FS microscope operating at 200 kV.

Optical properties of the AZO thin films

The optical properties of the AZO thin films are determined by a PerkinElmer Lambda 850 UV/VIS Spectrometer. The thin films were measured in transmission mode with a step size of 1 nm.

Electrical properties of AZO thin films

The sheet resistance of the AZO thin films was measured with a four point wafer probe (Veeco FPP-5000), while the mobility of the carriers is determined by Hall probe measurements. The latter is based on the Hall effect. The underlying physical principle is the Lorentz force: An electrical current is induced in the AZO thin film parallel to the substrate while a magnetic field is applied perpendicular to the substrate, resulting in charge carriers subjected to the Lorentz force. The electrons will drift away from their initial direction toward the side of the sample, inducing a negative electrical charge on this side of the sample. A potential drop across the two sides of the sample will be obtained, the Hall voltage. By measuring the Hall voltage V_H with known values for the induced current I, the magnetic field B and sheet resistance R_s, one can define the Hall mobility μ:

$$\mu = \frac{|V_H|}{I\ B\ R_s} \qquad \text{Eq.1}$$

For determining the Hall mobility, contacts were fixed at the corners of the samples. These contact should be ohmic. Otherwise the measurements are unreproducible due to charging of the sample. Therefore, a sandwich of Au and In contacts are deposited on the thin films. First, gold contacts of ± 25nm are sputtered, followed by soldering In on top of it. Finally, the contacts of the equipment were fixed at the indium contact. Each represented value of the resistivity, sheet resistance or carrier mobility/concentration is an average of at least 5 measurements. The setup used to measure the Hall mobility of the carriers was in-house made. A magnetic field of 0.3 tesla was used to determine the Hall mobility. A current source of Keithley (6220 Precision current source) and a multimeter of Fluke (8846A 6-1/2 digit Precision multimeter) were used to perform the measurements.

Reference list

1. Gans, P., *HySS2009: Hyperquad Simulation and Speciation*. 2009, Protonic Sofware: http://www.hyperquad.co.uk/hyss.htm.
2. Coelho, A., *TOPAS-Academic,Version 4.1*. 2007, Coelho Software: Brisbane, Austrilia.
3. Montoya, E., et al., *Evaluation of top, angle, and side cleaned FIB samples for TEM analysis.* Microscopy Research and Technique, 2007. **70**(12): p. 1060-1071.

List of publications

A1 publications

- Vernieuwe, K., Feys J., Cuypers, D., & De Buysser, K. (2015). Ink jet printing of aqueous inks for single layer deposition of Al doped ZnO thin films. Journal of the American Ceramic Society. (*submitted*)

- Vernieuwe, K., Cuypers, D., Houthoofd, K. & De Buysser, K. (2015). Thermal processing of aqueous precursor solution for the fabrication of Al doped ZnO thin films. (*in progress*)

- Vernieuwe, K., Cuypers, D., & De Buysser, K. (2015). Printing of Al doped ZnO pattern starting from aqueous ink. (*in progress*)

- Vernieuwe, K., Lommens, P., Martins, J., Van den Broeck, F., Van Driessche, I., & De Buysser, K. (2013). Aqueous ZrO 2 and YSZ colloidal systems through microwave assisted hydrothermal synthesis. *MATERIALS*, *6*(9), 4082–4095.

C1 publications

- Vernieuwe, K., Lommens, P., Van den Broeck, F., Martins, J., Van Driessche, I., & De Buysser, K. (2012). Microwave synthesis of ZrO_2 and yttria stabilize ZrO_2 particles from aqueous precursor solutions. *MRS Proceedings* (Vol. 1449). Presented at the MRS 2012 Spring Meeting, Warrendale, PA, USA: Materials Research Society.

International conference contributions

- Vernieuwe, K., Lommens, P., Van Driessche, I., & De Buysser, K. (2015). Ink jet printing of transparent conductive oxide thin films and patterns. *EMN Ceramics meeting, Abstracts*. Presented at the Energy, Materials, and Nanotechnology (EMN) Ceramics meeting 2015. (*oral presentation*)

- Vernieuwe, K., Feys, J., Lommens, P., Van Driessche, I., & De Buysser, K. (2014). Chemical solution deposition of aqueous Al-doped ZnO precursors via ink-jet printing. *Transparent Conductive Materials, 5th*

International symposium, Abstracts. Presented at the 5th International symposium on Transparent Conductive Materials (TCM 2014). (*oral presentation*)

- Vernieuwe, K., Lommens, P., & De Buysser, K. (2014). Chemical solution deposition via ink jet printing of aqueous Al-doped ZnO precursors. *New Materials, 6th Forum, Abstracts*. Presented at the 6th Forum on New Materials (part of CIMTEC 2014). (*oral presentation*)

- Vernieuwe, K., Lommens, P., Feys, J., Mys, N., & De Buysser, K. (2013). Ink jet printing of transparent conductive oxide thin films. *Sol-Gel, 17th International conference, Abstracts*. Presented at the 17th International Sol-Gel Conference (Sol-Gel 2013). (*poster presentation*)

- Vernieuwe, K., Lommens, P., Martins, J., Van Driessche, I., & De Buysser, K. (2012). Microwave assisted synthesis of zirconia and YSZ colloidal solutions. *E-MRS Fall meeting, Abstracts*. Presented at the E-MRS 2012 Fall meeting. (*oral presentation*)

- De Buysser, K., Lommens, P., Vernieuwe, K., Arin, M., Tomov, R., Glowacki, B., & Van Driessche, I. (2011). Advanced aqueous YSZ inks for ink-jet printing of electrolyte layers in SOFC. *E-MRS Spring meeting, Abstracts*. Presented at the E-MRS 2011 Spring Meeting. (*poster presentation*)

- De Buysser, K., Lommens, P., Arin, M., Vernieuwe, K., & Van Driessche, I. (2010). Aqueous sol-gel processing of YSZ-thin layers. *MRS Spring Meeting, Abstracts*. Presented at the 2010 MRS Spring Meeting, Materials Research Society (MRS). (*poster presentation*)

National conference contributions

- Vernieuwe, K., Lommens, P., Van den Broeck, F., Martins, J., Van Driessche, I., & De Buysser, K. (2012). Synthesis of ZrO2 and YSZ nano-particles for thin film applications. *ChemCYS book of abstracts*. Presented at the Chemistry conference for Young Scientists 2012 (ChemCYS 2012). (*poster presentation*